Bioinspired propeller propulsion : reconfiguration and intermittency

Tristan Aurégan

THÈSE DE DOCTORAT
D'UNIVERSITÉ PARIS CITÉ

Spécialité : Physique

École doctorale n°564: Physique en Île-de-France

réalisée

au Laboratoires de Physique et Mécanique des Milieux Hétérogènes, et Matière et Systèmes Complexes

sous la direction de Benjamin THIRIA et Sylvain COURRECH DU PONT

présentée par

Tristan AURÉGAN

pour obtenir le grade de :

DOCTEUR D'UNIVERSITÉ PARIS CITÉ

Sujet de la thèse :

Propulsion bioinspirée par hélice : reconfiguration et intermittence

Bioinspired propeller propulsion : reconfiguration and intermittency

Présentée et soutenue publiquement le 18 septembre 2023

devant le jury composé de :

Pr.	Camille Duprat	École polytechnique	Rapportrice
Pr.	Médéric Argentina	Université Côte d'Azur	Rapporteur
Pr.	Eva Kanso	University of Southern California	Examinatrice
Pr.	Christophe Eloy	Centrale Marseille	Examinateur
Pr.	Benjamin Thiria	Université de Paris	Directeur
Pr.	Sylvain Courrech du Pont	Université de Paris	Directeur
MCf.	Sophie Ramananarivo	École polytechnique	Membre invité

Résumé

Cette thèse s'intéresse à la propulsion par hélice au travers de deux nouveaux concepts bioinspirés : la reconfiguration et l'intermittence, avec un objectif d'amélioration de l'efficacité de la propulsion. La reconfiguration consiste à rendre les pales souples afin qu'elles se déforment passivement sous l'action de l'écoulement. De récents travaux de Cognet et al. (2017) ont montré que dans le cas d'une éolienne, cette stratégie permet d'extraire de l'énergie dans une large gamme de vitesses de vent. La flexibilité permet à l'éolienne d'adopter passivement une forme optimale, ce qui est actuellement effectué de manière active à l'aide de moteurs.

Le second axe pour améliorer l'efficacité de la propulsion est l'intermittence : une stratégie de locomotion observée chez certaines espèces d'oiseaux et de poissons qui consiste à alterner des phases de propulsion actives (l'animal bat des ailes ou de la queue) et des phases passives (en vol plané ou simplement en se laissant glisser). Cette stratégie semble a priori néfaste pour l'efficacité de la propulsion, car les accélérations et décélérations sont souvent associées à un cout énergétique supplémentaire. Cependant, de précédentes études ont montré que pour certaines espèces, cette stratégie permet au contraire de réduire la consommation énergétique lorsqu'elle est associée à un changement de forme durant la phase passive qui permet de réduire la résistance exercée par le fluide environnant sur l'animal (Weihs, 1974; Li et al. (2021, 2023)). Cette thèse a donc un double objectif : explorer la possibilité de transposer les résultats obtenus sur les éoliennes aux hélices dans l'eau pour les rendre plus efficaces et discuter de l'applicabilité de la stratégie de propulsion intermittente aux hélices.

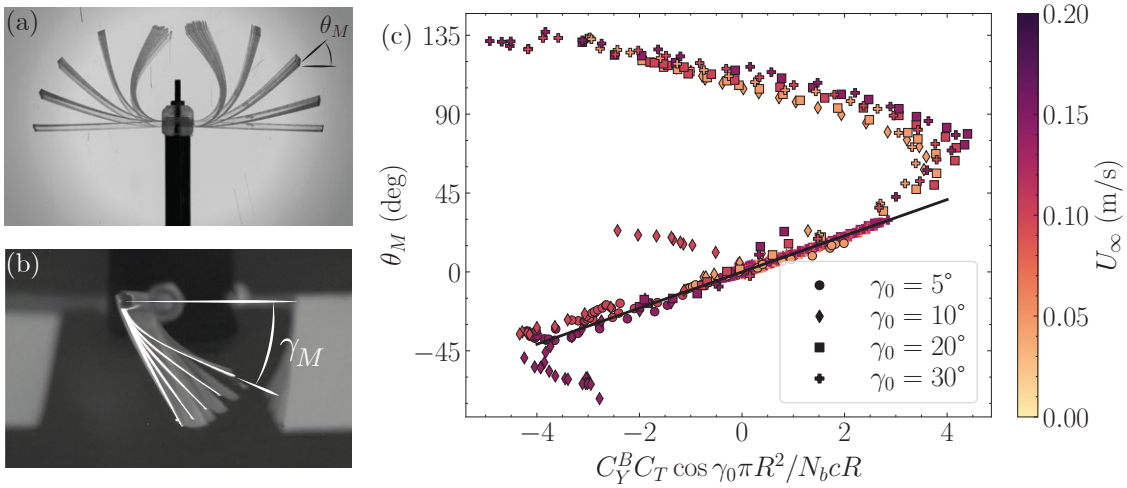

Figure 0.1: (a) Déformation de l'hélice entièrement flexible. Superposition d'images à plusieurs vitesses de rotation, l'écoulement vient du haut de l'image. (b) Déformation de l'hélice avec un bord d'attaque rigide. Superposition d'images à plusieurs vitesses de rotation, l'écoulement vient du haut de l'image. Le bout de la pale est éclairée par un laser. (c) Angle de flexion en bout de pale en fonction d'un nombre de Cauchy modifié par le coefficient de poussée. La couleur indique la vitesse de l'écoulement. Les symboles avec un contour noir correspondent aux pales très flexibles, les autres aux pales légèrement flexibles. La ligne de tendance en noir a une pente de 0.18 rad.

Elle se compose essentiellement de travaux expérimentaux à échelle réduite dans un canal hydrodynamique spécialement conçu à cet effet. Nous utilisons des hélices à géométrie simplifiée pour mettre en valeur les mécanismes physiques importants, au détriment de l'efficacité. Dans un premier temps,

nous explorons le problème d'interaction fluide-structure d'une hélice flexible dans l'eau et mettons en avant les mécanismes clés de la déformation. Puis nous étudions l'efficacité de la propulsion intermittente à l'aide d'une hélice déformable.

Grâce à une première hélice avec des pales entièrement souples ressemblant à des rubans (Fig. 0.1, (a)), nous étudions un nouveau problème d'interaction fluide-structure. Les pales peuvent se plier et se tordre, ces deux rotations étant couplées par le forçage hydrodynamique (dans le cas de nos hélice flexible dans l'eau la force centrifuge est négligeable). Nous mesurons à la fois la déformation de flexion des pales et la force de poussée associée. Selon les conditions précises de l'expérience, d'importantes déformations vers l'amont ou vers l'aval peuvent être observées. Dans la limite des petites déformations, une loi d'échelle basée sur des arguments géométriques permet de prédire la direction et d'estimer l'amplitude de la flexion. La déformation de flexion en bout de pale θ_M pour les déformations modérées vérifie :

$$\theta_M \sim C_Y^B \left(1 + 1/\lambda^2\right) (\gamma_0 - \arctan 1/\lambda), \tag{0.1}$$

avec C_Y^B le nombre de Cauchy de flexion, un nombre sans dimension comparant l'importance relative de la force hydrodynamique par rapport à l'élasticité de la pale. L'angle γ_0 est l'angle de calage de la pale : l'angle entre le pied de pale et le plan de rotation. Enfin, λ est la vitesse de rotation réduite (ou tip speed ratio en anglais, $\lambda = R\Omega/U_\infty$) un paramètre clé de l'étude des rotors.

L'absence de mesure précise de la torsion empêche de prédire exactement la déformation dans le cas des grandes déformations (la pale peut se plier de plus de 90 deg.). Pour dépasser cette limite, nous utilisons la poussée produite par le rotor (à travers le coefficient de poussée C_T) pour estimer le forçage sur les pales. L'angle de flexion en bout de pale vérifie alors :

$$\theta_M \sim C_Y^B C_T \cos\gamma_0 \frac{\pi R^2}{N_b c R}, \tag{0.2}$$

Cette relation met en valeur un lien fort entre la déformation de flexion et la poussée produite par l'hélice : étant donné une géométrie d'hélice, mesurer la déformation permet de déduire la poussée (Fig. 0.1, (c)).

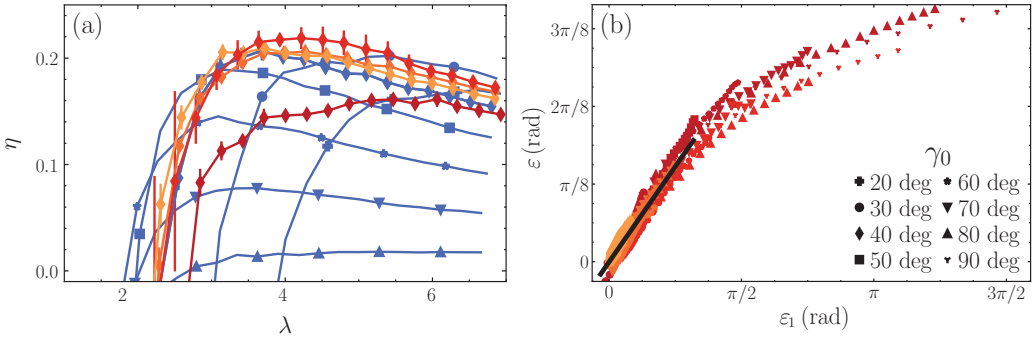

Figure 0.2: (a) Efficacité η de l'hélice en fonction de la vitesse réduite λ. (b) Déformation en bout de pale ε en fonction de son expression théorique ε_1. La couleur indique la flexibilité de la pale : le bleu correspond aux pales rigides et le gradient de jaune à rouge correspond à des pales de plus en plus flexibles. Les symboles correspondent à l'angle de calage γ_0.

Dans un second temps, nous étudions une hélice dont le bord d'attaque est rigide : seule la déformation de torsion est autorisée (Fig. 0.1, (b)). Rendre cette hélice flexible permet de s'adapter passivement aux changements de conditions extérieures si la flexibilité est bien choisie. Cet effet

est par exemple visible dans la Fig. 0.2 (a) où l'on trace l'efficacité de l'hélice η en fonction de la vitesse réduite λ. La performance de l'hélice rigide servant de référence est tracée en bleu pour plusieurs angles de calage γ_0, représentés par différents symboles. Les losanges de jaune à rouge correspondent à des hélices de plus en plus flexibles avec un angle de calage de 40 deg. Dans le cas optimal (losanges rouge clair) l'hélice flexible est plus efficace que l'hélice rigide quelque soit son angle de calage. L'angle de torsion de l'hélice rigide s'adapte passivement, lui permettant de rester efficace dans un large gamme de vitesses réduites $\lambda \in [3, 5.5]$.

Connaître l'angle de la pale par rapport au plan de rotation est ainsi crucial pour déduire l'efficacité de la propulsion. Une modélisation simple de la pale en poutres attachées par des ressorts de torsion au bord d'attaque permet d'obtenir l'équation régissant l'angle de torsion de la pale γ :

$$\gamma(r) = \gamma_0 - C_Y^S u_p^2 \left(C_L(\alpha)\cos\alpha + C_D(\alpha)\sin\alpha\right)\delta_{AC}^{LE}, \tag{0.3}$$

avec C_Y^S le nombre de Cauchy correspondant à la géométrie du problème, u_p la norme locale de la vitesse et α l'angle local d'incidence sur la pale. δ_{AC}^{LE} est la distance entre le point d'application de la force hydrodynamique et le bord d'attaque, et C_L et C_D sont respectivement les coefficients de portance et traînée du profil d'aile utilisé. Un développement limité cette équation nous permet d'obtenir la valeur théorique ε_1 de la déformation en bout de pale $\varepsilon = \gamma_M - \gamma_0$, en loi d'échelle. Cette loi d'échelle est tracée sur la Fig. 0.2 (b) et décrit bien l'évolution de l'angle en bout de pale pour des déformations modérées.

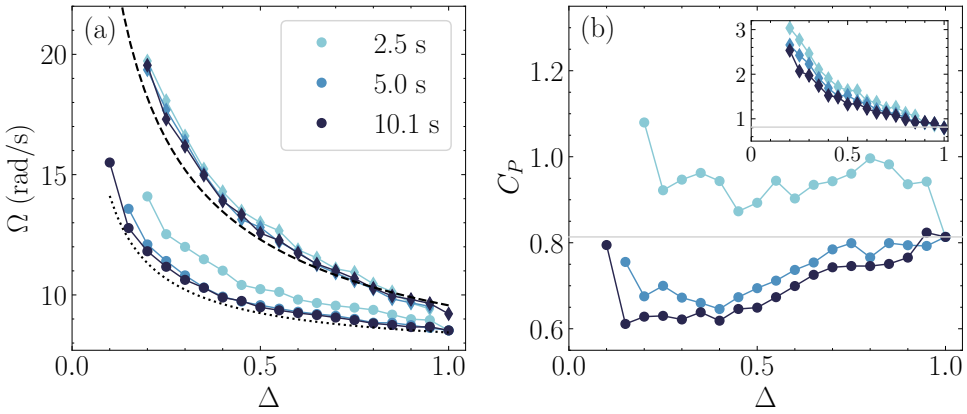

Figure 0.3: (a) Vitesse de rotation dans la phase active Ω en fonction du rapport cyclique Δ pour plusieurs périodes (couleurs). Les losanges correspondent à l'hélice rigide et les cercles à l'hélice pliable. Les courbes en tirets et en pointillés sont obtenues à l'aide de l'Eq. (0.4) pour les hélices rigides et pliables respectivement. (b) Coefficient de puissance C_P en fonction du rapport cyclique Δ. L'hélice rigide est tracée séparément dans l'insert. La ligne grise horizontale correspond au cout associé au régime continu ($\Delta = 1$). Ces données sont obtenues avec une vitesse d'écoulement de 0.11 m/s.

Une autre stratégie bioinspirée pour améliorer l'efficacité de la propulsion est l'intermittence et consiste à alterner les phases de propulsion actives et passives pour réduire le cout énergétique moyen. Cette stratégie est utilisée chez plusieurs espèces de poissons ou d'oiseaux. Nous construisons une expérience capable de reproduire cette stratégie pour un bateau à hélice : l'hélice est actionnée périodiquement et le bateau se déplace librement dans l'eau. Pour que la propulsion intermittente soit efficace il est crucial que la force de traînée s'exerçant sur le bateau soit réduite dans la phase

passive. Nous avons donc fabriqué une hélice capable de s'ouvrir et de se fermer passivement lorsque le moteur se met en marche, à l'aide de charnières permettant aux pales de se refermer sur l'axe de rotation.

L'expérience consiste alors à actionner l'hélice périodiquement pendant une fraction Δ de la période du mouvement (fraction aussi appelée rapport cyclique). La vitesse de l'écoulement est fixée et la vitesse de rotation de l'hélice qui permet l'équilibre du système doit être trouvée manuellement pour réussir l'expérience. Cette vitesse de rotation dans la phase active de propulsion est tracée sur la Fig. 0.3 (a) et augmente lorsque le rapport cyclique diminue. Cette vitesse de rotation Ω peut être prédite grâce à l'équilibre des forces en moyenne sur le bateau :

$$\Omega = \Omega_c \sqrt{\frac{C_{D,C}}{C_{D,B}} \left(\frac{1}{\Delta} - 1 \right) + 1}, \tag{0.4}$$

avec Ω_c la vitesse de rotation associée à la propulsion en continu à la même vitesse moyenne (à $\Delta = 1$). $C_{D,C}/C_{D,B}$ correspond au ratio entre le coefficient de traînée dans la phase passive et celui dans la phase active. Ces coefficients sont mesurés séparément et permettent de prédire la vitesse de rotation à imposer (courbes en tirets et pointillés de la Fig. 0.3 (a)).

Le coût de la propulsion est mesuré en calculant la puissance mécanique moyenne au cours d'un cycle à l'aide de capteurs de couple et de vitesse de rotation. Le coefficient de puissance C_P est obtenu en comparant ce coût à la puissance typique dissipée par le frottement de l'eau à une vitesse donnée. En utilisant l'hélice pliable, le coût de la propulsion peut être réduit de 25 % comparé à la propulsion continue à la même vitesse (Fig. 0.3 (b)). Sur une large gamme de rapports cycliques et pour les périodes les plus longues ($T > 5$ s), la propulsion intermittente est plus efficace que la propulsion en continu (trait gris horizontal). Ce n'est cependant pas le cas de l'hélice rigide (en insert) : dans ce cas la traînée n'est pas suffisamment réduite dans la phase passive et la propulsion continue est la plus efficace.

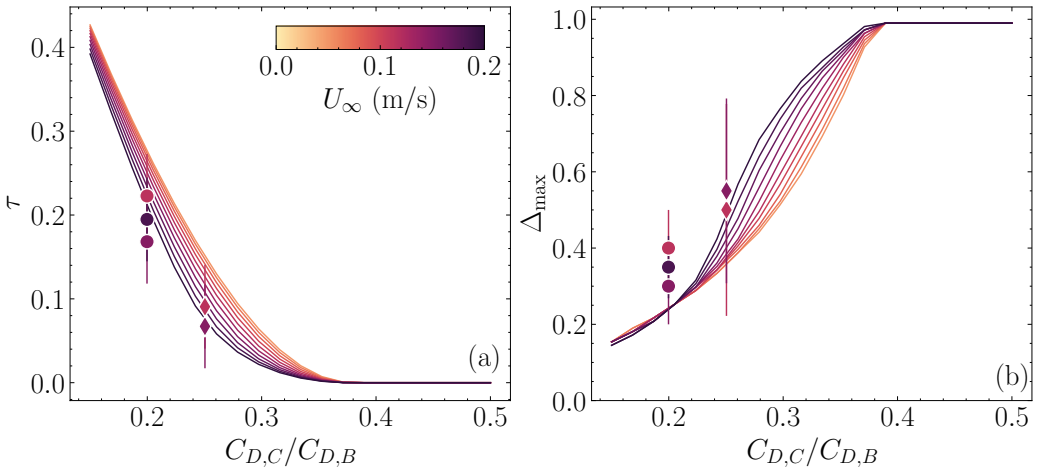

Figure 0.4: (a) Amélioration relative du coût de la propulsion intermittente par rapport à la propulsion continue pour le cycle intermittent optimal, en fonction du contraste de traînée. Les lignes représentent le résultat du modèle et les symboles les points expérimentaux. (b) Rapport cyclique correspondant au cycle intermittent optimal.

Afin d'obtenir le contraste de traînée à partir duquel l'intermittence devient plus efficace que la propulsion en continu, nous construisons un modèle capturant la dynamique du bateau au cours

du cycle. Ce modèle calcule la vitesse instantanée du bateau à partir des forces qui s'appliquent sur celui-ci et permet d'en déduire le coût énergétique moyen. Tous les paramètres du bateau et de l'hélice ont été mesurés au préalable et ce modèle est ainsi capable de prédire le coût énergétique d'un cycle de propulsion intermittent, sans paramètre d'ajustement. Pour un contraste de traînée et une vitesse moyenne donnés, nous calculons le cycle ayant le coût énergétique le plus faible. Sur la Fig. 0.4 (a), nous traçons l'amélioration du cout de propulsion par rapport au cycle continu τ. Ce modèle capture correctement les deux séries d'expériences que nous avons réalisées avec les pales pliables et prédit le résultat suivant : si la traînée n'est pas réduite d'au moins 65 % durant la phase passive, le régime continu est le plus efficace. Pour des contrastes de traînée sous cette limite, τ augmente rapidement et le rapport cyclique associé au cycle optimal Δ_{max} s'approche de zéro.

Les stratégies bioinspirées explorées dans cette thèse présentent un intérêt important pour l'amélioration de l'efficacité de la propulsion maritime. Des hélices souples pouvant s'adapter passivement aux variations de vitesse de rotation peuvent par exemple compenser les variations rapides de vitesse dans le sillage de la coque d'un navire. L'intermittence possède un potentiel important de réduction du coût de la propulsion. Elle nécessite en revanche de modifier l'ensemble du système hélice et bateau pour que la traînée soit suffisamment réduite dans la phase passive.

Remerciements

Je souhaite adresser me remerciements aux membres du jury qui ont accepté de relire et corriger mon manuscrit. La discussion scientifique autour des problématiques rencontrées pendant ma these a été enrichissante et m'a permis de prendre du recul sur les résultats de ces trois années. J'aimerais remercier mes directeurs de these pour leur accompagnement qui m'a permis d'apprendre à avancer un projet de recherche dans la durée. Sylvain a toujours apporté un regard nouveau et des propositions originales pour débloquer la situation. Benjamin a su garder une légèreté agréable dans ses explications et m'a aidé à garder le bon cap au quotidien.

L'excellente ambiance dans le laboratoire a rendu mon experience de these particulièrement appréciable et j'aimerais remercier tous ceux qui y contribuent : Fred, Claudette, Philippe et Damien en particulier. J'ai passé de très bon moments scientifiques ou non avec nombre de personnes du laboratoire aux Arènes, et meme si faire la liste complete ici serait trop long, ca a été un plaisir de partager ces trois années avec vous tous qui faites du PMMH un endroit aussi spécial.

L'équipe BIOMIM a évidemment été centrale dans cette bonne ambiance générale et a fait que j'ai toujours été content d'aller au laboratoire. Pouvoir faire une pause et trouver quelqu'un avec qui discuter a tout moment a rendu le travail de thèse très agréable. En particulier, Roméo m'a appris toutes les bonnes techniques de fabrication, me transformant de "touriste" en véritable doctorant. Partager le quotidien de la thèse avec Baptiste et Gatien du début à la (presque) fin a été un privilège grace a leur complicité, bonne humeur et disponibilité pour discuter science, échecs, Tour de France ou colormap. Gauthier a été une source intarissable de rire et de bons moments, autour d'une manip ou a la salle d'escalade. La course du mercredi midi et les débats avec Vincent ont été une pause précieuse pendant la redaction, 10/10. Camille a ramené le BIO dans la salle BIOMIM, et avec, sa gentillesse et de nombreux gâteaux qui manquaient depuis le depart de Roméo. Merci enfin à Alexis pour son assistance sur mes problèmes numériques et sa positivité a toute épreuve.

Hors du laboratoire, merci aux amis qui m'ont soutenu pendant ma these : Gwendal, Goulven et surtout Jules avec qui, comparer nos experiences de thèse autour d'une partie de palet ou a l'escalade a permis de prendre du recul lorsque c'était nécessaire. Merci enfin à mes parents et ma sœur pour leurs conseils et leurs mots d'encouragement tout au long de ces trois années.

Contents

Chapter 1

Introduction

1.1 Context of the study

The globe is warming due to anthropogenic emissions of greenhouse gases (IPCC, 2022). In particular, maritime transport is responsible for about 3% of the annual emissions (IMO, 2020) and must therefore reduce its impact on the environment. Practical solutions are available, such as reducing traffic, slowing down ships or upgrading outdated propulsion systems to new standards. In this context, the search for new ideas on how to further improve the efficiency of transportation can be very useful in achieving climate goals.

One novel research axis which may yield such efficiency improvements is bio-inspiration: the process of observing natural systems in search of alternative ways to solve complex problems traditionally addressed by engineers. It can open unexplored paths and sometimes lead to breakthroughs in non-biological fields, with examples ranging from the shape of the nose of the Shinkansen (a bullet train in Japan), that mimics the beak of the kingfisher, to tape that imitates the paws of geckos (Ng et al., 2021).

We propose to study of marine propulsion by means of two bioinspired strategies: reconfiguration and intermittency. Reconfiguration is the introduction of flexibility into a usually rigid system and the tuning of this flexibility to adapt to changing external conditions. It has already been successfully applied to wind turbines in a previous study by our group (Cognet et al., 2017). In this study, the shape of the rotor blade can passively adapt to changing external conditions and adopt the most efficient shape. In the case of a wind turbine, shape change allows energy to be extracted over a wider range of wind speeds compared with a rigid blade wind turbine. With propellers, reconfiguration could improve the efficiency of propulsion in off-design conditions. Most ship propellers operate in the wake of the ship's hull (Regener et al., 2018). As a result, they experience constantly varying flow speeds throughout the rotation. Passively adjusting to compensate for varying flow speeds would also greatly improve energy efficiency.

The second strategy is intermittency: a locomotion type found in fish and birds that involves passive gliding between active strokes. Intermittency has been found to reduce the cost of locomotion compared to continuous motion (Weihs, 1974; Rayner et al., 2001; Li et al., 2023). In the case of propellers, intermittency corresponds to switching the motor turning the propeller on and off periodically. Intermittent propulsion in the case of marine propellers has never been explored in

previous studies because accelerations are often associated with increased power dissipation, which reduces efficiency. However, it has been shown in the case of fish and birds that the cost of motion can be reduced if there is a shape change between the phases of motion: either gliding or streamlining. This shape change reduces the resistance exerted by the fluid on the animal in the passive phase and is beneficial for efficiency. Therefore, a propeller that dynamically changes shape is needed to mimic this strategy, coupling the intermittency and reconfiguration strategies.

In the following, we recall previous works relevant to the study of shape-changing propellers and intermittent propulsion. We first make a summary of the study of bioinspired reconfigurating structures, then detail the literature on intermittent locomotion in fish. Finally, we review the most important results on flexible rotating structures, either from wind turbines or ship propellers.

1.1.1 Reconfiguration

Reconfiguration is the ability of a structure to change shape under the influence of a fluid loading. The deformation caused by the flow modifies the force applied on the structure. This force change may then be used for instance to protect the structure against wind gusts or passively adapt to flow changes. In his seminal work of 1969, Vogel observed that many plant leaves change shape when exposed to high velocity air flows (Fig. 1.1, (a)). This passive mechanism reduces the force exerted by the air on the leaf and therefore allows it to survive strong gusts. The force generated by a flow pushing on a bluff body is called the drag, and can take several forms depending on the characteristics of the flow and the body. These properties are summarized in the Reynolds number that compares the relative importance of the inertial and viscous effects in the fluid. For a flow with a typical velocity U and a kinematic viscosity ν, interacting with an object of size L, the Reynolds number reads:

$$\mathcal{R}e = \frac{UL}{\nu}. \tag{1.1}$$

In the cases where the Reynolds number is larger than 1000, the drag force D exerted by a flow on a bluff body takes the form:

$$D = \frac{1}{2}\rho S U^2 C_D, \tag{1.2}$$

where ρ is the density of the fluid, and S is the frontal area of the object. C_D is a dimensionless number called the drag coefficient. For flows where $\mathcal{R}e > 1000$ the drag coefficient depends only on the shape of the object and is a constant of the flow velocity (Hoerner, 1965). The drag force therefore increases with the square of the flow velocity.

In the case of tuliptree leaves (Fig. 1.1, (a)) however, Vogel (1989) showed that the force grows slower than this expected behavior. The leaves roll up upon themselves and reduce the surface exposed to the wind, reducing the drag force. Instead of growing like the flow velocity squared, the force increases with a smaller exponent: about 1 for leaves. The leaves are therefore said to reconfigure: their shape adapts to the intensity of the wind. Similar results were found with other types of leaves, algae, or even small trees. All of these species follow drag laws scaling with the velocity with an exponent smaller than 2. The exact value of the exponent however differs between systems (Vollsinger et al., 2005; Harder et al., 2004; de Langre, 2008). In extreme case it is even possible to find systems where the drag is independent of the flow speed (Barois and de Langre, 2013; Marzin et al., 2022).

Artificial and model reconfigurating structures are often used to describe shape change theoretically. In particular, the two dimensional problem of a flexible cylinder in a flowing soap film was studied by Alben et al. (2002, 2004). Like the leaf, a flexible cylinder clamped in its midpoint bends when subjected to the flow and reduces the drag force applied upon it (Fig. 1.1 (b)). The authors emphasized the

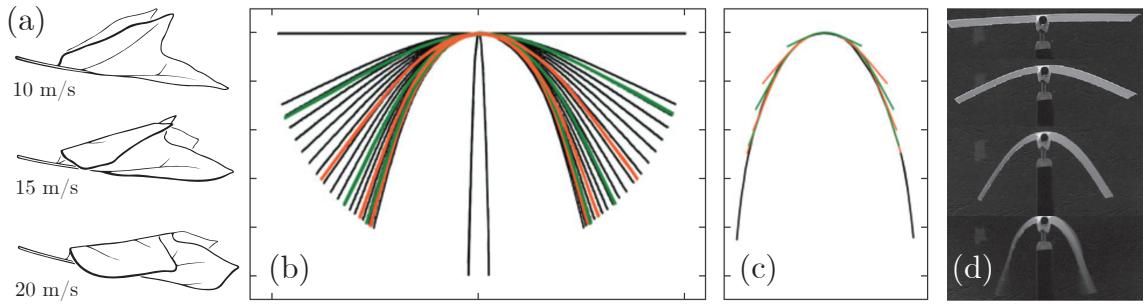

Figure 1.1: Example of reconfigurating systems. (a) Tuliptree leaf reconfigurating in high winds (from Vogel (2003)). (b) Shape of a flexible cylinder attached in the center in a soap film flow coming from the top, (c) same shape but the lengths have been dilated by L_0 (Extracted from Alben et al. (2002)). (d) Flexible plate in an air stream (Adapted from Gosselin and de Langre (2011)).

presence of an intrinsic length scale of the fluid-structure interaction problem: $L_0 = (2E/\rho f U^2)^{1/3}$, where E is the Young modulus of the cylinder and f the film thickness. They measured the shape of the deformed cylinder and showed that it is self similar: when the lengths are streched by L/L_0, all the shapes superimpose on a universal quasi-parabolic shape (Fig. 1.1 (c)). The curvature of the cylinder due to the fluid drag is concentrated in a region of size L_0.

The plant experiment was revisited by Schouveiler and Boudaoud (2006), using artificial leaves made out of flexible discs with a radial cut from the center to the edge. These discs roll upon themselves similarly to the tuliptree leaf under high speed flows. They were able to describe the evolution of the drag coefficient with the flow velocity using potential flow theory. Gosselin and de Langre studied flexible plates (Gosselin et al. (2010), Fig. 1.1, (d)) and poroelastic balls (Gosselin and de Langre, 2011) in an airstream. They highlighted two important parameters: first, the Cauchy (or elastohydrodynamical) number comparing the magnitude of the fluid forcing to the elasticity of the material:

$$C_Y = \frac{\rho L^3 U^2}{2EI}, \tag{1.3}$$

where I is the second moment of area, a geometric property of the object. Second, they introduced the reconfiguration number:

$$\mathcal{R} = \frac{D}{D_0}, \tag{1.4}$$

where D_0 refers to the drag of the rigid object with the same geometry. The reconfiguration number quantifies the effect of the flexibility by comparing the drag of the object with the one of its undeformed counterpart. While the Cauchy number is small the reconfiguration number is equal to one: the effect of flexibility is negligible. For $C_Y \gtrapprox 1$ the reconfiguration number decreases as the object adapts to reduce the drag force.

The force on the object in the numerator of the Cauchy number must be rescaled by the drag coefficient to correspond the actual loading on the object. Doing so defines a rescaled Cauchy number $\widetilde{C_Y} = C_Y C_D$, where C_D is the drag of the undeformed object. All effects related to the shape of the objects are taken into account in the drag coefficient and therefore, the reconfiguration number for very different objects collapses onto a single curve as a function of the scaled Cauchy number (Fig. 1.2), showing the universality of the reconfiguration of these structures.

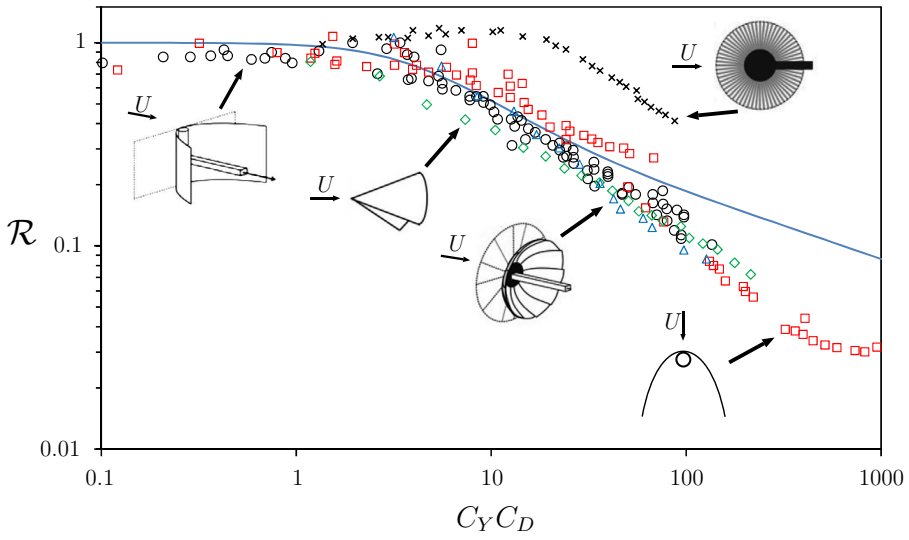

Figure 1.2: Reconfiguration number $\mathcal{R}$ as a function of the rescaled Cauchy number $\widetilde{C_Y} = C_Y C_D$ for different objects. Black circles correspond to flat plates in the work of Gosselin et al. (2010). Green lozenges correspond to cones rolling up in Schouveiler and Boudaoud (2006). Blue triangles are discs cut along several radii in Gosselin et al. (2010). Red squares are cylinders in 2D soap films from Alben et al. (2002). Black crosses are poroelastic balls from Gosselin and de Langre (2011). Figure extracted from Hassani (2016).

1.1.2 Intermittency in biolocomotion

Structures deforming by the action of flows are not always passive: fluid-structure interaction problems are for instance encountered almost everywhere in animal locomotion. Most animal bodies are flexible, and therefore propulsion through a fluid creates shape changes similarly to the reconfiguration of leaves. In contrast to the previous cases, the forcing initially comes from the body rather than the flow. Examples span large scales: from flexible millimeter-sized cilia to the flukes of the largest cetaceans: passive cambering improves efficiency (Fish et al., 2006; Costello et al., 2023). Flexibility is a key element of locomotion, among other examples, insects have been shown to rely on wing bending to propel themselves efficiently through the air (Ramananarivo et al., 2011).

One aspect of particular interest in biolocomotion is intermittency: the ability to dynamically reconfigure to save energy. Many species utilize an intermittent gait when moving instead of continuous motion (Kramer and McLaughlin, 2001). This strategy at first glance seems energetically unfavorable: accelerations often lead to an increased overall dissipation compared with motions at a constant velocity. However, several species of fish and birds seem to prefer this gait precisely for energy efficiency (Videler, 1981; Muller et al., 2000; Ribak et al., 2005; Wu et al., 2007; Xia et al., 2018; Coughlin et al., 2022).

In birds, there are two distinct intermittent flight modes: either gliding or bounding (Rayner et al., 2001). Gliding corresponds to the bird gaining height by actively flapping its wings and gliding down with the wings open. Bounding corresponds to the same strategy but with the wings flexed in the passive phase. For most birds gliding is energetically advantageous at most speeds while bounding is only interesting at high speeds (Wu et al., 1975; Tobalske, 2010; Taylor et al., 2010). The ability to store potential energy in the active phase is key to the energy efficiency of this flight mode

(Paoletti and Mahadevan, 2014). This technique is however not accessible to propulsion at the surface of water, and therefore we focused on fish swimming.

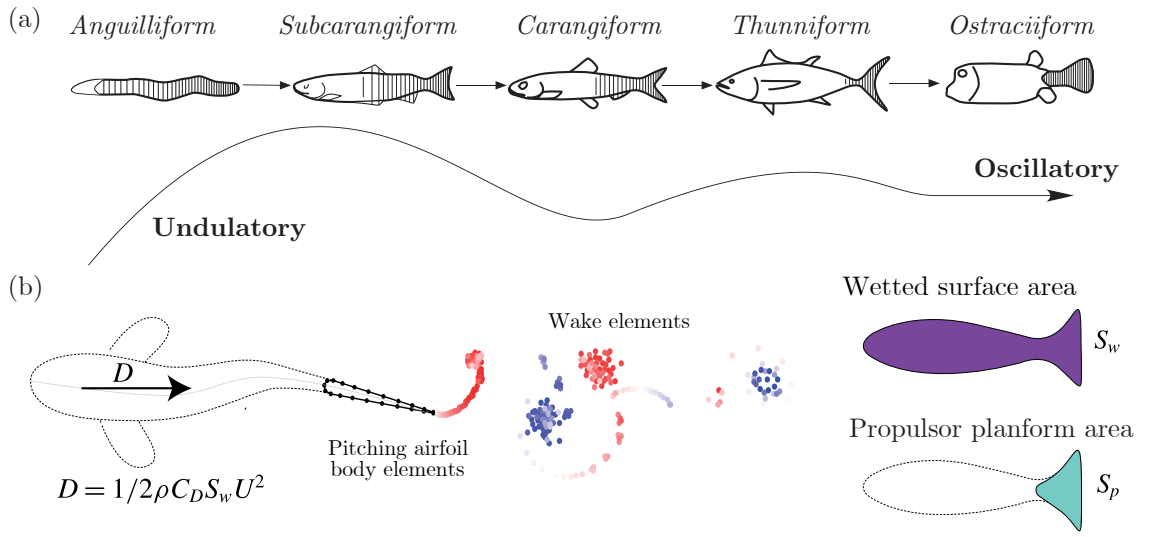

Figure 1.3: (a) Categories of fish swimming kinematics (Adapted from Sfakiotakis et al. (1999); Vatanabe et al. (2008)) (b) Schematic of a swimming fish, numerically separating the propulsive active part (the tail) and the passive part (the body) (Adapted from Akoz and Moored (2018)).

Fish swimming kinematics vary widely between species (Fig. 1.3, (a)): from anguiliform for long and slender fish to thunniform for fish with wide and short tails like tunas (Sfakiotakis et al., 1999; Blake, 2004; Webb et al., 2011; Lauder, 2015; Di Santo et al., 2021). Lighthill (1971) created the elongated body theory, a model capable of describing the force generation from all these different kinematics, using only the tail tip movement. Efforts were then made to find commonalities in aquatic locomotion: the swimming kinematics can be summed up in one parameter called the Strouhal number St, that compares the typical velocity of the tip of the tail fA where f is the frequency and A the amplitude of the tail beat, to the swimming velocity U: $St = fA/U$. For many high Reynolds number swimming and even flying animals, this number is in a narrow range between 0.2 and 0.4 (Triantafyllou et al., 1991, 1993; Eloy, 2012; Gazzola et al., 2014). In this regime, the wake of the animal has a very particular shape with vortices alernatively on either side of the body. These vortices are oriented such that they produce a backwards jet on average and are called a reverse Bénard-von Kármán vortex street.

Still, important discrepancies remain between swimmers, the two most notable being the relative size of the tail compared to the body, and the type of motion adopted by the tail. The first one is measured by the Lighthill number: $\mathrm{Li} = S_w/S_pC_D$, where S_w is the wetted surface of the fish, S_p the surface of its propulsor, and C_D is the drag coefficient of the whole fish (Eloy (2012); Akoz and Moored (2018), see Fig. 1.3 (b)). The second important distinction between types of locomotion is the tail actuation. Simplifying the motion of a fish tail to that of a 2-dimensional airfoil (Fig. 1.3 (b)), there are two degrees of freedom available: pitch and heave. Pitch consists of angular oscillations around the leading edge of the wing, while heave corresponds to side-to-side motion. Any other 2 dimensional motion of a fish tail can be modeled by a combination of the two. As a result, a large body of literature has focused on finding the thrust and efficiency of such motions (Triantafyllou et al., 1991; Floryan et al., 2017a, 2018; Moored and Quinn, 2019; Van Buren et al., 2019; Wu et al., 2020).

In fish, intermittent locomotion is also called burst and coast. The fish activates its tail for one or two

beats and then glides passively using the kinetic energy accumulated during the active phase (see Fig. 1.4). Weihs (1974) was the first to theoretically investigate the efficiency of this type of gait. He showed that intermittent locomotion could be more energy efficient than continuous swimming if the drag experienced by the fish was reduced during the gliding phase. Indeed, undulatory swimming increases the drag produced by the body of the fish during the burst phase by a factor of up to three times the drag at rest during the coast phase. The mechanism leading to a high drag contrast between the two phases of the cycle is achieved via a combination of a geometrical effect (the body is aligned with the flow during the coast phase) and a dynamical one (the skin friction is increased during the burst phase due to the motion of the body), that increases the drag while the tail is moving (Ehrenstein et al., 2014; Godoy-Diana and Thiria, 2018; Akoz and Moored, 2018). Weihs showed that this drag contrast is crucial for taking advantage of intermittent kinematics. In particular, his model shows that intermittent locomotion is the most efficient swimming strategy when the drag during the coast phase is half the drag during the burst phase.

Figure 1.4: (a) Chronophotography of *Hemigrammus rhodostomus* swimming in a channel, the flow is coming from the top and time is from left to right. Courtesy of B. Lafoux. (b) Schematic of the time dependent velocity of a fish swimming in a burst and coast gait.

Some experimental works have successfully measured this drag contrast. First, (Videler, 1981) estimated that the drag of a swimming cod is about 3.3 times greater than that of a gliding fish. With koi carps and using a PIV setup to measure the fish's wake, Wu et al. (2007) found a fourfold increase in drag in the active phase. The same study also concludes that burst and coast allows the fish to reduce the cost of swimming by 45% compared to steady swimming at the same average speed. To our knowledge, this work is the only experimental estimate of the energy savings of intermittent propulsion in live fish.

Other authors have been able to simulate 3D flows around a body kinematics directly extracted from measurements of fish swimming (Chung, 2009; Xia et al., 2018; Ashraf et al., 2020). It is then possible to vary the parameters accessible to the fish such as tailbeat frequency and amplitude or the fraction of the period spent actively propelling (also called duty cycle). Li et al. (2021, 2023) have shown that fish use parameters that are very close to the optimal choice to minimize their energy expenditure. Burst and coast locomotion in fish therefore results in reductions in energetic cost of up to 26% compared to continuous motion at the same speed (Fig. 1.5 (b)).

Akoz and Moored (2018) performed numerical simulations of intermittently pitching airfoils (Fig. 1.3 (b)). They found that the cost of motion at a given speed can be significantly reduced (Fig. 1.5, (a)) even if the drag of the body is unchanged between the two phases (Akoz et al., 2019). By modeling the unsteady forces on the airfoil, they showed that there are both drag-producing and thrust-producing inviscid contributions when pitching the airfoil. They later added the heave contribution (Akoz et al., 2021) and showed that heave dominated motions do not benefit from intermittency. Heaving motion creates thrust through circulation around the airfoil, creating a small amount of drag compared with pitching motion, which is primarily based on added mass. Swimmers who benefit the most from intermittent locomotion therefore have small Lighthill numbers (i.e., large tails) and perform mostly

pitching motions.

Finally, Floryan et al. (2017b) have studied intermittent locomotion experimentally, using a pitching airfoil in water. The airfoil is fixed and intermittently actuated. To make the comparison with burst and coast the authors have to make two strong assumptions: (i) the flow remains quasi-steady in the accelerated case, such that no effect is lost by keeping the foil stationary and (ii) the forces generated by the airfoil are independent of the incoming flow velocity (shown in a previous study from the same authors: Floryan et al. (2017a)). They found also in this case that intermittent motion can be more efficient than continuous swimming at the same mean speed.

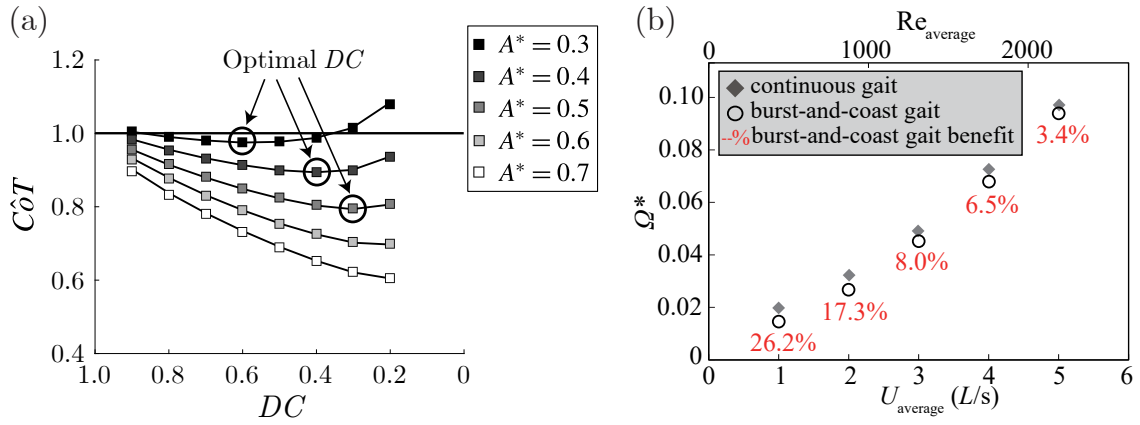

Figure 1.5: (a) Cost of transport for a pitching airfoil, relative to the cost of transport of continuous motion at the same speed, as a function of the duty cycle. Different curves and colors correspond to different dimensionless tail amplitudes. Note that the x-axis is inverted (Adapted from Akoz and Moored (2018)). (b) Cost of locomotion Ω^* of a small fish as a function of mean speed for continuous and optimal intermittent motions (Adapted from Li et al. (2023)).

1.1.3 Rotors

Our goal is to apply the concepts of reconfiguration and intermittency to underwater propulsion. Intermittent propulsion with a propeller is essentially unexplored in the literature. However, flexible rotors have recently attracted engineering interest due to new blades made of composite materials. These are very light and can be made into any shape, but tend to deform more than traditional alloy blades. Designers of wind turbines or propellers must therefore take these deformations into account (Marsh, 2004; Hansen, 2015; Young et al., 2016).

Using flexible materials in rotors is however not a new idea: Winston (1968) explored the possibility of using extremely flexible helicopter blades to improve weight and easier storage. The blades are so flexible that they bend under their own weight and are straightened when rotating by the centrifugal force. In these conditions, important couplings between the flexibility and the fluid loading occur, generating aeroelastic instabilities (Tang and Dowell, 1993). The blade can start oscillating along its torsion axis in a phenomenon called flutter (de Langre, 2006). The aerodynamic lift on the blade amplifies the oscillations with a potentially destructive result. Sicard and Sirohi (2012, 2016) studied these instabilities in detail for ribbon-like helicopter blades and found that they can be damped by modifying the location of the center of gravity. By placing small masses at the tip of the blades near their leading edge, the aerodynamic force acts to stabilize the blade.

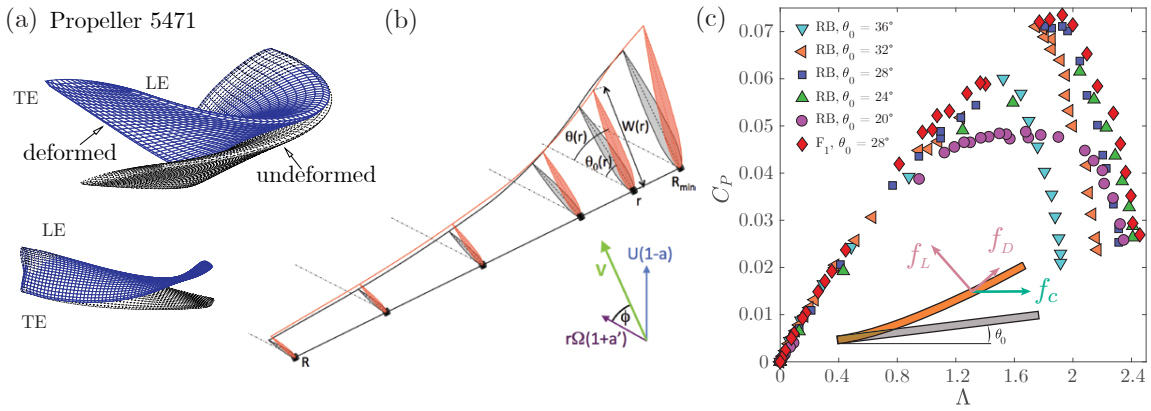

Figure 1.6: (a) Shape of a composite marine propeller blade deforming under hydrodynamic load. LE and TE respectively refer to leading and trailing edges (Adapted from Young (2008)). (b) Wind turbine blade deforming and changing its effective angle with the flow (Extracted from Cognet et al. (2020)). (c) Dimensionless power[1] C_P extracted by a wind turbine for varying external conditions. Red diamonds correspond to a wind turbine with flexible blades while all the other symbols are rigid wind turbines with various blade pitch. Λ is the tip speed ratio and θ_0 is the pitch angle. The inset displays a section of the blade deforming under the action of three forces: the centrifugal force f_c, the aerodynamic lift force f_L, and the aerodynamic drag force f_D (Adapted from Cognet (2017)).

Flexibility in rotor blades can also be utilized to enhance performance. Typically, blades are designed for a specific operating condition; however, wind turbines operate across a broad spectrum of wind speeds. In order to maintain peak efficiency, many modern wind turbines incorporate motors to adjust the angle of the blades. Changing the shape of the blades to adapt to the exact conditions. Drawing inspiration from the reconfiguration seen in natural systems, Cognet et al. (2017) showed that it is possible to do this same shape change passively, using flexibility alone (Fig. 1.6, (b) and (c)). Two forces act on the wind turbine blade: the aerodynamic load and the centrifugal force. These two forces act in opposite directions (Fig. 1.6, inset of (c)). Balancing their relative importance allows the blade deformation to be controlled precisely. Cognet et al. (2020) therefore showed that given a wind turbine geometry and a site's wind speed distribution, it is possible to find material properties (density and flexibility) for the blades such that the efficiency of the rotor is improved. Recently Durán Venegas et al. (2019) have proposed a mathematical description for this problem, for a rotor in which both fluid forcing and centrifugal force bend and twist the blades as they rotate.

In the specific case of marine propellers, an extensive body of literature has focused on the effects of flexible composite propellers on hydrodynamic efficiency (Marsh, 2004; Young et al., 2016; Hussain et al., 2021). The first simulations and experiments of Young (2008) showed the potential of composite propellers flexing to alter the performance under normal or cavitating conditions and dampen the vibrations of the structure (Fig. 1.6, (a)). This work highlighted the importance of the fiber layup direction in controlling the mechanical response of the blades. The resulting anisotropy may be used to improve performance, as shown by Motley et al. (2009). A coupling between the bending and twisting deformations of the blade can make the blade passively adapt to variations of external conditions. In particular, they showed that propellers can passively adapt to remain efficient when operating in the spatially varying wake of the hull of a ship.

[1]The power coefficient C_P represents the fraction of the power available in the incoming wing extracted by the wind turbine. With Q and Ω the torque and angular velocity of the rotor respectively, the power coefficient is $C_P = Q\Omega/(1/2\rho\pi R^2 U_\infty^3)$. ρ is the fluid density, R is the radius of the turbine and U_∞ the wind velocity.

During the course of this thesis, Eldemerdash and Leweke (2021) studied experimentally a model scale propeller with highly flexible blades. Using flow field visualization and blade tracking they observed large deformations up or downstream depending on the angle of the blades and the angular velocity. Under braking conditions, when the rotor produces negative thrust, large amplitude fluctuations of the blade shape are observed. They are interpreted as the blade rotating in the vortex generated by its own wake, a phenomenon called the Vortex Ring State in helicopters. Building upon the model created by Durán Venegas et al. (2019), they are able to accurately predict the small deformations of the rotor (Eldemerdash, 2023).

1.2 A blade element description of rotors

Rotors are particular systems due to their screw geometry. The description of their behavior requires a careful analysis of the local flow velocity as well as the geometrical properties of the rotor. An approach to describe the local and global loads on a rotor is described in detail below. Models relying on this approach are used throughout the thesis, adding each time a different layer of complexity: folding blades, flexibility, or curvature effects. We explain here the general technique allowing the estimation of these loadings, and derive a few classical results on propellers.

1.2.1 Blade element model

A classical tool used in the analysis of rotating systems (boat or plane propellers, wind turbine etc.) is the blade element model. It consists in dividing the rotor in small spanwise cuts along each blade and analyzing them separately. Sections along the same blade are supposed independent of each other and multiple blade interactions are neglected. The technique detailed here applies to rotors subjected to flows along their axis of rotation (i.e. propellers or turbines) but the specific details could be modified to work for rotors with flows perpendicular to the rotation (for instance, helicopter rotors). This division of the global problem can be thought of as dividing the incoming flow into concentric streamtubes that pass through the rotor and only interact with the blades at a single radius, not influencing the adjacent tubes (See Fig. 1.7). The approach here is dedicated to steady flows, if there are important variations faster than a typical rotation of the propeller, the analysis should be modified.

Dividing the problem in such a way allows us to transform the 3D problem of the flow around a rotating structure into a series of 2D problems around an airfoil. This transformation allows a very fast and simple estimation of the forces involved at the expense of several strong hypotheses:

- Radial flows are neglected: they are typically smaller than the axial or orthoradial flows and do not generate circulation around the blades. The radial flow therefore do not contribute to the lift force which is the main source of thrust. Near the tip or root, vortices are generated due to finite size effects and therefore important radial flows are present, they are neglected here.

- The rotor self-induction is not considered: when analyzing a streamtube passing through a propeller, the exact axial velocity at the location of the rotor is not the one far upstream. The flow is slightly accelerated before reaching the rotor. In the same way its angular velocity is not zero due to the rotor itself. This effect can be taken into account using the Blade Element Momentum Theory which is extremely common in the engineering of wind turbines (Glauert, 1983; Sørensen, 2011; Masters et al., 2011). However, this tool often requires semi-empirical corrections to be quantitative (Snel et al., 1994; Corrigan and Schillings, 1994; Mario, 2012;

MacNeill and Verstraete, 2017) which may be problem dependent. Our goal is to build a minimal model describing the behavior of a rotor in general, so we neglect these effects.

- Flow curvature effects are neglected: when interacting with a section of the blades, the flow is considered to be 2D and planar. In reality, the flow is along a tube. These curvature effect are all the more important when the blades occupy a large angular sector. A geometrical consequence of this effect is analyzed in Sec. 4.1 where it is particularly important.
- The problem is supposed axisymmetric: there are no variations of flow conditions during the rotation (for instance due to the presence of a hull). An example on the modifications required to take into account spatially varying flow conditions is detailed in Sec. 2.2.3

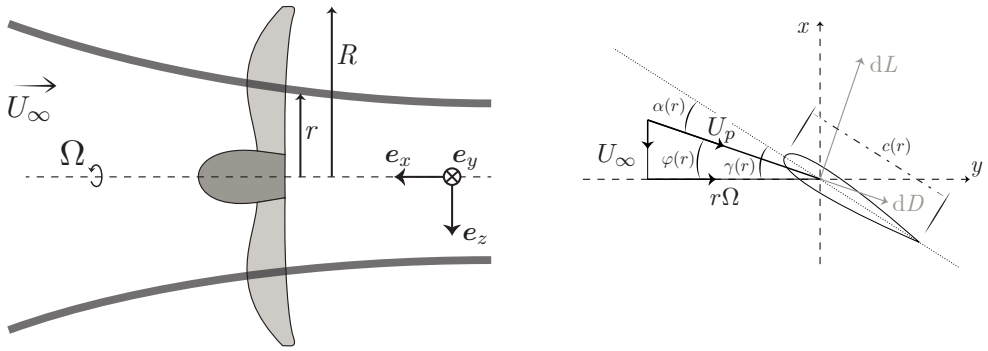

Figure 1.7: (left) Schematic of a streamtube interacting with a rotor. (right) Definition of the angles on a 2D profile interacting with the streamtube.

The definitions and schematic of the model are show in Fig. 1.7: the incoming axial flow has a velocity U_∞, and the propeller is rotating with an angular velocity Ω. The streamtube interacts with the blade at a radius r. Looking at a 2D section in particular (right figure, the x direction corresponds to the axis of rotation and the y axis to the plane of rotation), the blade has a chord length $c(r)$ and a local angle with respect to the plane of rotation $\gamma(r)$. At the root of the blade, this angle is γ_0: the pitch angle. In typical plane or ship propellers, the blades are twisted along the span, such that $\gamma(r) \neq \gamma_0$ in general. The pitch angle is a key property of the rotor and can be adjusted during the rotation in the case of wind turbines Hansen (2015) or plane propellers Glauert (1983). The incoming flow has an x component of norm U_∞ and a y component of magnitude $r\Omega$, such that the local velocity is $\mathbf{U}_p = U_\infty \mathbf{e}_x + r\Omega \mathbf{e}_y$. A key parameter of the study of rotating structures is tip speed ratio or reduced velocity $\lambda = R\Omega/U_\infty$, such that the angle φ between the flow and the plane of rotation reads:

$$\tan\varphi = \frac{U_\infty}{r\Omega} = \frac{R}{r\lambda}. \tag{1.5}$$

The angle of attack of the airfoil at this particular location is thus:

$$\alpha(r) = \gamma(r) - \varphi(r) = \gamma(r) - \arctan\frac{R}{r\lambda}. \tag{1.6}$$

This angle of attack on a 2D airfoil generates a force due to the circulation of the fluid around the profile. This infinitesimal force is usually divided into a component in the direction of the incoming flow: the drag $\mathrm{d}D$, and its orthogonal counterpart: the lift $\mathrm{d}L$.

These two forces are proportional to the square of the local velocity $|\mathbf{U}_p|^2$ and read:

$$\mathrm{d}L = \frac{1}{2}\rho c(r)\mathrm{d}r\,|\mathbf{U}_p|^2\,C_L, \quad \mathrm{d}D = \frac{1}{2}\rho c(r)\mathrm{d}r\,|\mathbf{U}_p|^2\,C_D \tag{1.7}$$

where ρ is the fluid density and $\mathrm{d}r$ is the infinitesimal width of the section of the blade. The lift C_L and drag C_D coefficients are dimensionless functions that relate the shape of the airfoil and the angle of attack to the forces produced. Their precise modeling is discussed in the following section (Sec. 1.2.2).

In the case of rotors, the quantities of interest are the thrust F_{thrust} (the force along the axis of rotation) and the torque Q (the moment required to spin the propeller). By projecting the lift and drag force along the x and y, we obtain:

$$\mathrm{d}F_{\text{thrust}} = \mathrm{d}L\cos\varphi - \mathrm{d}D\sin\varphi, \tag{1.8}$$

$$\mathrm{d}Q = r(\mathrm{d}L\sin\varphi + \mathrm{d}D\cos\varphi). \tag{1.9}$$

These forces are usually made dimensionless using the angular velocity of the rotor such that we can define the thrust and torque coefficients as:

$$C_T = \frac{F_{\text{thrust}}}{1/2\rho\pi R^2\,(R\Omega)^2}, \quad C_Q = \frac{Q}{1/2\rho\pi R^2\,(R\Omega)^2\,R}. \tag{1.10}$$

The reference surface used here is the area swept by the rotor as it spins[1]: πR^2. Combining Eqs. (1.7)-(1.10), we obtain for the infinitesimal thrust and torque coefficients:

$$\mathrm{d}C_T = \frac{c(r)\mathrm{d}r}{\pi R^2}\left(\left(\frac{r}{R}\right)^2 + \frac{1}{\lambda^2}\right)\left(C_L(\alpha)\cos\varphi - C_D(\alpha)\sin\varphi\right), \tag{1.11}$$

$$\mathrm{d}C_Q = \frac{r}{R}\frac{c(r)\mathrm{d}r}{\pi R^2}\left(\left(\frac{r}{R}\right)^2 + \frac{1}{\lambda^2}\right)\left(C_L(\alpha)\sin\varphi + C_D(\alpha)\cos\varphi\right). \tag{1.12}$$

The full thrust and torque coefficients are obtained by integrating $\mathrm{d}C_T$ and $\mathrm{d}C_Q$ over the span of the blades (from root to tip) and multiplying by the number of blades N_b. We use a dimensionless abscissa $s = r/R$ from $s_{\text{min}} = r_{\text{min}}/R$ to 1 and the coefficients read:

$$C_T = \int_{s_{\text{min}}}^{1} \sigma(s)\left(s^2 + \frac{1}{\lambda^2}\right)\left(C_L(\alpha)\cos\varphi - C_D(\alpha)\sin\varphi\right)\mathrm{d}s, \tag{1.13}$$

$$C_Q = \int_{s_{\text{min}}}^{1} \sigma(s)s\left(s^2 + \frac{1}{\lambda^2}\right)\left(C_L(\alpha)\sin\varphi + C_D(\alpha)\cos\varphi\right)\mathrm{d}s, \tag{1.14}$$

where $\sigma(s) = N_b c(s)/\pi R$ is called the solidity of the rotor. These expressions can be further simplified by noticing that

$$\cos\varphi = \frac{1}{\sqrt{1 + 1/(s\lambda)^2}}, \quad \sin\varphi = \frac{1/s\lambda}{\sqrt{1 + 1/(s\lambda)^2}}, \tag{1.15}$$

which finally gives

$$C_T = \int_{s_{\text{min}}}^{1} \frac{s}{\lambda}\sigma(s)\sqrt{1 + (s\lambda)^2}\left(C_L(\alpha) - \frac{C_D(\alpha)}{s\lambda}\right)\mathrm{d}s, \tag{1.16}$$

$$C_Q = \int_{s_{\text{min}}}^{1} \frac{s^2}{\lambda}\sigma(s)\sqrt{1 + (s\lambda)^2}\left(\frac{C_L(\alpha)}{s\lambda} + C_D(\alpha)\right)\mathrm{d}s. \tag{1.17}$$

[1] In the engineering literature on marine propellers a slightly different scaling convention can be found. Instead of the tip speed ratio, the advance ratio $J = U_\infty/nD$ is used where n is the angular velocity of the rotor in rotations per second $n = \Omega/2\pi$ and $D = 2R$ the diameter. The thrust and torque coefficients are consequently written as $K_T = F_{\text{thrust}}/(\rho n^2 D^4)$ and $K_Q = Q/(\rho n^2 D^5)$. One can convert between the two systems with $\lambda = \pi/J$, $C_T = 8/\pi^3 K_T$ and $C_Q = 16/\pi^3 K_Q$.

The regions of the blades that contribute most to the force generation are the regions near the tip (where $s\lambda \gg 1$) because the norm of the velocity is more important there. The thrust is mostly created by the lift on the blades: the drag coefficient is typically smaller than the lift and its contribution is scaled down by $s\lambda$. On the contrary, the torque is mostly created by the drag on the blade sections.

1.2.2 Flows around foils

As shown in the previous section, knowing the 2D flow and resulting forces around an airfoil for a given Reynolds number and angle of attack is key to estimating the performance of a rotor. This problem has an extensive body of literature around it as it is of prime interest for many engineering applications such as plane wings, sails and rotors. The lift and drag coefficients, *a priori* depend only on two parameters (except from the airfoil shape itself): the angle of attack α and the chord-based Reynolds number: $\mathcal{R}e = Uc/\nu$, with c the chord. The coefficients can either be directly measured through experiments keeping the angle of attack and Reynolds numbers constant, through analytical modelling or through simulations.

In high Reynolds number flows, typically from $1\,000$ onwards, a simplifying assumption can be made: the lift and drag coefficients have a weak dependence on the Reynolds number (compared with the angle of attack) (Lissaman, 1983). This allows the possibility of making experiments at scale without conserving the Reynolds number (which is difficult since the product Uc must be kept constant if the fluid is unchanged). The Reynolds number mostly influences the boundary layer around the airfoil: depending on $\mathcal{R}e$, it can either be turbulent or laminar, attached to the profile or detached. In particular, for relatively low Reynolds numbers, the classical stall phenomenon (during which the boundary layer separates from the profile and the lift force suddenly drops) can disappear in the force measurements (Alam et al., 2010; Mateescu and Abdo, 2010).

In the experiments described in the manuscript, the Reynolds number is defined using the local velocity norm in a given blade section:

$$\mathcal{R}e = \frac{c(r)\sqrt{U_\infty + r\Omega}}{\nu}. \tag{1.18}$$

Thus, its exact value varies along the span of the blade and with the angular velocity of the rotor. The typical range explored in experiments, from slow velocities at the blade root to high velocities at the tip is $\mathcal{R}e \in [750, 10\,000]$. In this range of Reynolds number the coefficients mostly depend on the angle of attack. Therefore, scaling the system — changing only the Reynolds number by increasing the flow velocity or size — will have only a small effect on the performance (Sunada et al., 1997).

Several properties are expected of the lift and drag coefficients as functions of the angle of attack. If the airfoil profile is symmetric, zero angle of attack results in zero lift. Similarly, if the profile is fore-aft symmetric the lift should be zero for $\alpha = \pi/2$. Added to that the function $C_L(\alpha)$ should be antisymmetric since a negative angle of attack results in negative forces. Finally, the lift force at small angle of attack should be linear with α according to thin airfoil theory (Kaushik, 2019). In contrast, the drag coefficient should be symmetric, with a minimum in zero and maximal when perpendicular to the flow.

For airfoil with a thin flat shape, which we will often use in the following, a very common and simple model for the lift and drag coefficients that verifies the properties above can be written as follows (Cognet et al., 2017; Timmer, 2010):

$$C_L(\alpha) = C_L^1 \sin\alpha\cos\alpha, \quad C_D(\alpha) = C_D^0 + C_D^1 \sin^2\alpha, \tag{1.19}$$

with $C_L^1, C_D^0,$ andC_D^1 constants that depend on the airfoil shape. This law uses a single coefficient to

describe the small angle of attack lift slope as well as the maximal lift reached which can be difficult to fit onto experimental data (usually $C_L^1 \approx 2, C_D^0 \approx 0.1$ and $C_D^1 \approx 2$).

Recently Li et al. (2022) studying small scale gliders, proposed a simple law able to better describe the force produced over the whole range of angles of attack. It matches the limiting cases of small and high angle of attacks using a smooth function

$$f(\alpha) = \frac{1}{2}\left(1 - \tanh\left(\frac{\alpha - \alpha_0}{\delta}\right)\right),$$

where α_0 is the stall angle and δ represents the smoothness of the stall. The lift and drag then read:

$$C_L(\alpha) = f(\alpha)\, C_L^1 \sin\alpha + (1 - f(\alpha))\, C_L^2 \sin 2\alpha, \tag{1.20}$$

$$C_D(\alpha) = f(\alpha)\, (C_D^0 + C_D^1 \sin^2\alpha) + (1 - f(\alpha))\, C_D^{\pi/2} \sin^2\alpha. \tag{1.21}$$

This model thus has 5 coefficients of fit, which allows it to have a richer phenomenology.

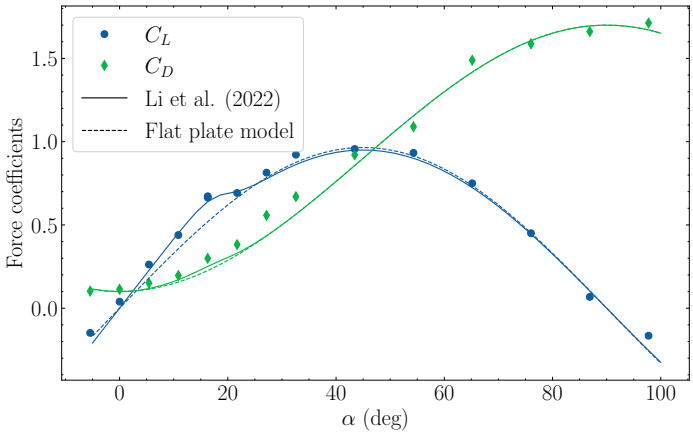

Figure 1.8: Lift and drag coefficients as a function of the angle of attack for a flat plate at Reynolds number 4500. Lines show fits of the data for two models.

We measured the lift and drag forces generated by a wing profile using a modified version of our setup (similar to the one described in Sec. 2.2.1). The wing profile has a similar shape to the one used with the propellers but is scaled up by a factor 2 in order to have a similar Reynolds number ($\mathcal{R}e = 4500$). Fig. 1.8 displays the lift and drag coefficients associated. For each of the two models, we adjusted the coefficients to fit this data. We find for the flat plate model: $C_L(\alpha) = 1.93 \sin\alpha\cos\alpha$, and $C_D(\alpha) = 0.10 + 1.6\sin^2\alpha$. This model fits well the data, except for small angles of attack where we see that the lift increases more rapidly. The model developed by Li et al. (2022) takes into account this effect. We find the following coefficients: $a_0 = 19$ deg, $\delta = 4$ deg and $C_L^1 = 2.4, C_L^2 = 0.95, C_D^0 = 0.1, C_D^1 = 2, C_D^{\pi/2} = 1.6$. While the agreement with the experimental lift at small angle of attack is improved, the drag is not significantly modified by using this formula.

In the rest of this manuscript, we mostly use the flat plate model for its simplicity. More complex laws such as the one from Li et al. (2022) could easily be used instead to more accurately model stall on the blades. However, it is important to keep in mind that the stall phenomenon is strongly Reynolds number dependent, especially in the lower limit of $\mathcal{R}e$ studied here (Lissaman, 1983; Mateescu and Abdo, 2010; Alam et al., 2010). Corrections should therefore depend on the local Reynolds number on the blade, which adds complexity without substantially improving the accuracy of the models.

1.2.3 Propeller performance

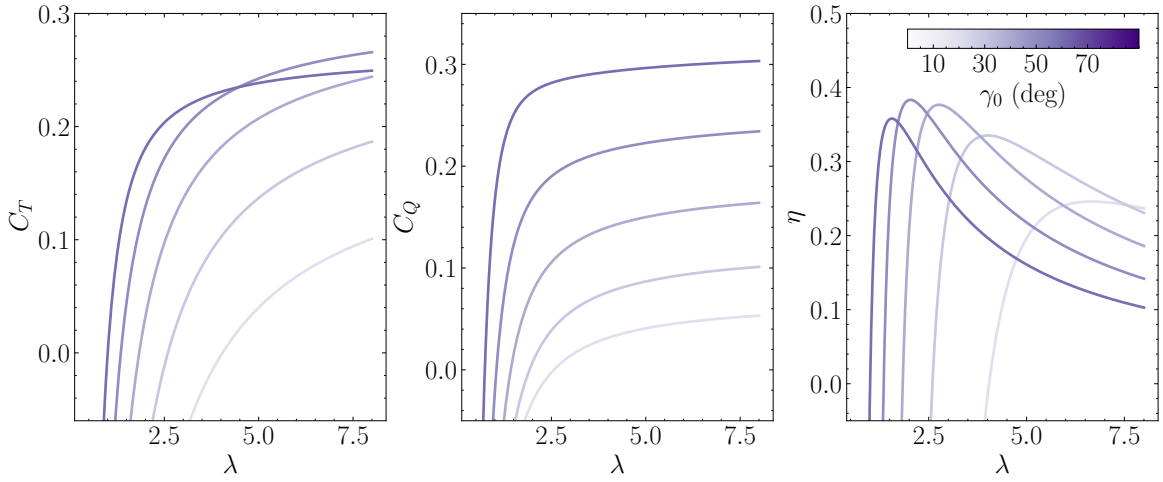

Figure 1.9: Performance curves of a propeller as a function of the tip speed ratio. From left to right: thrust coefficient, torque coefficient and efficiency. Colors indicate the pitch angle γ_0.

Once the propeller geometry and lift and drag coefficients are known, we can compute the thrust and torque using Eqs. (1.16) for any tip speed ratio. For this example we use the same shape (number of blades, chord, radius, etc.) as the propeller described in Sec 3.2, but this choice does not qualitatively change the results presented here. We introduce a parameter measuring the hydrodynamic efficiency of the propeller:

$$\eta = \frac{F_{\text{thrust}} U_\infty}{Q\Omega} = \frac{C_T}{\lambda C_Q}. \tag{1.22}$$

It compares the useful power $F_{\text{thrust}} U_\infty$ to the total mechanical power invested $Q\Omega$ and is the figure that engineers optimize after matching thrust requirements. We show the evolution of the thrust, torque, and efficiency as a function of the tip speed ratio in Fig. 1.9. The colors show the effect of changing the pitch angle of the blades (i.e., setting $\gamma(s) = \gamma_0$).

Looking at the thrust and torque curves at a given pitch angle, we can define three regions. At very low tip speed ratio, $C_T < 0$ and $C_Q < 0$: the flow creates a torque that spins the propeller and creates a backwards thrust. This region corresponds to wind turbines. The torque coefficient always becomes positive first defining a region where $C_T < 0$ and $C_Q > 0$. Spinning the propeller too slow compared with the flow speed creates a braking force. Finally, the thrust becomes positive, and we have $C_T > 0$ and $C_Q > 0$, energy is spent to create a forward pointing thrust force. The λ threshold between these regions get smaller as we increase the pitch angle γ_0. The onset of positive thrust can be approximated by stating that the angle of attack near the tip must be positive, giving

$$\lambda > \frac{1}{\tan \gamma_0}, \tag{1.23}$$

which indeed decreases as γ_0 approaches $\pi/2$.

The corresponding efficiency is well-defined only for positive torque. For each pitch angle it reaches a maximum for a tip speed ratio slightly greater than the onset of positive thrust and then declines. For each tip speed ratio, there is one pitch angle which maximizes the efficiency of the rotor. This optimal pitch angle $\gamma_0^{\text{opt}}(\lambda)$ is a decreasing function of the tip speed ratio: high pitch angles are only

efficient at small tip speed ratios. As a consequence, to remain as efficient as possible throughout the range of tip speed ratio, the pitch angle γ_0 needs to be modified accordingly. In practice, aircraft propellers and wind turbines use motors to actively adapt the pitch angle to the conditions. This technique is rarely found in marine propellers because of its complexity in the marine environment but would add significant efficiency improvements.

To build an efficient propeller, engineers want to optimize the thrust to torque ratio. Using the associated definitions in Eq. (1.16), we can compute the local efficiency for each blade section (for a given r and λ). One way to maximize the global efficiency is to maximize the infinitesimal contribution from each section by changing the local pitch angle: for each section we compute $\gamma(s)$ such that $\mathrm{d}C_T/(\lambda \mathrm{d}C_Q)$ is maximized. We therefore create an optimal spanwise distribution of pitch angle that generates a very efficient propeller.

In Fig. 1.10, we show this distribution along with the local flow angle φ (computed for $\lambda = 4$) as a function of the spanwise position. We see that both follow the same trend keeping an almost constant difference between them. This behavior can be rationalized using the following argument: maximizing the thrust can be approximated as maximizing the lift on each section, while minimizing the torque corresponds to minimizing the drag. Thus thrust to torque ratio is maximal at the same time as the lift to drag ratio on a particular blade section. For the flat plate model used here, the lift to drag ratio is shown in Fig. 1.10 (right) and we can see that it reaches a maximum between 15 and 20 degrees, about the same as the difference between the optimal propeller twist and the local flow angle. For the flat plate the optimal angle of attack is $\alpha_{\text{opt}} = 17$ deg. A well functioning propeller needs to have a local angle of attack close to maximum lift to drag ratio on most of the blade, achieved by having important twist between root and tip.

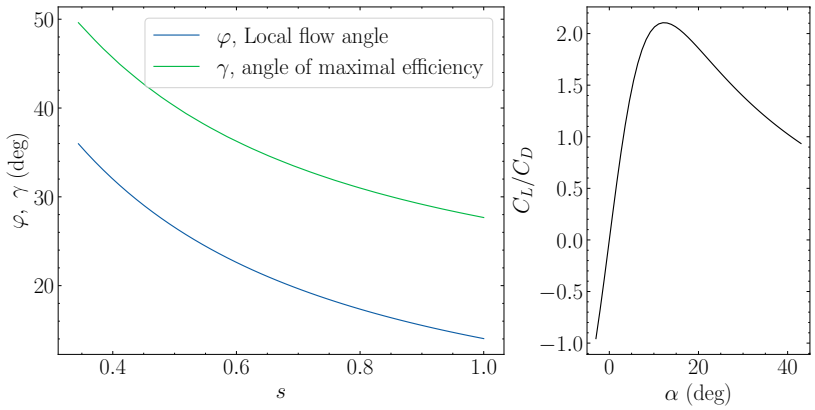

Figure 1.10: (left) (blue) Local flow angle φ (See. Fig. 1.7) and (green) optimal twist as a function of the dimensionless spanwise coordinate s. Computed at a tip speed ratio $\lambda = 4$. (Right) Lift to drag ratio C_L/C_D as a function of the angle of attack for the flat plate model used.

The dimensionless parameters involved in the problem of a flat bladed propeller are the geometrical properties: $c/R, r_{\text{min}}/R, \gamma_0$ and the hydrodynamical parameters λ and $\mathcal{R}e$. Changing the flow velocity at a constant tip speed ratio only influences the resulting coefficients (thrust or torque) through the Reynolds number. Its influence is limited to modifying the lift and drag coefficients, which are expected to vary only by a small amount. Modifying the flow speed at a constant tip speed ratio therefore does not affect the thrust and torque coefficients.

The blade element model is a useful tool to model the experimental observations and will be used several times in the thesis. Its simplicity allows us to highlight the important mechanisms at play.

Thesis outline

Our goal is twofold: first, to study the deformation of a flexible propeller in a flow to investigate whether the propulsive efficiency can be improved using a technique similar to that of Cognet et al. (2017) in the case of a wind turbine. A propeller that can passively deform and adapt to a change in tip speed ratio would greatly improve efficiency when operating in the wake of a ship's hull. Second, we want to explore the possibility of using intermittency to reduce propulsion energy consumption. The results cited previously show that the drag of the whole system (boat and propeller) must be significantly reduced when gliding in order for this technique to be more efficient than continuous motion. Therefore, we also need to design a shape changing propeller to achieve this drag reduction.

Chapter two presents the setup and tools used to address these questions. We will describe the free surface water channel that was built specifically for this project and the systems that were used to hold the propellers and sensors.

Chapter three presents our results on shape changing propellers. We discuss the deformations and forces experienced by two different propellers. The first is built to improve our understanding of the fluid-structure interaction problem of a flexible rotor in water: it has slender ribbon-like blades that experience large amplitude bending and torsion. We will show how the direction and magnitude of the deformations can be understood through a geometric argument and highlight a strong link between loads and deformations. The second propeller studied is focused on improving the efficiency: its design is based on the work of Cognet (2017). We will show that using this propeller with the right flexibility can improve the resilience to a change in the tip speed ratio. We will predict its torsional deformation using a simple scaling law.

Finally, chapter four addresses the new problem of intermittent propulsion with a propeller. In a first part, we describe the shape-changing propeller used to reduce drag during gliding. Using a modified blade element model, we are able to explain its reconfiguration. We will then use it dynamically in a novel experimental setup capable of reproducing the time-dependent burst and coast motion of fish. Using this setup and the shape changing propeller, we will show that it is possible to reduce the cost of motion by using intermittent propulsion. A time-dependent model of the motion of the boat will help us identify the constraints on the boat and propeller system that make intermittent motion more efficient than continuous motion.

Bibliography

AKOZ, E., HAN, P., LIU, G., DONG, H., and MOORED, K. W. (2019). Large-Amplitude Intermittent Swimming in Viscous and Inviscid Flows. *AIAA Journal*, vol. 57(9):pp. 3678–3685 6

AKOZ, E., MIVEHCHI, A., and MOORED, K. W. (2021). Intermittent unsteady propulsion with a combined heaving and pitching foil. *Physical Review Fluids*, vol. 6(4):p. 043101 6

AKOZ, E. and MOORED, K. W. (2018). Unsteady propulsion by an intermittent swimming gait. *Journal of Fluid Mechanics*, vol. 834:pp. 149–172 5, 6, 7

ALAM, M. M., ZHOU, Y., YANG, H. X., GUO, H., and MI, J. (2010). The ultra-low Reynolds number airfoil wake. *Experiments in Fluids*, vol. 48(1):pp. 81–103 12, 13

ALBEN, S., SHELLEY, M., and ZHANG, J. (2002). Drag reduction through self-similar bending of a flexible body. *Nature*, vol. 420(6915):pp. 479–481 2, 3, 4

ALBEN, S., SHELLEY, M., and ZHANG, J. (2004). How flexibility induces streamlining in a two-dimensional flow. *Physics of Fluids*, vol. 16(5):pp. 1694–1713 2

ASHRAF, I., WASSENBERGH, S. V., and VERMA, S. (2020). Burst-and-coast swimming is not always energetically beneficial in fish (Hemigrammus bleheri). *Bioinspiration & Biomimetics*, vol. 16(1):p. 016002 6

BAROIS, T. and DE LANGRE, E. (2013). Flexible body with drag independent of the flow velocity. *Journal of Fluid Mechanics*, vol. 735:p. R2 2

BLAKE, R. W. (2004). Fish functional design and swimming performance. *Journal of Fish Biology*, vol. 65(5):pp. 1193–1222 5

CHUNG, M.-H. (2009). On burst-and-coast swimming performance in fish-like locomotion. *Bioinspiration & Biomimetics*, vol. 4(3):p. 036001 6

COGNET, V. (2017). *Optimisation des éoliennes à axe horizontal par l'utilisation de pales flexibles*. Ph.D. thesis, Université Paris Cité 8, 16

COGNET, V., COURRECH DU PONT, S., DOBREV, I., MASSOUH, F., and THIRIA, B. (2017). Bioinspired turbine blades offer new perspectives for wind energy. *Proceedings of the Royal Society A: Mathematical, Physical and Engineering Sciences*, vol. 473(2198):p. 20160726 1, 8, 12, 16

COGNET, V., COURRECH DU PONT, S., and THIRIA, B. (2020). Material optimization of flexible blades for wind turbines. *Renewable Energy*, vol. 160:pp. 1373–1384 8

CORRIGAN, J. J. and SCHILLINGS, J. J. (1994). Empirical model for stall delay due to rotation. In *American Helicopter Society Aeromechanics Specialists Conference*. San Francisco, CA 9

COSTELLO, J. H., COLIN, S. P., GEMMELL, B. J., DABIRI, J. O., and KANSO, E. A. (2023). A fundamental propulsive mechanism employed by swimmers and flyers throughout the animal kingdom. *Journal of Experimental Biology*, vol. 226(11):p. jeb245346 4

COUGHLIN, D. J., CHROSTEK, J. D., and ELLERBY, D. J. (2022). Intermittent propulsion in largemouth bass, Micropterus salmoides, increases power production at low swimming speeds. *Biology Letters*, vol. 18(5):p. 20210658 4

DE LANGRE, E. (2006). Frequency lock-in is caused by coupled-mode flutter. *Journal of Fluids and Structures*, vol. 22(6):pp. 783–791 7

DE LANGRE, E. (2008). Effects of Wind on Plants. *Annual Review of Fluid Mechanics*, vol. 40(1):pp. 141–168 2

DI SANTO, V., GOERIG, E., WAINWRIGHT, D. K., AKANYETI, O., LIAO, J. C., CASTRO-SANTOS, T., and LAUDER, G. V. (2021). Convergence of undulatory swimming kinematics across a diversity of fishes. *Proceedings of the National Academy of Sciences*, vol. 118(49):p. e2113206118. Publisher: Proceedings of the National Academy of Sciences 5

DURÁN VENEGAS, E., LE DIZÈS, S., and ELOY, C. (2019). A strongly-coupled model for flexible rotors. *Journal of Fluids and Structures*, vol. 89:pp. 219–231 8, 9

EHRENSTEIN, U., MARQUILLIE, M., and ELOY, C. (2014). Skin friction on a flapping plate in uniform flow. *Philosophical Transactions of the Royal Society A: Mathematical, Physical and Engineering Sciences*, vol. 372(2020):p. 20130345 6

ELDEMERDASH, A. (2023). *Fluid-structure interaction of strongly deforming flexible rotors*. Ph.D. thesis, Aix Marseille Université 9

ELDEMERDASH, A. and LEWEKE, T. (2021). Fluid–structure interaction of a flexible rotor in water. *Journal of Fluids and Structures*, vol. 103:p. 103259 9

ELOY, C. (2012). Optimal Strouhal number for swimming animals. *Journal of Fluids and Structures*, vol. 30:pp. 205–218 5

FISH, F. E., NUSBAUM, M. K., BENESKI, J. T., and KETTEN, D. R. (2006). Passive cambering and flexible propulsors: cetacean flukes. *Bioinspiration & Biomimetics*, vol. 1(4):p. S42 4

FLORYAN, D., VAN BUREN, T., ROWLEY, C. W., and SMITS, A. J. (2017a). Scaling the propulsive performance of heaving and pitching foils. *Journal of Fluid Mechanics*, vol. 822:pp. 386–397 5, 7

FLORYAN, D., VAN BUREN, T., and SMITS, A. J. (2017b). Forces and energetics of intermittent swimming. *Acta Mechanica Sinica*, vol. 33(4):pp. 725–732 7

FLORYAN, D., VAN BUREN, T., and SMITS, A. J. (2018). Efficient cruising for swimming and flying animals is dictated by fluid drag. *Proceedings of the National Academy of Sciences*, vol. 115(32):pp. 8116–8118 5

GAZZOLA, M., ARGENTINA, M., and MAHADEVAN, L. (2014). Scaling macroscopic aquatic locomotion. *Nature Physics*, vol. 10(10):pp. 758–761 5

GLAUERT, H. (1983). *The Elements of Aerofoil and Airscrew Theory*. Cambridge University Press 9, 10

GODOY-DIANA, R. and THIRIA, B. (2018). On the diverse roles of fluid dynamic drag in animal swimming and flying. *Journal of The Royal Society Interface*, vol. 15(139):p. 20170715 6

GOSSELIN, F., DE LANGRE, E., and MACHADO-ALMEIDA, B. A. (2010). Drag reduction of flexible plates by reconfiguration. *Journal of Fluid Mechanics*, vol. 650:pp. 319–341 3, 4

GOSSELIN, F. P. and DE LANGRE, E. (2011). Drag reduction by reconfiguration of a poroelastic system. *Journal of Fluids and Structures*, vol. 27(7):pp. 1111–1123 3, 4

HANSEN, M. O. L. (2015). *Aerodynamics of Wind Turbines*. Routledge. Google-Books-ID: LcblCAAAQBAJ 7, 10

HARDER, D. L., SPECK, O., HURD, C. L., and SPECK, T. (2004). Reconfiguration as a Prerequisite for Survival in Highly Unstable Flow-Dominated Habitats. *Journal of Plant Growth Regulation*, vol. 23(2):pp. 98–107 2

HASSANI, M. (2016). *Elastic Reconfiguration of Bending and Twisting Rods in Air Flow*. Ph.D. thesis, Polytechnique Montréal 4

HOERNER, S. F. (1965). *Fluid-Dynamic Drag* 2

HUSSAIN, M., ABDEL-NASSER, Y., BANAWAN, A., and AHMED, Y. M. (2021). Effect of hydrodynamic twisting moment on design and selection of flexible composite marine propellers. *Ocean Engineering*, vol. 220:p. 108399 8

IMO (2020). *Fourth IMO Greenhouse Gas Study 2020*. London: International Maritime Organization (IMO). 1

IPCC (2022). *Climate Change 2022: Impacts, Adaptation and Vulnerability*. Summary for Policymakers. Cambridge University Press, Cambridge, UK and New York, USA 1

KAUSHIK, M. (2019). Thin Airfoil Theory. In KAUSHIK, M., editor, *Theoretical and Experimental Aerodynamics*, pp. 127–144. Springer, Singapore 12

KRAMER, D. L. and MCLAUGHLIN, R. L. (2001). The Behavioral Ecology of Intermittent Locomotion. *American Zoologist*, vol. 41(2):pp. 137–153 4

LAUDER, G. V. (2015). Fish Locomotion: Recent Advances and New Directions. *Annual Review of Marine Science*, vol. 7(1):pp. 521–545 5

LI, G., ASHRAF, I., FRANÇOIS, B., KOLOMENSKIY, D., LECHENAULT, F., GODOY-DIANA, R., and THIRIA, B. (2021). Burst-and-coast swimmers optimize gait by adapting unique intrinsic cycle. *Communications Biology*, vol. 4(1):pp. 1–7 6

LI, G., KOLOMENSKIY, D., LIU, H., GODOY-DIANA, R., and THIRIA, B. (2023). Intermittent versus continuous swimming: An optimization tale. *Physical Review Fluids*, vol. 8(1):p. 013101 1, 6, 7

LI, H., GOODWILL, T., JANE WANG, Z., and RISTROPH, L. (2022). Centre of mass location, flight modes, stability and dynamic modelling of gliders. *Journal of Fluid Mechanics*, vol. 937:p. A6 13

LIGHTHILL, M. J. (1971). Large-amplitude elongated-body theory of fish locomotion. *Proceedings of the Royal Society of London. Series B. Biological Sciences*, vol. 179(1055):pp. 125–138 5

LISSAMAN, P. B. S. (1983). Low-Reynolds-Number Airfoils. *Annual Review of Fluid Mechanics*, vol. 15(1):pp. 223–239 12, 13

MACNEILL, R. and VERSTRAETE, D. (2017). Blade element momentum theory extended to model low Reynolds number propeller performance. *The Aeronautical Journal*, vol. 121(1240):pp. 835–857 10

MARIO, H. (2012). Aerodynamic Propeller Model for Load Analysis. MSc Thesis 9

MARSH, G. (2004). A new start for marine propellers? *Reinforced Plastics*, vol. 48(11):pp. 34–38 7, 8

MARZIN, T., DE LANGRE, E., and RAMANANARIVO, S. (2022). Shape reconfiguration through origami folding sets an upper limit on drag. *Proceedings of the Royal Society A: Mathematical, Physical and Engineering Sciences*, vol. 478(2267):p. 20220592 2

MASTERS, I., CHAPMAN, J. C., WILLIS, M. R., and ORME, J. A. C. (2011). A robust blade element momentum theory model for tidal stream turbines including tip and hub loss corrections. *Journal of Marine Engineering & Technology*, vol. 10(1):pp. 25–35 9

MATEESCU, D. and ABDO, M. (2010). Analysis of flows past airfoils at very low Reynolds numbers. *Proceedings of the Institution of Mechanical Engineers, Part G: Journal of Aerospace Engineering*, vol. 224(7):pp. 757–775 12, 13

MOORED, K. W. and QUINN, D. B. (2019). Inviscid Scaling Laws of a Self-Propelled Pitching Airfoil. *AIAA Journal*, vol. 57(9):pp. 3686–3700 5

MOTLEY, M., LIU, Z., and YOUNG, Y. (2009). Utilizing fluid–structure interactions to improve energy efficiency of composite marine propellers in spatially varying wake. *Composite Structures*, vol. 90(3):pp. 304–313 8

MULLER, U., STAMHUIS, E., and VIDELER, J. (2000). Hydrodynamics of unsteady fish swimming and the effects of body size: comparing the flow fields of fish larvae and adults. *Journal of Experimental Biology*, vol. 203(2):pp. 193–206 4

NG, L., ELGAR, M. A., and STUART-FOX, D. (2021). From Bioinspired to Bioinformed: Benefits of Greater Engagement From Biologists. *Frontiers in Ecology and Evolution*, vol. 9 1

PAOLETTI, P. and MAHADEVAN, L. (2014). Intermittent locomotion as an optimal control strategy. *Proceedings of the Royal Society A: Mathematical, Physical and Engineering Sciences*, vol. 470(2164):p. 20130535 5

RAMANANARIVO, S., GODOY-DIANA, R., and THIRIA, B. (2011). Rather than resonance, flapping wing flyers may play on aerodynamics to improve performance. *Proceedings of the National Academy of Sciences*, vol. 108(15):pp. 5964–5969 4

RAYNER, J. M. V., VISCARDI, P. W., WARD, S., and SPEAKMAN, J. R. (2001). Aerodynamics and Energetics of Intermittent Flight in Birds. *American Zoologist* 1, 4

REGENER, P., MIRSADRAEE, Y., and ANDERSEN, P. (2018). Nominal vs. Effective Wake Fields and Their Influence on Propeller Cavitation Performance. *Journal of Marine Science and Engineering*, vol. 6(2):p. 34 1

RIBAK, G., WEIHS, D., and ARAD, Z. (2005). Submerged swimming of the great cormorant *Phalacrocorax carbo sinensis* is a variant of the burst-and-glide gait. *Journal of Experimental Biology*, vol. 208(20):pp. 3835–3849 4

SCHOUVEILER, L. and BOUDAOUD, A. (2006). The rolling up of sheets in a steady flow. *Journal of Fluid Mechanics*, vol. 563:p. 71 3, 4

SFAKIOTAKIS, M., LANE, D., and DAVIES, J. (1999). Review of fish swimming modes for aquatic locomotion. *IEEE Journal of Oceanic Engineering*, vol. 24(2):pp. 237–252 5

SICARD, J. and SIROHI, J. (2012). Experimental Study of an Extremely Flexible Rotor for Microhelicopters. *Journal of Aircraft*, vol. 49(5):pp. 1306–1314 7

SICARD, J. and SIROHI, J. (2016). Aeroelastic stability of a flexible ribbon rotor blade. *Journal of Fluids and Structures*, vol. 67:pp. 106–123 7

SNEL, H., HOUWINK, R., and BOSSCHERS, J. (1994). Sectional prediction of lift coefficients on rotating wind turbine blades in stall. Tech. Rep., Netherlands: N. p. 9

SUNADA, S., SAKAGUCHI, A., and KAWACHI, K. (1997). Airfoil Section Characteristics at a Low Reynolds Number. *Journal of Fluids Engineering*, vol. 119(1):pp. 129–135 12

SØRENSEN, J. N. (2011). Aerodynamic Aspects of Wind Energy Conversion. *Annual Review of Fluid Mechanics*, vol. 43(1):pp. 427–448 9

TANG, D. M. and DOWELL, E. H. (1993). Experimental and theoretical study for nonlinear aeroelastic behavior of a flexible rotor blade. *AIAA Journal*, vol. 31(6):pp. 1133–1142 7

TAYLOR, G. K., TRIANTAFYLLOU, M. S., and TROPEA, C., editors (2010). *Animal Locomotion*. Springer Berlin Heidelberg, Berlin, Heidelberg 4

TIMMER, W. A. (2010). Aerodynamic characteristics of wind turbine blade airfoils at high angles-of-attack. In *3rd EWEA Conference - Torque 2010*, p. 8. European Wind Energy Association 12

TOBALSKE, B. W. (2010). Hovering and intermittent flight in birds. *Bioinspiration & Biomimetics*, vol. 5(4):p. 045004 4

TRIANTAFYLLOU, G. S., TRIANTAFYLLOU, M. S., and GROSENBAUGH, M. A. (1993). Optimal Thrust Development in Oscillating Foils with Application to Fish Propulsion. *Journal of Fluids and Structures*, vol. 7(2):pp. 205–224 5

TRIANTAFYLLOU, M. S., TRIANTAFYLLOU, G. S., and GOPALKRISHNAN, R. (1991). Wake mechanics for thrust generation in oscillating foils. *Physics of Fluids A: Fluid Dynamics*, vol. 3(12):pp. 2835–2837 5

VAN BUREN, T., FLORYAN, D., and SMITS, A. J. (2019). Scaling and Performance of Simultaneously Heaving and Pitching Foils. *AIAA Journal*, vol. 57(9):pp. 3666–3677 5

VATANABE, S. L., PIRES, R. F., NAKASONE, P. H., and SILVA, E. C. N. (2008). New configurations of oscillatory flow pumps using bimorph piezoelectric actuators. In DAVIS, L. P., HENDERSON, B. K., and MCMICKELL, M. B., editors, *The 15th International Symposium on: Smart Structures and Materials & Nondestructive Evaluation and Health Monitoring*, p. 69300U. San Diego, California 5

VIDELER, J. (1981). Swimming Movements, Body Structure and Propulsion in Cod Gadus morhua. *Symposia of the Zoological Society of London*, vol. 48(1):pp. 1–27 4, 6

VOGEL, S. (1989). Drag and Reconfiguration of Broad Leaves in High Winds. *Journal of Experimental Botany*, vol. 40(8):pp. 941–948 2

VOGEL, S. (2003). Nature's Swell, But Is It Worth Copying? *MRS Bulletin*, vol. 28(6):pp. 404–408 3

VOLLSINGER, S., MITCHELL, S. J., BYRNE, K. E., NOVAK, M. D., and RUDNICKI, M. (2005). Wind tunnel measurements of crown streamlining and drag relationships for several hardwood species. *Canadian Journal of Forest Research*, vol. 35(5):pp. 1238–1249 2

WEBB, A., BANKS, J., PHILLIPS, C., HUDSON, D., TAUNTON, D., and TURNOCK, S. (2011). Prediction of passive and active drag in swimming. *Procedia Engineering*, vol. 13:pp. 133–140 5

WEIHS, D. (1974). Energetic advantages of burst swimming of fish. *Journal of Theoretical Biology*, vol. 48(1):pp. 215–229 1, 6

WINSTON, M. M. (1968). A hovering investigation of an extremely flexible lifting rotor. Tech. Rep., NASA 7

WU, G., YANG, Y., and ZENG, L. (2007). Kinematics, hydrodynamics and energetic advantages of burst-and-coast swimming of koi carps (Cyprinus carpio koi). *THE JOURNAL OF EXPERIMENTAL BIOLOGY*, vol. 210(12):pp. 2181–2191 4, 6

WU, T. Y.-T., BROKAW, C. J., and BRENNEN, C., editors (1975). *Swimming and Flying in Nature: Volume 2*. Springer US, Boston, MA 4

WU, X., ZHANG, X., TIAN, X., LI, X., and LU, W. (2020). A review on fluid dynamics of flapping foils. *Ocean Engineering*, vol. 195:p. 106712 5

XIA, D., CHEN, W.-s., LIU, J.-k., and LUO, X. (2018). The energy-saving advantages of burst-and-glide mode for thunniform swimming. *Journal of Hydrodynamics*, vol. 30(6):pp. 1072–1082 4, 6

YOUNG, Y. (2008). Fluid–structure interaction analysis of flexible composite marine propellers. *Journal of Fluids and Structures*, vol. 24(6):pp. 799–818 8

YOUNG, Y. L., MOTLEY, M. R., BARBER, R., CHAE, E. J., and GARG, N. (2016). Adaptive Composite Marine Propulsors and Turbines: Progress and Challenges. *Applied Mechanics Reviews*, vol. 68(6):p. 060803 7, 8

Chapter 2

Experimental setup

This section describes the experimental tools used in during the thesis. First the hydrodynamic channel in which all the experiments were performed, then the different model scale boats used to house the sensors and their instrumentation. Finally we describe the material properties of the flexible sheets we use to build elastic propeller blades.

2.1 Hydrodynamic channel

2.1.1 Description

We show a simplified sketch of the channel in Fig. 2.1, the goal of the channel is to accommodate two types of experiments: first the study of any type of rotor by producing a steady, uniform flow at any desired velocity. Second the study of the intermittent motion: the device carrying the rotor must be allowed to move freely along the axis of the channel. Thus, the channel must be long enough to accommodate this motion while maintaining uniform conditions.

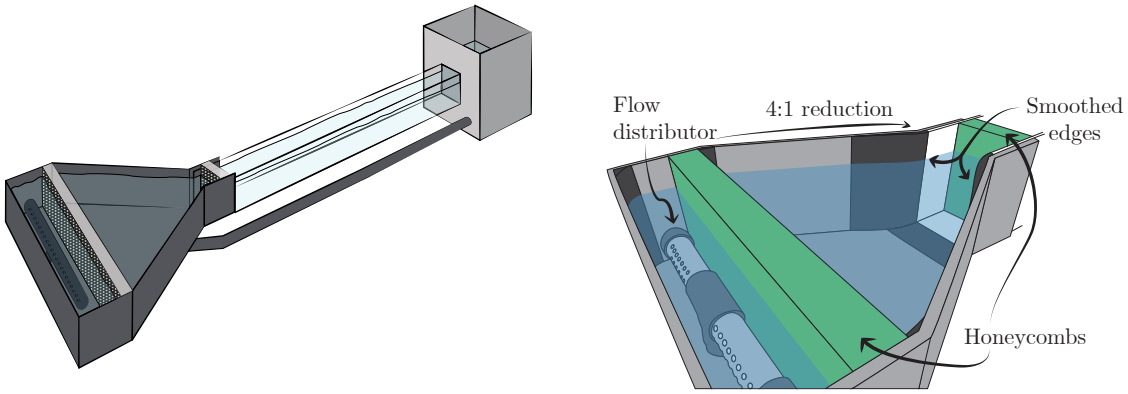

Figure 2.1: Simplified sketch of the free surface canal, (right) zoom on the convergent section.

As a consequence, the channel is built with a very long test section (30 cm x 20 cm x 2 m) and with a free surface. We chose the frontal area and rotor size such that the blockage in the channel stays limited to not qualitatively change the flows studied (Whelan et al., 2009) (in practice always below 15%). Around this section, we built a return channel designed to keep the test conditions constant. A tank, which acts as a buffer and holds most of the water in the whole setup, is located at the end of the channel. This tank is connected to the pump that drives the flow (not visible in Fig. 2.1) with a PVC pipe. The flow generated by the pump is expelled upwards into a convergent section that ensures steady flow in the channel.

The pump (Pentair Whisperflo) is equipped with a variable frequency drive which allows us to adjust its rotational speed. The pump is designed to produce important flow rates with little added pressure, which is ideal for our application because the pressure drop in the entire channel is very small. When the entire chanell is mounted we measured fluxes from 2 to 10 l/s (i.e., flows from 5 to 25 cm/s). The pump has two drive modes: constant angular velocity or constant flux. The pump does not have a flux measuring sensor and uses a factory calibration to control the rotation rate using the electrical power drawn. The two modes produce a constant flow rate, but we will see below (Fig. 2.3) that the constant RPM mode allows us to obtain smaller velocities and is used throughout the thesis.

To transform the high speed, fluctuating flow generated by the pump into a steady, uniform flow in the test section, we use a convergent section that has three main roles:

- transform the fast flow, concentrated in a pipe into a flux source homogenous over the whole width and height of the channel,
- mitigate all the fluctuations that might be present in the initial source,
- uniformly accelerate the flow such that it can be used in the test section.

For the first objective, we use a T-shaped junction that is perforated with multiple holes so that the fast flow from the pump becomes multiple sources across the width of the channel (Fig. 2.1, right). These holes create localized jets that are directed away from the test section, towards a wall. The jets therefore dissipate most of their energy, and we obtain in a diffuse, near-zero velocity flow source. We then uniformly accelerate the flow by using a 4 to 1 reduction in width over 50 cm. To avoid boundary layer separation of the flow over the live edges, we added smooth 3D printed parts to hide these edges. Finally, to dampen the remaining fluctuations in the channel, we used two sets of honeycombs at the entrance and exit of the converging section. They are made of cylindrical straws aligned in a square pattern. A boundary layer develops inside each straw, forcing the flow to align with it. As a result, flow structures larger than the size of the straw disappear (Lumley and McMahon, 1967).

2.1.2 Calibration

To calibrate the flow speed in the channel and quantify the magnitude of the fluctuations, we have used two different tools: Particle Image Velocimetry (PIV) and Constant Temperature Anemometry (CTA).

The PIV technique consists of seeding the channel with polyamide particles that act as passive tracers: we illuminate them with a laser sheet placed vertically in the center of the channel and record their movement in this plane with a fast camera. The size of the particles is 100 µm so that they don't settle too fast at the bottom of the channel and still provide good contrast for the camera. We then process the images to extract the 2D velocity field in the illuminated plane. The algorithm compares

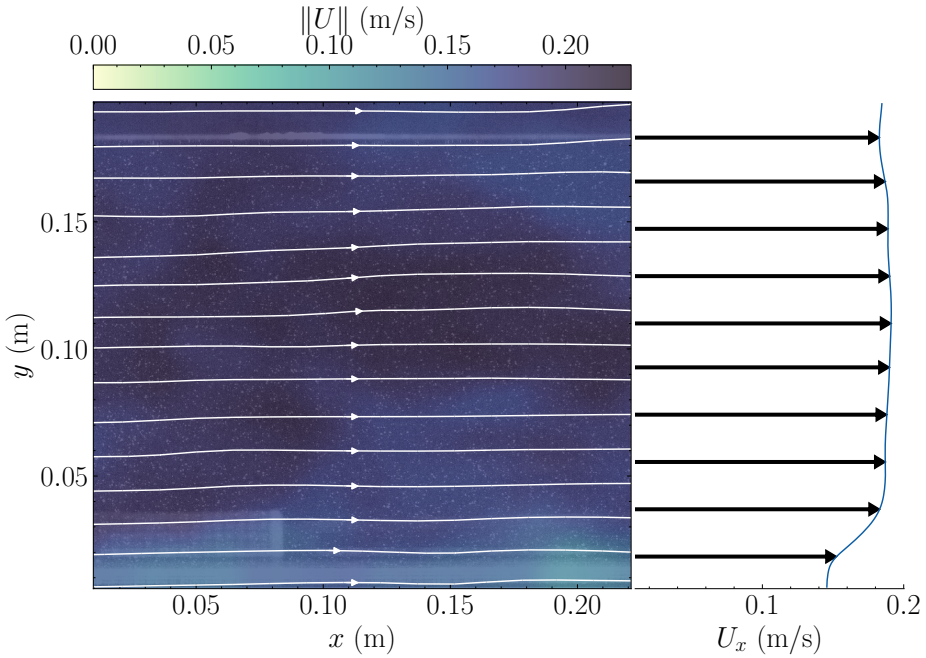

Figure 2.2: Example of flow field obtained using PIV. (left) Instantaneous snapshot of the reconstructed flow (superimposed with the raw image). Colors show the velocity norm while streamlines show its direction. (right) Time and space averaged vertical velocity profile

two successive images to extract the field in the following way: the first image is sliced into small windows (in our case a square with a side of 61 pixels, out of a 1216x1200 image), and then the algorithm looks in the second image where the correlation with the small window is best. This gives the best estimate of the displacement of the particles in the window and thus an average velocity vector for that window (Tropea et al., 2007). This operation is then repeated for every window, for every frame, and we obtain a time dependent, 2D velocity field. It should be noted that any out-of-plane velocity cannot be detected using this method.

In Fig. 2.2 (left) we show an example of the instantaneous field in the channel. We see that the flow speed is very homogeneous in speed (color) except at the very bottom with only minor disturbances in the vertical direction. We also plot the time and x averaged (over 10 s and 0.2 m) velocity profile on the right, and we can confirm that the flow is homogeneous in the vertical direction in the middle of channel. At the bottom we see smaller velocities, indicating the presence of a boundary layer. We can measure the size of this boundary layer in the middle of our test section and see that 95% of the mean flow speed is always reached about 2 cm above the bottom wall. Even we did not measure it directly, it is most likely that similar boundary layers develop on the side walls.

We show the mean flow speed in the channel for both pump setting modes in Fig. 2.3. Both modes have a linear relationship with the flow speed. However, the constant flux mode (blue dots) is no longer linear for small fluxes and cannot produce mean velocities below 0.1 m/s. The constant RPM mode stays linear with the flow rate down to 0.05 m/s and since both modes produce similar fluctuations around the mean speed, we use the constant RPM mode in the following.

It should be noted that one advantage of the constant flux mode overlooked here is the feedback loop within the pump. When making important changes in the RPM setting the pump suddenly accelerates which produces back and forth oscillations in the channel. On the contrary, the constant

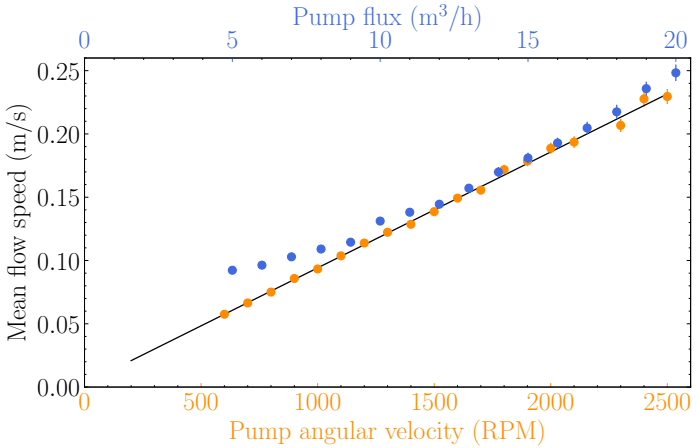

Figure 2.3: Mean flow speed in the channel as a function of the pump angular velocity and indicated flow rate. Error bars indicate the standard deviation of the flow speed. (black line) Best fit of the constant RPM data: $U\,[\mathrm{m/s}] = 9.16 \times 10^{-5}\Omega_{\mathrm{pump}}[\mathrm{RPM}] + 2.57 \times 10^{-3}[\mathrm{m/s}]$.

flow rate mode progressively accelerates and directly settles on the right velocity. In the following we thus take care of waiting for the oscillations to dampen before starting an experiment after changing the flow velocity.

In order to make experiments as close to an open water situation as possible, the intensity of the fluctuations in the incoming flow must be kept to a minimum. Indeed, when a boat is moving through initially still water, the incoming flow on the propeller is only due to the boat speed and thus not fluctuating at all. In the experiments we change the frame of reference by imposing a constant velocity, and the fluctuations must also be minimal to imitate the open water situation. The quantity that measures the amount of fluctuations in the flow is the turbulence intensity and is defined as:

$$\tau_U = \frac{\sqrt{1/3\left(u_x'^2 + u_y'^2 + u_z'^2\right)}}{\overline{U}}, \tag{2.1}$$

where $\overline{U}$ is the mean flow speed (which is only horizontal in our case) and u_i' is the fluctuation in the i direction.

Two problems arise when trying to measure the turbulence intensity in the channel using PIV: First, the velocity component out of the laser plane is not accessible. Although its mean contribution is expected to be zero, its standard deviation has no reason to be. The second problem is that PIV has a finite resolution and if there are smaller flow structures, they won't be taken into account in the standard deviation. In our case, the size of the interrogation window is about 1 cm. If the incoming flow is indeed turbulent, the classical energy cascade results in important contribution from structures which can be as small as the Kolmogorov scale (Frisch, 1995). This scale is defined as

$$\eta_K = \left(\frac{\nu^3}{\epsilon}\right)^{1/4}, \tag{2.2}$$

where ν is the kinematic viscosity of water and ϵ the turbulent kinetic energy of the incoming flow: $\epsilon = 1/2\left(u_x'^2 + u_y'^2 + u_z'^2\right)$. If the turbulence intensity in the channel is about 5% at a velocity of 0.1 m/s, this gives a minimal scale of 0.4 mm. The PIV alone is thus not able to correctly measure it.

The first problem can be solved by approximating the fluctuations in the transverse direction to be the same as the ones in the vertical direction: both directions perpendicular to the main flow should

have fluctuations of the same order of magnitude. To overcome the second issue however, we need to use a different measuring method.

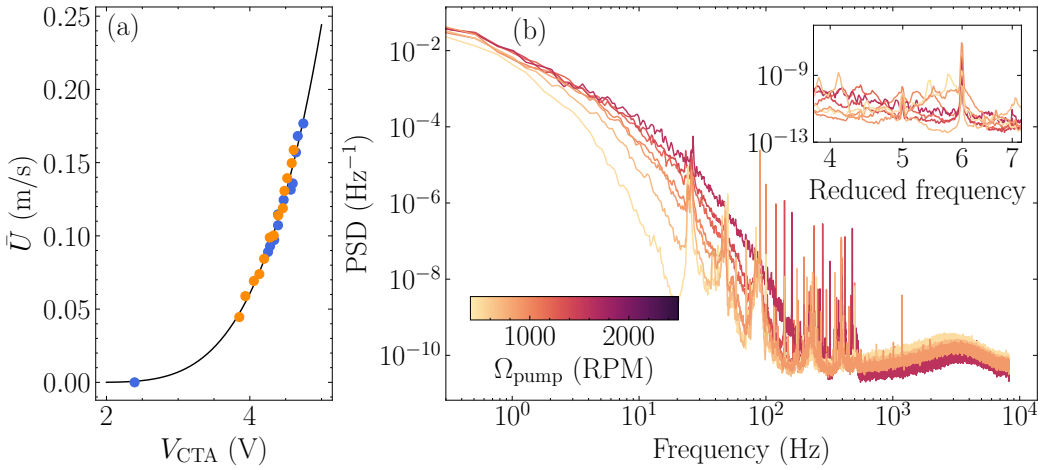

Figure 2.4: (a) Calibration of the hot-wire probe using the PIV data for both pump modes (blue) constant pump flux, (orange) constant RPM. (Black line) Best fit using the King's law: $\bar{U} = 1.82 \times 10^{-3}(V_{\mathrm{CTA}} - 1.60)^4$ with V_{CTA} in V and $\bar{U}$ in m/s. (b) Power spectral density (normalized by the mean speed) of the hot-wire measurements. Colors correspond to different pump angular velocity. (inset) Same PSD but the frequency axis is normalized by the angular velocity of the pump.

We use hot-wire anemometry to better measure the intensity of the fluctuations in the channel. It allows for point wise measurements of the flow speed with very high temporal resolution. Its principle is based on measuring the temperature of a tiny wire exposed to the flow. It is heated by a current flowing through it and cooled by the flow carrying away heat energy. In our case we use Constant Temperature Anemometry where the temperature of the wire is held constant, and thus its resistance as well through a feedback loop. This means that a change in flow speed is measured through a change in the current flow through the wire. We use the MiniCTA circuit from Dantec Dynamics to control the hot-wire probe: it has a bandwidth of above 10 kHz and can be used in water applications. The probe is specially designed to work in conducting liquids and is made out of a 70 µm quartz fiber, 3 mm long covered by a nickel film with a thickness of 0.1 µm. The probe is straight and mainly sensitive to flows which are perpendicular to the axis of the fiber. We place it horizontally, perpendicular to the incoming flow, in the middle of the channel. The relationship between the sensor resistance R_w, the current flowing through it I_w and the flow speed U is known to follow Kings's law for incompressible flows (Tropea et al., 2007):

$$\frac{R_w I_w^2}{R_w - R_a} = A + BU^{0.5}, \tag{2.3}$$

where R_a is the resistance of the unheated sensor and A and B are constants which depend on the wire and fluid properties (e.g., fluid temperature). We thus monitored the fluid temperature (mainly controlled by the thermostat of the lab room) with a thermometer when using this sensor. The output from the MiniCTA is a voltage V_{CTA} proportional to I_w and thus we expect the relationship between U and V_{CTA} to be of the form $U = a_1 + a_2 V_{\mathrm{CTA}}^4$ where a_1 and a_2 are constants.

Fig. 2.4 (a) shows how the hot-wire is calibrated using the PIV measurements with both pump modes. On the right we show the power spectral density of the signal. We see a rapid decrease of the energy density as the frequency increases: above 100 Hz (the time resolution of the PIV) the most energetic

mode remaining beyond this value is 10^3 less important than the mean flow. We can also notice that the energy is spread over all frequencies below 10 Hz. The high frequency peaks have a relatively low energy associated. The peak at 25 Hz present in all measurements most likely has an electrical origin since it is not visible in the PIV. The peaks from 100 Hz onwards seem to be noise created by the pump, indeed when plotting the spectrum against the reduced frequency (f/Ω_{pump}) in the inset, we can see a peak for all curves at a value of 6, the number of blades of the pump's propeller.

The hot-wire measurement was performed before the honeycombs were installed, and the PIV was performed before and after. Although the exact turbulence intensity is not available for the final version of the channel, comparing the hot-wire and PIV results is still useful to get the order of magnitude of the fluctuations. Fig. 2.5 shows the intensity of the fluctuations in the channel for both configurations, for both pump modes. First, the hot-wire and PIV measurements are of the same order of magnitude for the channel without honeycombs (hollow bullets and triangles). The similarity of both measurement methods means that the structures we miss with PIV due to too coarse spatial or temporal resolution have low energy associated with them. Then, the effectiveness of the honeycombs in reducing the fluctuations in the channel is easily verified: from 15 to 20%, the turbulent intensity is reduced to below 5 % for all flow velocities. Since we do not study the small details of the flow, this value is satisfactory.

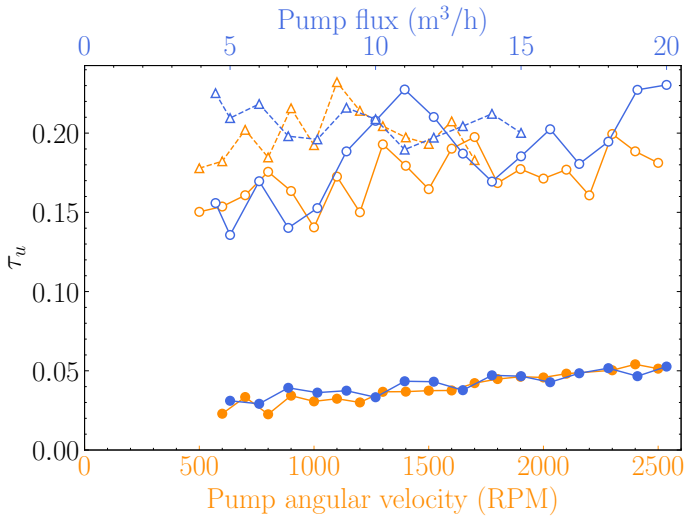

Figure 2.5: Fluctuation intensity in the channel as a function of the pump setting. The color indicates the pump mode as in Fig. 2.3. Hollow markers correspond to the channel without the honeycombs installed, while the full ones are with both of them installed. Bullets represent PIV measurements while triangles show hot-wire data.

To avoid depending on the calibration of the pump, we finally added a flow meter (GPI TM200-N-P) in the return channel of the experiments. The magnitude of the flux is encoded by the angular velocity of a small impeller placed in the pipe. We can simply measure the water height in the channel to obtain the mean velocity.

2.2 Boat hangar

This section describes the different "boats" that were used during this thesis. Their aim is to hold all the required sensors and protect them from the surrounding water. We use different iterations

throughout the thesis, either because the previous one had limitations or because new constraints required important changes. We detail here their inner workings as well as the trade-offs that each design implies.

They are presented here chronologically. The first version is used in Sec. 3.1, the second one is used in Sec 3.1.4. The final boat is used in Secs. 3.2 and 4.

2.2.1 Submarine

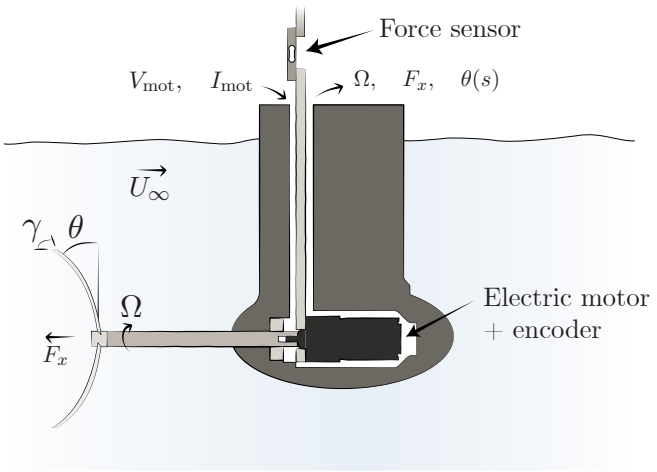

Figure 2.6: First design of the hull

The first boat (Fig. 2.6) has a very simple design that allowed us to spin a propeller in the flow at a desired angular velocity and record the force. A small electric motor (Portescap 22N78 311P), held in place by a metal rod, turns a shaft to which the blades are attached. The shaft is oriented upstream so that the incoming water flow is undisturbed when it reaches the blades. The motor has a 5 to 1 gearbox attached to it to be able to spin the blades through water without stalling. We measure the angular velocity of the propeller by placing a small magnet on the shaft and a Hall effect sensor in front of it. Each time the magnet passes in front of the sensor, the output goes from 0 to 5V. By measuring the frequency of the output signal, we can measure the angular velocity.

The motor and encoder are protected from the water by a 3D-printed hull, which is assembled in two parts, joined by screws and an O-ring to make the seam watertight. This hull is designed to minimize its impact on the surrounding flow: it adopts an airfoil profile in thin sections and is as thin as possible around the motor. The shaft is held in place by a bearing, and the seal is made by putting grease between the hull and the shaft. We attached the entire boat to a bending force sensor (CZL616C, measuring up to ± 7.65 N) placed vertically and parallel to the incoming flow. This sensor thus measures the total axial force (thrust + drag) during the experiment and is attached at the other end to a fixed point in the laboratory.

This boat was used to measure the thrust and deformation of a fully flexible propeller (Sec. 3.1). We tried to measure the power required to turn the propeller using the electrical power consumed by the engine. However, two problems arose: (i) there is a lot of dissipation in the system, which is difficult to quantify (Joule effect in the motor, losses in the gearbox or in the bearing), and (ii) the efficiency of the motor itself: its conversion rate between electrical and mechanical power is not a constant over the range of angular speeds (as shown in the manufacturer's documentation). Overcoming these

difficulties would have added too much uncertainty to the power measurement, so we decided to use a dedicated torque sensor in the second version.

2.2.2 Semi-submerged boat

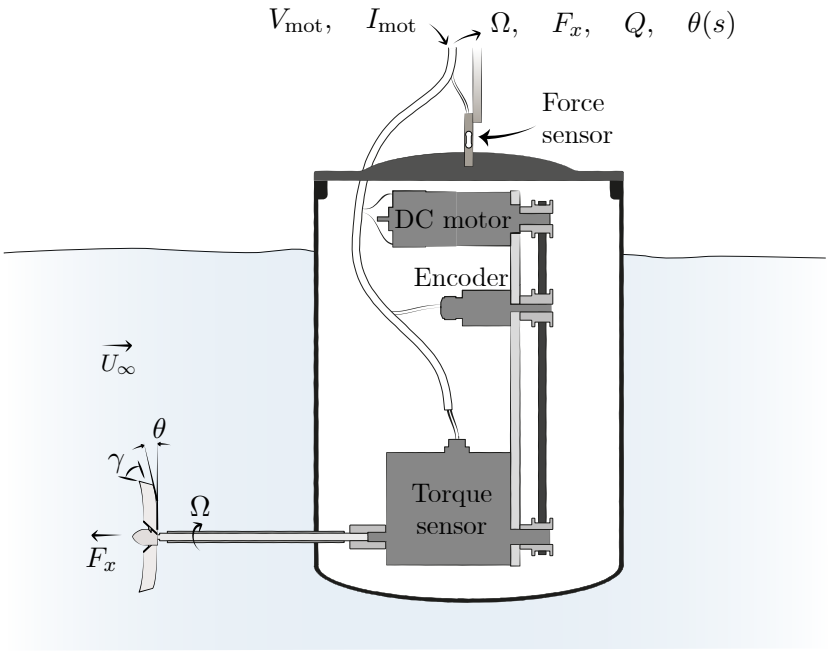

Figure 2.7: Second design of the hull, adding a torque sensor

This second design (Fig. 2.7) is an improvement of the first. The main idea remains the same: a shaft facing the incoming flow, upstream of the hull, is rotated by an electric motor. The main difference is the addition of a torque sensor (Burster 8661 4050 V0000, measuring up to ± 0.05 N.m) between the motor and the propeller. It can measure the torque required to turn the propeller while the shaft is rotating. This measurment is done by strain gauges placed on the rotating shaft, which deform in response to the torque. The signal measured by these gauges is then transmitted without contact to a stationary receiver.

The new electric motor (Micromotors PS150-24-25) is more powerful and has an integrated 25-fold gear reduction. Placing the motor and torque sensor in line would mean a hull more than 20 cm long. To avoid too much hull disturbance in flow, we instead used the vertical space above the torque sensor and a pulley and belt system for the transmission. Finally instead of the Hall effect sensor, we used an off the shelf encoder instead (RLS RE22). The force sensor is the same as with the previous boat (CZL616C).

The first boat had a tendency to leak water through the gap between the rotating shaft and the hull, even in the presence of grease. To better protect the sensors, we used a stern tube (or "tube etambot" in French) from a model boat company. It is a long shaft and tube with a small tolerance between the two that can be filled with grease and provides a much better seal against water. This boat was used to measure the thrust and torque of the fully flexible propeller (Sec. 3.1.4).

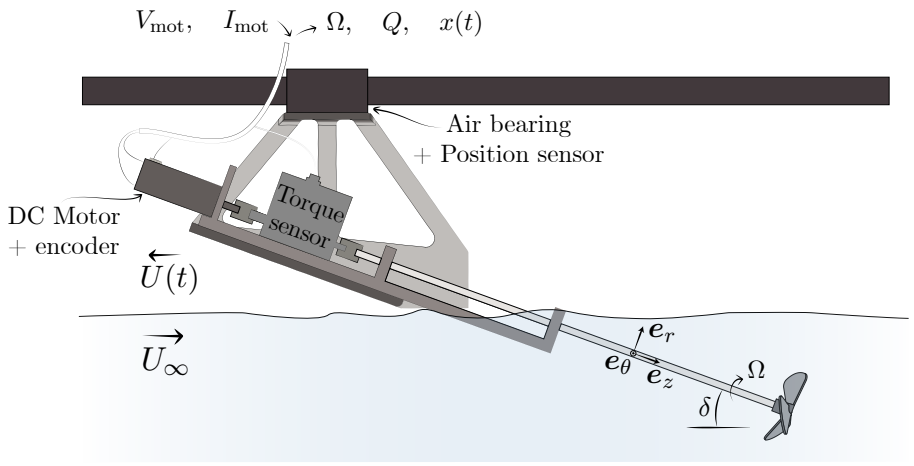

Figure 2.8: Schematic of the final boat, with all the sensors out of the water.

2.2.3 Surface boat

Description

The final design is different from the previous ones and results from the difficulties in precisely measuring the torque at this small scale. The friction is disproportionally important when reducing the size compared to a full scale boat. In physically interesting regimes, the parasitic torque can be as important as the hydrodynamic torque. This parasitic torque, which we measured before experiments also varies with the precise operating conditions (temperature of the grease, amount of grease / water in the tube, etc.), making it difficult to use the results. We eliminated this problem of sealing the sensors from water by tilting the shaft such that the sensors are out of the water channel, but the propeller still is in the middle of the channel. The compromise is that the propeller is now tilted by 20 degrees: the effects of this tilt are analyzed in the following section.

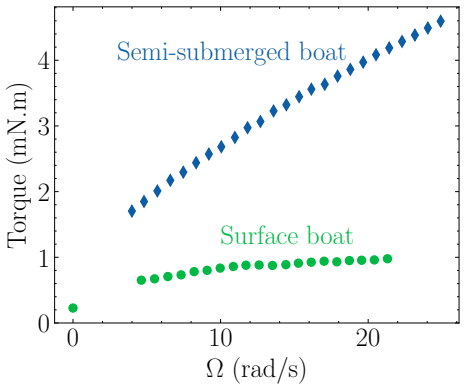

Figure 2.9: Torque with no propeller for the second and third boats.

The rest of this boat is very similar to the previous one, but all inline (Fig. 2.8). The DC motor (Micromotors PS150-24-25) is at the end of the shaft to control the rotation, and we measure the angular velocity with the Hall effect sensor + magnet similarly to the first boat. It is then attached to the torque sensor (Burster 8661 4050 V0000) and the final part of the shaft is held in place by two stainless steel ball bearings — one of which is submerged — that have very small friction (see Fig. 2.9).

This boat is used for the intermittent locomotion experiment, so it must be able to glide back and forth in the channel. The hull is attached to a carriage on a linear air bearing. This guide rail is a 75mm x 99mm bar and a matching carriage machined to tight tolerances. Pressurized air is then introduced by a tube directly into the moving carriage, and is vented in the gap between it and the rail. The air stream creates a film that levitates the carriage. As a result, the only friction experienced

during motion is the shear in the lubricating air film, which is much smaller than any force in the problem studied.

The final sensor in the system is a position sensor (Baumer U500.DA0.2-UAMJ.72F) mounted on the carriage. It sends ultrasonic pulses to a screen at one end of the channel and measures the time it takes for the pulses to return to the sensor. It produces an analog signal proportional to the distance to the screen and can thus track the position of the boat in the channel in a time-resolved manner. This sensor is sensitive to the speed of sound in the room, which itself scales as the square root of the temperature. So we were careful not to have rapid temperature changes.

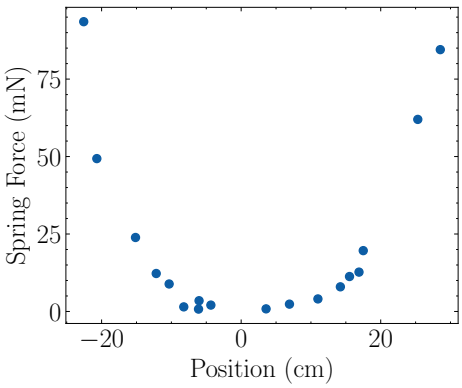

Figure 2.10: Force due to the cables attached to the carriage.

While the friction on the linear air bearing is negligible, the force from the cable supplying air to the carriage — and the smaller electrical cables — is not. This cable is a plastic tube that we mounted as high above the rail as possible to minimize the return force it produces. To characterize the force it generates, we released the carriage alone with zero initial speed from various positions in the channel and measured the acceleration from the position signal immediately after release. We show the norm of the corresponding force (simply dividing by the mass of the carriage) in Fig. 2.10 as a function of the initial position on the rail. The force has a flat profile in the center and then increases sharply, starting at 10 cm from the center. While the amplitude of this force is small (10 mN compared to 100 mN for typical drag), since we want the boat to be stationary on average in the channel, the hydrodynamic thrust and drag will cancel each other out, leaving this force as the only net contribution. Therefore, in the Burst and Coast experiments, special care was taken to ensure that the average position of the boat was in the location where the spring force was minimal (within $\pm$ 2 cm).

Force sensing experiments: In order to measure properties of the rotor (Sec. 3.2 and 4.1) we needed to perform experiments with the boat fixed but measuring the force in the direction of the flow. We attached a traction / compression force sensor (FUTEK LSB210) between the carriage and a fixed point in the laboratory. The linkage between the force sensor and the carriage is a ball joint such that, when the pressurized air is turned on, the carriage can freely levitate up or down and transmits all the longitudinal force to the sensor. This design has the added advantage that, unlike previous designs, the highly sensitive force sensor does not carry the weight of the boat below it. The linear air bearing levitates the boat and propeller, but transmits all the longitudinal force to the sensor. We noticed that the combination of the new sensor and this design resulted in a much smaller drift — and resulting uncertainty — of the force measurement.

Control and acquisition In this case, like the previous ones, the control and acquisition of the signals is handled by a National Instruments card (NI USB-6221). This allows the automation of the experiments: any desired signal can be programmed in the computer and sent as an analog voltage to the DC motor (with a sampling frequency of 4096 Hz). The card is able to produce the right voltage, but the associated power is very low and not able to directly drive the motor. We thus amplify the analog signal with a high power, low frequency amplifier with a gain of 3.6 (KEPCO BOP 36-6M). At the same time, the device records the multiple signals coming from the experiment, which can be divided in two categories: analog and digital. Analog signals (force, torque, intensity, and position) are directly measured and later converted into the associated physical quantity using the sensor calibration. Digital signals (angular velocity and flow rate) encode their value in the time interval between two consecutive pulses from 0 to 5V.

To ensure synchronicity between all signals they are acquired as analog signals, and a rising edge detection algorithm later converts them into their associated physical value in software. We sample at 32 768 Hz to ensure that this algorithm functions correctly. This sample rate is way too fast for all analog signals and we therefore downsample all signals by a factor 32 once the digital to analog conversion is done. Our effective acquisition frequency is 1024 Hz. The force signal is pre-amplified by a signal conditioner (SCAIME CPJ) which is designed specifically to amplify the signal coming from analog force sensors, while minimizing noise. The torque sensor does not require the same treatment as an amplification is built into the sensor.

Tilted propeller

As shown in Fig. 2.8 the shaft and the propeller are at an angle to the incoming flow, breaking the symmetry of the system. Indeed, on one side of the propeller the angular velocity and the flow velocity combine in such a way that the blade experiences faster flow with a larger angle of attack. On the other side the opposite effect occurs, creating a variation of lift and drag forces with a period identical to the rotation rate. The net effect of this tilt besides periodically varying the thrust is to create a yawing moment (a rotation to the left of the channel in our case). This phenomenon occurs when a propeller-driven aircraft tilts up to generate more lift when landing and is known as p-factor or asymmetric blade effect (Rostami et al., 2022).

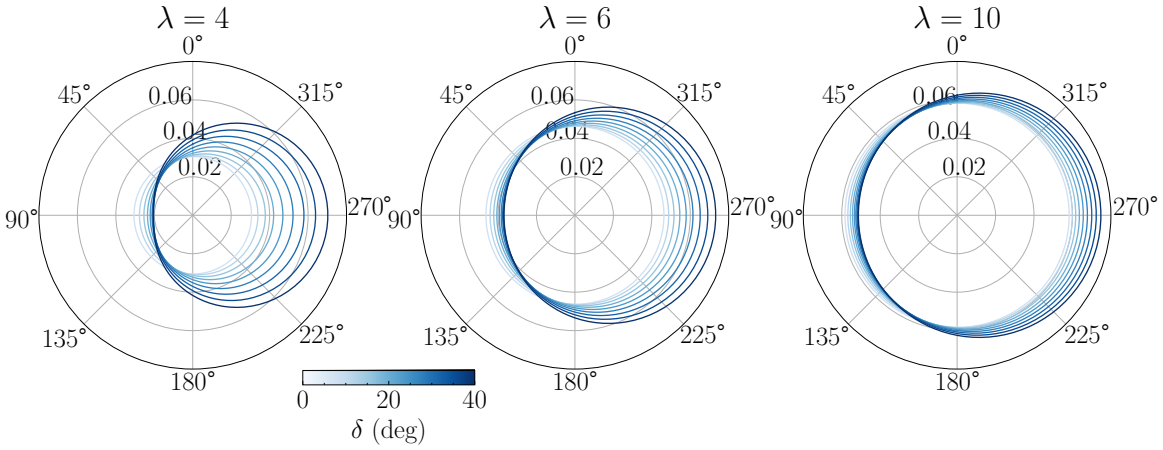

Figure 2.11: Force normal to the rotor (along the shaft direction) as a function of the angular position during the rotation (as seen from the front of the boat) on a single blade. The force is normalized by $1/2\rho\pi R^2(R\Omega)^2$. Color indicates the tilt angle. The three polar plots correspond to increasing tip speed ratios λ from left to right.

This section quantifies the effect on thrust, torque and eventual side loads due to this tilt δ of the shaft which is 20 degrees in our case. The local velocity is the combination of the flow velocity and the angular velocity. In the rotating frame aligned with the shaft $(\boldsymbol{e}_r, \boldsymbol{e}_\theta, \boldsymbol{e}_z)$ (see Fig. 2.8), the total flow velocity can be projected as:

$$\mathbf{U}_p = \begin{pmatrix} U_\infty \sin\delta \cos\Omega t \\ r\Omega - U_\infty \sin\delta \sin\Omega t \\ U_\infty \cos\delta \end{pmatrix}_{(\boldsymbol{e}_r, \boldsymbol{e}_\theta, \boldsymbol{e}_z)}, \tag{2.4}$$

where Ω is the angular velocity and t the time. The tilt of the shaft therefore creates a varying velocity during the rotation.

A radial velocity exists along the blades, for instance when $\Omega t = 0 \mod \pi$ (i.e., when the blade is aligned with the flow, above or below the shaft). This radial velocity is small when the tilt angle δ also is, and does not interact with the blades to create lift forces. Its effect will thus be neglected in the analysis below.

For a blade element at a radius r, the norm of the incoming velocity normal to the blade is:

$$\|\mathbf{U}_p \times \boldsymbol{e}_r\|^2 = (U_\infty \cos\delta)^2 + (r\Omega - U_\infty \sin\delta \sin\Omega t)^2, \tag{2.5}$$

and the angle between the local incoming flow and the plane of rotation verifies:

$$\tan\varphi = \frac{\cos\delta}{r\Omega/U_\infty - \sin\delta\sin\Omega t}. \tag{2.6}$$

The quantity $r\Omega/U_\infty = \lambda r/R$ is the local speed ratio. If it is large compared to 1 everywhere on the blade (fast rotating propeller) then the only effect of the tilt of the shaft is the reduction of the incoming velocity by $\cos\delta$. To analyze further the effect of the tilt, we compute the macroscopic properties (thrust, torque, and efficiency) of a flat bladed propeller with a pitch of 30 degrees. This analysis is done similarly to the one described in 1.2, adding in the position dependent velocity.

Fig. 2.11 shows the force normal to the rotor (parallel to the shaft) as a function of the position during the rotation for several tip speed ratios and tilt angles, computed for a single blade. When the blade is around 270 degrees (the propeller is rotating clockwise, meaning that it is going down and towards the incoming flow) the force is more important. This effect is increasingly important as δ is increased and λ is decreased. In this location the angular velocity and the incoming flow have an angle between them tighter than 90 degrees. The combination of the velocities results in (i) an increased local velocity norm and (ii) a smaller flow angle with the plane of rotation (or an increased angle of attack on the blade). Both modifications tend to increase the generated force and therefore much more thrust is produced on the right side of the rotor. As expected this effect is more important for smaller λ, since the fluctuation of U_∞ has more relative importance compared to the angular velocity. In extreme cases the angle of attack could even change direction on the left side of the rotor, but it is never the case for the parameters relevant to the problem here. The effect is important with a single blade as presented here but with three (like is the case in Sec. 3.2 and 4.1), the angular position dependence of the total force is averaged: when one blade is in the position of high thrust (270 deg) both the others are on the opposite side where less force is produced. As a result, the fluctuation of the force during one cycle due to the tilt is about 1% with 20 deg of tilt.

We can then compute the thrust and torque of the rotor for a given λ and δ. The torque is unchanged from the formula in 1.2 (Eq. (1.16)), however the thrust is directed up instead of forward and has to be projected horizontally (by multiplying by $\cos\delta$). In Fig. 2.12, we show the thrust, torque, and efficiency of a three bladed rotor with for several tip speed ratios as a function of the tilt angle. The net effect on thrust depends on the tip speed ratio: for small values of λ the accelerated flow on one half of the rotation more than makes up for the velocity deficit on the other side and the subsequent projection. As a result the thrust is slightly increased (light red curves, panel (a)). At higher tip speed ratios, the angular dependence effect is smaller and thus the only remaining effect of the tilt is the projection of the thrust force in the direction of motion (i.e., for $\lambda \gg 1$, $C_T(\delta) \sim \cos\delta$, visible in the dashed black line). For the torque the reasoning is similar, but the torque is always more important than the zero tilt value. At high tip speed ratio, the discrepancy reduces.

Finally, the efficiency ($\eta = C_T/\lambda C_Q$) is always reduced. At high tip speed ratio, we get the same scaling as the thrust: the tilt reduces the efficiency by a factor $\cos\delta$.

The effect of the tilt (in our case $\delta = 20$ deg.) is twofold: first, it reduces the performance of the rotor used by about 10% the normal operating conditions. This effect is not very important for our study

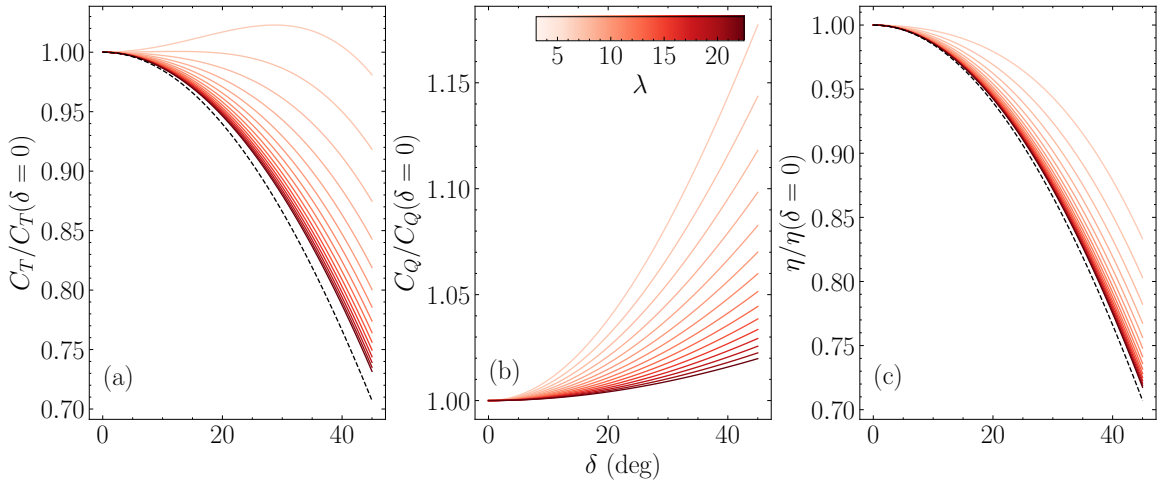

Figure 2.12: Relative variation of the dimensionless (a) thrust, (b) torque and (c) efficiency with the tilt angle. Colors indicate the tip speed ratio. (dashed line) cosine of the tilt angle

since we are not interested in the absolute values of thrust and efficiency but rather in their variations with respect to a reference case. Second, it changes the local conditions experienced by the rotor, which can have an impact on deformation throughout the cycle.

2.3 Materials

All the flexible blades used in the following are made out of flexible plastic sheets. This section describes how we separately measured their flexibility to model the deformations obseved. The blades used are cut out of sheets of different plastics: either polyethylene terephthalate (PET or Mylar) or polypropylene (PP) of different thicknesses. The main parameter of interest is the Young's modulus E of the material, which controls the amplitude of the deformations. In practice, we often need to compute the bending modulus of the studied blade: EI where I is the quadratic moment of area equal to $ce^3/12$, with c is the width of a section of the blade in a direction perpendicular to the bending direction and e the corresponding thickness.

To perform this measurement, we used a precise materials testing machine (INSTRON 5865): it is able to record force / displacement curves with forces in the 10^{-4} N range and displacements of the order of 0.1 mm. We measured the bending modulus of the blades used in Sec. 3.1 by a bending test: the 40 mm blade is held horizontal, and clamped at one end. The force sensor pushes down on the tip of the blade (the blades have a negligible deflection under their own weight). In the small deflection limit, the relation between the deflection δ_B and the force applied F_B reads (Marigo, 2014):

$$\delta_B = \frac{F_B L_B^3}{3EI}, \tag{2.7}$$

with L_B being the length of the blade (40 ± 0.5 mm in this case). The width of the blade is 5.8 ± 0.1 mm.

We show the result of the test for the four different materials used in Sec. 3.1 in Fig. 2.13. The curves stay linear throughout the range of deformation, indicating that we are still in within the regime of small deformation ($\delta_B/L_B < 10$ %). We measure the slope of this linear trend to obtain the bending modulus.

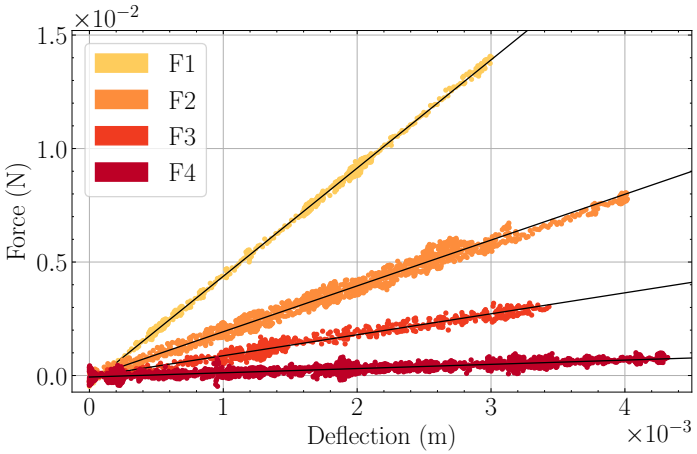

Figure 2.13: Force displacement curve for the four different blades (colors). Black lines are best fits for the slope of each blade.

To model the deformation of the slender blades, we also need to compute the twisting modulus of the material GJ. G is the shear modulus of the material, obtained from the Young's modulus and the Poisson ratio ν_{el} (assumed to be 0.43 both for PET and PP), $G = E/(2(1+\nu_{\text{el}}))$. J is the torsional moment of area, which in the case of a rectangular cross-section and $e \ll c$ reads $J = ce^3/3$ (Audoly and Neukirch, 2021; Audoly and Pomeau, 2010). The blades are numbered from least to most flexible and their properties are summed up in table 2.1. The blades F1 and F4 are used in Sec. 3.1 and in Sec. 3.1.4 the four materials described here are used, only the chord is modified: from 5.8 mm it is increased to 18 mm. The Young's modulus stays the same but the bending and torsion moduli are multiplied by about 3.

Blade type	Thickness e (μm)	Young's modulus (GPa)	Bending modulus (N.m^2)	Torsion modulus (N.m^2)
Rigid (Al)	460 ± 10	∞	∞	∞
F1 (Mylar)	330 ± 10	3.9 ± 0.2	$(69.4 \pm 8.1)\ 10^{-6}$	$(96.9 \pm 11.3)\ 10^{-6}$
F2 (Mylar)	270 ± 10	4.4 ± 0.5	$(41.7 \pm 10.1)\ 10^{-6}$	$(58.3 \pm 14.1)\ 10^{-6}$
F3 (Mylar)	200 ± 10	4.3 ± 0.7	$(16.5 \pm 4.69)\ 10^{-6}$	$(23.1 \pm 6.56)\ 10^{-6}$
F4 (Mylar)	110 ± 10	4.0 ± 0.5	$(3.67 \pm 0.64)\ 10^{-6}$	$(5.25 \pm 0.91)\ 10^{-6}$

Table 2.1: Relevant physical constants of the blades used in the experiments of Sec. 3.1.

In Sec. 3.2, we used slightly different blades only allowed one direction of bending. We model this bending as a pointwise torsional spring along the axis where the blade is clamped. To measure the spring constant we repeated the same bending test but along the chordwise direction and directly measured an effective spring constant. Doing so minimizes the uncertainty due to the width of the patch glued to the rigid rod. In this new version the experiment the width W_B is 30 ± 0.5 mm, and the length 12 ± 0.5 mm. The spring constant per unit width C_B that we measure is linked to the force and deformation through:

$$\frac{F_B L_B}{W_B} = C_B \arctan \frac{\delta_B}{L_B}. \tag{2.8}$$

The resulting curves are plotted in Fig. 2.14, and the associated spring constants are displayed in table 2.2.

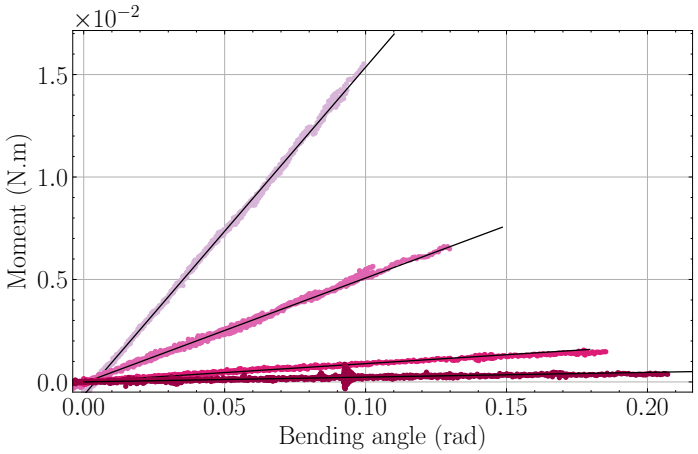

Figure 2.14: Moment due to the bending of the plastic sheet as a function of the bending angle $\arctan \delta_B / L_B$

Blade type	Thickness (µm)	Spring constant C_B (N)
Rigid	535 ± 10	∞
P1 (Mylar)	108 ± 10	$(16.0 \pm 1.8)\ 10^{-2}$
P2 (PP)	100 ± 10	$(5.11 \pm 0.75)\ 10^{-2}$
P3 (PP)	60 ± 10	$(0.871 \pm 0.12)\ 10^{-2}$
P4 (PP)	35 ± 10	$(0.232 \pm 0.046)\ 10^{-2}$

Table 2.2: Relevant physical constants of the blades used in the experiments of Sec. 3.2.

Bibliography

AUDOLY, B. and NEUKIRCH, S. (2021). A one-dimensional model for elastic ribbons: A little stretching makes a big difference. *Journal of the Mechanics and Physics of Solids*, vol. 153:p. 104457 36

AUDOLY, B. and POMEAU, Y. (2010). *Elasticity and Geometry: From Hair Curls to the Non-linear Response of Shells*. Oxford University Press 36

FRISCH, U. (1995). Turbulence: The Legacy of A. N. Kolmogorov 26

LUMLEY, J. L. and MCMAHON, J. F. (1967). Reducing Water Tunnel Turbulence by Means of a Honeycomb. *Journal of Basic Engineering*, vol. 89(4):pp. 764–770 24

MARIGO, J.-J. (2014). *Mécanique des Milieux Continus I*. École polytechnique 35

ROSTAMI, M., CHUNG, J., and NEUFELD, D. (2022). Vertical tail sizing of propeller-driven aircraft considering the asymmetric blade effect. *Proceedings of the Institution of Mechanical Engineers, Part G: Journal of Aerospace Engineering*, vol. 236(6):pp. 1184–1195 33

TROPEA, C., YARIN, A. L., and FOSS, J. F., editors (2007). *Springer Handbook of Experimental Fluid Mechanics*. Springer, Berlin, Heidelberg 25, 27

WHELAN, J. I., GRAHAM, J. M. R., and PEIRÓ, J. (2009). A free-surface and blockage correction for tidal turbines. *Journal of Fluid Mechanics*, p. 12 24

Chapter 3

Reconfigurating propellers

This chapter is dedicated to the study of shape-changing propellers through two designs. The first one has fully flexible blades, made out of plastic sheets, that can bend and twist along their span. Its purpose is to study the main drivers of deformation in a canonical case study and the effects of the deformation on the performance of the propeller.

In a second step, we analyze the performance of a propeller inspired from the work of Cognet (2017). This propeller is designed to passively adopt the shape which optimizes its efficiency. To do so, its bending deformation is not authorized and the twisting direction is reversed compared to the first propeller.

3.1 Fully flexible propeller

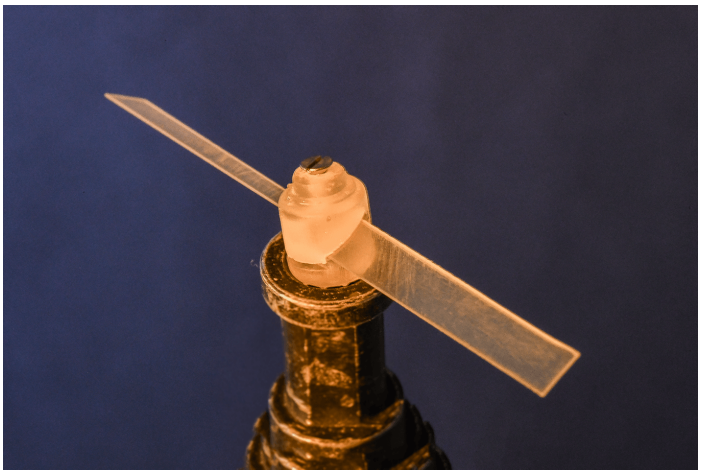

Figure 3.1: Fully flexible propeller

We experimentally study the canonical problem of a propeller with highly flexible blades where the main driver of deformation is the flow. The goal of this work is to get a better understanding of the

fluid forcing on the blades and its effect on the propeller thrust. The blades are made out of a flexible material and have a flat, rectangular shape tilted by an angle γ_0 (Fig. 3.1).

Eldemerdash and Leweke (2021a) have recently studied a very similar system of a rotor made out of slender, flexible plastic blades in water. They measured the flow field around the blades as well as the deformations and shown that important bending (greater than 90 deg in some cases) can be observed in forward motion as well as large amplitude oscillations in backward motion. In their study, the thrust is estimated for some parameters using the flow field but no direct measurement was made. In the present study, we directly measure the thrust produced by such a propeller and how it is modified by the blade deformation. We are interested in the propulsive performance of such a propeller in water. Thus, there are two key differences between this work and that of Eldemerdash and Leweke (2021a): we study only forward motion, and we use a wider range of pitch angles. These changes correspond to the parameters typically found in propellers of boat or airplanes moving forward instead of helicopters or small drones hovering. We use the mathematical description of the system based on the work of Durán Venegas et al. (2019) to show how the thrust of a flexible rotor is modified by the addition of flexibility. Then, we can understand the small deformations through the modification of the classical Cauchy number and link the bending of the blades with the thrust produced by the rotor. Using a second series of experiments and a numerical solution of the system, we show how the efficiency of such a rotor is modified.

3.1.1 Setup

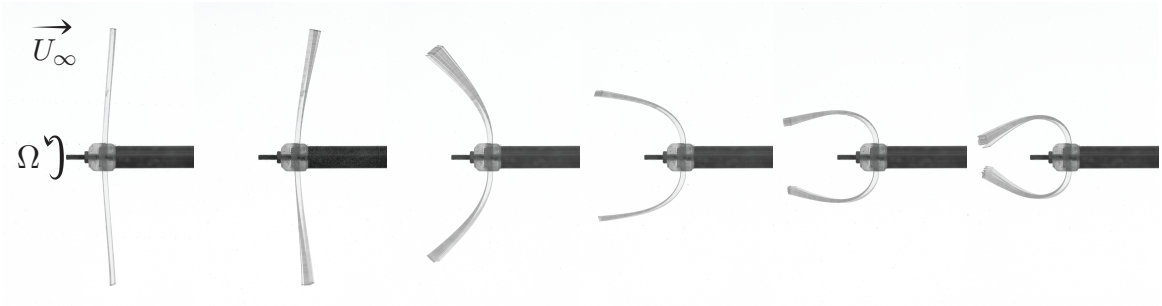

Figure 3.2: Typical deformation of the blades when the rotational velocity is increased (superposition of approximately 30 phase synchronous frames). Blades F4 with 20 deg pitch angle subjected to 0.08 m/s flow, with increasing rotational velocity ranging from 0 to 30 rad/s (left to right).

We first conducted experiments utilizing the initial boat design (Sec. 2.2.1) to investigate propeller thrust and deformation. The experiments involved three types of blades, all having a rectangular shape with specific dimensions: an external radius of 46 mm, an internal radius of 4 mm (referred to as R_{hub}), and a chord length of 6 mm. However, the blades differ in terms of thickness and material composition. For the purpose of reference, we employed rigid blades made from thin aluminum sheets. The two sets of flexible blades are crafted from mylar sheets, each having a distinct thickness. The physical characteristics of the blades are provided in Table 2.1. We used the least and most flexible blades defined in that table: F1 and F4.

To secure the blades onto the rotating shaft, we utilized 3D printed components featuring tilted slits. These slits allowed us to set the pitch angle relative to the plane of rotation, as illustrated in Fig. 3.1. Our experiments were carried out with pitch values of 5, 10, 20, and 30 degrees. The blades were attached to a shaft with a diameter of 4 mm and a length of 75 mm positioned in front of the hull.

We use a high speed camera (Phantom Miro M120) to directly measure the deflection of the blades under load. It is synchronized with the rotation of the blades using a Hall effect sensor. A frame is shot each time the blades are perpendicular to the line of sight of the camera (see Fig. 3.2). We compute the position of the centerline of the blades and correct for the out of plane bending of the blades, and therefore we can track the flexion angle. The torsion angle can also be estimated by measuring the apparent width of a section of the blade. However, this method has low precision and the torsion angles are small so that conclusive results cannot always be obtained.

In Fig. 3.3, we show a sketch of the required correction to obtain the bending angle. In general, the blade bends in 3 dimensions. However Eldemerdash and Leweke (2021a) showed that the twist of the blade is small (of the order of a few degrees compared to the pitch of the blades which is of tens of degrees). As a consequence, we can consider that the blade centerline is in a plane. This means that the vector $\mathbf{d}_1(s)$ defined locally in Fig. 3.4 is actually of constant direction. The plane containing the centerline is obtained by rotating the vertical plane of Fig. 3.3 around the vector $\mathbf{e}_z$ by the pitch angle of the blade: γ_0. The camera we used to measure the bending angle is placed 2 m away from the rotor and can thus be considered at infinity, capturing the shape of the blade as projected onto the vertical plane. The distances measured along the x axis are underestimated if not corrected. In order to get the actual shape of the blade in the plane of bending we correct the distances by a factor $1/\cos\gamma_0$.

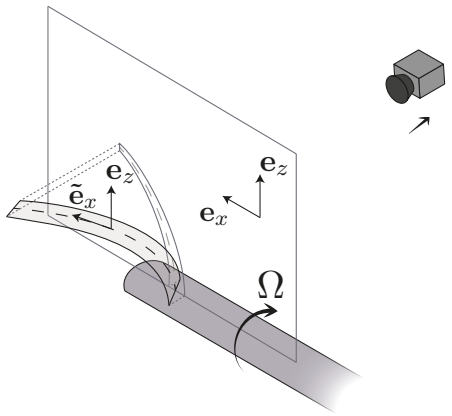

Figure 3.3: Schematic of the projection occurring when photographing the deformed blades.

For each set of parameters we capture at least 30 images, extract data separately and use the mean of the results as the bending angle. Similarly, we average values of rotational velocity and force measurements over 20 s, after a 10 s settling period when the electric motor is switched on. Technical details about the image processing are given in App. D.1.

3.1.2 Mathematical description

We obtain the equations describing the deformation of the blades similarly as in Durán Venegas et al. (2019) but with a few key differences. First the blades are submerged in water, modifying the balance of the forces acting on the blades. We also use important pitch angles (up to 30 degrees) and so small angles limits used in this article are not valid here. Finally, our blade shape is rectangular and flat, simplifying the constitutive relation.

Using Kirchhoff relations for a steady state in the local frame $(\boldsymbol{d}_1, \boldsymbol{d}_2, \boldsymbol{d}_3)$ described in Fig. 3.4, we have:

$$\begin{aligned} \frac{\partial \boldsymbol{T}_{\text{el}}}{\partial s} + \boldsymbol{f}_{\text{el}} &= \boldsymbol{0}, \\ \frac{\partial \boldsymbol{M}_{\text{el}}}{\partial s} + \boldsymbol{d}_3 \times \boldsymbol{T}_{\text{el}} + \boldsymbol{m}_{\text{el}} &= \boldsymbol{0}, \end{aligned} \tag{3.1}$$

where $\boldsymbol{f}_{\text{el}}$ and $\boldsymbol{m}_{\text{el}}$ are the external forces and moments per unit of length respectively. $\boldsymbol{T}_{\text{el}}$ and $\boldsymbol{M}_{\text{el}}$ are the internal forces and moments and $\boldsymbol{d}_3$ the vector tangent to the blade centerline (defined along

the centers of mass of each section). We define the Darboux vector:

$$\boldsymbol{\Omega}_{\text{el}} = \kappa_1(s)\boldsymbol{d}_1(s) + \kappa_2(s)\boldsymbol{d}_2(s) + \tau(s)\boldsymbol{d}_3(s), \tag{3.2}$$

with κ_1, κ_2 and τ the local curvatures in the local frame. Then the vectors $\boldsymbol{d}_i$ verify:

$$\frac{\partial \boldsymbol{d}_i}{\partial s} = \boldsymbol{\Omega}_{\text{el}} \times \boldsymbol{d}_i, \tag{3.3}$$

for $i = 1, 2, 3$. The geometry of the blades is such that they can be modeled as slender ribbons (Audoly and Pomeau, 2010), giving $\kappa_2 = 0$. The curvatures can be expressed via the angles θ and γ (see Fig. 3.4):

$$\frac{\partial \theta}{\partial s} = \kappa_1, \quad \frac{\partial \gamma}{\partial s} = \tau. \tag{3.4}$$

The constitutive law for inextensible ribbons is:

$$\boldsymbol{M}_{\text{el}} = EI\kappa_1 \boldsymbol{d}_1 + \frac{EJ}{2\,(1+\nu_{\text{el}})}\tau \boldsymbol{d}_3, \tag{3.5}$$

where ν_{el} is the Poisson ratio, E is the Young modulus, I is the second moment of area in the $\boldsymbol{d}_1$ direction and J the torsion modulus of the blade. The complete elastic energy for inextensible ribbons contains non quadratic and coupled terms between the bending and torsion curvatures (see Audoly and Neukirch (2021)). However here, given that our blades are slender and thin and that twisting curvature remains small the simpler relation (3.5) remains valid.

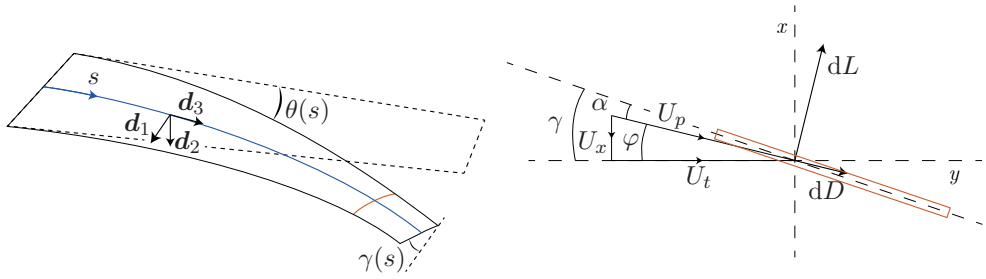

Figure 3.4: (left) Axes and angles definition on the blade. (right) Angles and definitions on a cut (orange line) of the blade

Bending equation

The external forces acting on a blade are both the hydrodynamic forces and the centrifugal force. We separate the fluid force in lift and drag coefficients acting on each section of the blade normal to its span (see orange cut in Fig. 3.4). In this frame, the force normal to the surface of the blade (per unit span) reads:

$$f_{\text{hydro}} = \frac{1}{2}\rho U_p^2 c \left(C_L(\alpha)\cos\alpha - C_D(\alpha)\sin\alpha\right), \tag{3.6}$$

where ρ is the fluid density, U_p the local apparent velocity (see Fig 3.4), c the chord of the blade, C_L and C_D are respectively the profile lift and drag coefficients and α is the local angle of attack. The centrifugal force tends to align the blade with the plane of rotation. It has in general a component in the $\boldsymbol{d}_2$ and $\boldsymbol{d}_3$ directions, however external forces in the $\boldsymbol{d}_3$ direction do not contribute to the bending

and twisting motions as can be seen in the second part of (3.1). The centrifugal force per unit span projected in the $\boldsymbol{d}_2$ direction reads:

$$f_{\text{centrifuge}} = A_b \rho_b \tilde{r} \Omega^2 \boldsymbol{e}_r \cdot \boldsymbol{d}_2, \tag{3.7}$$

where A_b is the cross-sectional area of the blade, ρ_b its density and Ω the rotation speed. The distance to the rotation axis is denoted as $\tilde{r}$. The vector $\boldsymbol{e}_r$ is the unit vector aligned with the direction of the centrifugal force: it is pointed from the axis of rotation outwards. The distance to the axis of rotation $\tilde{r}$ and the projection $\boldsymbol{e}_r \cdot \boldsymbol{d}_2$ can be computed analytically in the small twist limit (it is done in App. A) but their exact values are not necessary for the discussion here.

We combine the Kirchhoff equations (3.1) and the constitutive law (3.5). By projecting Eq. (3.1) along $\boldsymbol{d}_1$ we get:

$$\boldsymbol{d}_1 \cdot \frac{\partial \boldsymbol{M}_{\text{el}}}{\partial s} + T_{\text{el},2} + m_{\text{el},1} = 0, \tag{3.8}$$

where we denote the ith component in the local frame by the subscript i. Taking the derivative of the expression above, we need to compute the derivative of $\boldsymbol{d}_1 \cdot \partial \boldsymbol{M}_{\text{el}}/\partial s$ and using Eq. 3.2 and $\kappa_2 = 0$, we get:

$$\frac{\partial}{\partial s}\left(\boldsymbol{d}_1 \cdot \frac{\partial \boldsymbol{M}_{\text{el}}}{\partial s}\right) = \frac{\partial^2 M_{\text{el},1}}{\partial s^2} - \frac{\partial \tau M_{\text{el},2}}{\partial s}. \tag{3.9}$$

Once again, since there is no bending in the $\boldsymbol{d}_2$ direction, second term is zero. Using the constitutive law (3.5), we finally obtain the equation for θ:

$$EI \frac{\partial^3 \theta}{\partial s^3} = -\frac{\partial T_{\text{el},2}}{\partial s} = f_{\text{el},2}. \tag{3.10}$$

Using the expressions of the external forces projected in the direction normal to blade obtained in (3.6) and (3.7) we obtain the equation describing the bending of the blade during the rotation:

$$EI \frac{\partial^3 \theta}{\partial s^3} = \frac{1}{2} \rho U_p^2 c \left(C_L(\alpha) \cos \alpha - C_D(\alpha) \sin \alpha\right) - A_b \rho_b \tilde{r} \Omega^2 \boldsymbol{e}_r \cdot \boldsymbol{d}_2. \tag{3.11}$$

Twisting equation

The hydrodynamic center of a typical airfoil is located around $1/4$ of the chord and since the blades have a homogeneous and rectangular profile, their center of mass is located at mid-chord. Thus, the blades tend to twist and increase their pitch angle when they are generating lift due to the hydrodynamic moment. The centrifugal force tends to resist this twist and brings the blade towards the plane of rotation. To obtain an equation on the torsion curvature γ, we project the Kirchhoff equation along $\boldsymbol{d}_3$:

$$\boldsymbol{d}_3 \cdot \frac{\partial \boldsymbol{M}_{\text{el}}}{\partial s} + m_{\text{el},3} = 0. \tag{3.12}$$

Similarly to the bending equation, we develop the first term to get:

$$\boldsymbol{d}_3 \cdot \frac{\partial \boldsymbol{M}_{\text{el}}}{\partial s} = \frac{\partial M_{\text{el},3}}{\partial s} - \kappa_1 M_{\text{el},2}. \tag{3.13}$$

And since $M_{\text{el},2} = 0$ the equation describing the twist reads:

$$\frac{EJ}{2(1+\nu)} \frac{\partial^2 \gamma}{\partial s^2} = -m_{\text{el},3} \tag{3.14}$$

The moment along the span due to the hydrodynamic forcing is simply its projection along $\boldsymbol{d}_2$ times the distance from the point of application of this forcing to the center of the chord. We will denote this distance $\bar{\delta}^{ac}_{cm}$ (equal to $c/4$ in general). The centrifugal restoring moment is obtained in App. A and reads:

$$\mathrm{d}M_{\text{centrifuge}} = -\frac{\rho_b e \Omega^2 c^3}{24} \sin 2\gamma \cos\theta. \tag{3.15}$$

This moment is along the direction $\boldsymbol{d}_3$.

Finally, we obtain for the equation describing the twist:

$$\frac{EJ}{2(1+\nu)}\frac{\partial^2\gamma}{\partial s^2} = -\frac{1}{2}\rho_b c^2 U_p^2 \left((C_L(\alpha)\cos\alpha + C_D(\alpha)\sin\alpha)\,\bar{\delta}^{ac}_{cm} \right) + \frac{\rho_b e c^3 \Omega^2}{24} \sin 2\gamma \cos\theta. \tag{3.16}$$

Dimensionless system

In our problem the typical length scale is R and the typical velocity $R\Omega$. We use these quantities to make the equations of the deformation dimensionless and two Cauchy (or elastohydrodynamical) numbers appear: one for the bending of the blades and one for the twist. They compare the intensity of the hydrodynamic forces to the elastic moduli and read:

$$C_Y^B = \frac{\rho S_b (R\Omega)^2 R^2}{2EI}, \quad C_Y^T = \frac{\rho S_b (R\Omega)^2 R c (1+\nu)}{EJ}, \tag{3.17}$$

where $S_b = Rc$ is the planar surface of a blade. The system of elastic equations can thus be written:

$$\frac{1}{C_Y^B}\frac{\partial^3\theta}{\partial s^3} = u_p^2 \left(C_L(\alpha)\cos\alpha + C_D(\alpha)\sin\alpha\right) - 2d\frac{A_b}{S_b}\frac{\tilde{r}}{R}\boldsymbol{e}_r \cdot \boldsymbol{d}_2, \tag{3.18}$$

$$\frac{1}{C_Y^T}\frac{\partial^2\gamma}{\partial s^2} = -u_p^2 \left[(C_L(\alpha)\cos\alpha + C_D(\alpha)\sin\alpha)\,\delta^{ac}_{cm}\right] + \frac{1}{24}\frac{A_b}{R^2}\sin 2\gamma\cos\theta, \tag{3.19}$$

where $u_p = U_p/R\Omega$, $\delta^{ac}_{cm} = \bar{\delta}^{ac}_{cm}/c$, and $d = \rho_b/\rho$ is the density of the blade. Note that we refer to the dimensionless curvilinear abscissa as s for convenience. It is obtained by dividing the dimensional curvilinear abscissa by the span R. The dimensionless system lets us compare the order of magnitude of the different terms:

$$2d\frac{A_b}{S_b} \approx 10^{-2} \quad \text{and} \quad \frac{A_b}{24R^2} \approx 10^{-5} \quad \text{while} \quad u_p^2 \approx 1 + \frac{1}{\lambda^2} \approx 1. \tag{3.20}$$

The centrifugal force and moment are orders of magnitude smaller than the hydrodynamic contribution except for very large deformations (i.e., large Cauchy numbers). In the following we will neglect the centrifugal force and focus on the coupling between the elasticity and the fluid loading.

3.1.3 Effect of bending on thrust production

We perform the experiments at a fixed flow speed U_∞ (0.05 to 0.15 m/s) and pitch angle γ_0, and increasing the angular velocity from 0 to 35 rad/s. Fig. 3.5 shows the results of the experiments for $U_\infty = 0.15$ m/s and $\gamma_0 = 20$ deg. We plot two quantities of interest: the thrust produced by the rotor and the tip bending angle $\theta_M = \theta(s = R)$. We can see that both flexible blades exhibit significant bending deformations at large tip speed ratios. The F1 blades have similar thrust than their rigid counterparts while the F4 blades bend almost completely along this axis of rotation ($\theta_M > \pi/2$, see

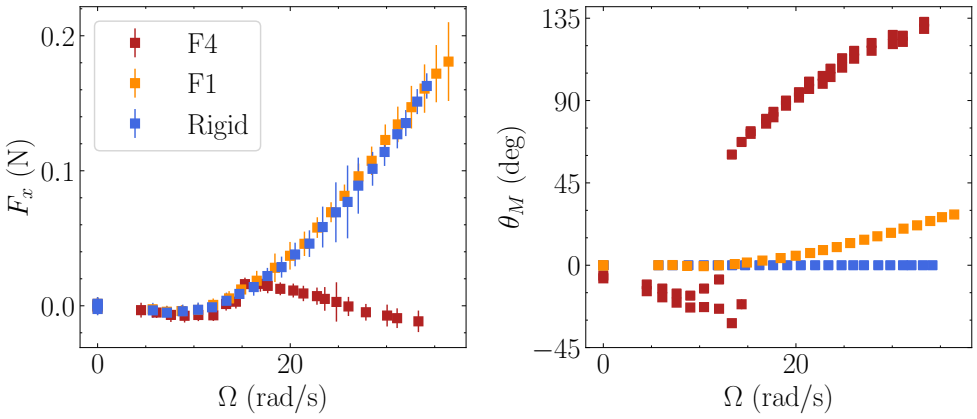

Figure 3.5: Thrust force generated by the rotor (left) and deflection of the tip of the blade (right) as a function of the rotation rate. Blue points correspond to the rigid blades, orange to the lightly flexible ones (F1 in Tab. 2.1) and red to the very flexible ones (F4 in Tab. 2.1). The error bars indicate the standard deviation of the measurement. The standard deviation of the tip bending angle is smaller than the marker size. All curves have the following parameters: $U_\infty = 0.15$ m/s, $\gamma_0 = 20$ deg. The F4 rotor exhibit two sets of points for the bending angle θ_M at a single angular velocity Ω because the two different blades composing the rotor bend differently.

Fig. 3.2) causing the production of negligible thrust. Note that at zero angular velocity, the upstream flow on its own is not strong enough to bend the F1 blades but does slightly bend the F4 blades backwards. These most flexible blades also exhibit sometimes different behaviors for the two blades with the same external conditions (see Fig 3.5 (right), red markers at 10 rad/s $< \Omega < 15$ rad/s). We believe that this discrepancy is most likely due to small experimental deviations on the exact clamp angle of the blades. A small pitch difference becomes significant when the loading on the blades varies rapidly with the angle of attack (i.e., when the angle of attack is close to zero). The different behavior between the two blades is therefore only visible close to the angular velocity where sign of the bending changes (Eldemerdash and Leweke (2021a) have also noticed a similar behavior in their experiments).

The thrust coefficient (defined in Eq. (1.10)) of the three rotors are shown in Fig. 3.6 for all pitch angles tested and a fluid velocity of 0.05 m/s. The most flexible blades (red markers) start at very low tip speed ratios with a performance similar to the rigid ones but very quickly significantly deviate from the reference behavior. At high tip speed ratios, whichever the pitch angle, F4 blades do not produce any thrust. For the intermediate blades F1 (orange markers) the thrust coefficient only decreases at very high tip speed ratios and for high pitch angles. Otherwise, we observe a similar performance for F1 blades and the rigid ones (even though the associated deformation may reach $\theta_M \approx 30$ deg) with a slight increase in thrust production for intermediate tip speed ratios.

We now consider the effect of the fluid loading on the rotor shape to link it with the observations on the thrust production above. This deformation is characterized by two functions along the blade: the bending angle $\theta(s)$ and the twist angle $\gamma(s)$. The twist is small in experiments (described in more extensive details in Eldemerdash and Leweke (2021a)) and so we will focus on the bending angle. Fig. 3.7 shows the tip bending angle for flexible blades as a function of the bending Cauchy number. As expected, for C_Y^B lower than one (corresponding to slow angular velocities and stiffer blades), the deformations are small. For larger angular velocities (larger C_Y^B), flexible blades exhibit widely

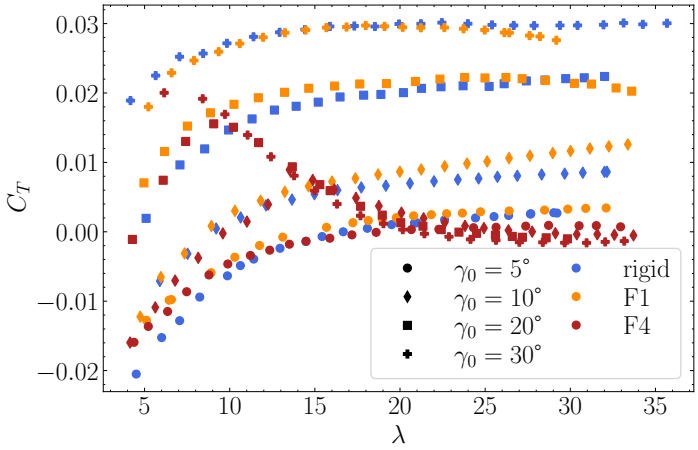

Figure 3.6: Thrust coefficient as a function of the tip speed ratio for all rotors tested at $U_\infty = 0.05$ m/s. Markers indicate the pitch angle, color indicates the blade type (blue: rigid blades, orange: F1 flexible blades, red: F4 flexible blades).

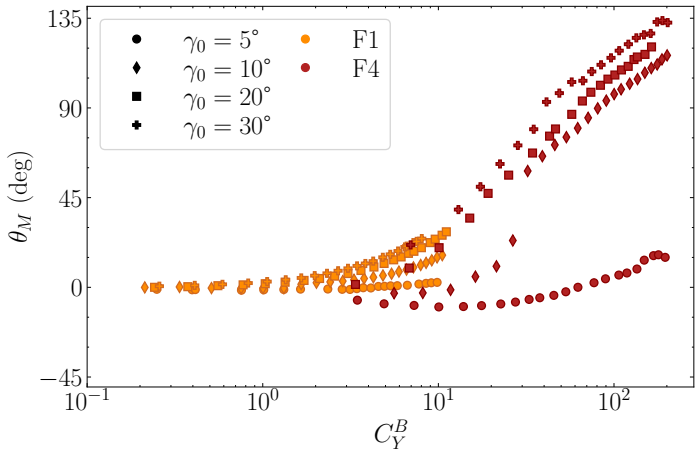

Figure 3.7: Tip bending angle θ_M as a function of the bending Cauchy number C_Y^B (defined in (3.17)) for all flexible blades tested at $U_\infty = 0.05$ m/s in log scale. Markers indicate the pitch angle, color indicates the blade type (orange: F1 flexible blades, red: F4 flexible blades).

different behavior depending on the pitch angle: the bending deformation is a fast-growing function of the pitch angle. The blades with pitch $\gamma_0 = 5$ deg bend backwards in almost every flow condition (also for larger incoming velocity U_∞, not shown in Fig. 3.7): it corresponds to a negative thrust produced by the rotor and a negative local lift on the blades causing them to bend downstream. The blades with a pitch angle of 10 degrees, however, bend backwards for small angular velocities but quickly jump to positive bending when the threshold between positive and negative thrust is reached (red diamonds, around $C_Y^B = 30$). It corresponds to the same threshold as the one described for the thrust: $\lambda > 1/\tan\gamma_0$, obtained in Sec 1.2. Similar behaviors can be observed with the F1 blades but with a much smaller amplitude. Changing the pitch angle by a few degrees can modify the resulting deformation from slightly backwards to 15 or 20 degrees forwards. In the range of parameters we explore, backwards bending is always much smaller in amplitude than forwards bending. This is because backwards bending can only occur for small tip speed ratios, which corresponds to relatively small Cauchy numbers in our case.

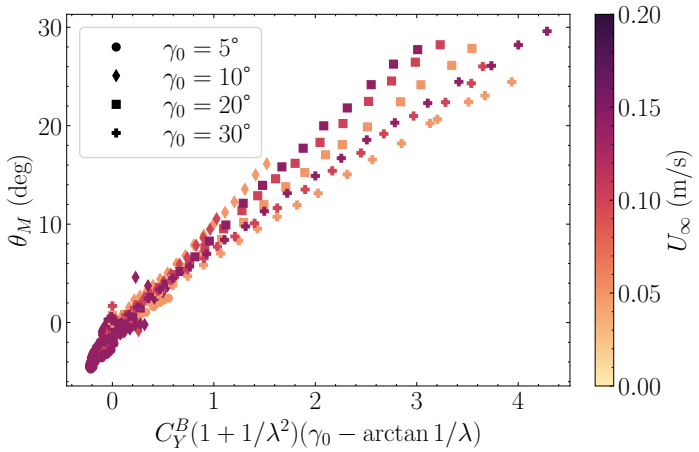

Figure 3.8: Tip bending angle θ_M as a function of a modified Cauchy number scaled by the tip velocity and angle of attack for the F1 blade.

In the following, we aim at understanding the different bending angle behavior depending on the pitch angle using a scaling law and geometric arguments. Because it is constructed using small deformation assumptions this scaling law will *a priori* be applicable only to small or moderate Cauchy numbers but gives insight into which physical phenomena drives the deformations. Deriving a scaling law for θ_M from equation (3.18) we obtain:

$$\theta_M \sim C_Y^B \left(1 + \frac{1}{\lambda^2}\right) \left(C_L(\alpha_M)\cos(\alpha_M) + C_D(\alpha_M)\sin(\alpha_M)\right), \tag{3.21}$$

where α_M is the angle of attack at the tip of the blade, where most of the hydrodynamic force is generated. We approximate the local apparent velocity at the tip by the combination of both the incoming flow velocity and angular motion (thus neglecting any induced velocity from the rotation). As a first approximation, using the zero twist limit, the angle of attack at the tip becomes

$$\alpha_M \approx \gamma_0 - \arctan\frac{1}{\lambda}. \tag{3.22}$$

In typical operating conditions, the tip angle of attack is small so that (i) the contribution from the lift coefficient is greater than the one from the drag coefficient, and thus we can neglect the second term in (3.21). (ii) we can use the linear aerodynamics limit where the lift coefficient is proportional

to the angle of attack, and we get:

$$\theta_M \sim C_Y^B \left(1 + \frac{1}{\lambda^2}\right)\left(\gamma_0 - \arctan\frac{1}{\lambda}\right) \tag{3.23}$$

In this scaling law, the Cauchy number is rescaled by the lift coefficient of the equivalent rigid rotor. This strategy is similar to the strategy employed in Gosselin and de Langre (2011) where the authors compare the reconfiguration of very different systems by rescaling the Cauchy number by the rigid drag coefficient of the system studied.

This scaling law is plotted in Fig. 3.8 for the F1 blades which experience moderate deformations. The rescaling gives a reasonable collapse onto a single line of slope approximately 0.15 rad. This indicates that the problem of knowing *a priori* the deformed shape of the blades can be simplified to a geometrical problem that consists in comparing two angles: the pitch angle γ_0 and the apparent flow angle at the tip $\arctan 1/\lambda$. In particular, the positive or negative bending of the blades is completely set by the sign of the modified Cauchy number. This result can be linked to an observation made by Eldemerdash and Leweke (2021b): when the bending angle of the blade changes sign it is associated with a change of sign of the vorticity created at the blade tip. This sign is itself directly correlated to the local angle of attack at the tip. Our approximation of the angle of attack (3.22) is therefore valid near zero.

Still, the dispersion of the points is fairly important, in particular at large bending angles. It is due to the multiple hypothesis made to obtain this law. The most important ones being the assumptions that there is no twist between the root and the tip of the blade (while the twist is small, since the lift coefficient is proportional to the angle of attack any deviation has a strong influence on the bending of the blades) and using only the tip values instead of the integral over the blades. The twist is visible in the experiments but difficult to measure accurately. We can still see from Eq. (3.19) that the forcing term for the twist is proportional to the forcing term for the bending angle. This identical scaling means that large deformations in the bending direction corresponds to important twist as well. It also explains why the linear dependency of the bending angle with respect to the modified Cauchy number shown in Fig. 3.8 for the F1 blades does not hold anymore for the large deformations experienced by the F4 blades.

In order to incorporate the effects of a small but non zero twist into a predictive scaling law, Eq. (3.22) has to be modified to include twist effects (e.g., a contribution proportional to the twisting Cauchy number). One other possible improvement to better estimate the effective angle of attack on the blades would be to couple the bending and twisting equations to a rotor model that computes the flow around the propeller (e.g., the classical Blade Element Momentum Theory (Glauert, 1983) or a more complete wake model like in Durán Venegas et al. (2019)).

In the following we derive a scaling law that allows to collapse the tip bending angle onto a master curve without explicitly taking the twist into account. In order to do so, we rewrite Eq. (3.18) using the theoretical thrust and torque coefficients:

$$\begin{aligned} C_T &= \frac{N_b}{1/2\rho\pi R^2(R\Omega)^2}\int_{R_{hub}}^{R}\frac{1}{2}\rho c U_p^2\left(C_L(\alpha)\cos\varphi - C_D(\alpha)\sin\varphi\right)\cos\theta \mathrm{d}r, \\ C_Q &= \frac{N_b}{1/2\rho\pi R^2 R(R\Omega)^2}\int_{R_{hub}}^{R}\frac{1}{2}\rho c U_p^2\left(C_L(\alpha)\sin\varphi + C_D(\alpha)\cos\varphi\right)\tilde{r}\mathrm{d}r, \end{aligned} \tag{3.24}$$

where N_b is the number of blades. Using the values at the tip of the blade (subscript M), the scaling

of these two coefficients is:

$$\begin{aligned} C_T &\sim \frac{N_b c R}{\pi R^2} U_p^2 \left(C_L(\alpha_M)\cos\varphi_M - C_D(\alpha_M)\sin\varphi_M\right)\cos\theta_M, \\ C_Q &\sim \frac{N_b c R}{\pi R^2} U_p^2 \left(C_L(\alpha_M)\sin\varphi_M + C_D(\alpha_M)\cos\varphi_M\right)\cos\theta_M. \end{aligned} \tag{3.25}$$

By replacing α by $\gamma - \varphi$ in the sines and cosines of the bending equation (Eq. (3.18)) and neglecting the centrifugal force we get:

$$\frac{1}{C_Y^B}\frac{\partial^3\theta}{\partial s^3} = U_p^2\left[\cos\gamma\left(C_L(\alpha)\cos\varphi - C_D(\alpha)\sin\varphi\right) + \sin\gamma\left(C_L(\alpha)\sin\varphi + C_D(\alpha)\cos\varphi\right)\right]. \tag{3.26}$$

Rewriting this equation as a scaling law, using the values at the tip and considering the fact that the twist is small compared to the pitch angle, we can substitute the lift and drag coefficients by the thrust and torque:

$$\theta_M \sim \frac{C_Y^B}{\cos\theta_M}\frac{\pi R^2}{N_b c R}\left(C_T\cos\gamma_0 + C_Q\sin\gamma_0\right), \tag{3.27}$$

We are interested in describing the small to moderate deformations of the rotor which means that we can make two simplifications to this relationship. First the cosine on the right hand side can be linearized to 1 in the small angles limit. Next, in normal propeller operating conditions, the thrust coefficient produced by the rotor is larger than the torque coefficient. The previous relationship can thus be simplified to:

$$\theta_M \sim C_Y^B C_T \cos\gamma_0 \frac{\pi R^2}{N_b c R}, \tag{3.28}$$

where we measure all the terms experimentally. This scaling law gives, for small deformations, a linear relationship between θ_M and integrated, measurable parameters of the rotor.

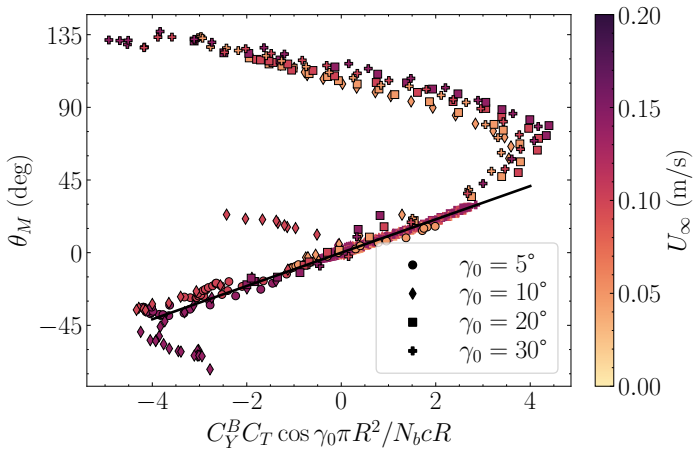

Figure 3.9: Flexion angle as a function of the modified Cauchy number scaled by the thrust coefficient. Colors indicate the flow velocity, markers show the blade pitch angle and markers with a dark edge color are from F4 blades while the others are from the F1 blades. The trend line in black has a slope of 0.18 rad.

This new scaling relationship is plotted in Fig. 3.9. For the F4 blades, in the cases where the two blades exhibit different behaviors we use the mean bending angle between the two blades since the thrust produced by the rotor is the result of the integration of the lift on both blades. All the data for small

bending angles (positive or negative) collapse on the same line. This region of linear relationship strikingly extends from -30 degrees to 40 degrees of bending, way further than the predictive scaling law (3.23). In this previous relationship we neglected any feedback from the deformation onto the loading itself as well as any twist along the blades. The collapse of all data on this curve but not in Fig. 3.8 shows that these assumptions are not true for moderate bending angles. However, the fact that our new scaling (3.28) works demonstrates that these non linearities are all taken into account in the thrust coefficient (or are small enough to not be visible).

We can then note that beyond the limits of the linearity of the scaling law, all the data still collapse on a single curve. This curve is not linear and features more dispersion than the linear part. Still it means that for all external conditions tested, the scaling law makes a link between the thrust produced by the rotor and the bending angle. For a given propeller geometry, for all (positive) pitch angle values, measuring one or the other is equivalent. For instance measuring only the bending deformation gives without ambiguity the thrust produced by the rotor if its bending Cauchy number and pitch angle are known.

3.1.4 Measuring the efficiency

Figure 3.10: Fully flexible propeller, with wider blades

Cognet et al. (2017) have shown that adding flexibility to rotating systems can improve the performance of a wind turbine. In this case the figure of merit is the power coefficient: the power extracted compared to the total kinetic power density of the incoming wind. In the case of propellers, the performance is measured by the efficiency: $\eta = F_{\text{thrust}} U_\infty / Q\Omega$, the ratio of useful power to total expanded power. This section describes the modified setup used to measure the efficiency of the fully flexible propeller and the challenges encountered.

In Sec. 1.2, we showed that an efficient propeller needs to have a local angle of attack α close to the one maximizing the lift to drag ratio on every blade section (α_{opt} is about 15 to 20 deg.). With our flat and rigid propellers, it is not possible as the local flow angle φ changes throughout the span. However, the local flow velocity and angle of attack are maximal near the tip, resulting in most of the force being generated there. A rigid propeller is efficient if the angle of attack near the tip is close to the optimal one.

When the tip speed ratio changes it is therefore necessary to modify the pitch angle γ_0 in order to compensate the change of the local flow angle φ. At the tip, this effect reads $\gamma_0 - \arctan 1/\lambda \approx \alpha_{\text{opt}}$.

For each tip speed ratio there is therefore a pitch angle that maximizes the efficiency, defining a curve $\gamma_0^{\text{opt}}(\lambda)$.

Wind turbine and aircraft propellers use motors to actively change the pitch angle of the blades and maximize efficiency. In the following, we investigate how flexibility changes the twist angle distribution, allowing for a passive modification of the angle of attack.

Setup

We repeated the experiments of the previous section with the aim of measuring the propulsive efficiency. There are a few key differences with the experiments of the previous section. First we added a torque sensor, which is required to record the mechanical power produced by the motor. To accommodate this new, larger sensor, we used a revised version of the hull (described in Sec. 2.2.2) which itself is larger. Finally, we used a long tube filled with grease to allow the shaft to come out of the hull while sealing the torque sensor from water.

Several issues arose when first attempting to perform the experiments directly with the same protocol as with the previous boat. First, the same force sensor became more unpredictable than previously. The larger volume of the new version of the hull creates an upwards force due to the large volume of air it encloses. This vertical load is taken up by the bending force sensor. Given its direction, it should not affect the horizontal force measurement, but we found that the zero force measurement often showed a slow drift which we interpret as being due to the two roles of the sensor: holding the boat in position (in both horizontal directions and in the vertical direction) as well as measuring the force in the direction of the flow. Measuring the reference force before every set of experiments (i.e., every 30 mins) did not seem to be sufficient to compensate for this effect.

Second, the shaft being surrounded by thick grease creates an important resistive torque (about 2 mN.m) which is about the same order of magnitude as the hydrodynamic torque from the propeller (Fig. 3.11). We measured this parasitic torque before every set of experiment to subtract it from the total torque measurement. However, we also noticed it had a tendency to vary as well, likely caused by the temperature increase of the grease or leakage of grease into the water.

Both the thrust and the torque are negative at very low tip speed ratios and positive in the opposite limit. Measurement precision is therefore of paramount importance in the region where the values are close to zero. As a result, we modified the setup in two ways: first, we modified the blades by multiplying their chord by three. This modification, according to Eq. (3.24) should at first order multiply the hydrodynamic thrust and torque by the same amount — the thrust and torque coefficients reflect this change as they are normalized by the area swept by the rotor instead of the blade surface area. Increasing the magnitude of the forces makes the fluctuations of the reference value smaller in comparison.

We also found that we obtained better repeatability by sweeping the angular velocity instead of using fixed values. We ramp up the angular velocity of the rotor very slowly to keep a steady system (50 s for a full cycle). We repeat angular accelerations and decelerations about 10 times, measuring the force reference every time the rotor has stopped. Then, we can suppress the force drift and match the data points with the same angular velocity. It should be noted that we cannot measure the torque drift with this technique as the torque measured when the rotor has stopped depends on residual solid friction on the shaft and thus varies every time. With these two modifications, we obtain typical torque measurements like the one in Fig. 3.11, where we plot the total torque (with the friction) and the reference torque for several repetitions of the same experiment (rigid blades, $\gamma_0 = 30$ deg, $U_\infty = 8.5$ cm/s). The repeatability of the torque measurement is good but the exact value at which the hydrodynamic torque is zero is difficult to estimate, due to fluctuations of the reference torque

(full lines). For this reason, we repeated every set of experiment at least thrice, at the expense of testing several mean speeds. At constant tip speed ratio λ, the effect of changing the mean speed is to modify the Reynolds and Cauchy numbers. The effect of the former is expected to be small (Sec. 1.2) and we used five different blade materials to explore a wide range of Cauchy numbers.

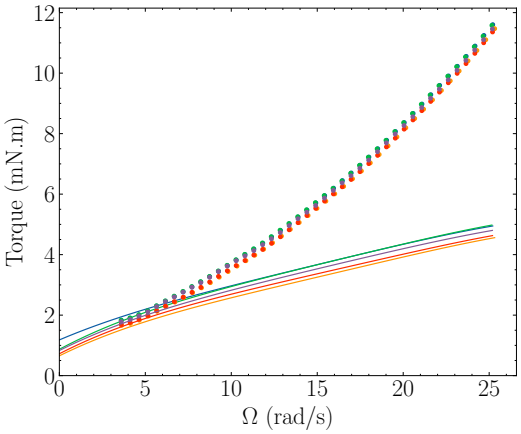

Figure 3.11: Examples of total torque measurements (dots) and the associated reference (full line) as a function of the angular velocity. Colors represent different repetitions. Rigid blades, $\gamma_0 = 30$ deg, $U_\infty = 8.5$ cm/s

The blades are slightly modified from the previous section (Fig. 3.10). They are three times as wide and thus cannot be attached in the same manner. The blades are glued to a glass fiber T shaped junction (over about 1 mm), held in place by a 3D printed hub with tilted slits. We used a rigid glass fiber propeller for reference and the four materials F1 to F4 described in Sec 2.3 — the values for the bending and torsion moduli should be multiplied by 3 due to the shape change. We also use increased pitch angles (20, 30, and 45 deg) since those are closer to the maximum efficiency for rigid propellers. Because we saw that the bending angle is linked to the thrust produced by the rotor in the previous section, we did not record the deformation in this configuration.

Data

In Fig. 3.12, we show the thrust coefficient C_T as a function of the tip speed ratio, for all the parameters tested (all blades and pitch angles). Since we use only one mean speed, each blade is characterized by a unique number obtained by taking the ratio between the Cauchy number C_Y^B and the tip speed ratio λ squared:

$$C_Y^B/\lambda^2 = \frac{\rho S_b U_\infty^2 R^2}{2EI}. \tag{3.29}$$

This value ranges from about 0.01 for the least flexible blade to 1 for the most flexible and measures the magnitude of the blades bending due to the incoming flow alone. A similar number could be obtained with the twisting Cauchy number C_Y^T. From yellow to red, the blades are increasingly flexible and blue indicates the rigid propeller.

The thrust coefficient of the rigid propeller follows the same general trend as the one found in the previous section and its magnitude is a bit less than three times as big. Like in the previous case, the least flexible blades (yellow) follow almost exactly the behavior of rigid propeller while the most flexible ones quickly decrease to zero as the tip speed ratio λ is increased. For smaller pitch angles, almost all blades exhibit a range of tip speed ratio where they produce more thrust than the rigid ones. The blades twisting results in an increased effective pitch angle $\gamma(s)$ near the tip of the blade. If the pitch angle γ_0 of the blade is too small compared to the one corresponding to maximal thrust, this twisting is beneficial. The thrust increase can only occur if the bending is limited as the bending deformation only reduces the thrust (Eq. (3.25)). At high pitch angles, increasing further the pitch begins to reduce the thrust. Thus, there does not seem to be any significant increase in thrust from using flexible blades at 45 deg.

The measurement of the torque coefficient has proven more challenging than that of the thrust coefficient (see Fig. 3.13). At low tip speed ratios, a significant relative uncertainty arises when comparing the reference torque to the hydrodynamic torque. Furthermore, the subsequent division $(R\Omega)^2$, especially when the angular velocity is small, results in a notable variation or discrepancy

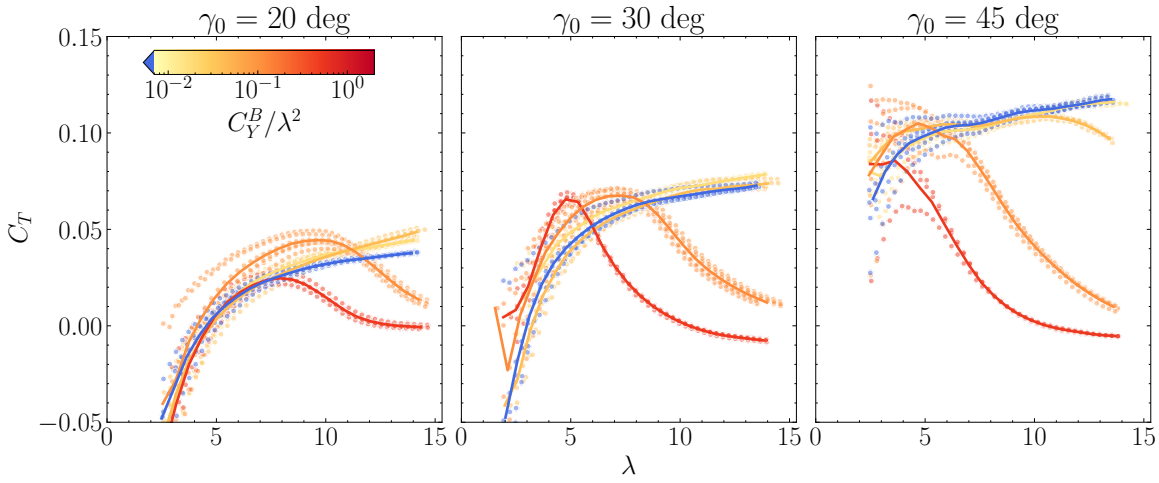

Figure 3.12: Thrust coefficient C_T as a function of the tip speed ratio λ, for three different pitch angles γ_0. Color indicates the flexibility of blade (see Eq. 3.29), with blue corresponding to fully rigid propellers. Dots correspond to individual realizations, the lines are the mean values.

between repeated measurements. Values either approach $-\infty$ as expected or exhibiting unexpected fluctuations that may lead to disproportionately large values. As a result, values below a tip speed ratio of about 5 to 8 depending on the pitch angle are difficult to interpret.

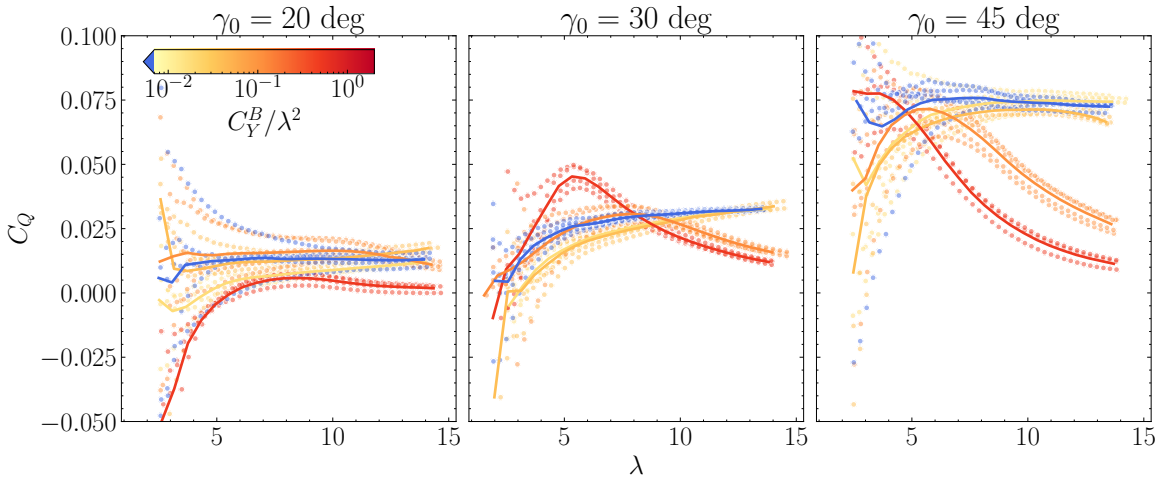

Figure 3.13: Torque coefficient C_Q as a function of the tip speed ratio λ, for three different pitch angles γ_0. Color and symbols are identical to Fig. 3.12

At high tip speed ratio however, we clearly see a reduction of the torque coefficient for the most flexible blades. This reduction is due to the important bending of the blades: at 45 deg, the F4 blades (red) reach a 90 deg bending for high tip speed ratios. The reduction of the moment arm between the furthest blade sections and the axis of rotation means that the torque increases slower than Ω^2 and thus the torque coefficient C_Q is reduced (the F4 blades even reach a torque plateau for high tip speed ratios). The thrust increase visible for the F4 blades at $\gamma_0 = 30$ deg and $\lambda \approx 5$, is associated with an increase of the torque coefficient. To know whether this simultaneous increase of the thrust and

torque is beneficial, we need to compute the efficiency. However, the large uncertainty on the torque coupled with its inclusion in the denominator of the efficiency greatly hinders the interpretability and readability of the experimental data, making it challenging to extract meaningful information.

To still get an idea of the evolution of the efficiency when using flexible blades, we plot in Fig. 3.14 a modified version of the efficiency where we do not remove the parasitic torque from the measurement:

$$\underline{\eta} = \frac{F_{\text{thrust}} U_\infty}{\underline{Q}\Omega}, \tag{3.30}$$

where $\underline{Q} = Q_{\text{hydro}} + Q_{\text{friction}}$ is the total torque measured, without removing the friction from the grease. Using the total torque regularizes the relative uncertainty issues mentioned above as the torque is now always positive and never approaches zero. However, it raises several issues: (i) the magnitude of the efficiency is reduced, (ii) the shape of all curves is modified because the friction torque Q_{friction} is an affine function of the angular velocity (Fig. 3.11) and (iii) any fluctuation of the friction torque might perturb the final result. The curves of Fig. 3.14 are thus presented to get a general idea of the behavior of the flexible blades, but most likely cannot be used quantitatively.

The maximal efficiency of the rigid propeller seems to be reached with 30 deg of pitch angle at about $\lambda = 10$. For the very flexible propellers, both the thrust and torque are reduced at high tip speed ratios and result here in the efficiency plummeting. This efficiency reduction shows that the bending deformation is always detrimental for efficiency as could be expected.

For the rigid propeller, the efficiency is larger with $\gamma_0 = 30$ deg than 20 deg, even at $\lambda = 15$ (the blue curve of the middle panel is always above the one in the left panel). This gap shows that setting a pitch angle of 20 deg is too small for all conditions tested here. Blade twist is therefore required to increase the angle of attack to its optimal value α_{opt}. We see indeed that the flexible blades seem to have a better efficiency than the rigid ones for $\gamma_0 = 20$ deg. The range where it is the case is at moderate λ for very flexible blades and at high λ for the less flexible F1 and F2 blades.

For larger pitch angles, the twist further increases the pitch, beyond the most efficient angle and results in a decrease of the efficiency. The evolution of the twist angle γ with the tip speed ratio and its effect on the efficiency is the subject of the following section, analyzing numerically the effect of elasticity in the system.

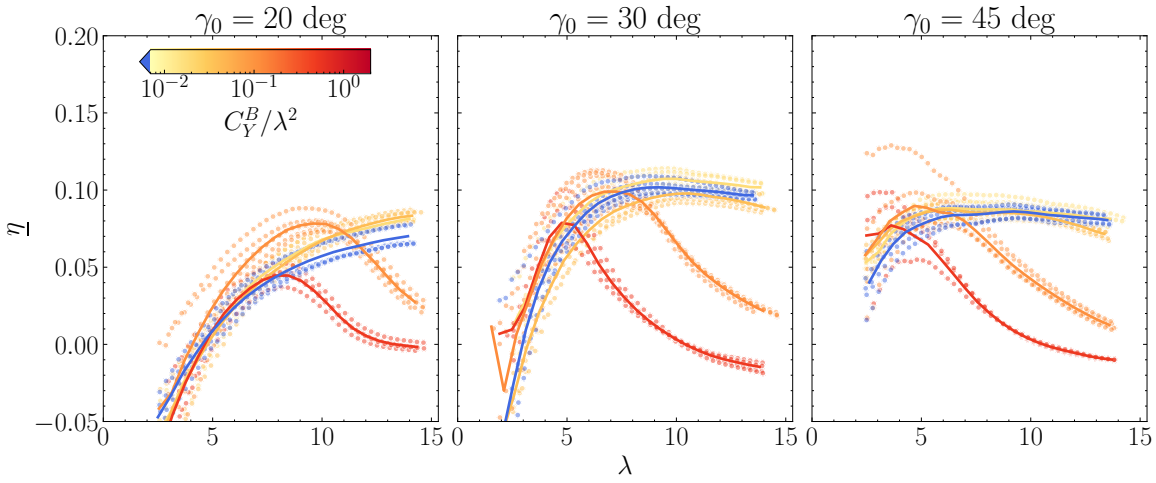

Figure 3.14: Modified efficiency $\underline{\eta}$ as a function of the tip speed ratio λ, for three different pitch angles γ_0. Color and symbols are identical to Fig. 3.12

3.1.5 Numerical efficiency improvements

We solve numerically equations (3.18) and (3.19) for the bending and twist angles. The aim of this model is to explore the phenomenology of blade behaviors that we can encounter with these fully flexible blades and shed light onto the potential efficiency improvement that this type of design could bring. It does not however, aim at being a quantitative predictor of the exact performance of our propeller, but rather a simple toy model. Numerous corrections to this type of model exist, the most common of which is the blade element momentum theory, widely used in engineering and modelling of wind turbines and propellers (Sørensen (2011); Glauert (1983); Masters et al. (2011); Snel et al. (1994)).

We employ the same methodology as in Sec 1.2: dividing the blade into spanwise sections. We solve the system using finite differences and a forward Euler discretization. The system is non-linear through the velocity norm and angle: in the plane normal to $\boldsymbol{d}_3$ at the curvilinear abscissa s, the axial velocity is $U_x = U_\infty \cos\theta$ and the orthoradial velocity is $U_t = \tilde{r}\Omega$, with $\tilde{r}$ the distance to the axis of rotation, computed in the small twist limit in Eq. (A.2). Therefore, the dimensionless velocity norm reads:

$$u_p^2 = \frac{\cos^2\theta}{\lambda^2} + \left(\frac{\tilde{r}}{R}\right)^2, \tag{3.31}$$

and the local angle of attack couples the bending and twist together:

$$\alpha = \gamma - \arctan\frac{R\cos\theta}{\lambda\tilde{r}}. \tag{3.32}$$

The boundary conditions for θ and γ also need to be added to solve the system. The blade is clamped at the hub and has no torque or force at the tip:

$$\theta|_{s=0} = 0,\ \left.\frac{\partial\theta}{\partial s}\right|_{s=1} = 0,\ \left.\frac{\partial^2\theta}{\partial s^2}\right|_{s=1} = 0, \text{ and } \gamma|_{s=0} = \gamma_0,\ \left.\frac{\partial\gamma}{\partial s}\right|_{s=1} = 0. \tag{3.33}$$

We keep the geometry of the blades a constant, as a result the ratio between the twisting and bending Cauchy numbers stays the same, equal to the of the blades.

In Fig. 3.15 we show the result of this computation versus the thrust C_T and bending angle θ_M data from the blades presented in Sec. 3.1 (the long and slender blades for which the ribbon model best applies). The qualitative agreement between experiments and the numerically integrated model is quite good given its simplicity. The phenomenology is well reproduced: see the sign of the bending angle as a function of the tip speed ratio and the pitch angle, and in particular the very quick sign change at about $\lambda = 4$ for the blades with a pitch angle of 20 degrees (red squares). The thrust variations are also captured, in particular the zero thrust limit at high λ for the F4 blades, or the slight overshoot and then decrease seen in the less flexible F1 blades.

The agreement unfortunately is not quantitative (see the different vertical scales) which was to be expected given the important assumptions regarding the flow around the blades (no induced velocities in particular). To a lesser extent, the elastic model used in not perfectly accurate for inextensible ribbons. We implemented the more complete model from Audoly and Neukirch (2021), and the difference was very small, even in the extreme bending cases. The plateau seen for the F4 blades with $\gamma_0 = 30$ deg is a result of a numerical threshold imposed to remove non-physical solutions: the blades fold further than 180 deg and start producing negative thrust.

We explored the parameter space (pitch angle γ_0 and tip speed ratio λ) for both rigid and flexible blades using this model (see Fig. 3.16). On the top row (rigid propeller), we find the classical behavior of a propeller. For all pitch angles, the thrust coefficient (panel (a)) is a growing function of the tip speed ratio and the threshold at which it becomes positive defines the region where the rotor is

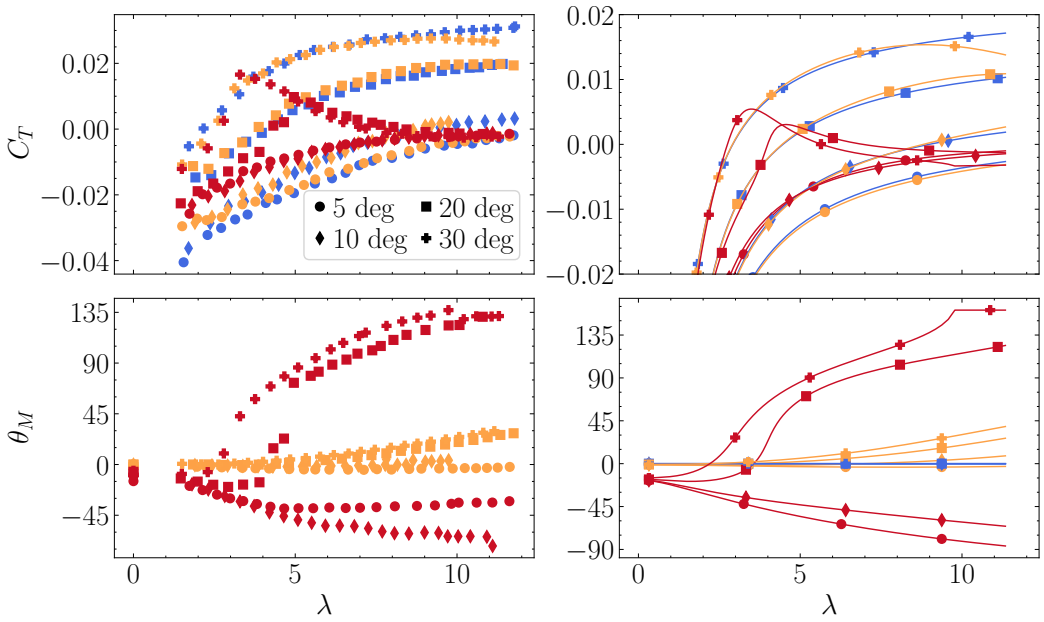

Figure 3.15: Comparison between experimental data (left) and the numerical model (right). (Blue) rigid blades, (orange) F1 blades (red) F4 blades. (top row) Thrust coefficient C_T, (bottom row) tip bending angle θ_M. Experiments are with the long and slender blades, $U_\infty = 0.15$ m/s.

acting as a propeller. Maximum thrust occurs for very high tip speed ratios around 50 deg. In the region of thrust production, the torque coefficient (panel (b)) is effectively independent of the tip speed ratio (this is specific to the geometry we use here) and grows rapidly with the pitch angle with a maximum at 90 deg (not shown). The resulting efficiency (panel (c)) is therefore maximal very close to the delimitation of positive thrust and then decreases when increasing either the tip speed ratio λ or the pitch angle γ_0. The maximum efficiency is reached for $\gamma_0 = 47$ deg and $\lambda = 2.6$. For a given tip speed ratio (i.e., at a given operating condition) the pitch angle that maximizes the efficiency $\gamma_0^{\text{opt}}(\lambda)$ is shown in red: it is a decreasing function of the tip speed ratio. It approximately corresponds to keeping a constant angle of attack at the tip of the blade. This angle is given by the gap between the red (most efficient pitch) and white (flow angle at the tip $\varphi(r = R)$) curves and is approximately 18 deg, very close to $\alpha_{\text{opt}} = 17$ deg.

Comparing these reference results to the behavior of a flexible blade (middle and bottom rows, at $\lambda = 4$, $C_Y^B = 1.2$) we highlight a few differences. At high tip speed ratios and especially for high pitch angles, the bending is extremely important ($\gtrsim 90$ deg, panel (h)). Both the thrust coefficient (panel (d)) and the efficiency (panel (f)) are therefore close to zero in this region.

In the region where the propeller produces negative thrust, the angle of attack is negative on most blade sections and therefore there is slight negative bending (panel (h)) and twist (panel (g)) (not visible because of the scale of the positive deformation). The limit between positive and negative bending (black line) is very similar to the limit of positive thrust (the same is true for the twist). This observation is coherent with the scaling law 3.28, and shows that the twist would follow a similar law. Finally, we see the small but finite amplitude of the twist ($\gamma_M - \gamma_0 \lesssim 15$ deg), that modifies the performance of the rotor.

Looking closer at the efficiency of the folding propeller, we plot in Fig. 3.17 (a) the efficiency as a function of the tip speed ratio only. In blue, we plot the curves obtained with the rigid propeller for

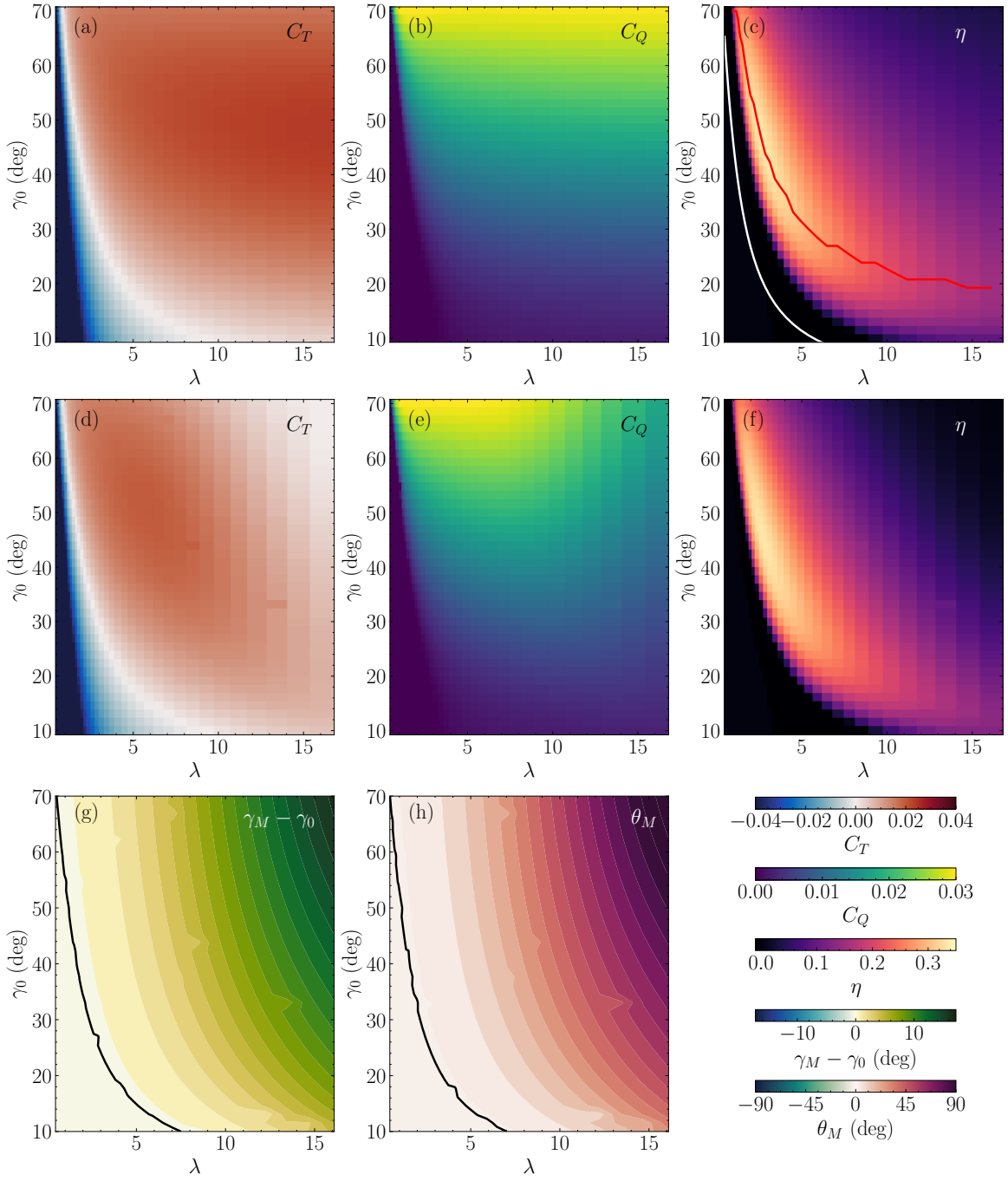

Figure 3.16: Maps of the results produced by the model as a function of the tip speed ratio λ and pitch angle γ_0. Top row corresponds to rigid blades, and the bottom two to flexible ones (about as flexible as the F2 blades). Panels (a) and (d) show the thrust coefficient C_T, panels (b) and (e) show the torque coefficient (C_Q) and panels (c) and (f) show the efficiency η. Panels (g) and (h) show the tip twist $\gamma_M - \gamma_0$ and bending angles θ_M respectively, with regularly spaced contours (the black lines highlights zero deformation).

various pitch angles and in black the maximal efficiency over all pitch angles (i.e., the envelope of the blue curves or the efficiency that can be obtained if the pitch angle is modified to follow $\gamma_0^{\text{opt}}(\lambda)$). On top of it, we plot the efficiency for flexible propellers with varying flexibility (yellow to red when increasing C_Y^B/λ^2) and a pitch angle of 30 deg (any other pitch angle would lead to a similar discussion).

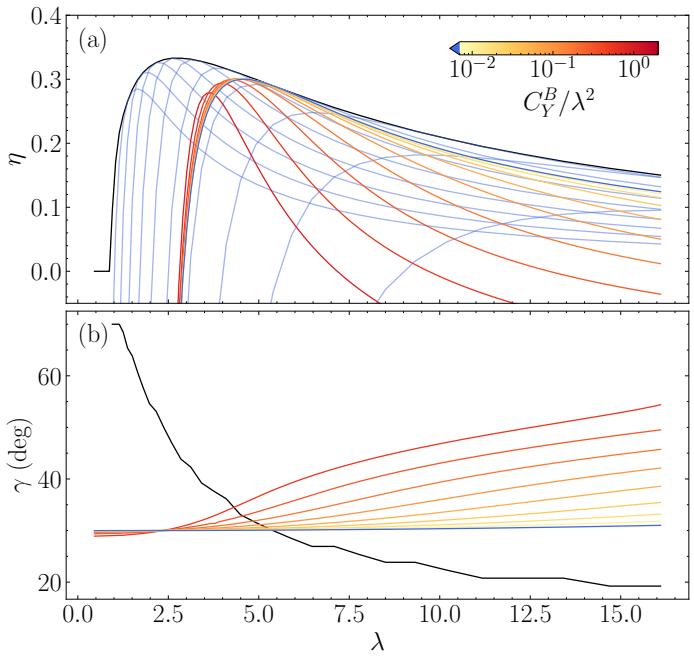

Figure 3.17: (a) Efficiency η as a function of the tip speed ratio λ. (light blue) Curves for different pitch angles with the rigid propeller. (black) Maximal efficiency for each λ. (yellow to red) Flexible propeller with varying Cauchy number. (b) Twist angle γ as a function of the tip speed ratio. (black line) Pitch angle giving the optimal efficiency for the rigid propeller (red line from Fig. 3.16). (yellow to red) Tip twist of the flexible propeller.

Flexible blades never exceed the envelope of the rigid blades: whichever the tip speed ratio, using the rigid propeller with the right pitch angle $\gamma_0^{\text{opt}}(\lambda)$ results in a better efficiency. The inefficacy of the flexible blades is due to the fact that (i) bending is always detrimental for efficiency, reducing the surface swept by the blades and (ii) the spanwise torsion of the blade is in the wrong direction. Efficient propulsion requires that the local twist angle γ follows the evolution of the local flow angle φ: decreasing from root to tip. However, the twist in the case of these blades always increases γ going from the root to the tip, further reducing the efficiency.

The flexible blades can be more efficient than a rigid propeller with the same pitch angle. At tip speed ratios smaller than the one reaching maximum efficiency ($3 < \lambda < 5$ here), the flexible blades are more efficient. The bending is limited in this region close to the zero thrust limit, reducing its detrimental effect on efficiency. In Fig. 3.17 (b) we plot the optimal pitch angle of the rigid blades $\gamma_0^{\text{opt}}(\lambda)$ (black curve) and the tip twist $\gamma(r = R)$ of the flexible ones with $\gamma_0 = 30$ deg (yellow to red). When $3 < \lambda < 5$, the pitch angle is smaller than the one required for maximal efficiency. The flexible blades twisting reduces this discrepancy. At a given tip speed ratio, increasing the twisting Cauchy number increases the efficiency up to a point where the sections of the blades near the tip have a pitch angle larger than α_{opt} and therefore generate drag, decreasing the efficiency. These results are coherent with the experimental observations in Fig. 3.14: the rigid blades with $\gamma_0 = 20$ deg have a

pitch angle too small for the tip speed ratios considered and thus all the flexible blades are more efficient. The most flexible ones are more efficient at lower λ. For more important pitch angles, any efficiency improvement occur at tip speed ratios λ smaller than the one where the rigid blades reach their maximum.

3.1.6 Concluding remarks

These first results, intended at characterizing in broad lines the phenomenology encountered when dealing with highly flexible propellers, allowed us to obtain the following main results. The centrifugal force is always negligible in the problem, the complexity of the deformations observed comes from a coupling of the bending and twisting deformations through the hydrodynamic lift force. Even though classical reconfigurating systems (Gosselin and de Langre, 2011; Alben et al., 2002; Schouveiler and Boudaoud, 2006; Marzin et al., 2022) are driven by the drag force, we found that the techniques used to predict deformations (rescaling the Cauchy number by a quantity describing the initial loading on the system) can be directly transposed to this system for moderate deformations. When the bending is extreme, we found that we can still link two macroscopic quantities of the rotor (tip bending angle and thrust), although not in a predictive manner.

Using a simple toy model coupling an inextensible ribbon model for the blade elasticity and a blade element model for the hydrodynamic loading, we show that we can qualitatively predict the deformation of the blades. The novel fluid-structure interaction problem is the main interest of these blades. The bending deformation always reduces the thrust and efficiency compared with a rigid propeller. The twisting deformation only ever increases the pitch angle and thus is interesting for efficiency only in the range where the prescribed pitch angle γ_0 is too small. This effect can be reversed if the center of mass (or pivot) of the blade is placed in front of the hydrodynamic center. This is the topic of the following section.

Finally, these first experiments allowed us to identify the important parameters and challenges of measuring the deformations and performance of these types of model scale propellers. The fact that the region of interest in terms of the performance of the blade studied overlaps with the region where the uncertainty is maximal resulted in important challenges in obtaining repeatable results. In particular, the difficulties in accurately measuring the torque — and to a lesser extent the force — led us to design the third type of boat that we use in the remainder of the thesis, which completely eliminates these problems.

3.2 Chordwise-flexible propeller

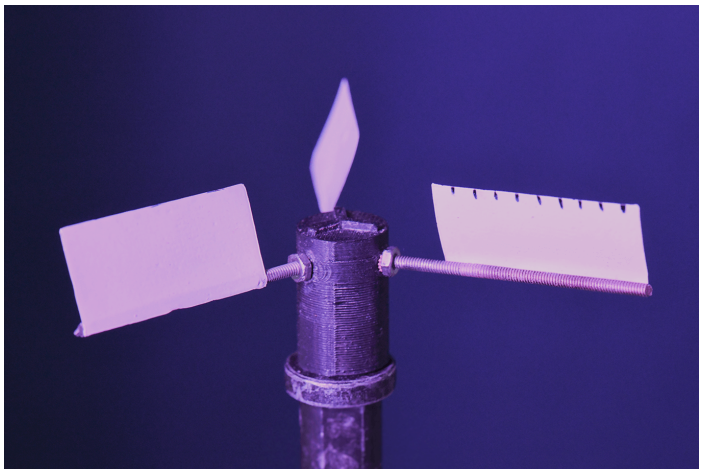

Figure 3.18: Semi-flexible propeller

This section describes a similar experiment to the one in the previous section but with a key difference: the pivot around which the blade rotates is the leading edge of the blade instead of its centerline. This design reverses the sign of the hydrodynamic twisting moment, reducing the local pitch angle instead of increasing it. The rigid leading edge also stops the bending of blades.

This concept is very similar to the one used by Cognet et al. (2017) in the case of wind turbines, with a rigid leading edge and a flexible blade. In this case, the hydrodynamic force increases the pitch angle while the centrifugal force decreases it. By balancing the two forces, the authors are able to follow the twist angle that maximizes the power extracted as a function of the tip speed ratio, thus extending the range of efficiency of the wind turbine. We investigate the possibility of obtaining a similar efficiency improvement in the case of propellers in water, where the force balance is modified in two ways. First, the centrifugal force is negligible for the same reasons as mentioned in the previous section. In addition, the lift force driving the deformation has an opposite sign between the case of a wind turbine and a propeller.

We first describe how the setup has been modified from the previous section, solving the main precision issues, and how we model the flexible propeller. We then analyze the effect of the deformation on thrust, torque, and efficiency in a particular case before describing how this flexible propeller can be used to improve efficiency in terms of magnitude and resilience. Finally, a first-order development of the governing equation allows us to compute a law that predicts the tip deformation of the propeller.

3.2.1 Setup and minimal model

We use blades with a rigid leading edge made of a small threaded shaft with flexible Mylar blades glued to it (Fig. 3.18). We sanded the threaded shaft in order to have a flat spot to glue the blades to. The blades and shafts are then threaded to the hub and fastened using nuts. This linkage allows us to change the pitch angle by varying the thread length. For reference, we also use rigid fiberglass blades made in the same way.

We used the third boat described in section 2.2.3, that allows us to measure simultaneously the thrust, torque and angular velocity of the rotor. We perform experiments by setting a flow velocity U_∞ and

an angular velocity Ω and recording the signals of thrust and torque for 20 s. The values presented below are the mean over the last 10 s. Each experiment was repeated at least twice and the errorbars in the following represent the standard deviation between repeated measurements. Similarly to the previous case we do not vary the flow speed across experiments, instead focusing on the angular velocity and blade material. We use a flow velocity of $U_\infty = 0.15$ m/s, the blades P1 to P4 defined in Sec. 2.3 and angular velocities ranging from 4 to 22 rad/s. We used pitch angles γ_0 from 30 to 80 deg with all the blades. We also tested the rigid blade at 20 deg and the flexible ones at 90 deg (when not rotating the blades are aligned with the flow).

At the same time, we use a high-speed camera to capture the shape of the blade at the tip. This camera is synchronized with the Hall-effect sensor on the boat and therefore takes 25 pictures per rotation of the propeller. The blade is illuminated by a laser sheet that illuminates the entire chord at a given radius. We always place it a 1 to 2 mm from the tip, corresponding to 90% of the maximum radius. We then extract the images where the blade is aligned towards the camera. Doing so means that we record the shape of the blade always in the same position in the rotation, where the incoming flow is modified due to the shaft tilt (it corresponds to $\Omega t = 3\pi/2 \mod 2\pi$ in the analysis from Sec. 2.2.3).

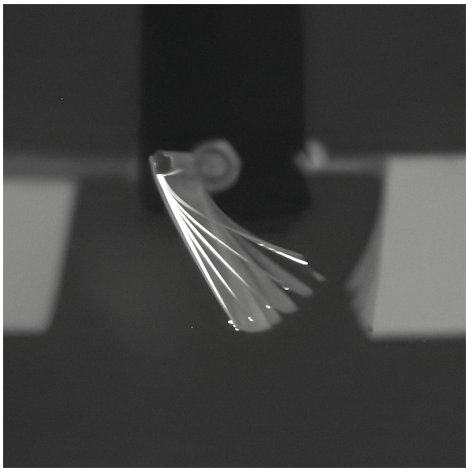

Figure 3.19: Example of the deformation of the blades as the angular velocity is increased. Obtained with $U_\infty = 0.15$ m/s, $\gamma_0 = 30$ deg and the P3 blades.

We employ a simpler modeling of the elasticity of the blade than in the previous section. Instead of solving for the shape of the blade as one single plate, we divide it into independent spanwise beams clamped at the leading edge (Fig. 3.20, (a)). This technique has been shown by Cognet (2017) to converge to the same solution when the number of beams is increased in the case of wind turbines. In doing so, we neglect the elastic energy associated with the torsion due to the different bending between root and tip. In experiments, it is small compared to the bending itself (Fig. 3.19). We make one further assumption: instead of describing the curvature of each beam along the chord, we reduce the curvature to its average deflection by modelling each beam as rigid but attached to the leading edge by a torsion spring (Fig. 3.20, (b)). Doing so, we neglect the effect of the chordwise curvature of the blade. The effect of this curvature is to modify the sectional aerodynamic coefficients C_L and C_D in a non-trivial way. We measured the effective spring constant with a bending test in Sec. 2.3.

Experimentally, we extracted the tip twist angle γ_M from the images of the deformed blade (Fig. 3.19). We used a Hough transform (Duda and Hart, 1972) to detect the main direction of the lit shape in the images. In practice, we measure the angle of the straight portion near the trailing edge (see App. D.2).

Mathematical description For a blade section a the distance r from the axis of rotation, we write the conservation of angular momentum at the leading edge of the blade:

$$0 = C\left(\gamma(r) - \gamma_0\right) + \frac{1}{2}\rho c U_p^2 \left(C_L(\alpha)\cos\alpha + C_D(\alpha)\sin\alpha\right)\bar{\delta}_{AC}^{LE}, \tag{3.34}$$

where C is the per unit width spring constant, γ_0 the pitch angle, U_p the local flow velocity, and $\bar{\delta}_{AC}^{LE}$ the distance between the aerodynamic center and the leading edge. This distance is modeled as being equal to $c/4$ in this whole section (Li et al., 2022). Using $R\Omega$ as a reference velocity and c as the

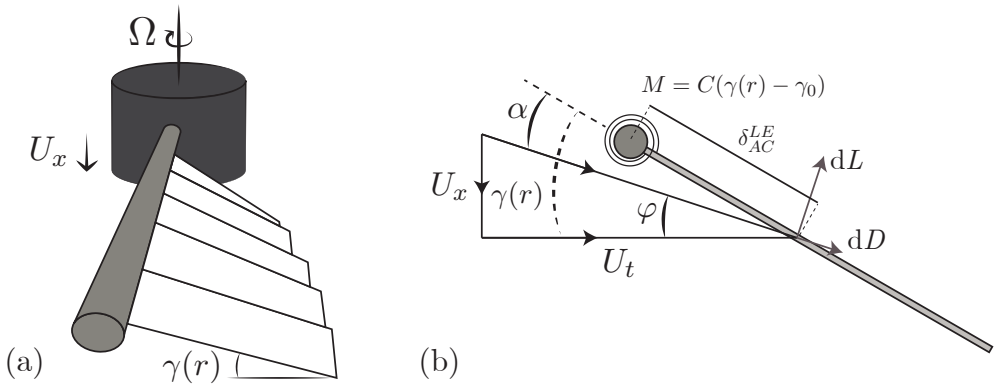

Figure 3.20: (a) Schematic of a blade twisting and its division into spanwise beams. (b) Definition of the angles on a single beam

reference length, we obtain a new Cauchy number:

$$C_Y^S = \frac{1/2\rho c^2 \left(R\Omega\right)^2}{C}, \tag{3.35}$$

such that the balance of torques read:

$$\gamma(r) = \gamma_0 - C_Y^S u_p^2 \left(C_L(\alpha)\cos\alpha + C_D(\alpha)\sin\alpha\right)\delta_{AC}^{LE}, \tag{3.36}$$

where $\delta_{AC}^{LE} = \bar{\delta}_{AC}^{LE}/c = 1/4$ and $u_p = U_P/R\Omega$. This equation is non-linear through the feedback from the hydrodynamic forcing: the angle of attack is $\alpha = \gamma - \varphi$.

Correcting for the tilt of the shaft The shaft is tilted and therefore the loading on the blades varies throughout the rotation. Using the model above, we estimate the resulting variation of the deformation. From the results obtained in Sec. 2.2.3 we have the angular position dependent angle of attack and velocity norm:

$$\alpha = \gamma - \arctan\frac{\cos\delta}{s\lambda - \sin\delta\sin\Omega t}, \text{ and } u_p^2 = \frac{\cos^2\delta}{\lambda^2} + \left(s - \frac{\sin\Omega t\sin\delta}{\lambda}\right)^2, \tag{3.37}$$

where $s = r/R$, Ωt is the angular position in the plane of rotation, and $\lambda = R\Omega/U_\infty$ the tip speed ratio. We solve Eq. (3.36) with the position dependent angular velocities at the tip of the blade and extract several quantities of interest. First, the average twist angle over a rotation $\widehat{\gamma_M}$. Second, $\gamma_M(\Omega t = 0 \mod \pi)$ the twist angle in the symmetric position (above or below the shaft). And third $\gamma_M(\Omega t = 3\pi/2 \mod 2\pi)$ the twist in the direction of the measurement. All of these are computed at the tip of the blade, where the deflections are the largest. We explored the parameter space of pitch angle γ_0, tip speed ratio λ and Cauchy number C_Y^S.

In Fig. 3.21 (left) we show that the average twist during a rotation and the twist in the symmetric configuration are essentially identical. The equality between averaged and symmetric twist angles shows that it is sufficient to perform computations assuming $U_x = U_\infty\cos\delta$ and $U_t = r\Omega$ instead of computing the deflection throughout the rotation. We use this result in subsequent numerical computations.

In Fig. 3.21 (right) we show the difference between the angle measured when $\Omega t = 3\pi/2 \mod 2\pi$ and the average angle during the cycle. We vary γ_0 and λ for a Cauchy number of about 1. The

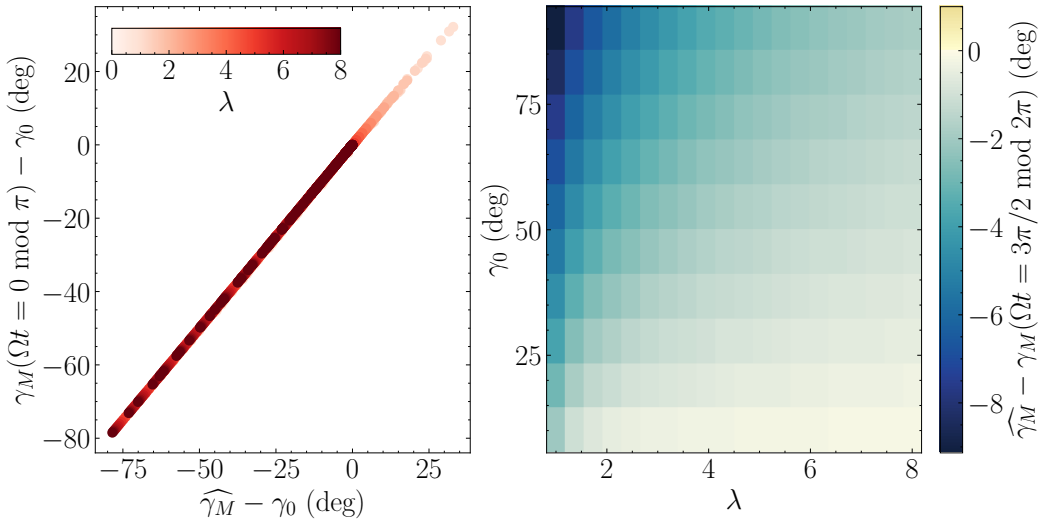

Figure 3.21: (Left) Tip twist angle in the symmetric position versus mean twist angle. The numerical data is computed for $10 \text{ deg} < \gamma_0 < 90 \text{ deg}$, $10^{-2} < C_Y^S < 30$ and $1 < \lambda < 8$. (right) Difference between the tip twist angle in the measurement position and the mean twist as a function of the pitch angle γ_0 and the tip speed ratio λ.

difference is a few degrees and is most important for small tip speed ratios. At the location of the measurement the blade is experiencing a larger velocity norm and a larger angle of attack. This larger angle of attack stems from the fact that the angle between the angular velocity and the flow velocity is narrower than 90 deg, and explains why the deflection measured is always larger than the mean value throughout the cycle. We therefore compute a theoretical correction $\gamma_{\text{corr}} = \widehat{\gamma_M} - \gamma_M(\Omega t = 3\pi/2 \bmod 2\pi)$, a function of γ_0, λ and C_Y^S. In the following, we apply this correction to our experimental result in order to compensate for the tilt of the shaft.

3.2.2 Passive twisting improves the efficiency

Typical experiment

We plot a typical example of the all the data that we measure in an experiment in Fig. 3.22. The left side (panels (a) to (d)) is experimental, the right side shows the corresponding numerical model. All data correspond to a pitch angle of $\gamma_0 = 60$ deg. Similarly to the previous section, the different blades correspond to different colors according to the Cauchy number rescaled by the tip speed ratio squared:

$$C_Y^S/\lambda^2 = \frac{1/2\rho c^2 U_\infty^2}{C}. \tag{3.38}$$

The P1 to P4 blades correspond to a value of C_Y^S/λ^2 respectively of 1.5×10^{-2}, 4.7×10^{-2}, 2.4×10^{-1}, and 1.04.

Blade flexiblity most often reduces the thrust and torque coefficients. On panel (a) we see that all but the least flexible blade produce less thrust than the rigid one. This is because the effect of the flexibility is here to reduce the pitch angle on the blade (panel (d)). Most often this results in a reduction of lift and therefore of the thrust produced. However, the maximum lift a flat plate can produce occurs when the angle of attack is about 45 deg (Sec 1.2.2). At high tip speed ratio, the angle

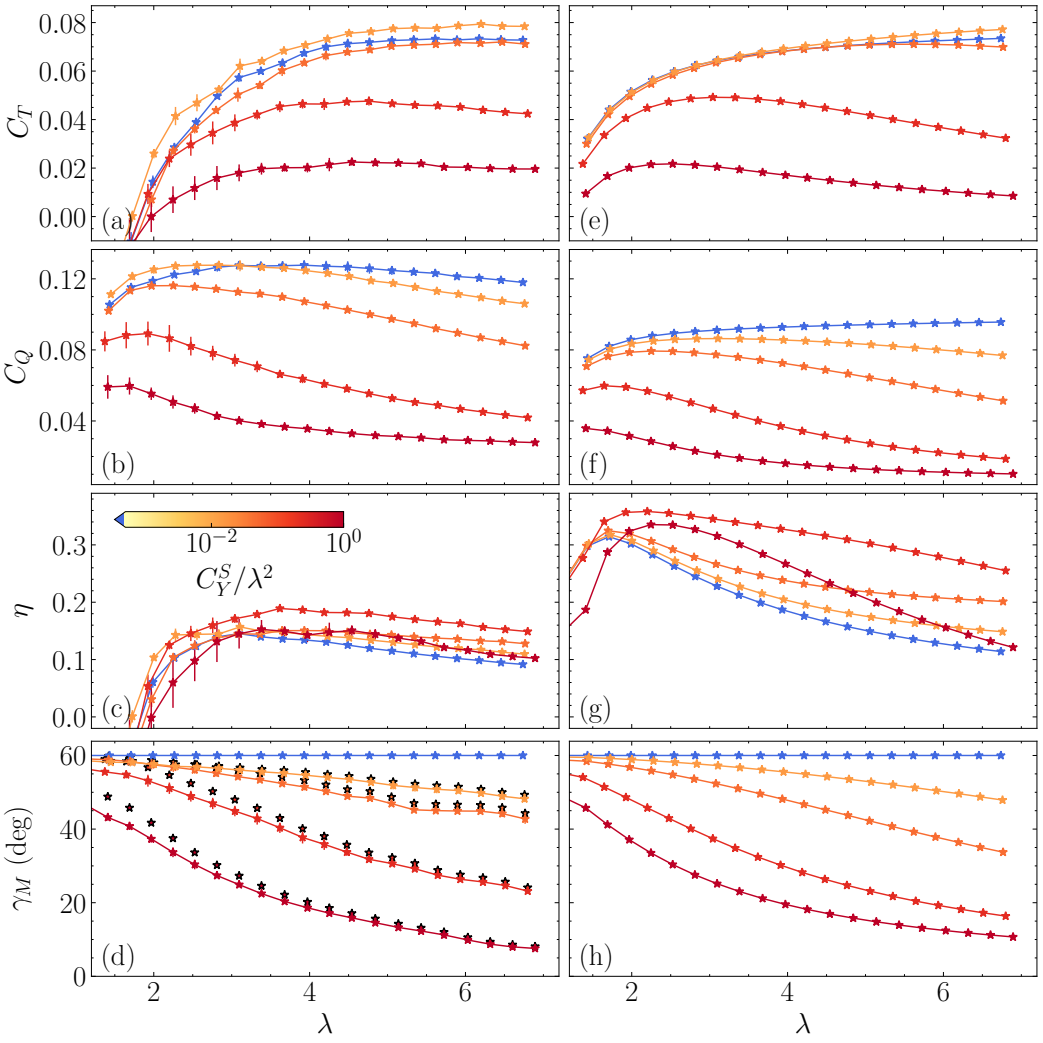

Figure 3.22: Propeller performance as a function of the tip speed ratio λ with a pitch angle of $\gamma_0 = 60$ deg. Panels (a) to (d) are experimental while (e) to (h) are numerical. Row 1 displays the thrust coefficient C_T, row 2 displays the torque coefficient C_Q, row 3 displays the efficiency η, and row 4 displays the tip twist angle γ_M. Left and right columns use the same vertical scales. Markers with dark edge color on panel (d) correspond to data that has been modified by adding γ_{corr}.

of attack $\alpha = \gamma - \varphi \approx \gamma$ reduces to the twist of the blade γ. Therefore, if $\gamma_0 = 60$ deg, improving the thrust by reducing the twist is possible. This is what we see for the least flexible blades (yellow curve). The mechanism that leads to the thrust reduction of the more flexible blades is different to the one in the previous section. It is due to a reduction of the angle of attack to smaller values than the one producing maximum thrust. In this case, even the most flexible blade still produce positive thrust at high tip speed ratio. At the same time, this reduction of the angle of attack leads to a quick decrease of the torque as well (panel (b)).

We can appreciate here the effect of changing the tools used to measure the thrust and torque. The uncertainty between experiments (error bars) is limited and only concerns low tip speed ratios, a range that is not the primary focus of this section.

Using this particular pitch angle ($\gamma_0 = 60$ deg), we can see that all flexible blades improve the efficiency of the propeller (panel (c)). This is because of the angle of attack on the rigid blade. At high λ, the angle of attack at the tip is approximately $\alpha \approx \gamma$, which in the case of the rigid blades corresponds to the pitch angle. However, in Sec. 1.2.2, we found an optimal angle of attack for the lift to drag ratio α_{opt} of about 17 deg. Reducing the angle of attack through twist is therefore almost always beneficial at high tip speed ratios. This mechanism creates an optimal Cauchy number: the red curve (P3 blades) is above the most flexible dark red one (P4 blades). If the twist reduces the angle of attack beyond α_{opt} over most of the blade, then the efficiency will reduce again. This is visible in the last panel (d) where the most flexible dark red points are below 10 deg at high tip speed ratio. This mechanism is summed up in Fig. 3.23. We focus here on the tip of the blade because it is where most of the force is generated as the velocity norm grows like the square of the distance to the axis of rotation. However, the global shape of the blade is modified: the tip is more twisted than the root creating a spanwise torsion (bottom row of Fig. 3.23).

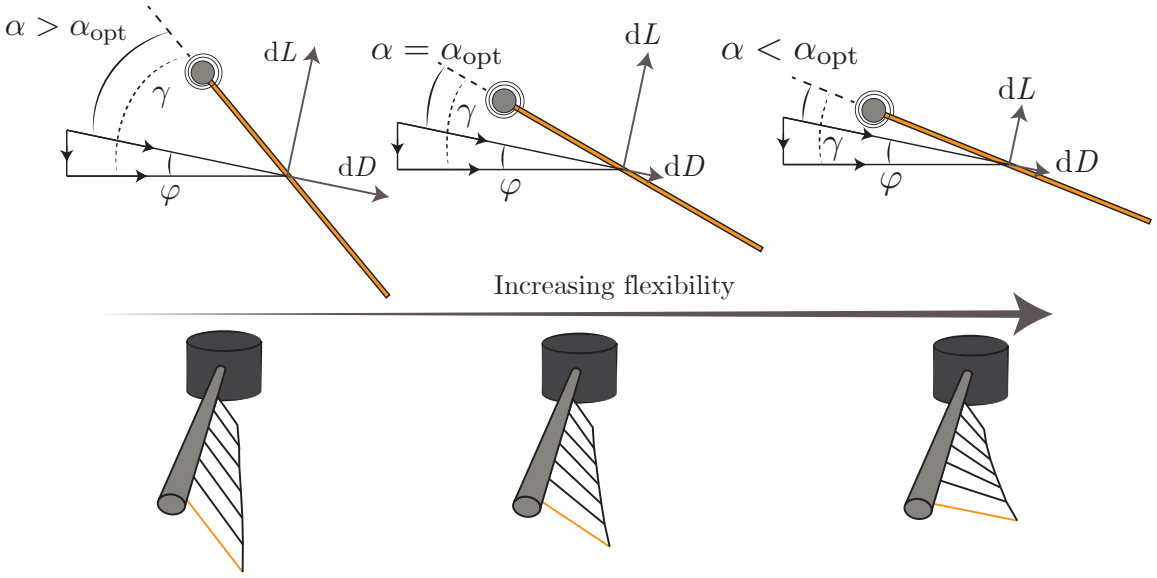

Figure 3.23: Schematic of the mechanism that leads to improved efficiency. (Top row) Evolution of the angle of attack with the material flexibility for one given blade section. (Bottom row) Evolution of the global shape of the blade.

Finally, we can see the effect of the proposed correction of the tip twist angle γ_M. Markers with a dark edge color correspond to the data corrected by adding γ_{corr}: transforming the raw data measured on the side of the rotor to the mean angle over a whole rotation. The effect of this modification is

to decrease the tip deflection by a small amount (less than 5 deg) with a smaller contribution as λ grows larger.

On the right column of Fig. 3.22, we plot the results obtained from solving Eq. 3.36 over the whole span of the blade, with the exact same parameters as the experiment. This very simple model produces very good predictions of the behavior of the rotor. In particular the deflection as a function of the tip speed ratio is very similar to the one obtained in the corrected experiments. Forces are well predicted as well, even if the torque is slightly smaller than in experiments: no losses due to flow curvature or finite blade size effects have been implemented in this model. The resulting efficiency is more important and more peaked than the one found in the experiments, yet the relative order between flexibilities is well respected. All the experimental data for the thrust, torque, and twist angle for other pitch angles can be found in App. C.

However, the model does not quantitatively agree with the experimental data. This means that our correction of the tip twist angle γ_{corr} is an approximation of the real correction required. It still has the right direction and order of magnitude and the tip angle data in the following is the corrected one.

There are two metrics that can be used to compare the efficiency of different propellers. The first and most natural one is to compare the maximal efficiency: when the conditions are optimal, what is the best performance that a propeller can produce ? The second one in contrast, compares the resilience to a change of external conditions: how flat is the efficiency versus tip speed ratio curve near its optimum ? We will see in this section that these flexible blades can improve the efficiency on both fronts.

Resilience to variations of tip speed ratio

The most important efficiency improvement is the resilience to changes of external conditions. This metric is the direct equivalent of the result obtained by Cognet et al. (2017). In Fig. 3.24 panel (a), we plot the efficiency as function of the pitch angle for all the blades with $\gamma_0 = 40$ deg, the optimal pitch angle for the flexible blades. To compare the optimal flexible blades with the rigid ones, we also plot the efficiency curves for every pitch angle for the rigid blades (in blue). Markers indicate the pitch angle, with 40 deg being indicated by diamonds.

The rigid efficiency curves all display a maximum for an intermediate tip speed ratio (except for $\gamma_0 = 80$ deg which remains very inefficient). The tip speed ratio corresponding to this optimum decreases when increasing the pitch angle: from $\lambda = 7$ at $\gamma_0 = 20$ deg, deg to $\lambda = 3$ at $\gamma_0 = 70$ showing the necessity to adapt the pitch angle to stay at an optimal efficiency. Conversely, this defines an optimal pitch angle for each tip speed ratio, that we denote as $\gamma_0^{\text{opt}}(\lambda)$ and is specific to this propeller geometry.

From $\lambda = 3$ to 5.5, the P3 blades (red) with $\gamma_0 = 40$ deg are as efficient or more than any rigid propeller. Their effective pitch angle is passively modified by the flow, maintaining a high efficiency for a wide range of tip speed ratios. The P3 blades are optimal as the less flexible P1 and P2 blades (yellow and orange) have an efficiency closer to their rigid counterpart while the more flexible P4 (dark red) have an overall reduced efficiency.

The efficiency of the propellers is closely linked to the twist angle γ along the span as shown in the schematic of Fig. 3.23. We want to know what the evolution of the tip twist angle should be in order to have a blade that remains as efficient as any rigid one. We therefore plot in Fig. 3.24 panel (b) the tip twist angle for all the blades with $\gamma_0 = 40$ deg (yellow to red, blue for the rigid blades). In addition to that, we plot $\gamma_0^{\text{opt}}(\lambda)$ measured experimentally (in black): the pitch angle which results in

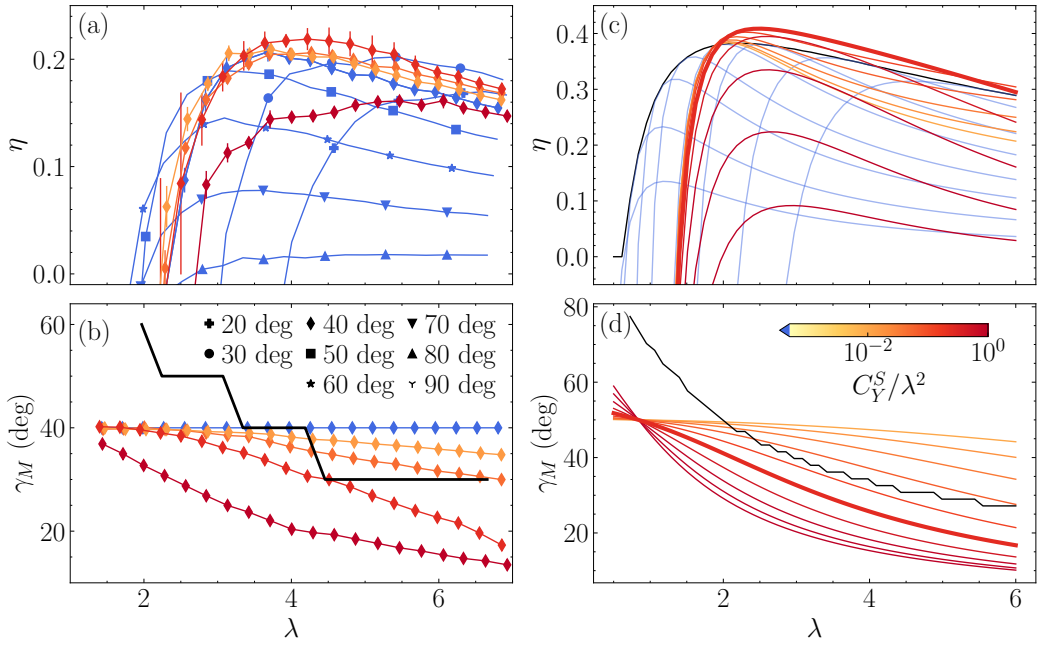

Figure 3.24: Efficiency and tip twist as a function of the tip speed ratio. Left column corresponds to experimental results, right column to numerical computations. (a) Efficiency of the $\gamma_0 = 40$ deg flexible propellers (diamonds, yellow to red). (blue) Rigid propeller with various pitch angles (differentiated with markers). (b) Associated tip twist. (black curve) Optimal pitch angle of the rigid blades $\gamma_0^{\text{opt}}(\lambda)$. The tip twist is corrected by adding γ_{corr}. (c) Numerical efficiency with $\gamma_0 = 50$ deg for the flexible blades (yellow to red). (blue) Rigid propeller with various pitch angles. (black) Efficiency of an optimally adjusted rigid propeller. (d) Numerical tip twist for the flexible blades. (black) Optimal pitch angle $\gamma_0^{\text{opt}}(\lambda)$.

the largest efficiency of the rigid blades for each tip speed ratio. It is modified in steps because the rigid propeller experiments were carried out every 10 deg of pitch angle. To maximize efficiency, the tip twist should be close to the optimal pitch angle. Indeed, the P4 blades, which are far from $\gamma_0^{\text{opt}}(\lambda)$ are very inefficient. The slope of the tip twist γ_M for the P3 blades matches approximately the curve $\gamma_0^{\text{opt}}(\lambda)$ in the range $\lambda \in [3, 5.5]$. The exact value is however slightly smaller than was expected using the rigid blade data.

In panels (c) and (d), we plot the numerical equivalents to the experimental data from panels (a) and (b). Panel (c) shows the efficiency with several flexible blades (yellow to red) with pitch angle $\gamma_0 = 50$ deg. The value of γ_0 plotted here is not the same as the experimental one because it numerically corresponds to higher efficiencies. However, the same discussion is possible with other pitch angle without changing the results. Added to that we plot several efficiency curves for rigid propellers, with various pitch angles (light blue) as well as the maximum efficiency reachable in black (the efficiency of a rigid propeller following $\gamma_0^{\text{opt}}(\lambda)$ or the envelope of the blue curves). The red curve with a bold line shows the optimal flexible blade for this pitch angle. It remains more efficient than any rigid propeller for $\lambda \in [1.95, 6]$.

Panel (d) displays the corresponding tip twist. The black line corresponds to $\gamma_0^{\text{opt}}(\lambda)$. Similarly to the experimental result, the most efficient flexible propeller has a tip twist curve that follows the same evolution as the optimal pitch angle, but a few degrees below it.

In contrast to the previous propeller studied, the effect of flexibility is to decrease the twist angle and reduce the angle of attack. As a consequence, the flexible propellers passively adjust to a change in external conditions: if λ increases, the angle of attack increases, increasing the loading on the blade and decreasing the twist angle, that finally reduces the angle of attack and compensates for the increased λ. They have therefore an overall increased efficiency.

Maximal efficiency

The flexible blades reach a higher maximum efficiency than the rigid ones. For a pitch angle of 40 deg the P3 blades are more efficient than any rigid ones at around $\lambda = 4$. We interpret this observation as being due to the spanwise distribution of twist along the blade (See Fig. 3.23, bottom row). In the previous analysis we only considered the tip angle because it corresponds to the location where most of the force is generated. However, the whole blade deforms in response to local constraints. For the same tip twist, the shape adopted by the rest of the blade can modify the resulting forces. This torsion effect is secondary compared with having the right angle near the tip.

In Fig. 3.25 (panel (a), green curve) we show the twist as a function of the spanwise position s on the blade for $\gamma_0 = 40$ deg and $\lambda = 4$ (close to maximum efficiency)[1]. Close to the hub, there is almost no deflection: $\gamma \approx \gamma_0 = 40$ deg. The angle γ decreases when going from the root ($s = 0.3$) to the tip ($s = 1$) of the blade. This trend follows the same evolution as the local flow angle $\varphi = \arctan(\cos\delta/(s\lambda))$ (blue curve) and therefore reduces the angle of attack fluctuations ($\alpha = \gamma - \varphi$) on the blade compared with a rigid one where $\gamma(s) = \gamma_0$. In panel (b), we show the global efficiency optimum obtained with the numerical model using an optimization algorithm searching the $(\gamma_0, \lambda, C_Y^S)$ parameter space: the curves for the twist and flow angle keep an almost constant difference. This difference is close to the optimal angle of attack that maximizes the lift to drag ratio: $\alpha_{\text{opt}} = 17$ deg.

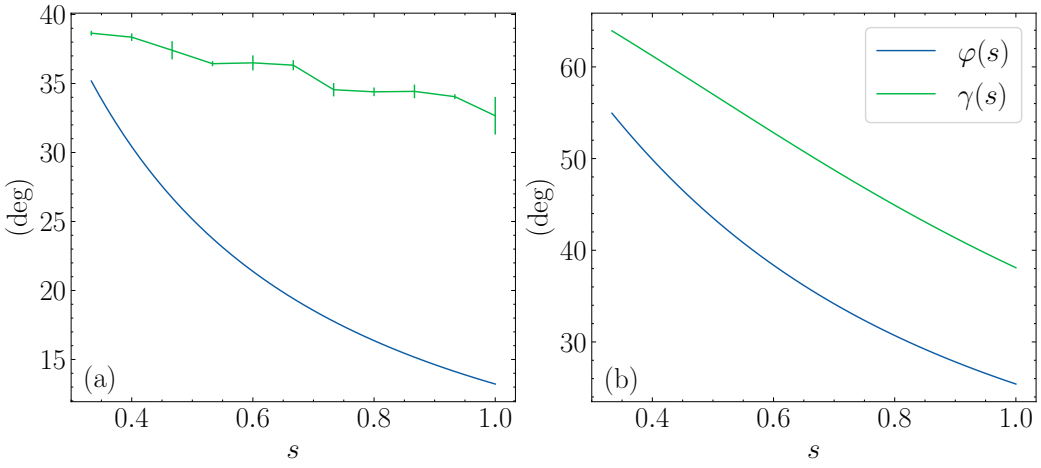

Figure 3.25: Local flow angle $\varphi(s)$ (blue) and twist $\gamma(s)$ (green) as a function of the spanwise position s. (a) The twist corresponds to experimental data for the P3 blades at $\gamma_0 = 40$ deg and $\lambda = 4$. (b) The twist corresponds to the global efficiency optimum obtained with the numerical model ($\gamma_0 = 70$ deg, $\lambda = 2.1$, and $C_Y^S/\lambda^2 = 0.93$). In either case the flow angle is obtained via $\varphi = \arctan(\cos\delta/(s\lambda))$.

The strategy for maximizing efficiency is the same as was noticed in Sec. 1.2.2: keep the angle of attack as close to α_{opt} as possible on most of the blade. The numerical solution keeps the angle of

[1] We measured it at several spanwise positions by moving the laser sheet.

attack $\alpha = \gamma - \varphi$ between 12 and 15 deg almost everywhere. Experimentally, we are not able to reproduce this solution: the P4 blades (dark red markers) should have more spanwise torsion but are almost never more efficient than the less flexible P3. Two factors might cause this discrepancy: first, the important chordwise curvature of the blades when highly deformed is detrimental for hydrodynamic efficiency. Flexible blades are less efficient than ones with a torsion spring as in the model. Second, we use a flexible plate instead of an assembly of independent beams. This might prevent us from reaching the 30 deg of spanwise torsion required for this optimal solution as the elastic energy associated with the spanwise torsion is no longer negligible and a model taking into account the plate geometry is required.

Still, the much more moderate evolution of the pitch angle in the optimal experiment (Fig. 3.25, panel (a)) allows the angle of attack to stay close to the one of maximal lift to drag ratio. At the tip, $\alpha \approx 20$ deg and at mid span it is about 15 deg, resulting in high lift to drag ratio over most of the blade (Fig. 1.8). This spanwise torsion allows the flexible blades to be more efficient than any rigid blades. It should be noted that we would most likely not see this improvement in maximum efficiency if the shape of the propeller at rest were twisted to maximize the performance of the rigid propeller.

Effect of the pitch angle

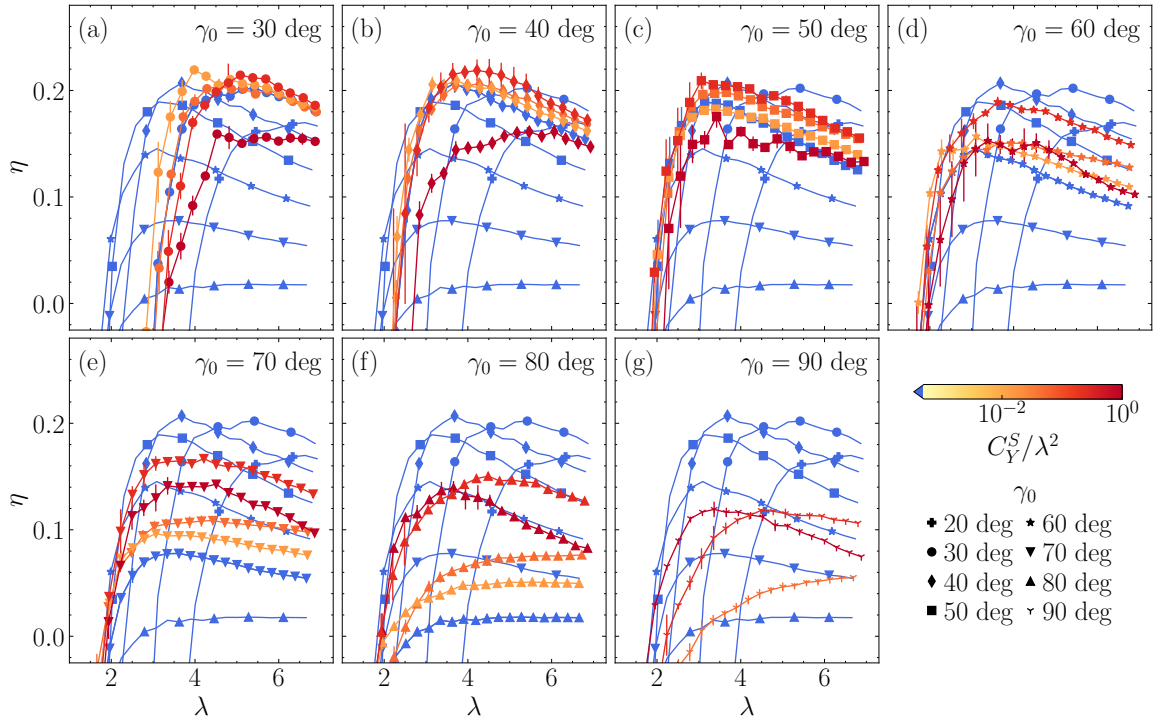

Figure 3.26: Efficiency as a function of the tip speed ratio. Colors indicate blade flexibility (blue) rigid, (yellow to red) increasingly flexible blades. Markers indicate pitch angle. Each panel corresponds to a single pitch angle from 30 to 90 deg. For reference, the efficiency of the rigid blades with every pitch angle is plotted on each panel.

Finally, we can compare how the efficiency curve of Fig. 3.24 is modified by changing the pitch angle. In Fig. 3.26, we plot the equivalent graph for all pitch angles tested. In each panel we plot

all the flexible curves with a particular pitch angle (yellow to red) and all the rigid curves in the background.

The benefits of using flexible blades are most visible at high pitch angle: when the efficiency associated with the rigid blades is extremely poor. The blade that most often achieves maximum efficiency is the P3 blade (light red markers), except for the largest pitch angle ($\gamma_0 \geq 80$ deg) where even more twist is required, and the most flexible P4 blades (dark red markers) are more efficient. For pitch angles of 30, 40, and 50 deg there are flexible blades which are more efficient than any rigid ones.

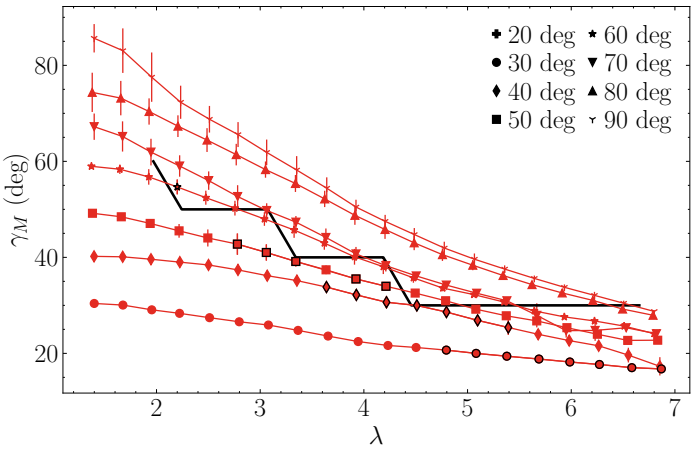

Figure 3.27: (red curves) Tip twist angle γ_M as a function of the tip speed ratio for several pitch angles (markers). Data obtained with the P3 blades. (blue curve) Pitch angle γ_0 which maximizes the efficiency of the rigid blades as a function of λ. Dark edge colors correspond to data points with an associated efficiency larger than any rigid propeller at the same tip speed ratio. The tip twist has been corrected by adding γ_{corr}.

In Fig. 3.27, we plot the tip twist for every pitch angle using the P3 blades. The black line corresponds to $\gamma_0^{\text{opt}}(\lambda)$ obtained experimentally. Using the P3 blades ($C_Y^S/\lambda^2 = 0.24$, red markers), the slope of the tip twist curve is similar to the one of the optimal pitch angle curve, indicating that they are well suited to improve the overall efficiency of the propeller. The data points with an efficiency larger than any rigid propeller have a dark edge color. The $\gamma_0 = 40$ deg (lozenges) curve is the most efficient in the range $3 < \lambda < 5.5$. The data points corresponding to high efficiency show that the tip twist should be slightly smaller than the optimal pitch angle for the rigid blades at a given λ. This result is due to the spanwise torsion of the blade. At high tip speed ratio λ all the P3 blades except from the one with $\gamma_0 = 20$ deg most likely have a too important curvature to be efficient.

3.2.3 Evolution of the twist angle

We have seen that knowing the tip twist is a good indicator to predict the efficiency of a flexible blade. Therefore, in the following we will focus on predicting its evolution with the three parameters of the problem (pitch angle γ_0, tip speed ratio λ, and Cauchy number C_Y^S).

We derive a law for small deformations by developing at the first order Eq. (3.36). The tip deformation $\varepsilon = \gamma_M - \gamma_0$ is small, and the angle of attack reads:

$$\alpha \approx \varepsilon + \alpha_0, \tag{3.39}$$

where $\alpha_0 = \gamma_0 - \arctan\cos\delta/\lambda$ is the angle of attack on the undeformed blade. We then develop the expression in the right hand side of Eq. (3.36):

$$C_L(\alpha)\cos\alpha \approx C_L(\alpha_0)\cos\alpha_0 + \varepsilon\left(-C_L(\alpha_0)\sin\alpha_0 + \frac{\partial C_L}{\partial\alpha}\Big|_{\alpha_0}\cos\alpha_0\right) \tag{3.40}$$

$$C_D(\alpha)\sin\alpha \approx C_D(\alpha_0)\sin\alpha_0 + \varepsilon\left(C_D(\alpha_0)\cos\alpha_0 + \frac{\partial C_D}{\partial\alpha}\Big|_{\alpha_0}\sin\alpha_0\right). \tag{3.41}$$

We therefore obtain the approximated law for the deformation ε:

$$\varepsilon = -C_Y^S u_p^2 \delta_{AC}^{LE}\left(C_N(\alpha_0) + \varepsilon\frac{\partial C_N}{\partial\alpha}\Big|_{\alpha_0}\right), \tag{3.42}$$

where $C_N(\alpha) = C_L(\alpha)\cos\alpha + C_D(\alpha)\sin\alpha$ is the normal force coefficient and

$$\frac{\partial C_N}{\partial\alpha}\Big|_{\alpha_0} = -C_L(\alpha_0)\sin\alpha_0 + \frac{\partial C_L}{\partial\alpha}\Big|_{\alpha_0}\cos\alpha_0 + C_D(\alpha_0)\cos\alpha_0 + \frac{\partial C_D}{\partial\alpha}\Big|_{\alpha_0}\sin\alpha_0. \tag{3.43}$$

Finally, we use $u_p^2 = 1 + \cos^2(\delta)/\lambda^2$ and obtain the following relationship for the small twist deformation:

$$\varepsilon = -\frac{C_Y^S\left(1+\cos^2(\delta)/\lambda^2\right)\delta_{AC}^{LE}\,C_N(\alpha_0)}{1 + C_Y^S\left(1+\cos^2(\delta)/\lambda^2\right)\delta_{AC}^{LE}\,\partial C_N/\partial\alpha|_{\alpha_0}} \equiv \varepsilon_1. \tag{3.44}$$

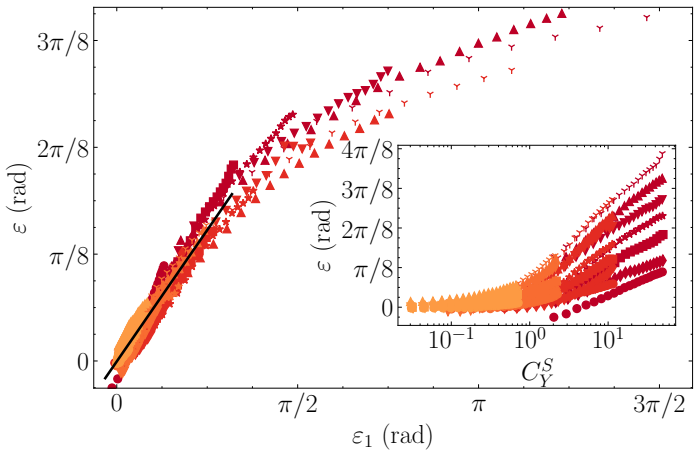

Figure 3.28: Twist deformation ε as a function of its first order linearized value ε_1. (Black line) Linear fit for the moderate deformations (< 30 deg) of slope 0.65. (Inset) Deformation as a function of the Cauchy number only. The tip twist has been corrected by adding γ_{corr}.

We use the flat plate lift and drag coefficients obtained in Sec. 1.2.2 to compute the first order linearized deformation ε_1. Using these functions, we verified that none the terms in Eq. (3.43) are negligible and that their total is of order one, meaning that first order development is required to capture the deformation of the blades. We plot the result in Fig. 3.28, and the deformation indeed follows a linear trend with its theoretical value for small deformations. The slope of this trend is 0.65 in radians, and it holds up to a deformation of about 40 deg. Beyond this value, for very flexible and high pitch blades, the slope decreases, but the data remains relatively collapsed. This scaling of the deformation is robust to changes of the exact coefficients used to compute the normal force C_N. We have used the ones fitted onto the lift and drag experiment in Sec. 1.2.2 but found that variations of 20% in these coefficients still collapses the data, although with a different slope.

The scatter of the data in the linear part is still relatively important (most of the points are within 5 degrees of the black line). Knowing the exact lift and drag coefficients (corrected for small Reynolds number or rotational effects) could help improve the accuracy of the formula. One other source may also be the uncertainty on the exact pitch angle manually set at the beginning of the experiment. Finally, taking into account the chordwise curvature may also improve the results, although significant curvatures are only obtained for large deformations.

3.3 Conclusion

In this chapter, we have introduced new bioinspired flexible propellers and studied their deformation and efficiency. The first part deals with the canonical problem of a fully flexible propeller with slender ribbon-like blades. This propeller exhibits extreme bending deformations towards the incoming flow as well as moderate twisting deformations. Under the assumption of small deformations, a scaling law based on geometric arguments allows us to predict the direction and estimate the amplitude of the bending. In the general case, we establish a strong relationship between the bending deformation and the thrust produced by the propeller: given a propeller geometry, the measurement of the deformation allows the deduction of the thrust.

This propeller presents an interesting fluid-structure interaction problem: the two directions of deformation are coupled by the hydrodynamic forces, and the loading is mainly due to the lift force instead of the drag. However, it is very inefficient. Using a combination of experiments and analytical results, we show that bending is always detrimental to the efficiency. Torsion can improve the efficiency of a given propeller by reducing the gap between the tip twist angle and the most efficient pitch angle. However, this occurs in a limited range of tip speed ratios, and we show that a rigid propeller with the optimal pitch angle $\gamma_0^{\text{opt}}(\lambda)$ will always be more efficient.

In a second part, we used propellers inspired from the works of Cognet et al. (2017, 2020) that are able to passively adapt to a change of external conditions. This propeller is flexible only in the chordwise direction, and the pivot point for its twist deformation is the leading edge. The difference between this problem and that of a flexible blade wind turbine is twofold: first, centrifugal force is always negligible in our problem, and therefore the material flexibility is the only adjustable property (its density is not relevant in this problem). Second, in order to remain as efficient as the best rigid blade over the entire range of tip speed ratios, the flexible wind turbine only needs to twist by 8 to 10 degrees. This is very different from the 40 degrees that the optimal flexible propeller must follow, which results in significant curvature effects that limit efficiency.

In experiments our best flexible blades can passively adjust to a change in tip speed ratio. In the range $3 < \lambda < 5.5$, we have found a pitch angle γ_0 and flexibility C_Y^S/λ^2 such that the flexible blades remain at least as efficient as the rigid ones following the optimal pitch angle $\gamma_0^{\text{opt}}(\lambda)$. This range corresponds to a 20 deg variation of $\gamma_0^{\text{opt}}(\lambda)$. We numerically found an even more efficient flexible propeller with a deformation that perfectly matches the spanwise variations of the local velocity. This solution is not accessible with the design used here because of the real blades have chordwise curvature and cannot match the extreme spanwise torsion required. One perspective of this work could therefore be to concentrate the flexibility near the leading edge, avoiding curvature effects and getting closer to the model of the torsion spring. Another possibility is to tune the chordwise flexibility along the span. This may allow the flexible blades to have a local angle of attack close to α_{opt} on all blade sections.

We used the tip twist angle as the unique information about the deformation of the blade. We show that comparing this tip twist angle to the optimal pitch angle $\gamma_0^{\text{opt}}(\lambda)$ in the rigid case, we can find

the most efficient pitch angle for the flexible blades. The tip twist follows a complex evolution with all the parameters (γ_0, C_Y^S, λ); using a linear development of the governing equation in the small deformation limit we are able to produce a law that collapses all the tip twist angle data. This law requires to know the airfoil characteristics used in the propeller (lift and drag versus angle of attack), but is not sensitive to exact parameters.

Finally, anticipating slightly onto the next chapter about intermittent locomotion, we will see that an important criterion is the drag of the propeller when not rotating. Because the propellers used in the second part are able to adapt to drastic modifications of external conditions, they might be suitable for this type of application. We measured the drag of the non-rotating propeller alone at various pitch angles with the rigid blades (Fig. 3.29) and as expected it reduces when the blades approach a flag configuration ($\gamma_0 = 90$ deg). A flexible blade would experience a similar drag as the deformation without rotation is small ($C_Y^S/\lambda^2 \ll C_Y^S$). Picking purposefully a very high pitch angle to minimize the drag while still maintaining a high efficiency might be a good strategy for intermittent locomotion. For instance, using the P3 blades with a pitch angle of 70 deg reduces the drag by 65% but retains 80% of the efficiency.

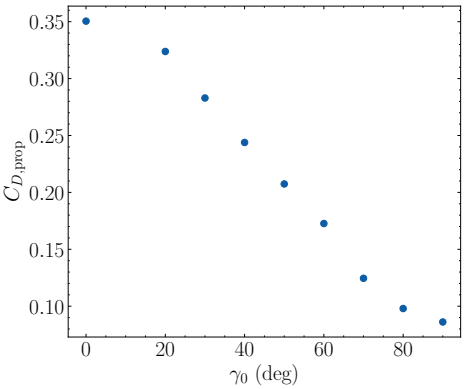

Figure 3.29: Drag coefficient of the rigid propeller as a function of the pitch angle. Obtained with $U_\infty = 0.15$ m/s.

Bibliography

ALBEN, S., SHELLEY, M., and ZHANG, J. (2002). Drag reduction through self-similar bending of a flexible body. *Nature*, vol. 420(6915):pp. 479–481 59

AUDOLY, B. and NEUKIRCH, S. (2021). A one-dimensional model for elastic ribbons: A little stretching makes a big difference. *Journal of the Mechanics and Physics of Solids*, vol. 153:p. 104457 42, 55

AUDOLY, B. and POMEAU, Y. (2010). *Elasticity and Geometry: From Hair Curls to the Non-linear Response of Shells*. Oxford University Press 42

COGNET, V. (2017). *Optimisation des éoliennes à axe horizontal par l'utilisation de pales flexibles*. Ph.D. thesis, Université Paris Cité 39, 61

COGNET, V., COURRECH DU PONT, S., DOBREV, I., MASSOUH, F., and THIRIA, B. (2017). Bioinspired turbine blades offer new perspectives for wind energy. *Proceedings of the Royal Society A: Mathematical, Physical and Engineering Sciences*, vol. 473(2198):p. 20160726 50, 60, 66, 72

COGNET, V., COURRECH DU PONT, S., and THIRIA, B. (2020). Material optimization of flexible blades for wind turbines. *Renewable Energy*, vol. 160:pp. 1373–1384 72

DUDA, R. O. and HART, P. E. (1972). Use of the Hough transformation to detect lines and curves in pictures. *Communications of the ACM*, vol. 15(1):pp. 11–15 61

DURÁN VENEGAS, E., LE DIZÈS, S., and ELOY, C. (2019). A strongly-coupled model for flexible rotors. *Journal of Fluids and Structures*, vol. 89:pp. 219–231 40, 41, 48

ELDEMERDASH, A. and LEWEKE, T. (2021a). Fluid–structure interaction of a flexible rotor in water. *Journal of Fluids and Structures*, vol. 103:p. 103259 40, 41, 45

ELDEMERDASH, A. S. and LEWEKE, T. (2021b). Deformation and wake of a flexible rotor in water. *Journal of Physics: Conference Series*, vol. 1934(1):p. 012006 48

GLAUERT, H. (1983). *The Elements of Aerofoil and Airscrew Theory*. Cambridge University Press 48, 55

GOSSELIN, F. P. and DE LANGRE, E. (2011). Drag reduction by reconfiguration of a poroelastic system. *Journal of Fluids and Structures*, vol. 27(7):pp. 1111–1123 48, 59

LI, H., GOODWILL, T., JANE WANG, Z., and RISTROPH, L. (2022). Centre of mass location, flight modes, stability and dynamic modelling of gliders. *Journal of Fluid Mechanics*, vol. 937:p. A6 61

MARZIN, T., LE HAY, K., DE LANGRE, E., and RAMANANARIVO, S. (2022). Flow-induced deformation of kirigami sheets. *Physical Review Fluids*, vol. 7(2):p. 023906 59

MASTERS, I., CHAPMAN, J. C., WILLIS, M. R., and ORME, J. A. C. (2011). A robust blade element momentum theory model for tidal stream turbines including tip and hub loss corrections. *Journal of Marine Engineering & Technology*, vol. 10(1):pp. 25–35 55

SCHOUVEILER, L. and BOUDAOUD, A. (2006). The rolling up of sheets in a steady flow. *Journal of Fluid Mechanics*, vol. 563:p. 71 59

SNEL, H., HOUWINK, R., and BOSSCHERS, J. (1994). Sectional prediction of lift coefficients on rotating wind turbine blades in stall. Tech. Rep., Netherlands: N. p. 55

SØRENSEN, J. N. (2011). Aerodynamic Aspects of Wind Energy Conversion. *Annual Review of Fluid Mechanics*, vol. 43(1):pp. 427–448 55

Chapter 4

Intermittent propulsion

In this chapter, we aim to build an experiment that applies the concept of burst and coast locomotion usually found in fish swimming to a new setting: propulsion with a classical boat propeller. The earlier studies (Weihs, 1974; Wu et al., 2007; Floryan et al., 2017a) have shown that the drag force experienced during the coasting phase of the motion is a key parameter of the problem. Fish experience up to four times less drag when gliding than when actively swimming. We mimic the passive drag reduction experienced by fish using a shape-changing propeller.

We will first describe the propellers used, and the mechanism of shape change in a static situation (the boat is fixed in the channel). We then measure the thrust and torque produced by this propeller in order to parametrize its behavior. We can then describe the complete setup of the intermittent locomotion experiment and data processing. Using cycle-averaged results, we demonstrate that efficient intermittent locomotion can be achieved with this shape-changing propeller. Finally, a model of the unsteady motion of the boat helps us find the conditions under which burst and coast locomotion is efficient.

4.1 Folding propeller

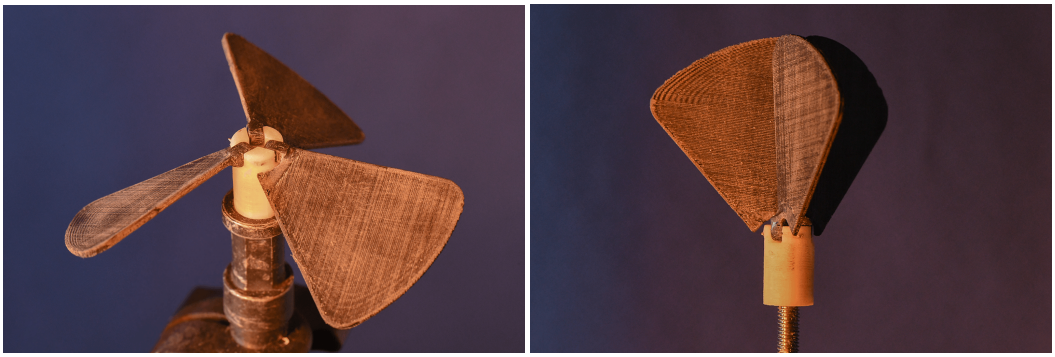

Figure 4.1: Folding propeller

The propeller used in the intermittent locomotion experiment has one main objective: to minimize its drag when not in use. Given the binary nature of the requirements — either functioning like a normal propeller or minimizing the drag without any regards for performance — an inelastic system is sufficient. Elasticity is used in the other propellers to set the amplitude of the response to a given loading. Here we want the propeller to start functioning normally as soon as a threshold in angular velocity is met.

We therefore use a propeller with rigid blades, mounted on hinges, allowing it to fold downstream. This propeller is completely passive: the blades react to any force applied on them by freely rotating around their pivot. This type of propeller is not completely new as commercial versions of this idea — with the blades either folding or feathering — are available[1]. These propellers are used to reduce the drag of sailing boats. These propellers are also used when designing missions where efficiency and range are the primary concerns: Chen et al. (2013) uses a similar design to build an underwater glider, retracting the propeller to increase glide efficiency in the descent. Yet to our knowledge no analysis of how these propellers open exist.

When idle, the flow pushes back on each blade, forcing it to fold along the central axis of the propeller and reducing its frontal area. When the propeller is spinning the blade experiences the centrifugal force, and the hydrodynamic lift and drag on the blade, both of which tend to open the blade as the angular velocity is increased. We will first measure and describe how this propeller opens and then parametrize its performance for use in the following section.

4.1.1 Setup and expected behavior

The folding propeller is composed of three flat, 3D printed blades. These blades have a maximum radius of $R = 45$ mm, a minimum radius of $R_{\text{hub}} = 6$ mm and a thickness of $e = 1.5$ mm. Because they need to produce enough thrust to overcome the boat's drag while remaining of a reasonable diameter, their shape is closer to marine propellers than the ones we used in the previous chapter. The chord increases linearly from 9 mm at the root and 44 mm at the tip. These blades are attached to a hinge, and are tilted to impose the pitch angle (Fig. 4.4). This hinge is attached to the hub and allows the blades to bend downstream but prevents them from extending upstream. When extended, the blades are perpendicular to the axis of rotation.

The boat is static in the channel, and we impose the incoming flow velocity U_∞. Then we increase the angular velocity, and for each value we record the shape of the propeller using a camera and measure the angle θ_e between the blades and the axis of rotation (defined by $\theta_e = 0$ deg when the blades are folded and $\theta_e = 90$ deg when fully extended, see Fig. 4.4). The tilt of the rotation axis with respect to the incoming flow introduces a small periodic variation of the angle θ_e over the course of one revolution. We always measure the opening angle when the blade crosses the symmetry axis of the setup (above the shaft) to negate the effect of the tilt. We repeated the experiments for three flow speeds (0.12, 0.15 an 0.18 m/s) and three pitch angles (15, 30 and 45 deg.). To identify any blade-blade interaction effects, we also repeated one experiment (30 deg, 0.18 m/s) with a single blade.

The expected behavior of such a propeller when the flow is increased is the following. When a blade is tilted with respect to the incoming flow by an angle θ_e, the velocity components on a blade section located at a radius r from the axis of rotation are modified. The flow velocity is decomposed in the spanwise direction and the component normal to the blade. Any spanwise force does not enter into the moment balance on the hinge, and we therefore neglect any contribution from this component. The remaining component, normal to the blade surface is $U_\infty \cos\delta \sin\theta_e$. Simultaneously, the distance to the axis of rotation is $r \sin\theta_e$ and thus the angular velocity is $r\Omega \sin\theta_e$. In particular,

[1] `https://gori-propeller.com/` or `https://www.darglow.co.uk/featherstream/`

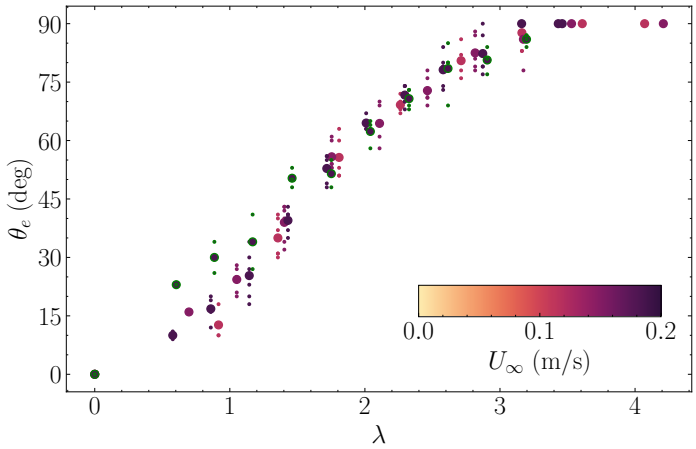

Figure 4.2: Opening angle θ_e as a function of the tip speed ratio for several mean speeds (color). (green edge color) Experiments with a single blade instead of three. Smaller dots correspond to individual realizations, larger ones to the mean.

we see that the local speed ratio $r\Omega/(U_\infty \cos\delta)$ (and therefore the angle of attack as well) remains the same whichever the opening angle θ_e.

The hydrodynamic moment on the hinge results from the integration of the lift and drag on each blade section. The remark above means that the hydrodynamic moment reads $M_{\text{hydro}}(\theta_e) = \sin^2\theta_e M_{\text{hydro}}(\theta_e = 90 \text{ deg})$. In particular its sign is fully dictated by the tip speed ratio $\lambda = R\Omega/U_\infty$ and does not depend on θ_e. Because our system is inelastic, and the centrifugal force is small, the equation setting the angle of the blades is $M_{\text{hydro}} = 0$. We therefore expect that the blades should be fully closed for low tip speed ratios (when $M_{\text{hydro}} < 0$) and switch to completely opened for higher λ.

Fig. 4.2 shows a very different behavior: the blades progressively open for $0 < \lambda < 3$. At a given tip speed ratio, the magnitude of the flow velocity does not change the opening angle θ_e. This discrepancy with the expected behavior is not a blade-blade interaction effect as even the propeller with a single blade (dots with green edge color) shows a similar behavior. We cannot see an angular velocity threshold at which the blades start to open because the motor we use cannot rotate slow enough.

The exact tip speed ratio obtained when self propelling depends on the relative proportions of the boat compared to the propeller. In our case it is always over 3.5. This propeller is therefore suitable for our original goal which was to have a rotor that changes shape between the active and passive phases. The mechanical properties (thrust, drag at rest or opened) of this rotor are parametrized in Sec. 4.1.3.

The following section proposes an explanation for the observation that the propeller opens progressively instead of switching between fully opened or fully closed states.

4.1.2 A geometrical coupling between the opening and pitch angles

The two forces that act on the blade are the hydrodynamic force and the centrifugal force. The ratio between them reads:

$$\frac{F_{\text{centrifuge}}}{F_{\text{hydro}}} \sim \frac{\rho_b Rce R\Omega^2}{\rho Rc\left((R\Omega)^2 + U_\infty^2 \cos^2\delta\right)} \sim \frac{\rho_b}{\rho}\frac{e}{R}\frac{1}{1+\cos^2\delta/\lambda^2} \approx 10^{-2}. \tag{4.1}$$

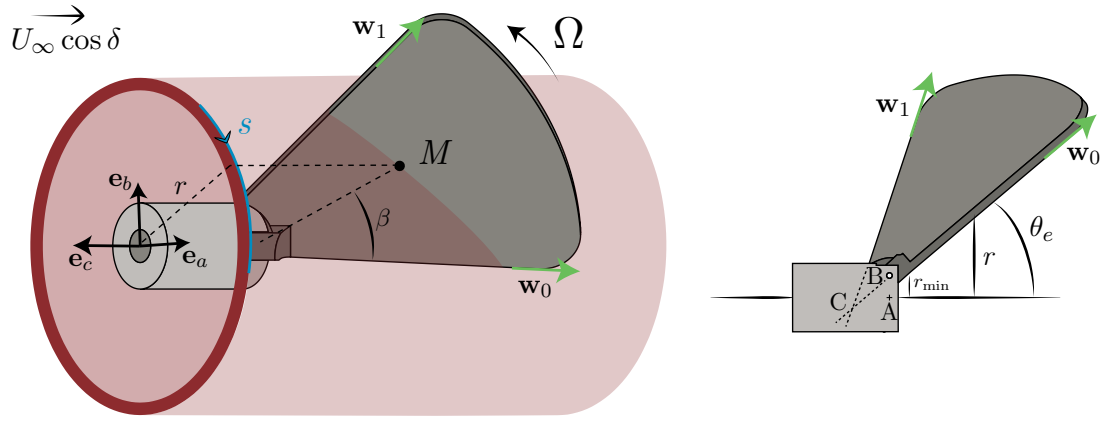

Figure 4.3: Schematic of the decomposition in ring elements.

Where ρ and ρ_b are the densities of the fluid and the blade respectively, c is the typical chord and e the thickness. This ratio is always small in our case, and as a result, we will neglect the centrifugal force in the following. This result can also be obtained from observing that the opening angle only depends on the pitch angle: if the centrifugal force played a role, the force balance would differ when changing the flow velocity.

The expected behavior that we previously derived is based on the analysis in section 1.2, where we separated the incoming flow into concentric rings that interact with a blade section but do not influence each other. When the blades are thin and perpendicular to the flow (as in the previous sections), this division is equivalent to discretizing the span of the blade. Here, however, because the blades are tilted and occupy a significant angular sector (about half of the frontal area is filled by the blades), this is not the case. As can be seen in Fig. 4.3, a given flow tube cuts the blade at an angle. This cut has a non-trivial shape which depends on the opening angle and the spanwise position, and results in a modified effective pitch angle and chord length.

In the following, we assume that the flow is arranged in concentric cylinders that do not interact with each other. The goal of the following calculations is to compute the shape of the intersection of each cylinder with the blade at a given opening angle θ_e. In particular, we want to obtain the effective pitch angle and chord length to derive the hydrodynamic moment on the hinge in a second part. The mathematical modeling is inspired from the works of Marzin et al. (2022) on origami folding: we parametrize the position of the blade by two vectors $\mathbf{w}_0$ and $\mathbf{w}_1$, attached respectively to the trailing and leading edges of the blade (green arrows in Fig. 4.3).

The axis $\mathbf{e}_a$ is defined such that when the blade is fully extended, $\mathbf{w}_0 = \mathbf{e}_a$. In the general case the blade is rotated about $\mathbf{e}_b$ by an angle $\frac{\pi}{2} - \theta_e$ such that

$$\mathbf{w}_0(\theta_e) = \sin\theta_e \mathbf{e}_a - \cos\theta_e \mathbf{e}_c. \tag{4.2}$$

The second base vector is obtained when fully extended by rotating first the vector $\mathbf{e}_c$ by the pitch angle γ_0 around $\mathbf{e}_a$ and then rotating $\mathbf{e}_a$ around the new $\mathbf{e}_c$ direction:

$$\mathbf{w}_1(\theta_e = \frac{\pi}{2}) = \cos\beta_{\text{max}}\mathbf{e}_a + \sin\beta_{\text{max}}\left(\cos\gamma_0\mathbf{e}_b - \sin\gamma_0\mathbf{e}_c\right), \tag{4.3}$$

where β_{max} is the angle between $\mathbf{w}_0$ and $\mathbf{w}_1$ (57 deg here). The general case is obtained by multiplying

the above result by the rotation matrix of angle $\frac{\pi}{2} - \theta_e$ around $\mathbf{e}_b$ and we obtain:

$$\mathbf{w}_1(\theta_e) = \begin{pmatrix} \cos\beta_{\text{max}} \sin\theta_e + \cos\theta_e \sin\gamma_0 \sin\beta_{\text{max}} \\ \sin\beta_{\text{max}} \sin\gamma_0 \\ -\cos\theta_e \cos\beta_{\text{max}} + \sin\theta_e \sin\gamma_0 \sin\beta_{\text{max}} \end{pmatrix}_{(\mathbf{e}_a, \mathbf{e}_b, \mathbf{e}_c)} \tag{4.4}$$

Let M be a point on the blade, C the point where the (virtual) leading and trailing edges meet, B the intersection of the trailing edge and the hinge and A an arbitrary fixed point on the axis of rotation (see Fig. 4.3 right). The vector $\mathbf{CM}$ reads

$$\mathbf{CM} = A_0 \mathbf{w}_0 + A_1 \mathbf{w}_1 \tag{4.5}$$

with A_0 and A_1 two constants. We parametrize the blades using the angle β between $\mathbf{CM}$ and $\mathbf{w}_0$ and the distance r from M to the axis of rotation. By imposing r, we ensure that we compute the shape of the blade at a constant radius i.e., the intersection with a cylinder. The point M verifies:

$$\mathbf{CM} \cdot \mathbf{w}_0 = \|\mathbf{CM}\| \cos\beta \tag{4.6}$$

$$(\mathbf{AM} \cdot \mathbf{e}_a)^2 + (\mathbf{AM} \cdot \mathbf{e}_b)^2 = r^2 \tag{4.7}$$

$$\|\mathbf{BM}\| \leq R - r_{\text{min}}. \tag{4.8}$$

The first equation gives a relationship between A_0 and A_1:

$$(A_0 + A_1 \cos\beta_{\text{max}})^2 = \left(A_0^2 + A_0 A_1 \cos\beta_{\text{max}} + A_1^2\right) \cos^2\beta, \tag{4.9}$$

which simplifies into:

$$A_0 = A_1 \left(-\cos\beta_{\text{max}} + \frac{\sin\beta_{\text{max}}}{\tan\beta}\right). \tag{4.10}$$

The second equation closes the system:

$$\begin{aligned}(\mathbf{AB} \cdot \mathbf{e}_a + (A_0 - \|\mathbf{BC}\|) \sin\theta_e + A_1 (\cos\beta_{\text{max}} \sin\theta_e + \cos\theta_e \sin\gamma_0 \sin\beta_{\text{max}}))^2 \\ + (A_1 \sin\beta_{\text{max}} \cos\gamma_0)^2 = r^2.\end{aligned} \tag{4.11}$$

By replacing A_0 we can solve analytically the system and get the shape of the intersection between the blade and a cylinder. The third equation ensures that the radius of the blade is never exceeded.

Fig. 4.4 shows examples of the shapes generated by this method. We can see that both the chord length and pitch angle are modified by the angle θ_e. Panel (b) shows the local angle with the horizontal:

$$\gamma(s, \theta_e, r) = \arctan \frac{\partial \mathbf{CM} \cdot \mathbf{e}_c}{\partial s}, \tag{4.12}$$

where $s = r\beta$ is the curvilinear abscissa along a cut. We can see that as the opening angle θ_e decreases, the mean pitch angle of the blade increases from the prescribed 30 degrees up to almost 90 degrees when the blades are completely folded.

In the following we model the complex shapes obtained previously by an effective chord and pitch angle that depend on the radial position r and the opening angle θ_e:

$$c(\theta_e, r) = \int_0^{\beta_{\text{max}}} \left\| \frac{\partial \mathbf{CM}}{\partial \beta} \right\| \mathrm{d}\beta \tag{4.13}$$

$$\gamma(\theta_e, r) = \underset{0 \leq s \leq s_{\text{max}}}{\text{mean}} \ \gamma(s, \theta_e, r) \tag{4.14}$$

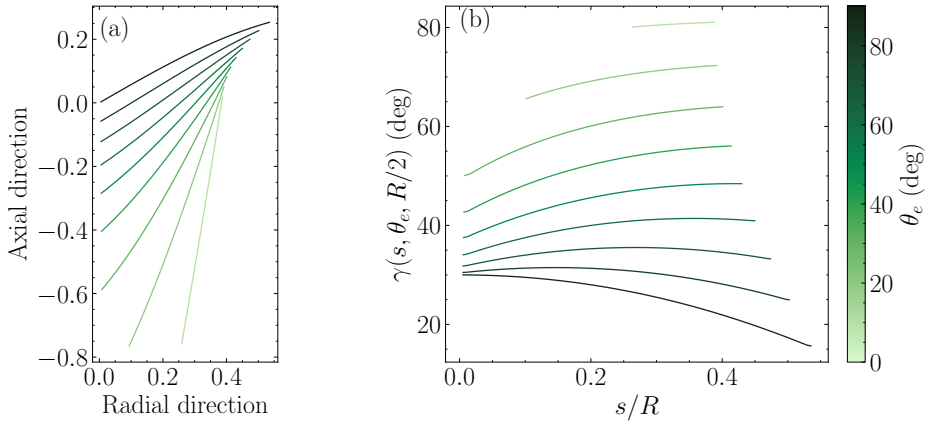

Figure 4.4: Geometry of the intersection between a ring and the blade for different opening angles (shades of green). Computed at $r = R/2$. (a) height as a function of the curvilinear abscissa (b) local angle with respect to the horizontal (defined in Eq. (4.12))

We can now compute the local lift and drag contributions. The local velocity on a blade cut has a vertical component $U_\infty \cos\delta$ and horizontal component $r\Omega$ (see Fig. 4.3). We can define the local angle of attack:

$$\alpha = \gamma(\theta_e, r) - \varphi(U_\infty, \Omega), \tag{4.15}$$

where $\varphi = \arctan U_\infty \cos\delta/(r\Omega)$.

The local velocity and angle of attack create local lift and drag forces (respectively $\mathrm{d}L$ and $\mathrm{d}D$), which in turn create a moment on the hinge with a moment arm $(r - r_{\min})/\sin\theta_e$:

$$M_{\text{hydro}} = \int_{r_{\min}}^{R} \frac{r - r_{\min}}{\sin\theta_e} \left(\mathrm{d}L\cos\varphi - \mathrm{d}D\sin\varphi\right). \tag{4.16}$$

We write the infinitesimal lift and drag forces in terms of lift and drag coefficients and obtain:

$$M_{\text{hydro}} = \int_{r_{\min}}^{R} \frac{1}{2}\rho c(\theta_e, r)\frac{r - r_{\min}}{\sin\theta_e}\left((U_\infty\cos\delta)^2 + (r\Omega)^2\right)\left(C_L(\alpha)\cos\varphi - C_D(\alpha)\sin\varphi\right)\mathrm{d}r. \tag{4.17}$$

Fig. 4.5 the experimental data and the integration from the model for three different pitch angles (colors) and three different flow velocities (markers). For all three pitch angles, the model captures with reasonable accuracy the progressive opening of the blades as a function of the tip speed ratio. The smaller the pitch angle, the higher the tip speed ratio required to extend the blades. It should be noted that the particular behavior of these propellers is a consequence of the fact that we placed the hinge at the trailing edge of the blade. Placing it at the leading edge would modify how they open, but most importantly would prevent the propeller from closing completely because the blades would obstruct each other.

The model always overestimates the forces and thus the opening angle of the propeller. This discrepancy might be due to the shape of the intersections shown in Fig. 4.4 being curved and therefore modifying the sectional lift and drag coefficients. Alternatively, the flow curvature might also modify the force balance. The blades occupy a large angular sector and therefore the lift and drag measured in a flat 2D setting might not apply directly here due to the curvature of the intersection between the cylinders and the blades. Semi-empirical correction for flow curvature effects in blade element model exist (Corrigan and Schillings, 1994), but we did not implement them.

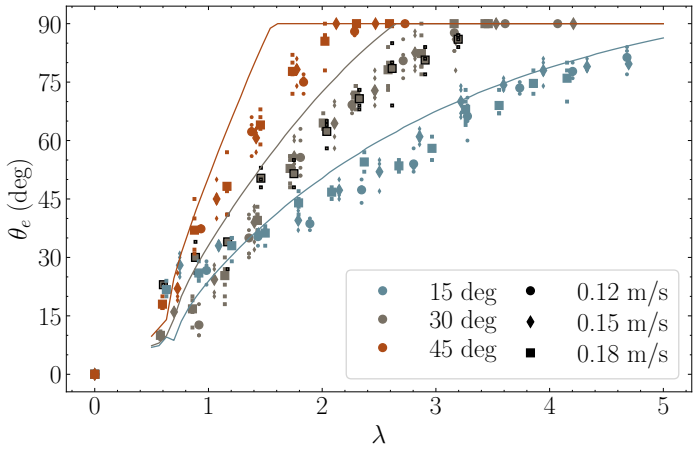

Figure 4.5: Opening angle as a function of the tip speed ratio. Color indicates pitch angle. Markers differentiate flow speed. Dark edge color shows experiments ran with one blade instead of three. The lines are from the blade element model described above.

We have found a numerical model that predicts the opening behavior of a foldable propeller. The coupling between the opening angle and the effective pitch angle (due to the large angular extent of the blades) makes them progressively open instead of all at once when reaching a threshold. The pitch angle is essentially 90 deg when the propeller is folded and progressively decreases back to its prescribed value when the blades open.

4.1.3 A parametrization of the folding propeller

In the next section, we will build a model of the unsteady motion dynamics. It requires information about the boat and propeller system such as drag, thrust, or torque. Therefore, in this section we make preliminary measurements of these quantities and parametrize their evolution to include them in the model. We use the bio-inspired propeller described in the previous section, which is able to change shape between the active and passive phases, thus mimicking the drag reduction observed in fish. For comparison, we also use a rigid propeller that has the same shape as the folding propeller when extended.

Thrust and torque

We evaluate the performance of both propellers by holding the boat in a fixed position with a traction/compression force sensor, thus measuring the axial force F_a: the sum of drag and thrust. Unlike all the propeller performance curves presented previously, we do not remove the boat's hull drag here. Indeed, we will be interested in the force balance when the boat is free to move, and therefore we need to take the hull drag into account. We define an axial force coefficient C_a in a similar manner as for the thrust:

$$C_a = \frac{F_a}{1/2\rho\pi R^2(R\Omega)^2} \tag{4.18}$$

The axial force and torque coefficients, are plotted in Fig. 4.6 as a function of the tip speed ratio, for the rigid and folding propeller, as well as a typical propeller curve extracted from Boswell (1971) (the exact propeller used has the reference 4381). For the latter, we have added the hull drag, such that

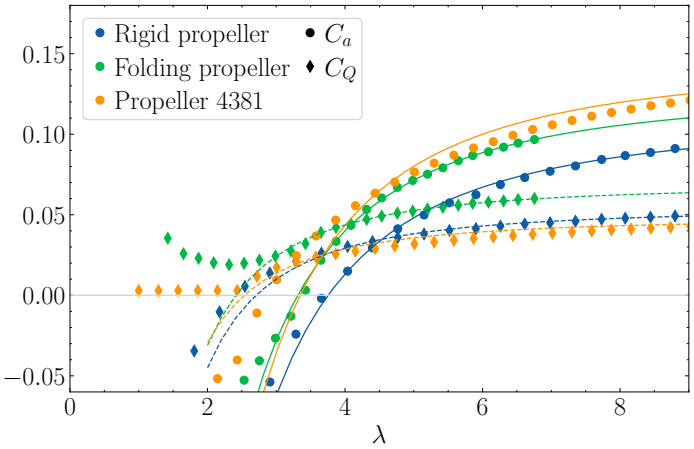

Figure 4.6: (•) Axial force C_a and (⧫) torque C_Q coefficients as a function of the tip speed ratio λ for several propellers. (green) Folding, (blue) rigid, and (orange) propeller 4381 from Boswell (1971). The full lines are the fits the axial force and the dashed those of the torque coefficient, using Eq. 4.19 and 4.20. Experiments with $U_\infty = 0.15$ m/s.

the curves are comparable. We see that all propellers follow the same general trend, although the propeller from the literature is obviously much more efficient (lower torque and higher thrust) than the very simple propellers we use. There is a discrepancy between the folding and rigid propellers, even though they should have the same shape when $\lambda > 3.5$ and the folding propeller is fully opened. Because the folding propeller produces a higher thrust associated with an increased torque, we interpret this fact as the result of the play in the hinges connecting the blades to the hub. This play allows the folding propeller to passively increase its pitch angle like the fully flexible propeller of Sec. 3.1. This discrepancy will not impact the results of this section as we are interested in the comparison with continuous motion for both propellers separately.

We parametrize the evolution of these coefficients with the tip speed ratio to model the unsteady dynamics of the boat. We are interested in the range $4 < \lambda < 8$ because it is the one explored in the experiments. The axial force can be divided into two components: the drag and the thrust. Our goal is to separate these two contributions by fitting the data in Fig. 4.6. The drag scales with the flow velocity squared and is negative, while the thrust scales with $(R\Omega)^2$ and is positive. By assuming that the coefficients of proportionality in both these scalings are constants (of λ and U_∞) we can write the axial force coefficient as:

$$C_a = a_T + \frac{c_T}{\lambda^2}, \tag{4.19}$$

where a_T and c_T are two fitting parameters, representing the thrust and drag respectively. The coefficient c_T represents the drag of the hull and of the rotating propeller (which may be different from the one of the non-rotating propeller). Similar separations have to be made in the case of fish swimming where the motion of the tail both produces thrust and increases the drag (Wu et al., 2007; Floryan et al., 2017a; Akoz and Moored, 2018).

Similarly, we model the torque as the sum of two contributions First, the incoming flow creates a torque that would spin the propeller is it was not attached — like a wind turbine — scaling as U_∞^2 and negative. Second the resistive torque due to the rotation of the propeller, positive and scaling as $(R\Omega)^2$. We thus also have:

$$C_Q = a_Q + \frac{c_Q}{\lambda^2} \tag{4.20}$$

with a_Q and c_Q two more fitting parameters. It should be noted that with the definitions above a_T

and a_Q are positive, while c_T and c_Q are negative. We fit these coefficients to the curves in Fig. 4.6 (lines). This simple model describes well the evolution of both coefficients for $\lambda > 3.5$ which is the regime which we are interested in. We sum up the exact values of the fitting coefficients in Table 4.1.

Propeller	a_T	c_T	a_Q	c_Q
Rigid	+0.1111	-1.6065	+0.0545	-0.4196
Folding	+0.1268	-1.3777	+0.0689	-0.4082
4381	+0.1452	-1.6259	+0.0492	-0.4066

Table 4.1: Fitting coefficients for the thrust and torque, for all propellers tested

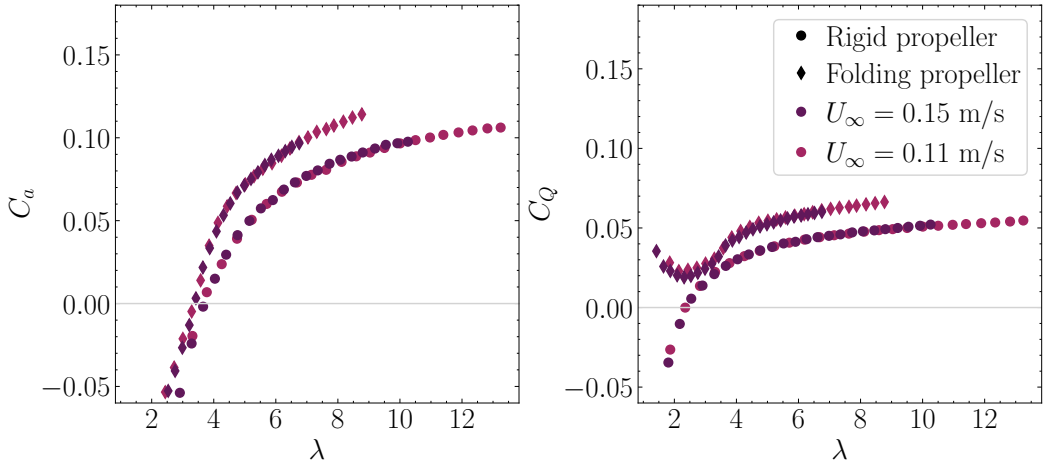

Figure 4.7: (left) Thrust and (right) torque coefficients for two different mean speeds, for both propellers.

In the intermittent locomotion experiment, the effective flow speed is constantly changing due to the acceleration of the boat. We thus repeated the force sensing experiment for another mean flow speed (0.11 m/s compared with 0.15 m/s previously). We show the result in Fig. 4.7 and we can see that once made dimensionless according to 1.10 and as a function of the tip speed ratio, both C_a and C_Q are independent of the flow speed (i.e., of the Reynold number). This means that the fitting coefficients found in Tab. 4.1 are indeed independent of the flow speed.

Drag

Finally, we also measured the drag of the boat in various configurations while the propeller is not spinning, representing the coasting phase. For several flow velocities we measured the drag of the boat without any propeller attached and with the rigid or folding propeller — which in this case is completely folded. We also measured the drag associated with using the rigid propeller, but letting it spin freely. To do so, we disconnect it from the motor because of the gearbox which prevents it from rotating if we keep it engaged.

We plot the drag coefficient $C_D = D/(1/2\rho S_{\text{boat}} U_\infty^2)$ in Fig. 4.8. For all configurations except for the disengaged propeller, the drag coefficient can be considered constant in our range of interest ($0.1\,\text{m/s} < U_\infty < 0.2\,\text{m/s}$). The presence of the rigid propeller add a substantial drag to the system, and therefore using the folding propeller is very interesting because it creates an important

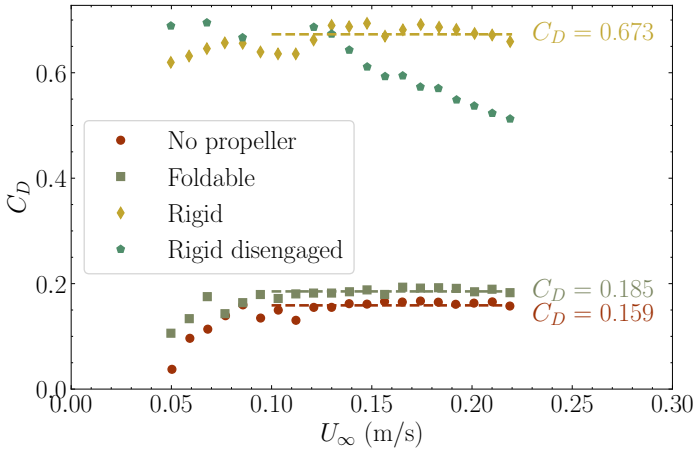

Figure 4.8: Drag coefficient as a function of the mean flow speed. The text corresponds to the value averaged for large mean velocities ($U_\infty > 0.1$ m/s).

drag contrast between active and passive phases. The drag in the active phase is computed using $C_{D,\text{Burst}} = -c_T S_{\text{boat}}/\pi R^2$ and the drag in the passive phase is the one directly measured in Fig. 4.8. This results in a drag contrast $C_{D,\text{Burst}}/C_{D,\text{Coast}}$ of about 0.2 for the folding propeller, similar to the ones encountered in fish swimming (Weihs, 1974; Wu et al., 2007). Using this model, we also find that the drag coefficient of the rigid propeller is increased when it is spinning. This results in a moderate drag contrast of about 0.65.

Freely spinning propeller Interestingly, letting the propeller spin due to the hydrodynamic torque applied by the flow reduces the drag compared to forcing it to stop, but does not result in a constant drag coefficient. A simple explanation for this phenomenon is that the torque generated by the flow tends to make the blades align with the relative flow they encounter. If the angle of attack on a particular section of the blade is positive, the torque slows the propeller, decreasing the angle of attack and if it is negative the propeller speeds up. Having the blades near zero angle of attack is then associated with a reduced axial force. The details are obviously more complex due to the different angle of attack at different spanwise positions, but the net effect is to reduce the drag. We do not explore this effect further but, instead of using folding propellers like we do in the following, one could instead use a clutch to disengage the propeller in the coast phase.

4.2 Intermittent locomotion experiment

4.2.1 Setup

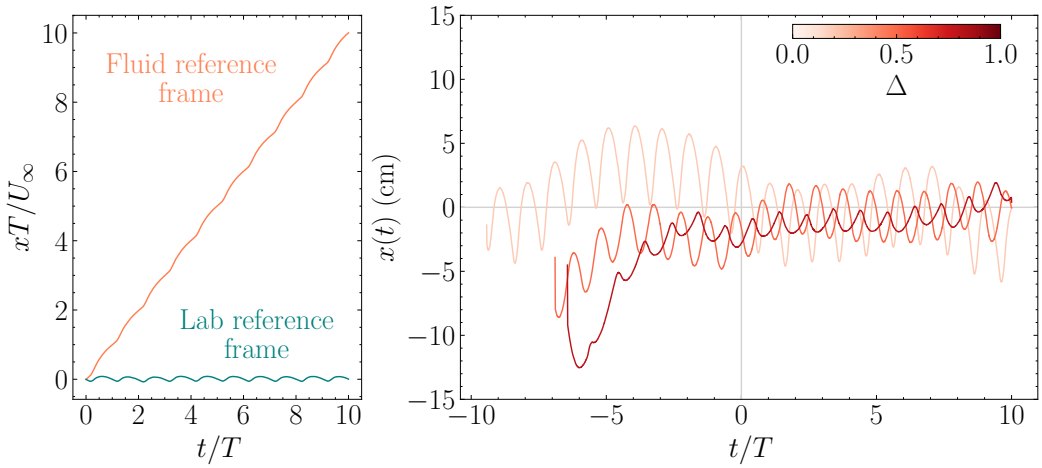

Figure 4.9: (Left) Position of the boat in the open water case (or in the fluid reference frame) (pink) and in the lab reference frame (cyan). Position is made dimensionless by the distance traveled during one cycle. Experimental signals obtained with the rigid propeller, $U_\infty = 0.18$ m/s, $T = 10$ s and $\Delta = 0.2$. (Right) Examples of trajectories in the Lab reference frame for different duty cycles (from white to red: 0.2, 0.5, and 0.8). Curves obtained with the rigid propeller, with $U_\infty = 0.11$ m/s and $T = 5$ s. The instant $t/T = 0$ corresponds to the moment from which we consider the boat to be stationary on average.

The experiments we perform aim to reproduce the problem of a boat in open water cruising at an average velocity U_∞ while using a burst and coast strategy. Because we are limited by the length of the channel, we change the frame of reference of the study to one that moves at the mean velocity of the boat (hereafter referred to as "lab frame"). This change of frame of reference transforms the accelerated and decelerated motion (while always moving forward) into a back and forth motion of finite amplitude in our channel (see Fig. 4.9 (left)). This transformation is a Galilean change of frame of reference: one is moving with a constant velocity U_∞ with respect to the other. As a result, the dynamics of the problem is unchanged.

The propeller is cyclically switched on and off, and we call the duty cycle (Δ) the ratio of the time spent in the active phase to the period T. During the active phase, the propeller rotates at a fixed angular velocity Ω. We release the boat from any position close to the center and let it evolve freely. An experiment is considered successful if the average position of the boat during ten consecutive cycles remains less than 2 cm away from the center of the channel (Fig. 4.9 (right) shows examples of successful experiments for different duty cycles). If it is not the case, we adjust the angular velocity until we reach an equilibrium. Once we have successfully performed one experiment, we can change the duty cycle or the flow velocity and repeat the process. In practice, we saw that the tube providing pressurized air to the linear bearing carriage helps the boat stay just in front or behind the center (discussed in Sec 2.2.3). We therefore tried to have a mean position as close to the center as possible. We repeated several runs for the same parameters and found on average a fluctuation of about 1% of the angular velocity and 3.5% for the average power during a cycle.

We chose the periods such that the boat does not lose a significant portion of its momentum during

the coast phase (corresponding to $U(t) = -U_\infty$ in our case). This time can be found by balancing the inertia of the boat with the dissipation due to drag:

$$m^* \frac{U_\infty}{(1-\Delta)t_{\max}} \sim \frac{1}{2}\rho S_{\text{boat}} U_\infty^2. \tag{4.21}$$

We find for the maximum period

$$t_{\max} \sim \frac{m^*}{1/2\rho S_{\text{boat}} U_\infty}, \tag{4.22}$$

where m^* takes into account the total mass of the system and the added mass due to the acceleration of the surrounding fluid. The typical order of magnitude of $t_{\max}$ in experiments is 10 s. We indeed find for the smallest duty cycle and for the rigid propeller that a substantial amount of the boat inertia has been dissipated in the coast phase. In practice, this limit corresponds to the boat moving at the same velocity as the fluid, and thus having very important position fluctuations in the channel, making reaching a stationary equilibrium more difficult.

A special case is the one of continuous motion, where we manually look for the right angular velocity such that, when releasing the boat right in the middle of the channel, it stays in position for about 30 s. In practice a small drift is always visible, and we repeated this process several times to ensure finding the right value.

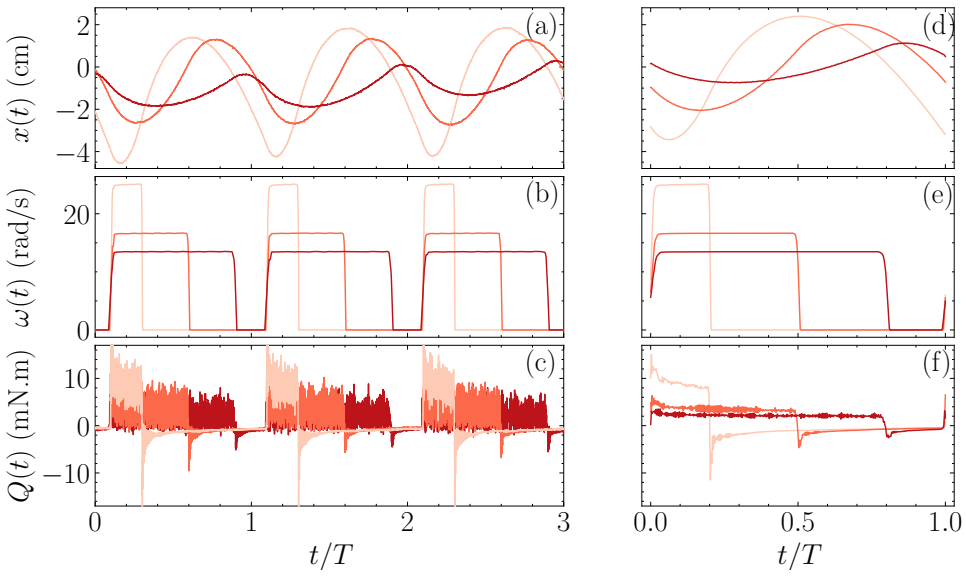

Figure 4.10: (a) to (c), Raw signals of position, angular velocity and torque, measured with the rigid propeller, $U_\infty = 0.11$ m/s and $T = 5$ s. Panels (d) to (e) show their phase averaged counterparts. Colors identify the duty cycle: from white to red 0.2, 0.5, and 0.8.

In Fig. 4.10 we show the instantaneous signals of position $x(t)$, angular velocity $\omega(t)$ ($\omega(t) = \Omega$ in the burst phase and 0 in the coast phase), and torque $Q(t)$ (frames (a) to (c), respectively). These signals are from successful experiments as the mean position stays close to $x = 0$. The boat starts each burst with backwards momentum and needs to end it with enough forwards momentum to keep a stationary position. The associated instantaneous torque is very noisy, and so we perform a phase averaging operation on the 10 periods that we measure to reduce the noise. By precisely detecting the beginning of each period, we are able to match each instant of one period with all the corresponding ones in the other repetitions. This phase average operation results in a drastic

reduction of the noise. We plot the result of this operation on panels (d) to (f). We can now see that the torque starts with an initially high value and decreases throughout the cycle. Some of this effect may be due to the rotational inertia of the propeller and surrounding water.

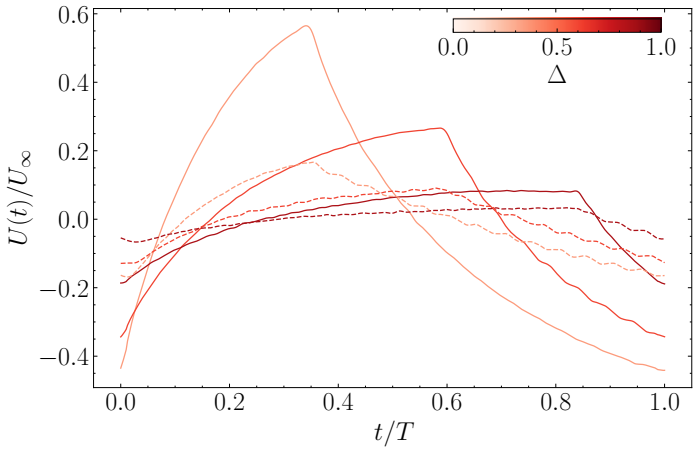

Figure 4.11: Instantaneous boat speed in the lab reference frame for the rigid propeller (solid line) and for the folding propeller (dashed line). Colors identify the duty cycle: from white to red 0.35, 0.6, and 0.85. Curves obtained with $U_\infty = 0.18$ m/s and $T = 10$ s.

From the position signal that we record, we are able to deduce the instantaneous velocity of the boat in the lab reference frame $U(t)$ by using a robust differentiation method (Savitzky and Golay, 1964). In Fig. 4.11, we show the result of this operation for both types of propeller. The amplitude of the velocity variations is much more important for the rigid propeller than for the folding one. Indeed, the drag being reduced on the boat during the coast phase means that there is less of a need to accelerate in the burst phase. This is one of the key aspects of efficient burst and coast locomotion as we will see in the following section. Similarly, for smaller duty cycles, the variations get increasingly important.

The parameter which we want to compute to assess the efficiency of burst and coast locomotion is the power requirement of each propulsion style. In our case it is the mechanical power $P(t) = Q(t)\omega(t)$. We plot this power in Fig. 4.12 panel (a), relative to the typical power dissipated when moving through a fluid at a velocity U_∞. This power comes from the product of drag scaling like $1/2\rho S_{\text{boat}} U_\infty^2$ and the mean velocity U_∞ such that:

$$P_0 = \frac{1}{2}\rho S_{\text{boat}} U_\infty^3. \tag{4.23}$$

Both the instantaneous torque and angular velocity increase in the burst phase when reducing the duty cycle, resulting in an almost five-fold multiplication of the instantaneous power requirement for $\Delta = 0.25$. However, whether a cycle is efficient requires comparing the energy expended per cycle and this discussion is the topic of the following section.

Other parameters of interest can be obtained from the experiment such as the instantaneous tip speed ratio $\lambda(t) = R\omega(t)/(U_\infty + U(t))$ (Fig. 4.12 panel (b)). At the beginning of the burst phase, the total velocity is small, and thus the tip speed ratio is high and decreases during the active phase as the boat accelerates. At constant angular velocity, the torque is a growing function of λ (See Sec. 1.2). The decreasing trend in the torque seen in Fig. 4.10 therefore might be explained by the evolution of $\lambda(t)$.

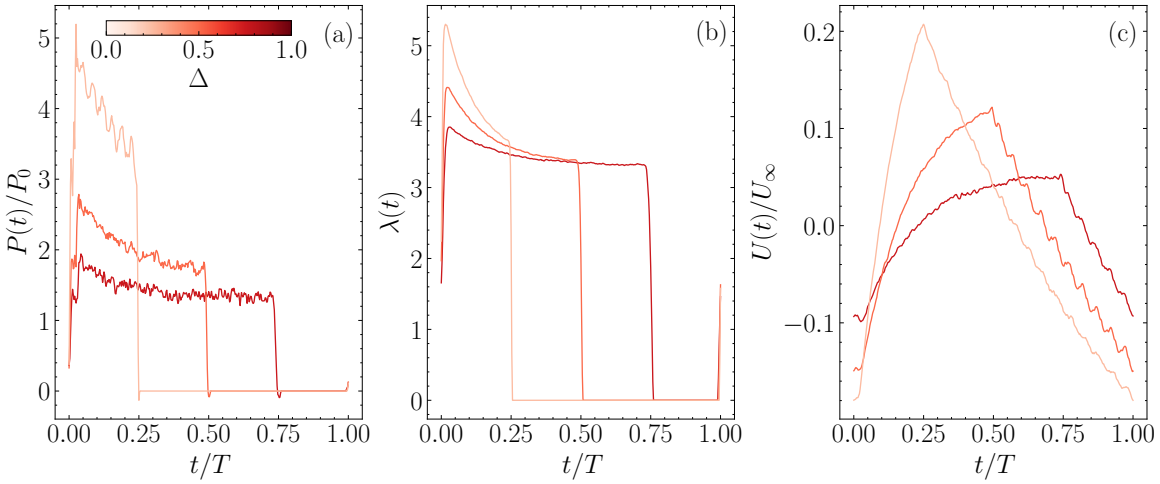

Figure 4.12: Instantaneous examples of (a) the dimensionless power, (b) tip speed ratio and (c) boat velocity. The characteristic power is $P_0 = 1/2\rho S_{\text{boat}} U_\infty^3$. Curves obtained with the folding propeller, $U_\infty = 0.18$ m/s and $T = 10$ s. Colors identify the duty cycle: from white to red 0.25, 0.5, and 0.75.

4.2.2 Cycle-averaged results

While the phase averaged signals of the previous sections give insights into the physical mechanisms at play in the problem, comparing intermittent and continuous locomotion requires quantities representing the whole cycle.

The force balance sets the angular velocity

The first quantity of interest is the angular velocity during the burst phase Ω (Fig. 4.13). It increases when decreasing the duty cycle: staying at a given mean velocity implies that drag during the whole cycle can be approximated as being the same for all duty cycles. Therefore, the total thrust required to counteract the drag is also similar, but needs to be generated within shorter time intervals ($\Delta \times T$) as the duty cycle decreases. As a result, the instantaneous thrust during the burst phase — and the angular velocity needed to produce it — increase with decreasing duty cycle. Another striking result is visible in Fig. 4.13: the period of the motion has no influence on the angular velocity, except for the shortest period at the lowest speed (light blue dots on panel (a)). Changing the mean velocity shifts all the curves globally: the tip speed ratio $\lambda = R\Omega/U_\infty$ of continuous motion is a constant. This result is derived from the propeller parametrization from the previous section: during continuous locomotion the only force acting on the boat is the axial force (the sum of the thrust and drag). From Eq. 4.19, we obtain the tip speed ratio for continuous motion:

$$\lambda_c = \sqrt{-\frac{c_T}{a_T}}. \tag{4.24}$$

We can then build a scaling law for the angular velocity dependence on the duty cycle. The typical scaling of the thrust produced by a rotor is

$$F_{\text{thrust}}(t) \sim \frac{1}{2}\rho\pi R^2 (R\omega(t))^2, \tag{4.25}$$

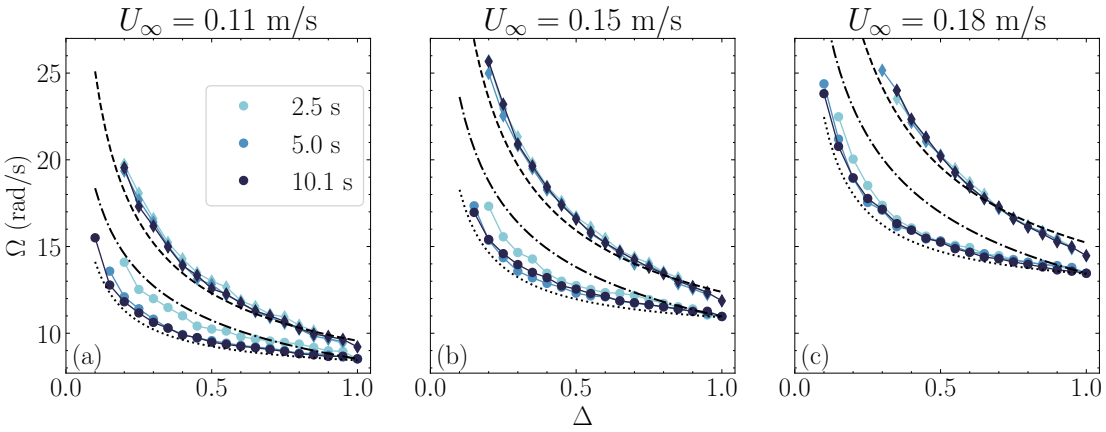

Figure 4.13: Angular velocity in the burst phase as a function of the duty cycle for three different periods and flow speeds. (♦) Rigid propeller, (•) folding propeller. (dashed line) scaling from Eq. (4.28) (using the rigid propeller parametrization). (dot dashed line) scaling $\Omega \sim \Delta^{-1/3}$ with the angular velocity of the continuous motion (folding propeller) as a reference value. (dotted line) scaling from Eq. (4.28) (using the folding propeller parametrization). Panels correspond to different mean velocities.

while the drag on the whole boat scales as:

$$D \sim \frac{1}{2}\rho S_{\text{boat}}(U_\infty + U(t))^2. \tag{4.26}$$

The balance of the forces on the boat during one cycle is $\langle F_x \rangle = \langle D \rangle$, where $\langle \cdot \rangle$ denotes the average over a cycle. The period of the motion does not affect the angular velocity required and therefore the force balance. As a consequence, we assume that the velocity variations around the mean are negligible (Fig. 4.11 shows that at most $(\delta U/U_\infty)^2 \lesssim 1/4$), such that (i) we can approximate the average drag by the drag at the average velocity and (ii) the thrust coefficient is constant throughout the burst phase. The thrust is active only during the burst phase and thus and thus the balance reads:

$$\frac{1}{2}\rho\pi R^2 (R\Omega)^2 \Delta \sim \frac{1}{2}\rho S_{\text{boat}} U_\infty^2 \langle C_D \rangle . \tag{4.27}$$

The drag coefficient is not a constant throughout the cycle. For the folding propeller it changes drastically when the propeller closes. The rigid propeller drag coefficient is also modified between the phases of motion according to the parametrization from Sec. 4.1.3. The average drag coefficient is therefore: $\langle C_D \rangle = C_{D,B}\Delta + C_{D,C}(1-\Delta)$. We use here $C_{D,B}$ and $C_{D,C}$ which are the drag coefficients of the burst and coast phases, respectively. We directly measured the drag coefficient in the coast phase, and we model the drag coefficient in the burst phase using the fit of the thrust (Fig. 4.6 and Tab. 4.1): $C_{D,B} = -\pi R^2 / S_{\text{boat}} c_T$. The scaling law for the evolution of the angular velocity therefore reads:

$$\Omega \sim \Omega_c \sqrt{\frac{C_{D,C}}{C_{D,B}}\left(\frac{1}{\Delta} - 1\right) + 1}, \tag{4.28}$$

with $\Omega_c = \lambda_c U_\infty / R$ the angular velocity of continuous motion. The drag contrast $C_{D,C}/C_{D,B}$ involved in this equation is equal to 0.20 for the folding propeller and 0.65 for the rigid one. We plot this scaling in Fig. 4.13 (dotted line and dashed line), the agreement with the data is good, especially

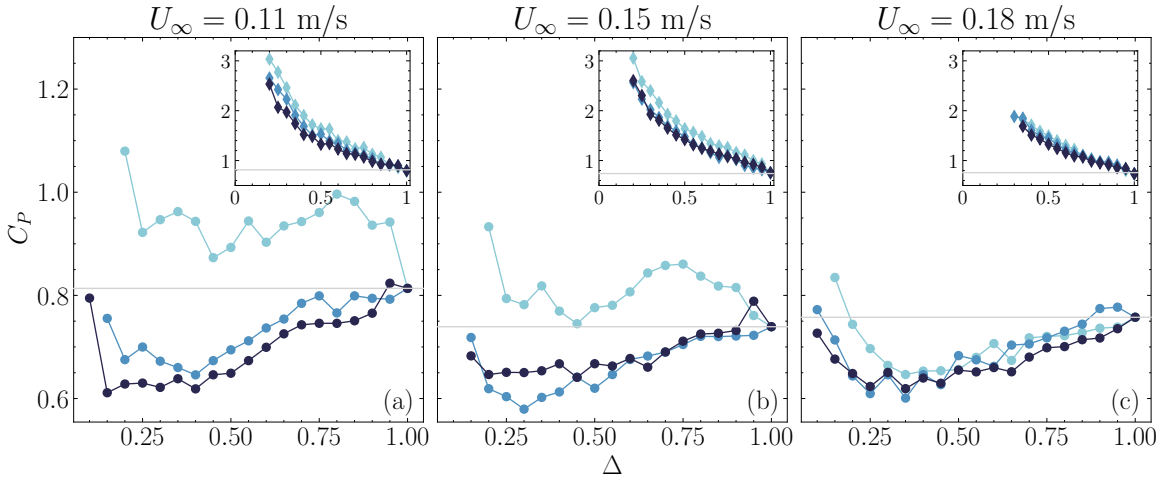

Figure 4.14: Power coefficient as a function of the duty cycle for the folding propeller for different velocities and different periods: from light to dark blue $T = 2.5, 5$ and 10 s. (light gray line) continuous power coefficient (corresponding to the rightmost point). Insets show the same graph but for the rigid propeller (Note the different vertical scale).

for the longer periods. This result validates the idea that velocity fluctuations play a minor role in setting the angular velocity. This model does not take into account period dependent effects and therefore cannot explain the difference observed for shorter periods.

Efficiency of burst and coast locomotion

To compare the efficiency of different styles of locomotion we introduce the power coefficient C_P defined as

$$C_P = \frac{\langle P(t) \rangle}{P_0} = \frac{\langle Q(t)\omega(t) \rangle}{1/2\rho S_{\text{boat}} U_\infty^3}. \tag{4.29}$$

Similarly to the thrust, the torque scales like the angular velocity squared (Eq. (3.24)). The torque is also modified when changing the tip speed ratio as the torque coefficient is not a constant (Eq. (4.20)). If this variation is small, at a given U_∞ and T, and neglecting velocity variations, this means that the power coefficient scales like:

$$C_P \propto \Omega^3 \Delta. \tag{4.30}$$

The power coefficient must be increasing for increasing duty cycle intermittent motion to be more efficient than continuous motion. A necessary criterion can therefore be written as:

$$\Omega(\Delta) < \Omega_c \Delta^{-1/3}. \tag{4.31}$$

This limit is plotted in Fig. 4.13 (dot dashed line) and we can already see, as expected, that intermittent locomotion with the rigid propeller has no chance of being efficient as the scaling from Eq. (4.28) with a drag contrast of 0.65 grows faster than $\Delta^{-1/3}$. The variation of the torque coefficient further reduces this limit as at low duty cycles, the propeller experiences a higher tip speed ratio in the burst phase and higher tip speed ratios are associated with an increased torque coefficient (Fig. 4.6).

From our measurements of instantaneous torque and angular velocity, we compute the power coefficient directly. We plot it in Fig. 4.14 for the folding propeller for the three different flow velocities

(panels (a) to (c)) and for the three different periods (color). For each flow velocity there is a set of parameters for which the intermittent motion is more efficient than the continuous motion (gray line). This energy saving reaches a maximum of 25% (for the slowest mean flow) and a reduction of 15% can be achieved at any flow velocity. For all tested velocities, the duty cycle that optimizes energy savings is about 0.3. The insets show the corresponding power for the rigid propeller. Consistent with the prediction from condition (4.31), burst and coast locomotion is always less efficient than continuous locomotion. In fact, it increases the cost by more than a factor of three.

The general trend in all cases tested is that longer periods are beneficial to efficiency. This result may be due to the rotational inertia of the propeller and the surrounding water that the motor must overcome at the beginning of each burst phase, but does not recover at the end of the burst. This constant cost is comparatively less important when using a longer period.

One interesting note is that the total power produced by the motor benefits even more from intermittency than the purely hydrodynamic analysis above (See Fig. 4.15). In all the results presented, we use the hydrodynamic torque, which is obtained by subtracting the parasitic torque due to friction in the bearings from the total torque. This parasitic torque has an almost constant value over the angular velocity range and therefore shorter bursts are associated with less power dissipated in the bearings. In a real situation, the cost would be measured on the total power, and so this additional reduction would be beneficial: a 15% energy saving from the hydrodynamic contribution alone becomes more than 20% savings with the added friction.

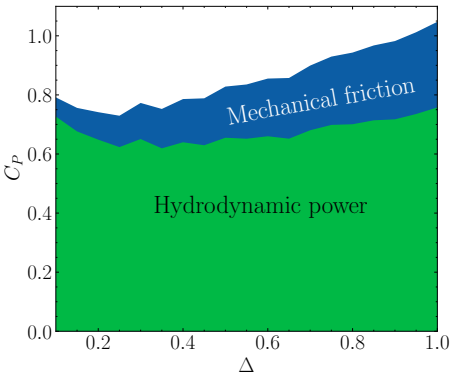

Figure 4.15: Power coefficient as a function of the duty cycle before (blue) and after (green) subtracting the power dissipated by mechanical friction. (Obtained with $U_\infty = 0.18$ m/s and $T = 10$ s.)

A side note on energy per distance

In all the above considerations, we compared cycles keeping the mean velocity constant. Not changing the end use (getting from point A to point B in a fixed time) is the natural choice for comparing locomotion styles. However, some authors, especially in the animal locomotion literature, compare cycles with a fixed actuation on a per-distance basis (Blake, 1983; Floryan et al., 2017b). This makes sense for animal locomotion, as physiological constraints may prevent access to the most efficient gait. However, energy savings are then dominated by reductions in average speed, as power scales with the cube of speed. In animals, metabolic rate (a constant energy expenditure over time) can partially compensate for this effect, but it is not present in our system.

To investigate what would happen in a system where the angular velocity is fixed, but the mean velocity allowed to change we follow the steps proposed in Floryan et al. (2017b) for propulsion with a pitching airfoil. We compare the energy expenditure per distance traveled with the same angular velocity — for fish swimming the tail beat frequency and amplitude is fixed. The energy ratio between intermittent and continuous motion, travelling a distance d, reads:

$$\zeta = \frac{P(\Delta)d/U_\infty(\Delta)}{P_c d/U_c} = \frac{P(\Delta)U_c}{P_c U(\Delta)}, \tag{4.32}$$

where U_c and P_c are the velocity and power associated with the continuous cycle. We did not perform constant actuation experiments and thus U_c and P_c are computed from the static thrust and torque measurements that we performed. Using the data obtained when the boat was fixed in Sec. 4.1.3, for

a given angular velocity we have:

$$U_c(\Omega) = \frac{R\Omega}{\lambda_c}, \quad P_c(\Omega) = \frac{1}{2}\rho\pi R^2 (R\Omega)^3 C_Q \left(\frac{R\Omega}{U_c}\right). \tag{4.33}$$

For a given period, mean flow velocity U_∞, and duty cycle Δ, we measure the angular velocity and power required to sustain intermittent motion. We then calculate the average velocity and power required to sustain continuous motion at the same angular velocity using the equations above.

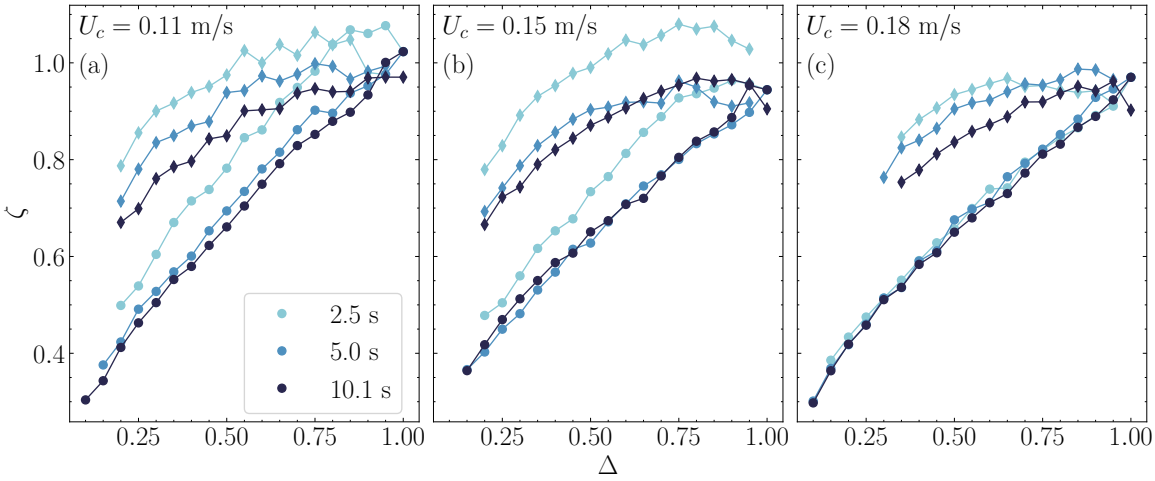

Figure 4.16: Energy ratio between intermittent and continuous motion per distance travelled. Colors and symbols are identical to Fig. 4.14

We plot the ratio ζ in Fig. 4.16 and, as expected with this metric, intermittent locomotion is almost always advantageous compared with continuous locomotion. In the previous sections, coasting did not cost any energy, but required more thrust to be generated in the burst phase to maintain a constant average speed. Here, coasting is truly "free" because we have removed the mean velocity constraint.

Amplitude of velocity variations

An important parameter of intermittent locomotion is the amplitude of the variations in velocity (Weihs, 1974, 1981). Indeed, the main source of dissipation added when using burst and coast, is the quadratic dependence of the drag with the velocity at high Reynolds numbers. The effect of this quadratic dependence is that the average drag when using intermittent locomotion is greater than the drag at the average velocity:

$$\langle D \rangle \sim \frac{1}{2}\rho S_{\text{boat}} \left\langle (U_\infty + U(t))^2 \right\rangle = \frac{1}{2}\rho S_{\text{boat}} \left(U_\infty^2 + \langle U(t) \rangle^2 \right) > \frac{1}{2}\rho S_{\text{boat}} U_\infty^2. \tag{4.34}$$

This variation in velocity can be estimated using the coast phase dynamics: the only force acting on the boat is the drag and the equation of motion reads

$$m^* \frac{\mathrm{d}U}{\mathrm{d}t} = -\frac{1}{2}\rho S_{\text{boat}} C_D (U_\infty + U(t))^2. \tag{4.35}$$

If the variations in velocity are small with respect to the mean speed, we can rewrite this equation as a scaling law:

$$m^* \frac{U_{\max} - U_{\min}}{(1-\Delta)T} \sim \frac{1}{2}\rho S_{\text{boat}} C_D U_\infty^2. \tag{4.36}$$

Finally, the amplitude of the velocity variations scale like

$$\mathcal{A}_u = (1-\Delta)T \frac{1/2\rho S_{\text{boat}} C_D U_\infty^2}{m^*}. \tag{4.37}$$

We plot the standard deviation of the velocity in Fig. 4.17 as a function of this scaling for both propellers using the drag coefficients measured in 4.1.3. We can see that it describes very well the scaling of the standard deviation of the velocity. The coefficient of this scaling law is 0.18.

Variations in velocity are also associated with a peak of tip speed ratio at the beginning of the cycle (See Fig. 4.12) which is also detrimental to performance as high tip speed ratios are linked to high torque coefficients. Everything else equal, minimizing the velocity variations seems beneficial for efficiency. However, we see in Fig. 4.14 that longer periods (associated with important amplitude) are generally more efficient than shorter ones. Added to that the scaling laws plotted in Fig. 4.13 do not take this effect into account and still describe well the evolution of the angular velocity Ω with the duty cycle Δ. These clues show that while high velocity variations add dissipation, the magnitude of this effect is small in the experiments compared with a change in the drag contrast or the period.

In the following we clarify the influence of the amplitude of the velocity variations on the performance using a model that describes the dynamic behavior or the boat during the cycle.

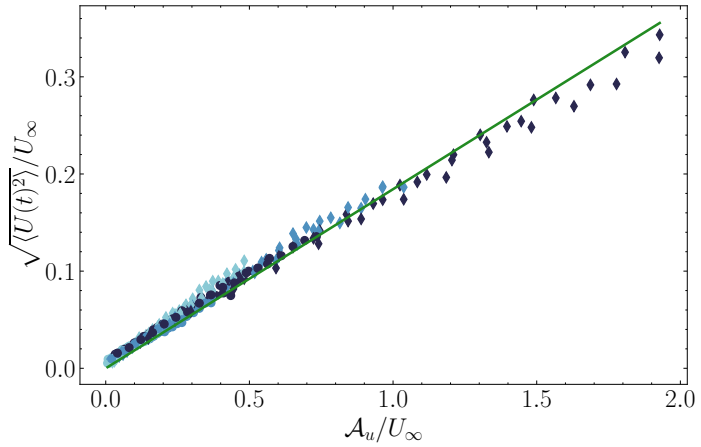

Figure 4.17: Standard deviation of the boat velocity as a function of the theoretical amplitude defined in 4.37. (green line) linear least square regression of the data with a slope of 0.18

4.2.3 Minimal drag reduction

In this section, we construct a model which is able to reproduce the dynamic motion of the intermittent locomotion experiment. The goal of this model is twofold: (i) to predict the exact parameters for which propulsion is most efficient (period, duty cycle, etc.) and (ii) to identify the region in the parameter space where burst and coast is more efficient than continuous motion. Because we have seen in Fig. 4.14 that long periods most efficient, we will in the following neglect any unsteady dissipative effect.

The main force acting on the boat throughout the cycle is the drag force. In a general unsteady setting, this force on a blunt object can be divided into three terms (Rivero et al., 1991):

$$D = \underbrace{\frac{1}{2}\rho S_{\text{boat}}(U_\infty^2 + U^2(t))C_{D,C}}_{\text{Quasi-steady}} + \underbrace{m_a \frac{\mathrm{d}U}{\mathrm{d}t}}_{\text{Added mass}} + \underbrace{F_H(t)}_{\text{History}}. \tag{4.38}$$

The first one is the quasi-steady drag, which is the same as the drag with a steady flow, with the time dependent velocity. The added mass is a potential correction, proportional to the acceleration which represents the inertia of the water the boat has to accelerate with it. This term is not dissipative as it simply adds more inertia to the motion: it slows the boat on acceleration but helps conserve momentum when slowing down. The last term is the history force, which contains all the remaining phenomena due to the acceleration. In the small Reynold number limit, this force takes the form of an integral over the whole history of the acceleration of the object (also called the Basset force). This remaining force might also contain unsteady wave drag (Dode et al., 2022) or shape specific vortex shedding along the live edge of the boat. Our goal is to construct a minimal model capable of describing the experimental observations of long period dynamics, and we will therefore neglect these contributions.

We divide the model according to the two phases of motion, assuming an instantaneous transition between the two.

In the coast phase the only force acting on the boat is the drag. The equation for the total velocity of the boat in this phase (U_1) reads:

$$m^* \frac{\mathrm{d}U_1}{\mathrm{d}t} = -\frac{1}{2}\rho S_{\text{boat}} U_1^2(t) C_{D,C}, \tag{4.39}$$

where $C_{D,C}$ is the drag coefficient during the coast phase, and $m^* = m_{\text{boat}} + m_a$ is the total inertia of the system taking into account the added mass.

In the burst phase the boat propels forward, and the drag is still resisting the motion. We have seen in Sec. 4.1.3 that the combination of these forces can be modelled in the as the sum of a term proportional to $(R\Omega)^2$ and a term proportional to U_2^2, with U_2 the total velocity in the burst phase. The equation of motion is:

$$m^* \frac{\mathrm{d}U_2}{\mathrm{d}t} = \frac{1}{2}\rho\pi R^2 \left(a_T (R\Omega)^2 + c_T U_2^2(t)\right), \tag{4.40}$$

where a_T and c_T are two coefficients as defined in Eq. (4.19) and Tab. 4.1.

Finally, the boat speed being periodic and continuous gives the boundary conditions:

$$U_2(\Delta T) = U_1(\Delta T), \quad U_1(T) = U_1(0). \tag{4.41}$$

We make this system dimensionless using the period T as the reference time and $R\Omega$ as the reference velocity. We denote the dimensionless velocities with a lowercase u and the dot ($\dot{u}$) denotes a dimensionless time derivative. The system now reads:

$$\dot{u_2} = M\left(a_T + c_T u_2^2\right), \tag{4.42}$$

$$\dot{u_1} = -M\frac{S_{\text{boat}}}{\pi R^2} C_{D,C} u_1^2, \tag{4.43}$$

$$u_2(\Delta) = u_1(\Delta), \quad u_1(1) = u_2(0). \tag{4.44}$$

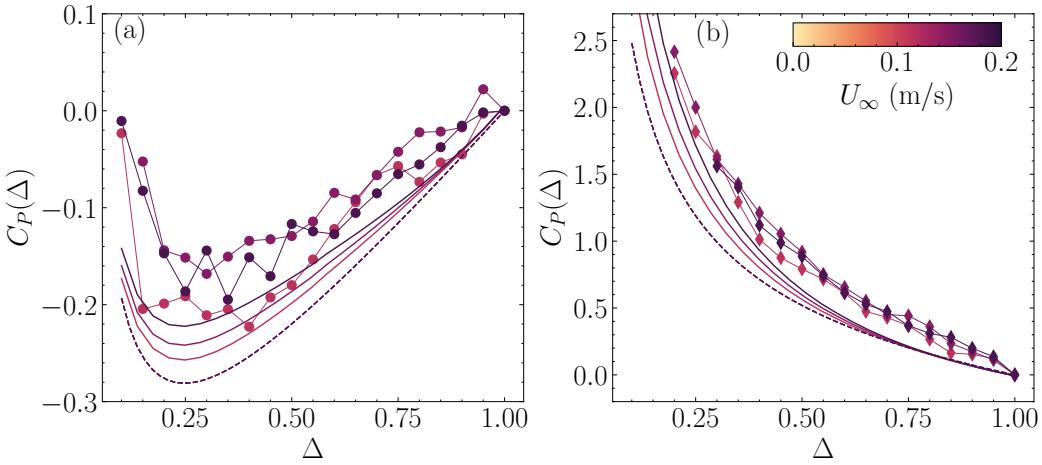

Figure 4.18: Power coefficient, relative to the continuous motion for (a) the folding propeller and (b) the rigid propeller ($T \geq 5$ s). (Full line) Result from the model with the same parameters, (dashed line) solution from Eq. 4.52.

The inertial number M is a dimensionless parameter that compares the fluid inertia to the one of the boat:

$$M = T\Omega \frac{\rho \pi R^3}{2(m + m_a)}. \tag{4.45}$$

The equations of motion integrate into:

$$\begin{aligned} u_2(t) &= \sqrt{\frac{-a_T}{c_T}} \tanh\left(\sqrt{-a_T c_T}\,(B + Mt)\right), \\ u_1(t) &= \left(A + M\frac{S_{\text{boat}}}{\pi R^2} C_{D,C}(t - \Delta)\right)^{-1}, \end{aligned} \tag{4.46}$$

where A and B are integration constants and the dimensionless time is also referred to as t for convenience. It should be noted that $\sqrt{-a_T c_T}$ is well-defined as a_T and c_T have opposite signs. The boundary conditions close the system, giving two equations for A and B:

$$\begin{aligned} \sqrt{\frac{-a_T}{c_T}} \tanh\left(\sqrt{-a_T c_T}\,(B + M\Delta)\right) &= A^{-1} \\ \sqrt{\frac{-a_T}{c_T}} \tanh\left(\sqrt{-a_T c_T} B\right) &= \left(A + M\frac{S_{\text{boat}}}{\pi R^2} C_{D,C}(1 - \Delta)\right)^{-1} \end{aligned} \tag{4.47}$$

We numerically solve the system for the parameters A and B using a root finding algorithm. Once the time dependent velocity $u(t)$ is known, we can compute all the other parameters of interest in the system: mean velocity $\langle u(t) \rangle$, time dependent tip speed ratio in the burst phase $\lambda(t) = 1/u_2(t)$, and finally the power coefficient using Eqs. (4.20), (4.29) and the table 4.1, giving:

$$\begin{aligned} C_P = \frac{\langle Q(t)\omega(t) \rangle}{1/2 \rho S_{\text{boat}} U_\infty^3} &= \frac{\pi R^2}{S_{\text{boat}}} \frac{1}{\langle u(t) \rangle^3} \int_0^\Delta C_Q\left(\lambda(t)\right) \mathrm{d}t \\ &= \frac{\pi R^2}{S_{\text{boat}}} \frac{1}{\langle u(t) \rangle^3} \int_0^\Delta \left(a_Q + \frac{c_Q}{\lambda^2(t)}\right) \mathrm{d}t. \end{aligned} \tag{4.48}$$

The parameters a_Q and c_Q are measured using the static experiments, and there are therefore no adjustable parameters in the model.

We plot the relative modification of power consumption compared to continuous motion in Fig. 4.18 for the model above (full line) and the experiments with a long period. The model is able to reproduce the power requirement for both propellers fairly well. In particular the duty cycle corresponding to optimal efficiency matches the experimental data. It tends to underpredict the power at low duty cycles, most likely because we have neglected unsteady dissipative effects.

Our model matches well with experiments, and in the following we use it to analyze the effect of changing the drag contrast $C_{D,C}/C_{D,B}$ and the inertial number M. The performance of intermittent locomotion is quantified by the maximal efficiency improvement:

$$\tau = -\min_{\Delta} \frac{C_P(\Delta) - C_P(1)}{C_P(1)}, \tag{4.49}$$

and the associated duty cycle:

$$\Delta_{\max} = \operatorname*{argmin}_{\Delta} \frac{C_P(\Delta) - C_P(1)}{C_P(1)}. \tag{4.50}$$

In addition to varying numerically the drag contrast, we also performed experiments with an increased boat draft (we increase the volume of the hull actually in water by changing the water depth). Doing this increases the hull drag which is present both in the active and passive phases and thus decreases the contrast (going from $C_{D,C}/C_{D,B} = 0.20$ to 0.26).

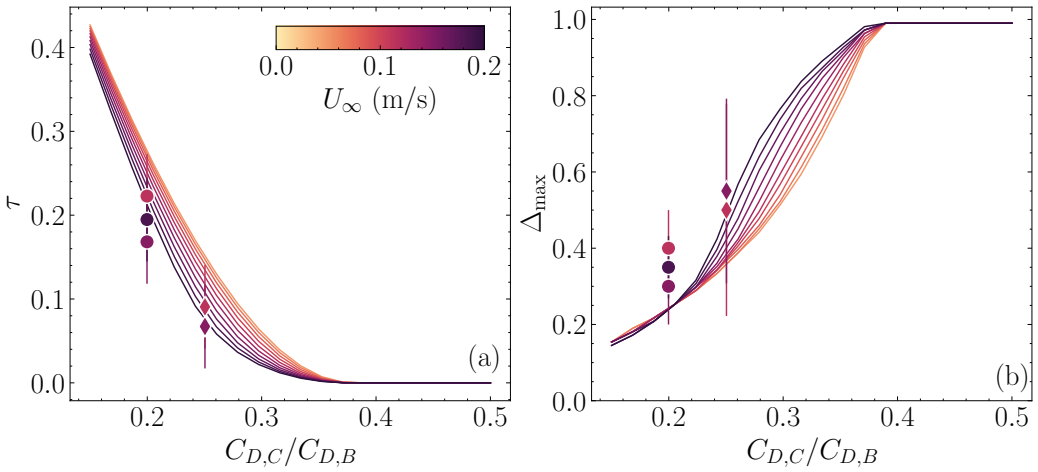

Figure 4.19: (a) Optimal efficiency improvement as a function of the drag contrast between the active and passive phases. Error bars correspond to uncertainty in the data: estimated by repeating experiments (b) Corresponding optimal duty cycle, as a function of the drag contrast. Error bars correspond to the width of the range where the power coefficient is less than 5% away from the optimum. Markers correspond to experimental points, where water depth is (•) 190 mm and (⧫) 200 mm. Full lines correspond the model.

We plot these two quantities for the model and the experimental data in Fig. 4.19 and we once again see a good agreement between both series of experimental points and the model. The model highlights a key result of the intermittent locomotion system: if $C_{D,C}/C_{D,B} \gtrsim 0.35$, continuous locomotion is the most efficient propulsion style. In other words, for burst and coast locomotion

to be more efficient than continuous locomotion, the total drag must be reduced by at least 65% in the coast phase. Below this threshold, the efficiency improvements increase monotonically when $C_{D,C}/C_{D,B}$ is reduced. At the same time, the duty cycle for which this optimum occurs is reduced and approaches zero.

Velocity variations

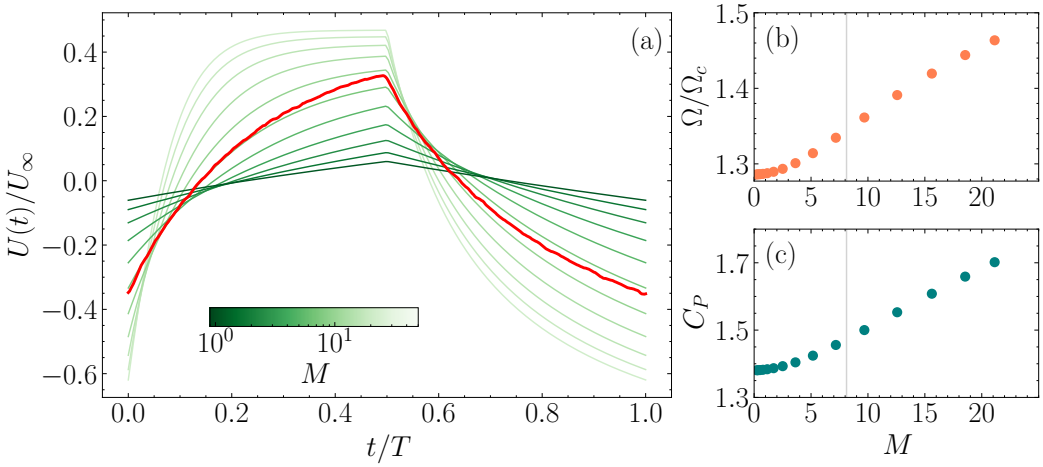

Figure 4.20: (a) Instantaneous velocity as a function of time for (red) experimental data, (green) model with different masses ($U_\infty = 0.15$ m/s, $T = 10$ s, $\Delta = 0.5$, rigid propeller). (b) and (c) associated angular velocity (compared to the angular velocity of continuous motion) and power coefficient respectively, as a function of the inertial number M. (gray line) Experimental value of M.

The model predicts that slower average speeds are benefit more from intermittent locomotion because the associated velocity variations are smaller, reducing the average drag and the variations of the tip speed ratio. The amplitude of the motion appears to play an important role in determining the efficiency of a given cycle, albeit secondary to drag reduction. This amplitude is modified by the period and the flow velocity, but also by the inertia of the system, visible in the inertial number M.

Fig. 4.20 shows the instantaneous velocity for experimental data ($M_{\text{exp}} \approx 8$), and numerical results with different M keeping the mean velocity constant (the angular velocity in the burst phase therefore varies). The resulting velocity profiles are widely different: from high accelerations and important velocity variations at low inertia (high M) to almost flat profiles at high inertia (low M). The associated angular velocity in panel (b) grows monotonically with M (i.e., when the relative inertia of the boat is reduced). This indicates that the required thrust to sustain the motion also grows: the average drag gets increasingly important for small inertia. The power coefficient also increases through two mechanisms: (i) at a constant mean velocity, the power coefficient is proportional to Ω^3 and (ii) when there are important velocity variations, the tip speed ratio peaks at the beginning of the cycle (See Fig. 4.12) and high tip speed ratios are associated with high torque. A similar result was also obtained by Li et al. (2023) in fish, were they found that important velocity variations are associated with poor energy efficiency. Optimized burst and coast strategies in fish involve moderate velocity variations and small periods.

Minimizing the velocity variations is therefore beneficial for the efficiency. This can be done by adding mass to the boat or shortening the period. Experimentally, we have seen that unsteady dissipative effects in practice limit the minimal possible period. In the experiments we have ($0.9 \lesssim M \lesssim 12$) and

in the numerical model we use a total mass $m^* = 3$ kg. We repeated a series of experiments with the folding propeller, adding a 4 kg weight to the boat ($U_\infty = 0.15$ m/s, $T = 5$ s). We found a very small 2% average decrease of the power coefficient throughout the range duty cycle. This reduction is smaller than the uncertainty of our experiments and highlights the diminishing returns when M approaches 0. This shows that in the case of our experiments, increasing the period is beneficial as it reduces the unsteady dissipative effects more than it increases the cost because of the amplitude of the velocity variations. However, we expect that there should be a limit period where the opposite occurs and the cost increases again with period. The velocity variations should begin to dominate when a significant amount of momentum is lost during the coast phase. This corresponds to the limit period $t_{\max}$ (defined in equation (4.22)).

Quasi-steady limit

In the extreme case of zero velocity variations in the active phase ($M \to 0$), the expression for the power coefficient can be further simplified:

$$C_P = \frac{\pi R^2}{S_{\text{boat}}} \left(\frac{R\Omega}{\langle U_\infty + U(t) \rangle} \right)^3 \int_0^\Delta C_Q \left(\lambda(t) \right) \mathrm{d}t \approx \frac{\pi R^2}{S_{\text{boat}}} \left(\frac{R\Omega}{U_\infty} \right)^3 \Delta C_Q \left(\frac{R\Omega}{U_\infty} \right). \tag{4.51}$$

Using Eq. 4.28, we can replace Ω and obtain:

$$C_P = \Delta \frac{\pi R^2}{S_{\text{boat}}} \left(\frac{R\Omega_c}{U_\infty} \right)^3 \left(\frac{C_{D,C}}{C_{D,B}} \left(\frac{1}{\Delta} - 1 \right) + 1 \right)^{3/2} \left[a_Q + \frac{c_Q \left(U_\infty / R\Omega_c \right)^2}{C_{D,C}/C_{D,B} \left(1/\Delta - 1 \right) + 1} \right], \tag{4.52}$$

where $R\Omega_c/U_\infty = \lambda_c = \sqrt{-c_T/a_T}$ is the tip speed ratio of continuous motion. This law does not depend on the inertial number M anymore: velocity variations have no influence on the power coefficient in this limit (nor do the period, or inertia). The flow velocity only enters the equation through the continuous tip speed ratio and therefore this law does not depend on the absolute velocity anymore. The dashed line in Fig. 4.18 displays this asymptotic limit, and we can see that even though it is very simplified, it predicts relatively well the evolution of the power coefficient. It obviously underpredicts the power requirement as we have neglected all the dissipation sources mentioned above.

This law is very similar to the one obtained by Floryan et al. (2017b), which in the case of intermittent propulsion with a pitching airfoil found $P \propto \Delta (C_{D,C}/C_{D,B} \left(1/\Delta - 1 \right) + 1)^{3/2}$ in our notations (the paper uses a slightly different convention). Their law is equivalent to having a constant torque coefficient throughout the range of tip speed ratio for us (i.e., $c_Q = 0$). This difference comes from the fact that the power coefficient in fish swimming scales like the Strouhal number cubed ($St = fA/U_\infty$ where f and A are respectively the tail beat frequency and amplitude), without a negative offset like in our case. In this simpler case, the onset of efficient burst and coast locomotion is equivalent to threshold of $\Omega(\Delta) < \Omega_c \Delta^{-1/3}$, which gives:

$$\frac{C_{D,C}}{C_{D,B}} \left(\frac{1}{\Delta} - 1 \right) + 1 < \Delta^{-2/3}. \tag{4.53}$$

By differentiating the previous relation with respect to Δ, we obtain that in this case burst and coast is more efficient than continuous motion only if:

$$\frac{C_{D,C}}{C_{D,B}} < \frac{2}{3}. \tag{4.54}$$

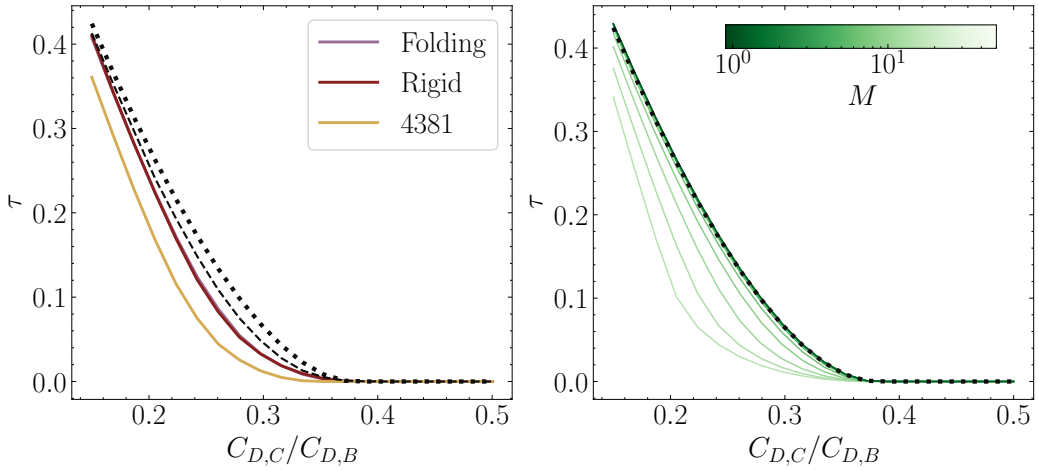

Figure 4.21: (left) Efficiency improvement for different propeller models as a function of the drag contrast. (dashed line) Efficiency improvement for the modified cycle with constant λ. (dotted line) Efficiency improvement with the analytical model, using the folding propeller. (right) Efficiency improvements changing the parameter M, (dotted line) Efficiency improvement with the analytical model

This threshold is much easier to reach than the one we found for propellers ($C_{D,C}/C_{D,B} < 35\%$), indicating that the burst and coast strategy is more suited to fish-like locomotion than our propeller based system.

Unfortunately, the more complex law 4.52 cannot give such a simple analytical threshold for efficient intermittent locomotion. In the following paragraphs we describe how this threshold is modified by the change of some parameters of our system. We plot the optimal efficiency improvement τ as a function of the drag reduction computed from the full model in Fig. 4.21 (right) for several inertial numbers M. We see as expected that the smaller M is (the higher the relative boat inertia), the more efficient burst and coast becomes. The values eventually converge as $M \to 0$ towards the scaling of Eq. 4.52 (dotted line), indicating that the analytical description above corresponds to the natural limit of infinite inertia. The zero velocity variation limit is equivalent to performing the experiments with a fixed boat instead of allowing it to move back and forth. Doing so results in an underprediction of the cost of the locomotion, even if unsteady dissipation is neglected. For all these curves, the threshold where burst and coast becomes more efficient than continuous locomotion ($C_{D,C}/C_{D,B} < 35\%$) is essentially unchanged.

In all the previous analysis of the efficiency improvement τ we have used the fitting coefficients from the folding propeller, but we can also use the slightly different ones from the rigid propeller or the propeller 4381. Doing so at fixed M and flow velocity, gives the curves on the left panel of Fig. 4.21 (full lines). The folding and rigid propellers curves superimpose while the more efficient propeller 4381 gives a slightly lower value at $C_{D,C}/C_{D,B} < 33\%$ (keeping in mind that we have had to manually add the hull drag to the fitting coefficients here). Still, the order of magnitude remains similar which consolidates the result, especially given that the propeller from the literature has a maximal efficiency of about 0.7, compared to 0.25 for ours.

Constant tip speed ratio cycle

Finally, another actuation type could be considered: instead of using a constant angular velocity burst phase, we can use a more progressive constant tip speed ratio burst phase. The total velocity is small at the beginning of the burst phase, and so the angular velocity as well. Both increase at the same time during the burst phase. This is more efficient than the constant Ω cycle as the acceleration is more progressive and the torque coefficient remains constant. However, it is more difficult to perform experimentally as it would be very sensitive external variations, or we would have to use a control algorithm to keep the tip speed ratio constant. We did not perform this type of experiment, but we can analyze numerically what the change would be.

Writing the system of equations Eq. (4.39) and (4.40) in this new setting gives:

$$\begin{aligned} \dot{u_1} &= -\frac{1/2\rho S_{\text{boat}} U_\infty C_{D,C}}{m^*} u_1^2(t), \\ \dot{u_2} &= \frac{1/2\rho\pi R^2 U_\infty}{m^*} T(a_T\lambda^2 + c_T) u_2^2(t), \end{aligned} \tag{4.55}$$

where we have used U_∞ as the reference velocity instead of $R\Omega$. By imposing the boundary conditions and $\langle u(t)\rangle = 1$, we obtain the tip speed ratio λ that is solution to the system. We plot optimal efficiency improvement using this cycle in Fig. 4.21 (left, dashed line) for the same parameters as the folding propeller. The constant λ cycle is indeed slightly more efficient than the one with constant Ω for all drag reductions. However, this improvement is very small: the high inertia limit is still more efficient than this cycle. One benefit of this cycle not visible here is that we have seen experimentally that shorter periods are less efficient, maybe because of the angular inertia that the motor has to overcome. Using the constant λ cycle might reduce this effect and thus make the cycle more efficient.

4.3 Conclusion

This chapter presents how intermittent locomotion — an idea inspired from studying fish swimming — might apply to the movement of a boat with a propeller. Using a small scale experiment able to reproduce all the unsteady effects of an open water test we describe the behavior of such a system. We measure the time dependent torque and angular velocity, allowing us to compute the cycle averaged energy cost of each propulsion strategy.

Comparing intermittent and continuous locomotion at the same mean velocity, we show experimentally that the burst and coast strategy can be more efficient than continuous locomotion. Using a bioinspired propeller able to dynamically reconfigure between the active and passive phases — reducing the drag of the system by 80% — the cost of sustaining the motion can be reduced by about 15% at any speed and up to 25% for the most efficient cycle. The longest periods avoid unsteady dissipative effects and are therefore the most efficient.

We develop an analytical model reproducing the main forces acting on the boat during the cycle, based on the scaling of the thrust and torque coefficients of the propeller. This model agrees well with the experiments with no fitting parameters once the important properties (drag, thrust, and torque) of the boat are measured. We highlight the importance of the drag contrast between the active and passive phases: the drag must be reduced by 65% in the coast phase in order for intermittent locomotion to have an energetic interest. Finally, we show that inertia plays a secondary role in the problem, but that high inertia, with small velocity variations is the most efficient.

An interesting perspective of this work is the precise role of the period of the motion. Experimentally, we see that longer periods are increasingly efficient. This trend should eventually be reversed, since

the model shows that increasing the period (or M) leads to higher velocity variations, which increase the cost of a given cycle. At some point, this effect should begin to dominate, as velocity saturates when the period is too long. We therefore expect that there should be an optimal period in between. Finding this optimum requires modeling the unsteady dissipation that occurs in the short period experiments. Another aspect not explored here, but relevant to the problem, is the accurate modeling of unsteady wave drag. Dode et al. (2022) recently found that the mean drag on a surface-piercing towed hull can be reduced if its velocity oscillates around a mean value. Therefore, setting the period accordingly can further reduce the energy required for propulsion. It should be noted that this effect occurs for Froude numbers and periods that are far from those we use, so our setup does not benefit (or suffer) from this effect.

Bibliography

AKOZ, E. and MOORED, K. W. (2018). Unsteady propulsion by an intermittent swimming gait. *Journal of Fluid Mechanics*, vol. 834:pp. 149–172 82

BLAKE, R. W. (1983). Energetics of leaping in dolphins and other aquatic animals. *Journal of the Marine Biological Association of the United Kingdom*, vol. 63(1):pp. 61–70 91

BOSWELL, R. (1971). Design, cavitation performance, and open-water performance of a series of research skewed propellers. Tech. Rep. 3339, Naval Ship Research and Development Center, Washington DC, USA, Department of Hydromechanics 81, 82

CHEN, M. Z., YU, M. J., ZHANG, M. A., YI, M. R., and ZHANG, M. Q. (2013). Folding Propeller Design and Analysis for A Hybrid Driven Underwater Glider. p. 9 76

CORRIGAN, J. J. and SCHILLINGS, J. J. (1994). Empirical model for stall delay due to rotation. In *American Helicopter Society Aeromechanics Specialists Conference*. San Francisco, CA 80

DODE, A., CARMIGNIANI, R., COHEN, C., CLANET, C., and BOCQUET, L. (2022). Wave drag during an unsteady motion. *Journal of Fluid Mechanics*, vol. 951:p. A15 94, 101

FLORYAN, D., VAN BUREN, T., ROWLEY, C. W., and SMITS, A. J. (2017a). Scaling the propulsive performance of heaving and pitching foils. *Journal of Fluid Mechanics*, vol. 822:pp. 386–397 75, 82

FLORYAN, D., VAN BUREN, T., and SMITS, A. J. (2017b). Forces and energetics of intermittent swimming. *Acta Mechanica Sinica*, vol. 33(4):pp. 725–732 91, 98

LI, G., KOLOMENSKIY, D., LIU, H., GODOY-DIANA, R., and THIRIA, B. (2023). Intermittent versus continuous swimming: An optimization tale. *Physical Review Fluids*, vol. 8(1):p. 013101 97

MARZIN, T., DE LANGRE, E., and RAMANANARIVO, S. (2022). Shape reconfiguration through origami folding sets an upper limit on drag. *Proceedings of the Royal Society A: Mathematical, Physical and Engineering Sciences*, vol. 478(2267):p. 20220592 78

RIVERO, M., MAGNAUDET, J., and FABRE, J. (1991). Quelques résultats nouveaux concernant les forces exercées sur une inclusion sphérique par un écoulement accéléré. (New results on the forces excerted on a spherical body by an accelerated flow). *Comptes Rendus de l'Academie des Sciences. Serie II*, vol. 312 94

SAVITZKY, A. and GOLAY, M. J. E. (1964). Smoothing and Differentiation of Data by Simplified Least Squares Procedures. *Analytical Chemistry*, vol. 36(8):pp. 1627–1639 87

WEIHS, D. (1974). Energetic advantages of burst swimming of fish. *Journal of Theoretical Biology*, vol. 48(1):pp. 215–229 75, 84, 92

WEIHS, D. (1981). Energetic advantages of Burst-and-Coast swimming of fish at high speeds. *Journal of Experimental Biology*, vol. 97(1):pp. 169–178 92

WU, G., YANG, Y., and ZENG, L. (2007). Kinematics, hydrodynamics and energetic advantages of burst-and-coast swimming of koi carps (Cyprinus carpio koi). *THE JOURNAL OF EXPERIMENTAL BIOLOGY*, vol. 210(12):pp. 2181–2191 75, 82, 84

Conclusion

This thesis explored the possibility of using new bio-inspired strategies to improve the energy efficiency of propulsion in water. It consists mainly of experimental work carried out at model scale in a water channel built for this purpose. We focused on two axes: reconfiguration and intermittency.

We built and analyzed the behavior of flexible propellers that can passively change their shape. The first one, a fully flexible propeller with ribbon-like flexible blades, proved to be a very interesting fluid-structure interaction problem. It has two deformation directions: bending and spanwise twisting, which are coupled by the hydrodynamic loading. Using a simple geometric argument, we were able to predict the direction and approximate magnitude of the moderate bending deformation. We showed that for any given deformation, there is a strong relationship between the bending angle and the thrust generated by the rotor, allowing the measurement of only one of these quantities.

However, this propeller design is very inefficient because of the bending, and therefore we explored another design with a rigid leading edge. In this case, the twisting deformation acts to reduce the angle of attack of the blades. By choosing the right material properties, we have shown that these blades can be more efficient than any rigid equivalent and passively adapt their pitch angle to varying conditions. The blades also experience spanwise torsion and as a result adopt a shape that improves their maximal efficiency. The tip twist is a key parameter to track the efficiency of the rotor, and we were able to predict its value using a linear development of the constitutive equation. For both flexible propellers, we built simple analytical models able to reproduce all the phenomenology observed in experiments.

We then studied intermittent locomotion by building a setup that can reproduce the back-and-forth motion of a fish swimming freely in a channel. We mimic the passive drag reduction that fish experience when gliding by using a shape-changing propeller. This propeller is inelastic, because we only need it to be in a fully open or fully closed position. We are able to describe its progressive opening by introducing a coupling between the opening angle and the pitch angle of the propeller.

Using this propeller, we have shown that cyclically turning the electric motor on and off can be more efficient than driving continuously at the same speed. This intermittent strategy leads to a reduction in propulsion cost of between 15 and 25%, depending on the average velocity. This is possible because the drag in the passive phase is sufficiently low. This drag reduction lowers the angular velocity required to propel the boat and thus the cost of the entire cycle. We were able to develop scaling laws that capture this effect and predict the required angular velocity. By modeling the time-dependent dynamics, we obtained the minimal drag reduction for intermittent locomotion to be efficient: drag must be reduced by at least 65%. The same model shows that velocity fluctuations play a minor role compared to other sources of dissipation. Experimentally, it is best to approach a quasi-steady regime.

Nomenclature

$(\boldsymbol{d}_1, \boldsymbol{d}_2, \boldsymbol{d}_3)$	Local frame along the centerline of the elastic blade
α	Angle of attack
α_{opt}	Angle of attack that maximizes the lift to drag ratio
$\bar{\delta}_{AC}^{LE}$	Distance between the aerodynamic center and the leading edge
$\bar{\delta}_{cm}^{ac}$	Distance between the aerodynamic center and the center of mass of a section
Δ	Duty cycle
δ	Tilt angle of the shaft
Δ_{max}	Duty cycle corresponding to maximal efficiency improvement
η	Efficiency $\eta = C_T/(\lambda C_Q)$
γ	Angle between the blade and the plane of rotation
γ_0	Pitch angle
λ	Tip speed ratio
$\mathbf{\Omega}_{\text{el}}$	Darboux vector
$\mathbf{f}_{\text{el}}$	External force of the elastic blade
$\mathbf{M}_{\text{el}}$	Internal moment of the elastic blade
$\mathbf{m}_{\text{el}}$	External moment of the elastic blade
$\mathbf{T}_{\text{el}}$	Internal force of the elastic blade
$\mathbf{U}_{\mathbf{p}}$	Local, relative flow velocity
ν_{el}	Poisson's ratio
Ω	Angular velocity
ω	Time dependent angular velocity
Ω_c	Angular velocity of the continuous motion
ρ	Fluid density
ρ_b	Blade density
σ	Solidity $\sigma = N_b c/(\pi R)$
τ	Maximal efficiency improvement compared with continuous motion
θ	Bending angle
θ_e	Opening angle
ε	Twisting deformation, $\varepsilon = \gamma_0 - \gamma$
φ	Local flow angle

ζ	Power expanded per unit distance, relative to continuous motion
A_b	Cross sectional area of a blade
$a_Q,\ c_Q$	Fitting coefficients for the torque
$a_T,\ c_T$	Fitting coefficients for the axial force
C	Torsion spring constant
c	Chord length
C_a	Axial force coefficient
C_D	Drag coefficient
C_L	Lift coefficient
C_N	Normal force coefficient
C_P	Power coefficient
C_Q	Torque coefficient, $C_T = Q/(1/2\rho\pi R^2 \left(R\Omega\right)^2 R)$
C_T	Thrust coefficient, $C_T = F_{\text{thrust}}/(1/2\rho\pi R^2 \left(R\Omega\right)^2)$
C_Y^B	Bending Cauchy number
C_Y^S	Twisting Cauchy number for the semi-flexible propeller
C_Y^T	Twisting Cauchy number
$C_{D,B}$	Burst phase drag coefficient
$C_{D,C}$	Coast phase drag coefficient
D	Drag force
d	Blade relative density, $d = \rho_b/\rho$
E	Young's modulus
e	Thickness
F_{thrust}	Thrust force
I	Quadratic moment of area
J	Torsion modulus
L	Lift force
M	Dimensionless quantity comparing the fluid versus boat inertia
m	Boat mass
m^*	Total mass, $m^* = m + m_a$
m_a	Added mass
N_b	Number of blades
P_c	Typical power dissipated by viscous drag
Q	Torque
R	Radius (maximum)
r	Radius (local)
r_{min}	Radius (minimum)
S_{boat}	Reference surface of the boat
S_b	Planar surface area of a blade
T	Period
U	Boat velocity
U_∞	Incoming flow velocity
u_p	Dimensionless velocity magnitude, $u_p = U_p/(R\Omega)$
U_t	Orthoradial velocity
U_x	Axial velocity

Appendix A

Fully flexible propeller

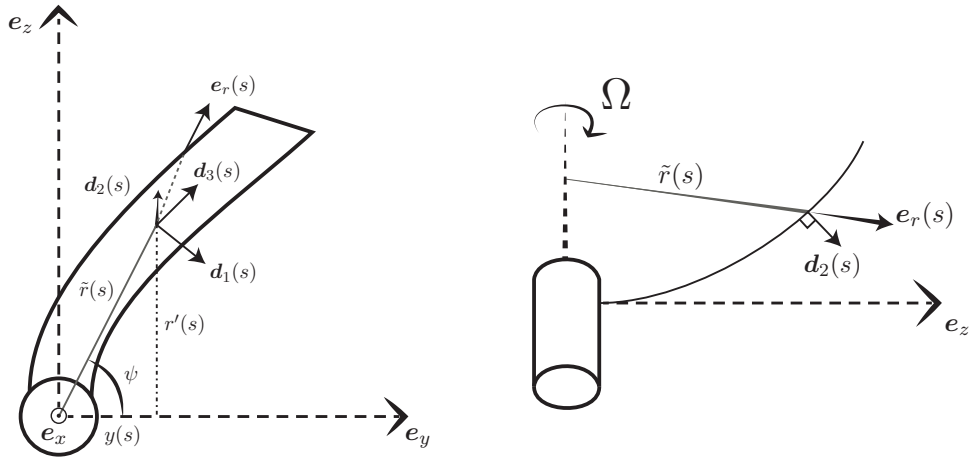

Figure A.1: Left, view of the bent blade in the $(\boldsymbol{e}_y, \boldsymbol{e}_z)$ plane (as seen from the incoming flow). Right, view obtained by rotating along $\boldsymbol{e}_y$ by γ_0 so as to see the blade from the side. Note that $\tilde{r}$ is coming from the back of the schematic here.

This appendix details the computation required to obtain the equation for the deformation of the fully flexible propeller in Sec. 3.1. In particular, in the limit of small twist we first obtain an expression for $\tilde{r}$ — the distance between a bend blade element and the axis of rotation. Then, we compute the projection $\boldsymbol{e}_r \cdot \boldsymbol{d}_2$ required to get the centrifugal force and finally reach the expression for the moment due the centrifugal force.

Distance to the axis of rotation We compute the distance $\tilde{r}$ to the axis of rotation, which in the case of no pitch and pure bending, reads:

$$\tilde{r} = r_{\text{min}} + \int_{r_{\text{min}}}^{R} \cos\theta \mathrm{d}r. \tag{A.1}$$

This formula does not hold in our case due to the finite pitch of the blades and the twist. The exact

formula requires integrating both bending and twisting angles along the span and adds a lot of unnecessary complexity. Indeed, in our system the twist is small compared to the pitch of the blades (seen in our and in Eldemerdash and Leweke (2021) experiments).

In the general case, $\tilde{r}(s)$ is the combination of its projection along the z and y directions: $\tilde{r}^2(s) = r'(s)^2 + y^2(s)$. Under the hypothesis that the twist is small, the z projection corresponds to $\tilde{r}(s)$ in the zero pitch case (i.e., looking at the blade from the side as in Fig. A.1 is the same as if the blade was flat.). The projection in the y direction corresponds to the displacement in the x direction in the case of zero pitch, then rotated around $\boldsymbol{e}_z$ by an angle γ_0 and finally projected onto $\boldsymbol{e}_y$. In other words: $y(s) = \int_{r_{\text{min}}}^{R} \sin\theta \mathrm{d}r \times \sin\gamma_0$. Finally we obtain:

$$\tilde{r}^2 = \left(r_{\text{min}} + \int_{r_{\text{min}}}^{R} \cos\theta \mathrm{d}r\right)^2 + \left(\sin\gamma_0 \int_{r_{\text{min}}}^{R} \sin\theta \mathrm{d}r\right)^2. \tag{A.2}$$

We compute the scalar product $\boldsymbol{e}_r \cdot \boldsymbol{d}_2$ by expressing both vectors in the frame of reference $(\boldsymbol{e}'_x, \boldsymbol{e}'_y, \boldsymbol{e}'_z)$, obtained by rotating the frame $(\boldsymbol{e}_x, \boldsymbol{e}_y, \boldsymbol{e}_z)$ around $\boldsymbol{e}_z$ by the pitch angle γ_0. We have:

$$\boldsymbol{e}_r = \cos\psi \boldsymbol{e}_y + \sin\psi \boldsymbol{e}_z, \tag{A.3}$$
$$\boldsymbol{d}_2 = \sin\theta \boldsymbol{e}'_z - \cos\theta \boldsymbol{e}'_x. \tag{A.4}$$

By writing $\boldsymbol{e}'_x$ in terms of $\boldsymbol{e}_x$ and $\boldsymbol{e}_y$, we can finally write:

$$\boldsymbol{e}_r \cdot \boldsymbol{d}_2 = \sin\psi(s)\sin\theta(s) - \cos\psi(s)\sin\gamma_0\cos\theta(s). \tag{A.5}$$

The angle ψ is obtained using the values of $r'(s)$ and $z(s)$:

$$\psi = \frac{r_{\text{min}} + \int_{r_{\text{min}}}^{R} \cos\theta \mathrm{d}r}{\sin\gamma_0 \int_{r_{\text{min}}}^{R} \sin\theta \mathrm{d}r}. \tag{A.6}$$

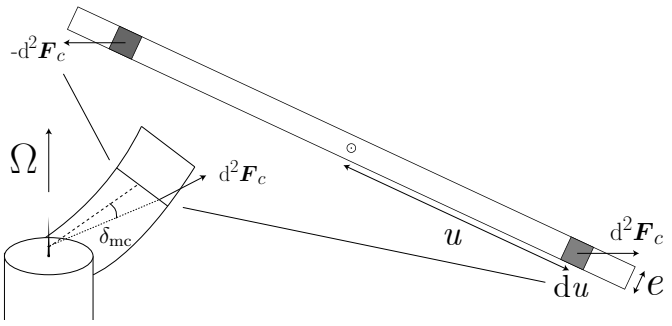

Figure A.2: Creation of a restoring moment due to the misalignment of the centrifugal forces.

Moment of the centrifugal force The centrifugal force creates a moment which tends to twist the blade towards the plane of rotation due to the misalignment of the centrifugal forces in a section (Fig. A.2). We compute its analytical expression also using the hypothesis that the twist is small compared to the pitch of the blades. In a small blade element at a radius r and chordwise coordinate u, the magnitude of the centrifugal force d^2F_c reads:

$$\mathrm{d}^2F_c = \rho_b e \Omega^2 \sqrt{\tilde{r}^2 + u^2\cos^2\gamma_0} \mathrm{d}u\mathrm{d}r. \tag{A.7}$$

This force is directed mostly radially but also slightly away from the center of rotation because of the offset u. The projection of this force in the orthoradial plane corresponds to a multiplication by $\sin\delta_{\text{mc}}$, where δ_{mc} verifies:

$$\tan\delta_{\text{mc}} = \frac{u\cos\gamma_0}{\tilde{r}}. \tag{A.8}$$

Finally, taking into account the bending of the local section of the blade, the infinitesimal centrifugal force reads:

$$\mathrm{d}^2F_c = \rho_b e\Omega^2 u\cos\gamma_0\cos\theta\mathrm{d}u\mathrm{d}r. \tag{A.9}$$

The moment along $\boldsymbol{d}_3$ created by this distribution of force is:

$$\mathrm{d}M_{\text{centrifuge}} = 2\int_0^{c/2} u\sin\gamma_0\mathrm{d}^2F_c(u). \tag{A.10}$$

After computing the integral (the result would differ if the blade had a varying thickness or chord), we find:

$$\mathrm{d}M_{\text{centrifuge}} = \rho_b e\frac{c^3}{24}\Omega^2\cos\theta\sin\gamma_0\mathrm{d}r \tag{A.11}$$

Appendix B

BEMT corrections

This section efforts made to improve the quantitative agreement between the blade element model and the experiments. In particular it describes the widely used blade element momentum theory (BEMT) originally developped by Glauert (1983). This model takes into account the induced velocities due to the rotation of the rotor and estimates them via the conservation of momentum. It is widely used as a preliminary step in the engineering of rotating structures, wind turbines of propellers (Sørensen, 2011; Masters et al., 2011; MacNeill and Verstraete, 2017; Jiménez et al., 2022; Mohd Zawawi et al., 2014). Many corrections exist, taking into account different limiting aspects: compressibility Jiménez et al. (2022), low Reynolds aerodynamics MacNeill and Verstraete (2017), or flow curvature Snel et al. (1994); Corrigan and Schillings (1994).

In the following we derive the BEMT model and compare various implementations with the experimental thrust and torque of the chordwise-flexible propeller (any other data set would lead to a similar discussion). We do not couple the BEMT with a model for flexibility in the example, so the blades are considered rigid. We do not explicitly include the effects of the tilt of shaft in the following, but it can be readily adapted, either by including a position dependent local velocity (See for instance Mario (2012)) or its average effect: reducing the thrust by a factor $\cos\delta$.

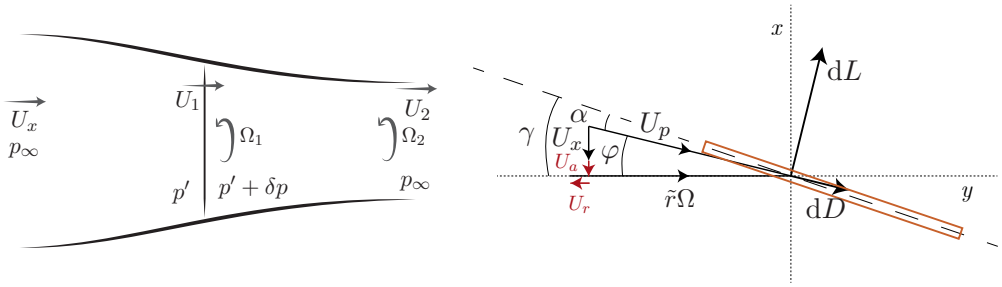

Figure B.1: Schematic of the actuator disk model (left) and definition of the induced velocities in red and associated angles (right)

Blade Element Theory

We consider a section of the blade, located at the curvilinear position s along the span of the blade. The axial and orthoradial velocities are modified by the induced velocities U_a and U_r respectively (see Fig. B.1). The axial velocity U_a is due to the fact that the flow is already slightly accelerated before reaching the rotor and the orthoradial velocity is due to the fluid being accelerated into rotation by the blades. The total axial velocity is therefore $U_x + U_a$, where U_x is U_∞ in the case of a flat rotor aligned with the flow, but in the case of a tilted rotor $U_x \approx U_\infty \cos\delta$. The total angular velocity is $r\Omega - U_r$. With the choice of directions for U_a and U_r, both of these induced velocities should be positive when the propeller is behaving normally (producing positive thrust and experiencing positive torque).

The total (local) velocity U_p and local flow angle φ read:

$$U_p^2 = (U_x + U_a)^2 + (r\Omega - U_r)^2\,, \quad \varphi = \tan^{-1}\frac{U_x + U_a}{r\Omega - U_r}. \tag{B.1}$$

We then use the same modelling as in Sec. 1.2, discretizing the flow in concentric annuli, interacting with a section of the blades. The thrust and torque therefore read:

$$\begin{aligned} \mathrm{d}F_{\text{thrust}} &= \frac{1}{2}\rho N_b c U_p^2 \left(C_L(\alpha)\cos\varphi - C_D(\alpha)\sin\varphi\right)\mathrm{d}r, \\ \mathrm{d}Q &= \frac{1}{2}\rho N_b r c U_p^2 \left(C_L(\alpha)\sin\varphi + C_D(\alpha)\cos\varphi\right)\mathrm{d}r. \end{aligned} \tag{B.2}$$

To solve the system and find U_a and U_r, we will find another way of expressing $\mathrm{d}F_{\text{thrust}}$ and $\mathrm{d}Q$.

Momentum Theory

We consider the propeller as an actuator disk through which the velocity is continuous but where there is a pressure jump δp (Fig. B.1, left). By writing Bernoulli's equation from infinitely upstream to the disk and from the disk to infinitely downstream, we get the system:

$$\begin{aligned} p_\infty + \frac{1}{2}\rho U_x^2 &= p' + \frac{1}{2}\rho U_1^2, \\ p' + \delta p + \frac{1}{2}\rho U_1^2 &= p_\infty + \frac{1}{2}\rho U_2^2. \end{aligned} \tag{B.3}$$

It should be noted that the angular velocity imparted to the flow in the wake of the propeller is expected to be small, such that it does not enter into the balance above. We thus have the relation,

$$\delta p = \frac{1}{2}\rho\left(U_2^2 - U_x^2\right). \tag{B.4}$$

The thrust produced by the propeller is the integration of the pressure around the actuator disk. In our simplified case this reduces to the change in pressure times the area of the rotor:

$$F_{\text{thrust}} = \pi R^2 \Delta p = \tilde{A}\frac{1}{2}\rho\left(U_2^2 - U_x^2\right). \tag{B.5}$$

The thrust can also be obtained through the increase of momentum of the flow as it passes through the disk. It can be expressed as the mass flow through the disk $\rho\pi R^2 U_1$ times the increase in velocity $U_2 - U_x$:

$$F_x = \pi R^2 \rho U_1 (U_2 - U_x) \tag{B.6}$$

Combining these two expressions we get that the velocity at the disk is the mean of the velocities up and downstream:

$$U_1 = \frac{U_2 + U_x}{2}. \tag{B.7}$$

To compute the local thrust and torque, we need to apply this reasoning not to the whole flow around the rotor, but to the previously defined streamtubes of the flow. The conclusions stay the same, only they need to be applied locally instead of to the whole disk. For the tube crossing the blade associated with the spanwise coordinate s, we have $U_1(s) = U_x(s) + U_a(s)$ (or $U_2(s) = U_x(s) + 2U_a(s)$). The thrust contribution of an annulus of radius r and thickness $\mathrm{d}r$ is obtained by writing the increase in momentum through the annular portion of the rotor:

$$\mathrm{d}F_{\text{thrust}}(r) = 4\pi r\rho(U_x + U_a)U_a\mathrm{d}r. \tag{B.8}$$

The conservation of angular momentum similarly gives $\Omega_1 = \Omega_2/2$. The torque contribution from the annulus is obtained by considering the angular momentum increase ($2U_r$), multiplied by the axial flow rate ($2\pi r\mathrm{d}r\rho(U_x + U_a)$), and the moment arm r, giving:

$$\mathrm{d}Q(r) = 4\pi r^2\rho(U_x + U_a)U_r\mathrm{d}r. \tag{B.9}$$

Combining equations (B.2), (B.8), and (B.9) we close the system for U_a and U_r:

$$\frac{1}{2}\rho N_b c U_p^2 \left(C_L(\alpha)\cos\varphi - C_D(\alpha)\sin\varphi\right) = 4\pi r\rho(U_x + U_a)U_a, \tag{B.10}$$

$$\frac{1}{2}\rho N_b r c U_p^2 \left(C_L(\alpha)\sin\varphi + C_D(\alpha)\cos\varphi\right) = 4\pi r^2\rho(U_x + U_a)U_r. \tag{B.11}$$

The typical length scale of the problem is R and the typical velocity is $R\Omega$. Thus, we denote the dimensionless velocities with a lowercase u and the solidity of the propeller: $\sigma = cN_b/\pi r$. We obtain the dimensionless set of equations:

$$\frac{\sigma}{8}u_p^2 \left(C_L(\alpha)\cos\varphi - C_D(\alpha)\sin\varphi\right) - \left(u_x + u_a\right)u_a = 0, \tag{B.12}$$

$$\frac{\sigma}{8}u_p^2 \left(C_L(\alpha)\sin\varphi + C_D(\alpha)\cos\varphi\right) - \left(u_x + u_a\right)u_r = 0 \tag{B.13}$$

with,

$$\tan\varphi = \frac{u_x + u_a}{r/R - u_r}, \quad u_p^2 = (u_x + u_a)^2 + \left(\frac{r}{R} - u_r\right)^2, \text{ and } \alpha = \gamma - \varphi. \tag{B.14}$$

Using a root finding algorithm, we can find u_a and u_r for any given blade section. This result finally allows us to compute the thrust and torque coefficients:

$$C_T = \int_{s_{\min}}^{1} \frac{N_b c}{\pi R}u_p^2 \left(C_L(\alpha)\cos\varphi - C_D(\alpha)\sin\varphi\right)\mathrm{d}s \tag{B.15}$$

$$C_Q = \int_{s_{\min}}^{1} \frac{N_b c}{\pi R}\frac{r}{R}u_p^2 \left(C_L(\alpha)\sin\varphi + C_D(\alpha)\cos\varphi\right)\mathrm{d}s. \tag{B.16}$$

In Fig. B.2 (resp. B.3) we show the thrust coefficient (resp. torque coefficient) from several models, compared with the experimental data from Sec. 3.2. Four of the models (blue, green, purple, and black) utilize the blade element defined in the beginning of the thesis (Sec 1.2) where the axial and orthoradial velocities are assumed to be the flow velocity and the angular velocity respectively,

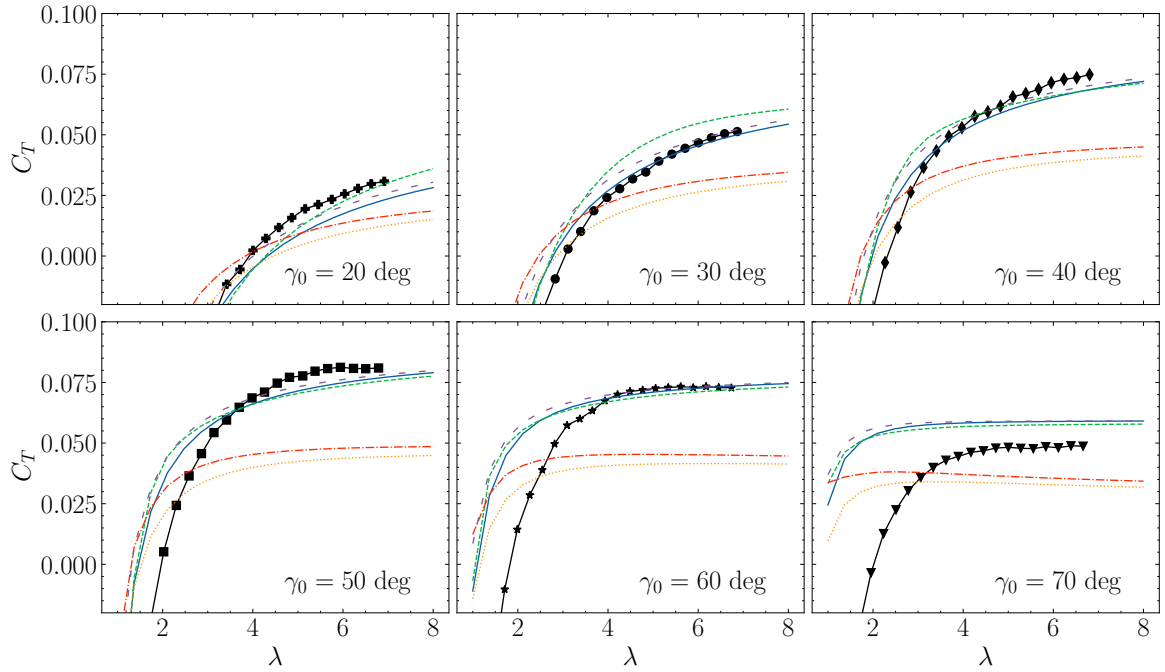

Figure B.2: Thrust coefficient versus tip speed ratio for various pitch angles γ_0. (•) Experimental data, (——) Blade element and flat plate model, (- - - -) Blade element and glider model, (- - -) Blade element, angular position dependence and flat plate model, (· · · · · ·) BEMT and flat plate model, (— · — · —·) BEMT, angular position dependence and flat plate model.

without self induction. The two remaining (red and orange) use the Blade Element Momentum Theory presented in this section. Without going into the details, it can be seen that the BEMT consistently underpredicts the thrust and torque. In contrast, the blade element model reaches the right order of magnitude for the thrust and is closer to the experimental torque. Forces are reduced when using the BEMT because the angle of attack is reduced when both induced velocities are positive. This is surprising as there is a large body of literature showing that the BEMT it an efficient tool to estimate the forces produced by a rotor, even in cases similar to ours (Eldemerdash, 2023; Jiménez et al., 2022; MacNeill and Verstraete, 2017; Durán Venegas et al., 2019). We identified several possible modifications to the models to help the quantitative agreement such as the effect of the tilt of the propeller, and the uncertainty on the sectional lift and drag coefficients.

All the curves in Fig. B.2 and B.3 incorporate the mean effect of the tilt: a reduction of the incoming velocity by $\cos\delta$ and a reduction of the thrust by the same amount because of the projection of the force normal to the rotor. We tested the effect of including the angular position dependent velocity (like in Sec. 2.2.3). For the simpler blade element model, the result is plotted in purple (- - -) to be compared with the reference case of a full blue line. Explicitly including the tilt result in an increase of the thrust produced, which reduces at high tip speed ratio. For the BEMT, this corresponds to dividing the flow a second time in annular tubes (Mario, 2012). The same effect is visible: the dot-dashed red line includes the full tilt effect and the dotted orange line does not. The tilt is not sufficient to explain the discrepancy between the BEMT and the experiments. Another clue that the issue is not the tilt is that using the data from boats 1 and 2 where the shaft is aligned with the flow leads to similar results.

Often times, corrections have to be added to the lift and drag coefficients to make BEMT quantitative

(Corrigan and Schillings, 1994; Snel et al., 1994; Masters et al., 2011; Jiménez et al., 2022). These semi-empirical corrections can model the effect of flow curvature, compressibility, stall, or tip losses. However, most of these reduce the thrust obtained in the model and thus cannot explain the discrepancy. We still tried to implement corrections for flow curvature and tip losses and verified that their effect does not explain the discrepancy between BEMT and experimental data (not shown). Some corrections incorporate several fitting parameters which may be problem dependent. Instead of fitting our model to the data, we decided to have a simple model which qualitatively predicts the thrust and torque. The blade element model is simpler and qualitatively fits better our experimental data. We therefore decided to use it instead of the full BEMT. Similarly, using the more complex 2D model for lift and drag from Li et al. (2022) does not improve the accuracy, and we therefore use the flat plate model.

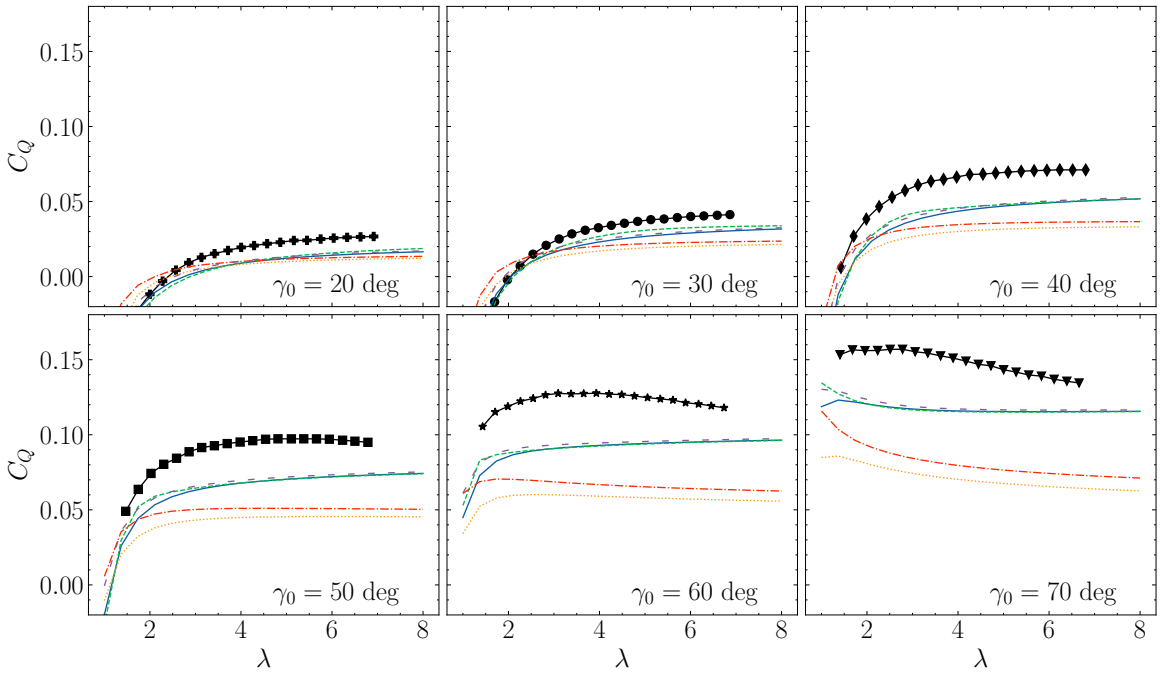

Figure B.3: Torque coefficient versus tip speed ratio for various pitch angles γ_0. (•) Experimental data, (——) Blade element and flat plate model, (- - - -) Blade element and glider model, (- - -) Blade element, angular position dependence and flat plate model, (· · · · · ·) BEMT and flat plate model, (— · — · —·) BEMT, angular position dependence and flat plate model.

Bibliography

CORRIGAN, J. J. and SCHILLINGS, J. J. (1994). Empirical model for stall delay due to rotation. In *American Helicopter Society Aeromechanics Specialists Conference*. San Francisco, CA 111, 115

DURÁN VENEGAS, E., LE DIZÈS, S., and ELOY, C. (2019). A strongly-coupled model for flexible rotors. *Journal of Fluids and Structures*, vol. 89:pp. 219–231 114

ELDEMERDASH, A. (2023). *Fluid-structure interaction of strongly deforming flexible rotors*. Ph.D. thesis, Aix Marseille Université 114

ELDEMERDASH, A. S. and LEWEKE, T. (2021). Deformation and wake of a flexible rotor in water. *Journal of Physics: Conference Series*, vol. 1934(1):p. 012006 108

GLAUERT, H. (1983). *The Elements of Aerofoil and Airscrew Theory*. Cambridge University Press 111

JIMÉNEZ, J., HOYOS, J., ECHAVARRIA MARTÍNEZ, C., and ALVARADO, P. (2022). Exhaustive Analysis on Aircraft Propeller Performance through a BEMT Tool *. *Journal of Aeronautics, Astronautics and Aviation, Series A*, vol. 54:pp. 13–24 111, 114, 115

LI, H., GOODWILL, T., JANE WANG, Z., and RISTROPH, L. (2022). Centre of mass location, flight modes, stability and dynamic modelling of gliders. *Journal of Fluid Mechanics*, vol. 937:p. A6 115

MACNEILL, R. and VERSTRAETE, D. (2017). Blade element momentum theory extended to model low Reynolds number propeller performance. *The Aeronautical Journal*, vol. 121(1240):pp. 835–857 111, 114

MARIO, H. (2012). Aerodynamic Propeller Model for Load Analysis. MSc Thesis 111, 114

MASTERS, I., CHAPMAN, J. C., WILLIS, M. R., and ORME, J. A. C. (2011). A robust blade element momentum theory model for tidal stream turbines including tip and hub loss corrections. *Journal of Marine Engineering & Technology*, vol. 10(1):pp. 25–35 111, 115

MOHD ZAWAWI, F., LV, P., PROTHIN, S., MORLIER, J., MOSCHETTA, J.-M., and BÉNARD, E. (2014). Study of a flexible UAV proprotor. *International Journal of Engineering Systems Modelling and Simulation*, vol. 6(3/4):pp. 149–161 111

SNEL, H., HOUWINK, R., and BOSSCHERS, J. (1994). Sectional prediction of lift coefficients on rotating wind turbine blades in stall. Tech. Rep., Netherlands: N. p. 111, 115

SØRENSEN, J. N. (2011). Aerodynamic Aspects of Wind Energy Conversion. *Annual Review of Fluid Mechanics*, vol. 43(1):pp. 427–448 111

Appendix C

Chordwise-flexible propeller data

We present here all the experimental data obtained with the chordwise-flexible propeller. The plots are presented similarly to Fig. 3.26, but show the thrust (Fig. C.1), torque (Fig. C.2), and twist angle (Fig. C.3). Colors indicate flexibility from yellow to red, with blue being assigned to the fully rigid blades. Each panel shows the data for a particular pitch angle, but the rigid blade data is plotted on each panel to facilitate comparisons (except for the twist angle).

Fig; C.4 displays the results of the numerical model, exploring the (γ_0, λ) plane. The top row corresponds to a rigid propeller and the bottom row to a flexible one ($C_Y^S/\lambda^2 = 0.24$). Comparing panels (a) and (d) shows how most of the time flexibility reduces the thrust, except for large pitch angles ($\gamma_0 > 45$ deg) where reducing the angle of attack to 45 deg is beneficial. At the same time, panels (b) and (c) show that the torque is always reduced resulting in an improved efficiency ((c) and (d)). The narrow range of efficient propulsion close to the positive thrust onset is widened to most of the domain explored. The tip twist (g) reduces when γ_0 or λ increase and is positive in the bottom left region of the plot (low λ and γ_0, when the angle of attack is negative on most of the blade).

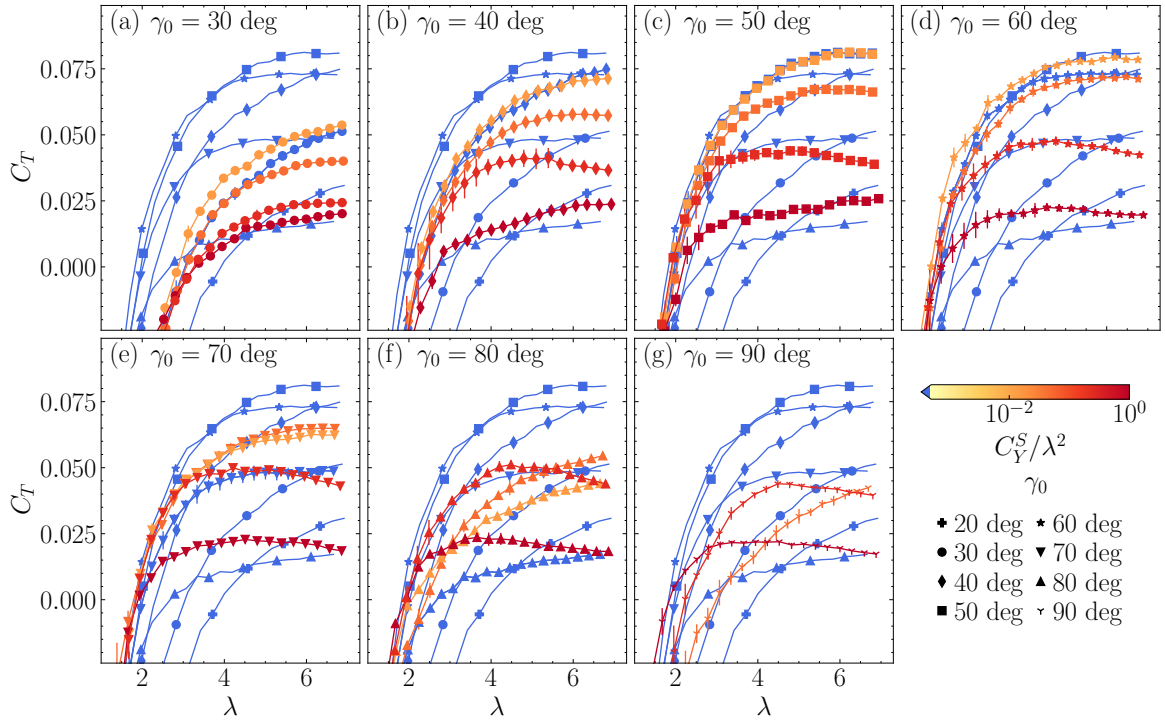

Figure C.1: Thrust coefficient as a function of the tip speed ratio. Colors indicate blade flexibility (blue) rigid, (yellow to red) increasingly flexible blades. Markers indicate pitch angle. Each panel corresponds to a pitch angle from 30 to 90 deg. For reference, the thrust of the rigid blades with every pitch angle is plotted on each panel.

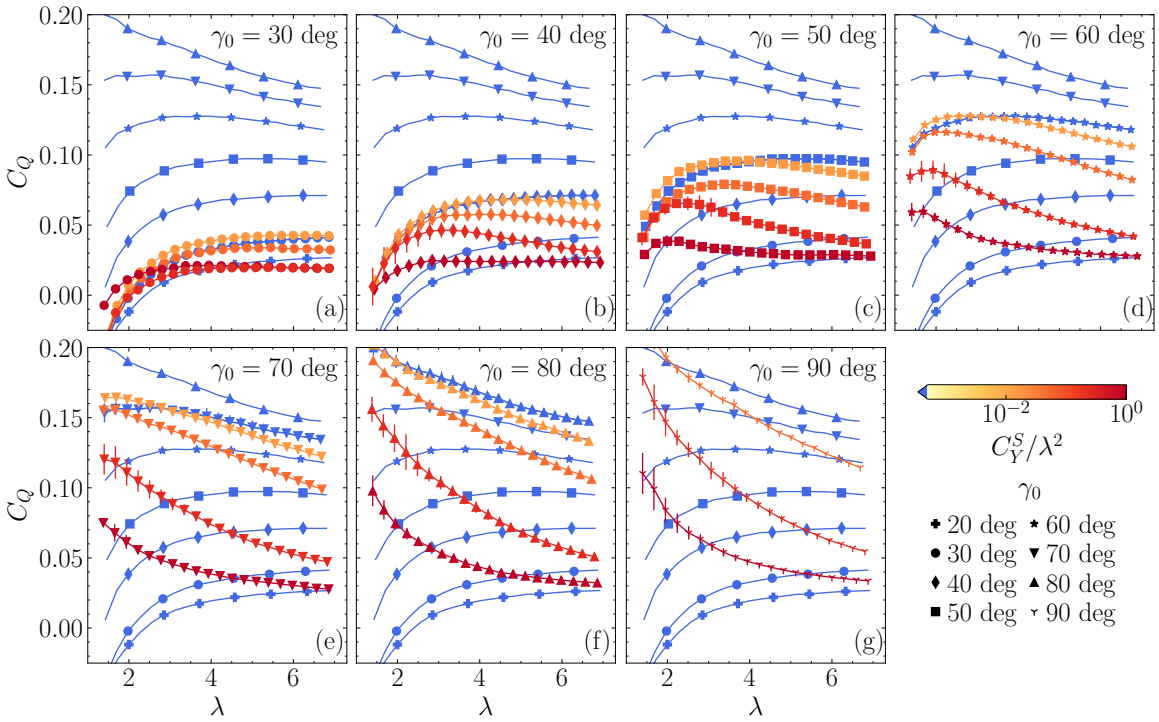

Figure C.2: Torque coefficient as a function of the tip speed ratio. Colors indicate blade flexibility (blue) rigid, (yellow to red) increasingly flexible blades. Markers indicate pitch angle. Each panel corresponds to a pitch angle from 30 to 90 deg. For reference, the torque of the rigid blades with every pitch angle is plotted on each panel.

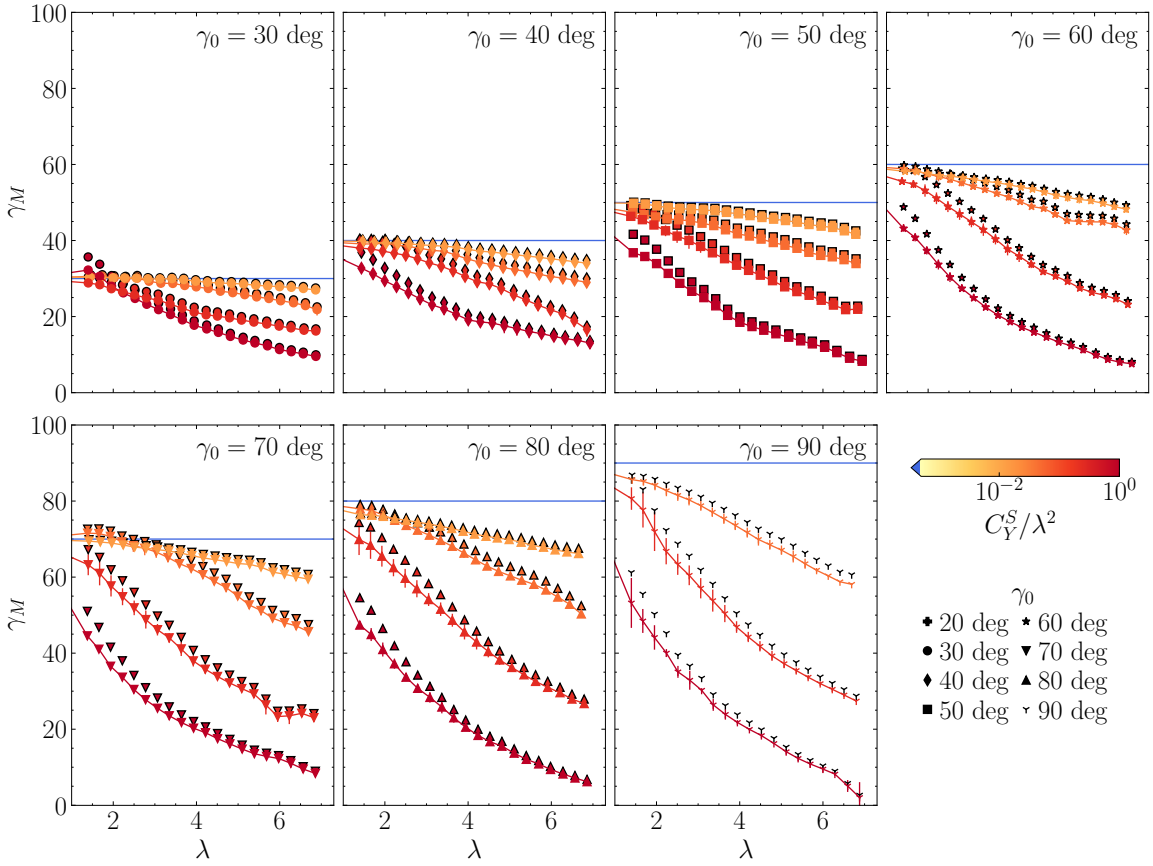

Figure C.3: Twist angle as a function of the tip speed ratio. Colors indicate blade flexibility (blue) rigid, (yellow to red) increasingly flexible blades. Markers indicate pitch angle. Each panel corresponds to a pitch angle from 30 to 90 deg. Dark edge colors correspond to the correction proposed in Fig. 3.21

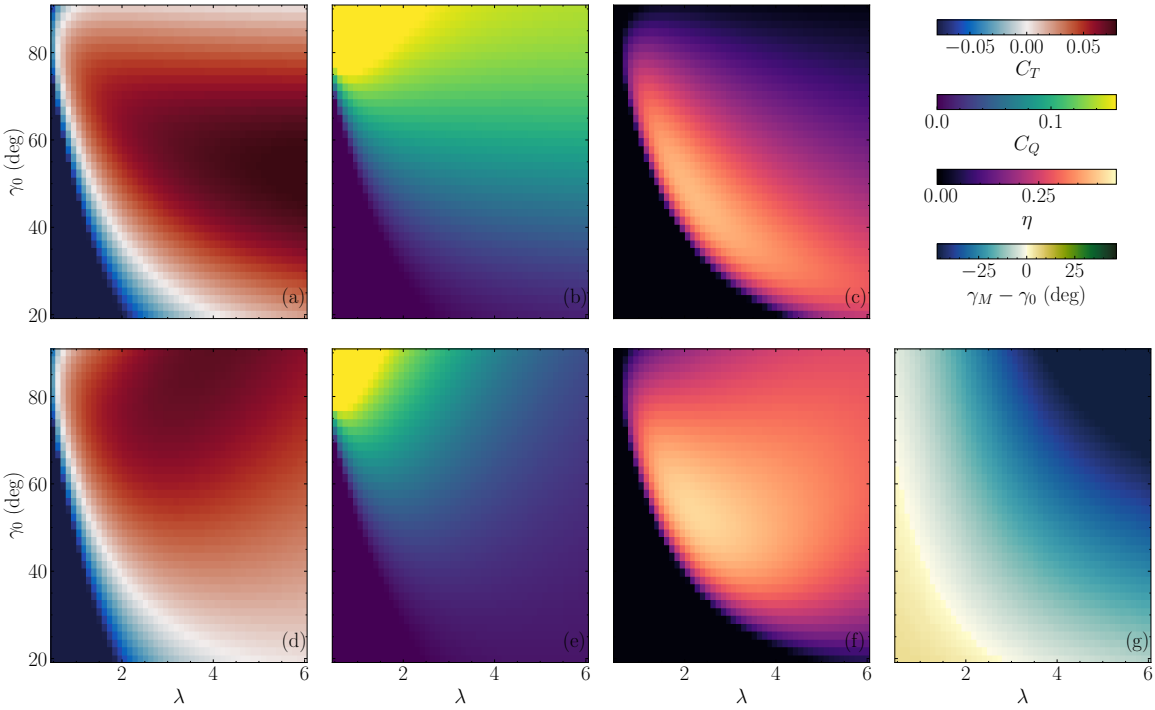

Figure C.4: Propeller performance from the numerical model. Top row corresponds to a rigid propeller, bottom one to a flexible propeller ($C_Y^S/\lambda^2 = 0.24$). Panels (a) and (d) show the thrust coefficient C_T, (b) and (e) show the torque coefficient C_Q, (c) and (f) show the efficiency η and panel (g) shows the tip deflection $\gamma - \gamma_0$.

Appendix D

Image processing

D.1 Fully flexible propeller

We detail here the processing required to go from the raw images of the rotor in Sec. 3.1 to the bending angle data. The steps are illustrated in Fig. D.1. We take 30 pictures (panel (a)) in the same operating conditions and each one of them is treated separately. The bending angle is the mean of the resulting data after removing the outliers with a median filter. The initial frame contains both blades and by symmetry, we can process the second blade in the same way as the first one.

Crop and contrast boost: we select only one blade (panel (b)) by cropping out the region of interest. In extreme cases, the tip of the blade can be above the hub of the rotor, in which case we hide the latter by making it fully white. We then enhance the contrast by an affine function of the pixel data.

Binarization: We threshold the image to make it binary (panel (c)). After filling every hole in the binary image, we label each non-zero connected region of the image and keep only the largest one, eliminating any noise or trace of particle in the flow.

Edge detection: We detect the edge of the blade (panel (d)) and compute a curvilinear abscissa s along the edge. To do so, we order the points along the edge, starting with the bottom left.

Tip detection: To detect the centerline, we first need to separate the leading and trailing edges and in order to do so we first need to detect the tip of the blade. We therefore compute the norm of the gradient along this edge, measuring abrupt changes in direction (panel (e)). By using a peak detection algorithm, we detect the two tips (green and orange dots) of the blade.

Alignment of the edges: We separate the leading and trailing edges, and we want to compute the coordinates of the centerline $x_c(s) = (x_{\mathrm{LE}}(s) + x_{\mathrm{TE}}(s))/2$ where LE and TE refer respectively to the leading and trailing edges (the same can be written for the z coordinate). We need a common parametrization of both edges in order compute the right quantity (because of the pixelization of the edges, they might not have the exact same length). We therefore compute the length of each edge in order to align them properly (visible in the black bars in panel (f)).

Centerline projection: Because the blade is tilted towards (or away from)the camera we need to correct the x coordinate of the centerline (cf. Fig. 3.3) by dividing by $\cos\gamma_0$. The uncorrected centerline is the blue line in panel (g) and the corrected one is the green dashed one (here $\gamma_0 = 20$ deg).

Bending angle: We finally compute $\theta(s) = \arctan \partial x/\partial z$ and obtain the blue curve in (h). To

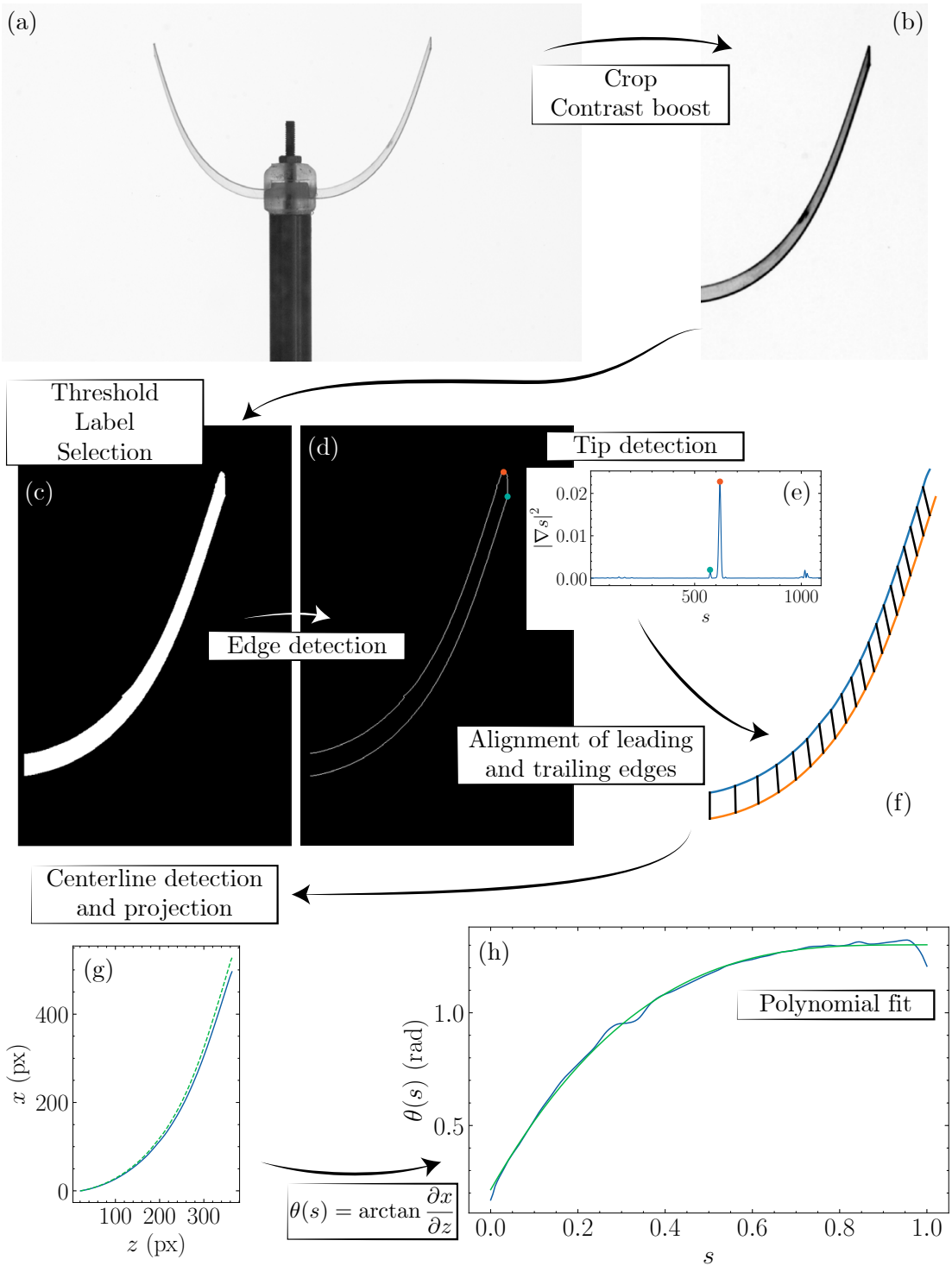

Figure D.1: Schematic of the processing to get from an image of the rotor to the spanwise distribution of bending angle. Details of each step are given in the text.

smooth out any remaining errors (such as the deflection near the tip), we fit $\theta(s)$ with a third degree polynomial.

D.2 Chordwise-flexible propeller

This section describes the processing used to extract the tip twist angle data from the series of pictures of the spinning rotor in Sec. 3.2. The camera is tilted in order to compensate the angle of the shaft. In contrast to the post-treatment of the fully flexible propeller, we trigger the camera 25 times per rotation not only when the blades are in the right position. We therefore first have to extract the images where the blades are perpendicular to the camera.

Reslice: We select a vertical slice of the image that the lit part of the blade cuts through when passing in front of the camera (panel (a), vertical red line) and plot the pixel data of each frame as a function of the vertical coordinate (white lines of panel (b) time is going upwards).

Detection of front facing images: Using a peak finding algorithm, we detect the frames where a blade is close to the horizontal line indicating the perfectly aligned position (blue line). Note that because 25 is not divisible by 3, the three blades are not photographed exactly in the same position: in the present case two are slightly below the middle and one is above. The maximal alignment error occurring because of this technique is $360 \text{ deg}/25 = 14.4$ deg up or downwards, which has little impact on the detected shape. From panel (c) onwards, we only use the front facing images.

Binarization: We crop the image and make it binary to prepare it for the next step. Because the background contains the nut used to fasten the blade as well as the other blades, the binarization is not as straightforward as a value threshold. Instead we use a combination of three thresholds: a pixel has a value of 1 in the binary image if it is brighter than the pixels in a wide region around it, the region close to it is sharper than most of the image, and it is bright enough.

Hough transform: Despite the efforts to detect only the blade in the binarization step, noise can be present or not all the blade may be detected. Instead of extracting the full shape of the lit part of the blade we use a Hough transform to extract its direction only. Its principle is to transform an image from regular 2D space to a position direction space. Each point in this space represents a line, defined by its slope (the angle we are looking for) and a distance from a reference point (here the top left corner of the image). The value of the Hough transform in this points simply is the number of pixel along the line with a value of 1. The result of this operation is plotted in panel (e), along with the maximum value at each given angle on top of it, since we are not interested in one particular location. The tip twist corresponds to the maximum of the curve. The result is shown in panel (f): the line captures the straight portion of the blade, near the trailing edge.

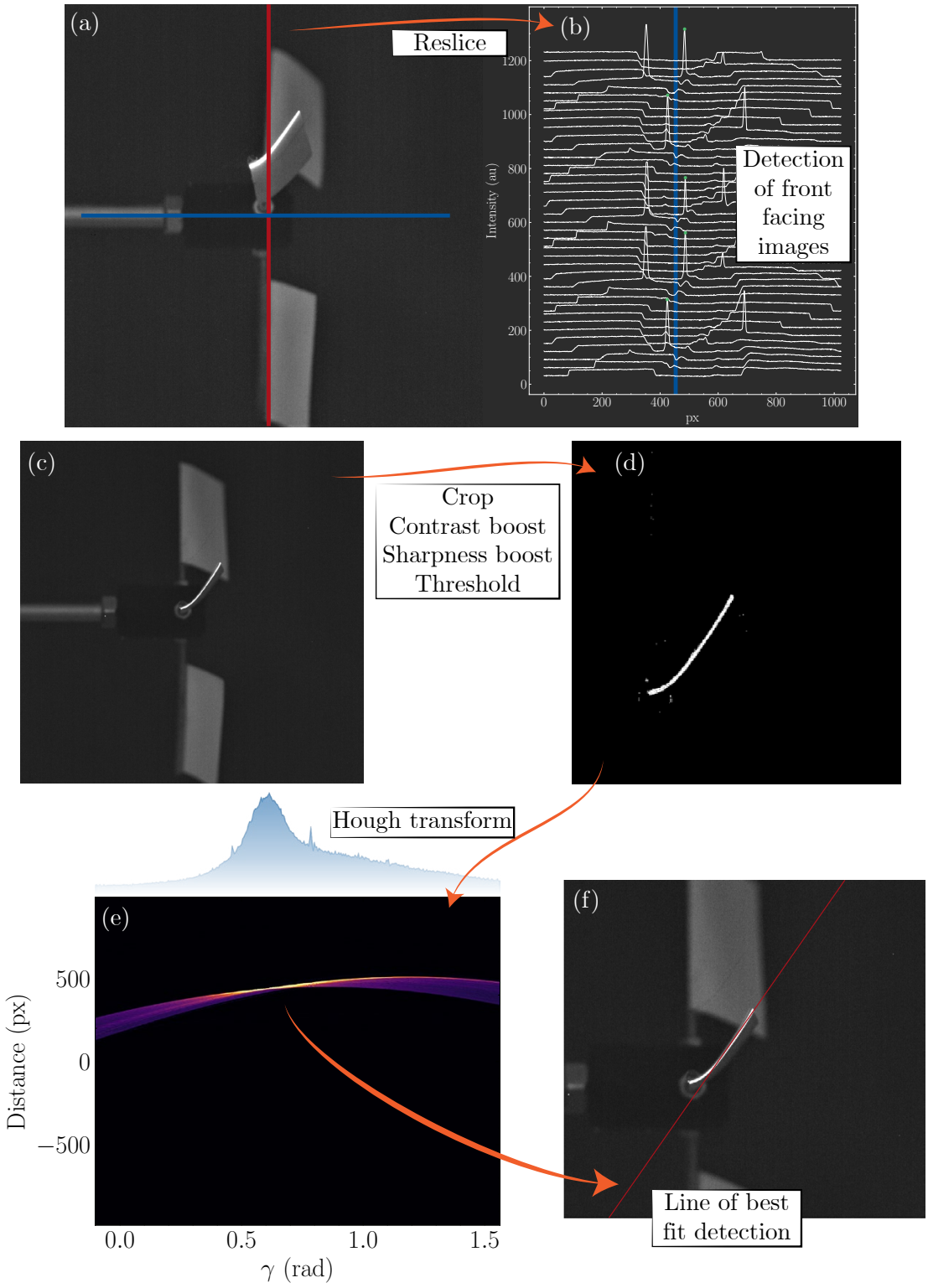

Figure D.2: Schematic of the processing to get from a sequence of images of the rotor to the tip twist angle. Details of each step are given in the text.

Résumé

Cette thèse expérimentale s'intéresse à la propulsion par hélice au travers de deux nouveaux concepts bioinspirés : la reconfiguration et l'intermittence. La reconfiguration consiste à rendre les structures déformables afin qu'elles s'adaptent aux forces qui s'exercent sur elles. De précédents résultats dans le cas des éoliennes ont montré que cette déformation peut être exploitée pour s'adapter passivement aux changements de conditions extérieures si la flexibilité du matériau est bien choisie. Cette capacité à changer de forme peut aussi être utilisée de manière dynamique pour se propulser de manière intermittente. Cette stratégie est adoptée par de nombreuses espèces de poissons ou d'oiseaux pour diminuer l'effort lié à la locomotion.

Les travaux présentés ici s'intéressent donc dans un premier temps au problème d'interaction fluide-structure constitué d'une hélice aux pales souples dans un écoulement d'eau. Nous mettons en évidence les lois régissant la déformation des pales lors de la rotation. L'efficacité de la propulsion est modifiée par ces déformations et une hélice à pales flexibles peut ainsi être rendue plus résiliente aux variations de vitesse que sa version rigide.

Dans un second temps, nous étudions la propulsion intermittente qui consiste à alterner les phases de propulsion actives et passives pour réduire le coût énergétique : dans notre cas, cela signifie actionner périodiquement l'hélice. Pour que la propulsion intermittente soit efficace il est crucial que la force de traînée s'exerçant sur le bateau soit réduite dans la phase passive. En utilisant une hélice capable de s'ouvrir et de se fermer passivement, nous montrons que le coût de la propulsion peut être réduit de 25% comparé à la propulsion continue à la même vitesse.

Abstract

This experimental thesis focuses on propeller propulsion through two new bio-inspired concepts: reconfiguration and intermittency. Reconfiguration involves making structures flexible to adapt to flow conditions. Previous results have shown that this deformation can be exploited to passively adapt to changing external conditions if the flexibility is appropriately chosen. This ability to change shape can also be exploited dynamically through intermittent propulsion, a strategy adopted by many fish and bird species to reduce the cost of locomotion.

The work presented here initially addresses the fluid-structure interaction problem of a propeller with flexible blades in a water flow. We highlight the laws governing the blade deformation during the rotation. These deformations modify the efficiency of propulsion, and a propeller with flexible blades can be made more resilient to velocity variations compared to its rigid version.

Next, we investigate intermittent propulsion, which involves alternating active and passive propulsion phases to reduce energy costs. In our case, this means periodically rotating the propeller. For intermittent propulsion to be effective, it is crucial to reduce the drag force acting on the boat during the passive phase. By using a propeller that can passively open and close, we demonstrate that propulsion costs can be reduced by 25% compared to continuous propulsion at the same speed.

Keywords
Bio-inspiration, Fluid-structure interactions, Energy
Bio-inspiration, Interaction fluide-structure, Énergie